PREPARATION OF NOBLE METAL FREE MIXED OXIDES: APPLICATIONS TO ENVIRONMENTAL CATALYSIS

PREPARATION D'OXYDES MIXTES A BASE DE METAUX ABONDANTS : APPLICATIONS POUR LA CATALYSE ENVIRONNEMENTALE

Acknowledgements

I would like to express my sincere gratitude to my supervisors Prof. Sebastien Royer and Prof. Jean-Philippe Dacquin for giving me the chance to perform the thesis work. During my period in France, they gave many helps for my work and living. It is my pleasure to work with them and study in "Catalytic Materials - MATCAT" research team.

I am also extremely grateful to my Chinese supervisor Prof. Hui Zhang. Thanks for his guidance and support during the five years study (Master and PhD) in Wuhan University. I wish to express my gratitude heartily to Prof. Jean-Francois Lamonier (Lille University, France) for the support to my experiments in catalytic oxidation of formaldehyde, and Prof. Anne-Sophie Mamede (Lille University, France) for the help of X-ray photoelectron spectroscopy analysis, as well to Dr. Jeremy Dhainaut (Lille University, France) for the discussion of experiments and results.

My sincere thanks also go to all my colleagues and friends from Laboratoire Unité de Catalyse et Chimie du Solide of Lille University and Advanced Oxidation Lab of Wuhan University for their kind help.

I gratefully acknowledge the fund support of China Scholarship Council (CSC) affiliated with the Ministry of Education of the P.R. China.

Finally, I would especially like to thank my family for always being there with encouragement and care.

Résumé

Au cours des dernières décennies, la degradation de l'environnement, en particulier la contamination de l'eau et la pollution de l'air, a été au centre des préoccupations mondiales. Il est devenu nécessaire de développer des procédés efficaces pour éliminer les polluants présents dans les eaux usées et dans l'air.

Les Procédés Avancés d'Oxydation (AOP), impliquant la formation d'espèces hautement réactives telles que les radicaux hydroxyles (HO•) et les radicaux sulfates (SO$_4$•$^-$), ont gagné en popularité en raison de leur capacité oxydante élevée permettant de dégrader une grande variété de molécules réfractaires. En plus de l'oxydant conventionnel H$_2$O$_2$, l'ozone est également une source potentielle de radicaux hydroxyles. Le peroxymonosulfate (PMS, HSO$_5^-$) de structure similaire à H$_2$O$_2$ peut être également décomposé pour former des radicaaux sulfate, d'autres espèces actives ayant la capacité à dégrader les contaminants organiques. Le procédé d'ozonation classique, et les systèmes catalytiques impliquant le peroxymonosulfate et les cycles redox des ions de métaux de transition (Fe^{2+}, Cu$^+$, Co^{2+}, *etc.*), souffrent de certains inconvénients intrinsèques dont la récuperation des ions métalliques, ce qui explique le développement de procédés catalytiques hétérogènes pour l'élimination des polluants organiques dans l'eau. Des problèmes similaires sont identifiés pour la dépollution en phase gazeuse. Bien que les procédés d'adsorption soient largement utilisés dans les installations industrielles pour éliminer les composés organiques volatils (COV), la durée de vie relativement courte des adsorbants et les exigences de traitement post saturation sont également des problèmes récurrents. La catalyse hétérogène s'impose alors comme une approche efficace et économiquement viable pour l'élimination des COV par oxydation complète en CO$_2$ et H$_2$O.

La recherche s'est naturellement orientée vers la préparation de catalyseurs peu

onéreux et composés d'éléments abondants. Les oxydes de type spinelle de formule générale AB_2O_4 et les pérovskites de formule générale ABO_3 (où A et B sont des ions métalliques) ont fait l'objet d'une attention particulière en raison de la disponibilité des éléments les constituant et de leur faible coût. Certaines propriétés telles que une flexibilité de composition, les états de valence des ions, les morphologies et les défauts de surface ont permis d'obtenir de bonnes performances catalytiques dans diverses applications (énergie, dépollution automobile). Par conséquent, l'utilisation de ces oxydes pour l'activation de l'ozone ou du PMS dans l'eau, mais également pour l'oxydation catalytique de COV dans l'air est particulièrement intéressante. Leur utilisation peut permettre un gain d'efficacité, favorisant leur développement industriel.

Dans ce travail, deux types de spinelles ($CuAl_2O_4$ et $CuFe_2O_4$) se sont révélées actives pour l'activation de l'ozone et du peroxymonosulfate, respectivement, en espèces réactives permettant de dégrader les colorants azoïques et le bisphénol A dans l'eau. Les pérovskites ($LaMnO_3$, et ses oxydes modifiés) ont d'abord été étudiées pour l'oxydation du formaldéhyde (HCHO) dans l'air à basse température. Les résultats ont indiqué que de nombreux facteurs affectent le système catalytique. Certains facteurs sont liés aux propriétés de surface des solides, tandis que d'autres sont liés aux conditions opérationnelles. Le manuscrit de doctorat est ainsi constitué de cinq études expérimentales:

Première étude: des oxydes mixtes $CuAl_2O_4$ ont été utilisés comme catalyseurs hétérogènes pour l'activation de l'ozone afin de dégrader les matières organiques dans l'eau. Les solides ont été caractérisés par SEM-EDS, physisorption d'N_2, DRX, IR-FT, MET et SPX. Nous avons démontré que le précurseur solide calciné à 300 ° C présentait la meilleure activité pour l'ozonation catalytique par rapport à la phase spinelle $CuAl_2O_4$ obtenue à des températures plus élevées. Ces performances ont été attribuées

aux meilleures propriétés texturales et à une densité plus élevée de sites actifs (groupes hydroxyles et acidité de Lewis). Le procédé oxyde-mixte / O_3 permet d'atteindre une élimination presque complète de la couleur de la solution (100 mg L^{-1}) à pH neutre en 25 min. La valeur de la vitesse de réaction a été déterminée à 0,112 min^{-1}, ce qui est nettement supérieur aux vitesses obtenues en présence d'oxydes simples (0,071 min^{-1} pour CuO / O_3, 0,074 min^{-1} pour Al_2O_3 / O_3). Cette performance catalytique est liée à un effet de synergie entre $\equiv Cu^{2+}$ et $\equiv Al^{3+}$, qui participent tous deux au mécanisme de formation des radicaux. Dans le mécanisme, les groupements hydroxyles et sites acides de Lewis seraient localisés sur les Al^{3+}, tandis que Cu^{2+} permettrait le transfert d'électrons avec l'ozone. L'interaction entre l'ozone chimisorbé et les groupements hydroxyles de surface initialement stabilisés sur $\equiv Al3+$ initie la génération d'espèces radicalaires réactives. Cette interaction conduit à la formation de $HO\bullet$ et de $O_2\bullet^-$ adsorbé sur la surface des sites Lewis. La réaction redox avec l'ozone est ensuite favorisée par la présence de $\equiv Cu^{2+}$ suivant la séquence des cycles redox $\equiv Cu^{2+}/\equiv Cu^+/\equiv Cu^{2+}$.

Deuxième étude: L'élimination du bisphénol A (BPA) dans l'eau par un processus d'oxydation impliquant du peroxymonosulfate (PMS) activé par des nanoparticules magnétiques (MNP) de $CuFe_2O_4$ est présentée. Les résultats indiquent qu'une élimination presque complète du BPA (50 mg/L) est possible en 60 min et une élimination du carbone organique total (COT) de 84,0% est atteint en 120 min à pH neutre en utilisant 0,6 g/L de $CuFe_2O_4$ MNPs et 0,3 g/L PMS. La production de radicaux réactifs (principalement des radicaux hydroxyles) a été confirmée par résonance paramagnétique électronique (EPR). Des mécanismes possibles de formation des radicaux dans le cas du système $CuFe_2O_4$ / PMS sont proposés sur la base des radicaux identifés et des résultats des analyses SPX. L'absence d'inhibition de la réaction par des piégeurs de radicaux libres tels que le méthanol et l'alcool tert-butylique suggère que

ces espèces peuvent ne pas être générées dans la solution, et les expériences avec des sondes au bleu de méthylène confirment que ce processus n'implique pas la génération de radicaux libres. Les radicaux responsables de la minéralisation du bisphénol A seraient ainsi liés à la surface, et seraient générés par un cycle redox en surface et impliquant à la fois Fe(III) et Cu(II).

Troisième étude: Une méthode simple sans tensio-actif, basée sur un processus de dissolution à l'acide utilisant une pérovskite comme précurseur, a été développée pour la preparation de matériaux méso / macroporeux. La transformation de la pérovskite de manganite ($LaMnO_3$) a été étudiée en utilisant les techniques de caractérisation suivantes: DRX, physisorption d'N_2, MEB, TEM-EDX, ICP, SPX et H_2-RTP. La transformation implique la dissolution du lanthane trivalent et du manganèse de la structure de la perovskite, et la dismutation des cations Mn^{3+} en solution en espèces MnO_2 et Mn^{2+}. Les propriétés oxydantes de l'acide utilisé pour le processus ont un impact important sur les propriétés texturales, de surface et redox des matériaux résultants. Plus précisément, l'extension de la durée de la lavage acide favorise l'augmentation de la surface spécifique et du volume des pores tout en développant des réseaux macro-mésoporeux interconnectés. Dans notre cas, le processus a permis l'obtention de la phase ε-MnO_2 avec une porosité hiérarchique. Des propriétés catalytiques intéressantes ont été mesurées pour ε-MnO_2 vis-à-vis de l'oxydation du HCHO, ainsi qu'une excellente stabilité catalytique. Ces performances peuvent être liées à des effets cumulés associés à la formation d'une morphologie méso / macroporeuse, une surface spécifique élevée, une réductibilité de surface améliorée, et une densité plus élevée d'espèces oxygénées actives de surface par rapport au précurseur pérovskite.

Quatrième étude: des pérovskites $LaMnO_3$ (LMO) promues par les métaux

alcalins et alcalino-terreux ont été préparées insertion à la synthèse ($La_{0.8}A_{0.2}MnO_3$ avec A = K^+, Na^+, Sr^{2+}, Ca^{2+}), imprégnation post-synthèse (LMO- Na) et traitement alcalin (LMO-OH). Les caractérisations RTP et SPX ont révélé que la réductibilité à basse température était favorisée dans les structures substituées (Sr, Na, K). Les pérovskites présentent un état d'oxydation moyen plus élevé sur le site B (Mn) et une formation plus importante d'espèces oxygène adsorbées, ainsi que de lacunes d'oxygène à la surface. Un effet remarquable des éléments substitués (K, Na, Sr) a été observé sur l'activité catalytique pour l'oxydation du formaldehyde. En comparaison, les activités des échantillons LMO-Na et LMO-OH étaient similaires à celle de LMO. Sur la base du T50 (correspondant à une conversion de HCHO de 50%), le classement des catalyseur en termes d'activité catalytique est : $La_{0.8}K_{0.2}MnO_3$ > $La_{0.8}Na_{0.2}MnO_3$ > $La_{0.8}Sr_{0.2}MnO_3$ > $LaMnO_3$ ≈ $La_{0.8}Ca_{0.2}MnO_3$ ≈ LMO-OH ≈ LMO-Na. Des tests de stabilité, dans des conditions humides et sèches, ont été effectués. Une désactivation progressive des pérovskites substituées (K, Na, Sr) a été observée, ce qui peut être dû à la perte d'espèces oxygène de surface et du reduction de la concentration de Mn^{4+} en surface. L'inhibition de l'adsorption du formaldehyde et de l'activation de l'oxygène à la surface du catalyseur pourrait également être à l'origine de la désactivation.

Cinquième étude: Une série de catalyseurs déficients en cation A, $La_{1-x}MnO_{3+\delta}$ (avec x = 0, 0.1, 0.2, 0.3 and 0.4) a été synthétisée pour étudier l'effet des lacunes cationiques de structure sur les propriétés plysico-chimiques des matériaux. Les résultats expérimentaux ont révélés que la diminution de la teneur en La, pour des rapports atomiques entre 1.0 et 0.8, entraîne la formation de lacunes et permet d'augmenter la concentration en espèce oxygène active sur la surface. Une diminution plus importante de la teneur en La ($La_{0.6}Mn$ and $La_{0.7}Mn$) entraîne la formation d'une phase pérovskite déficiente en La mais également la formation d'une phase externe

secondaire Mn_3O_4. La présence de Mn_3O_4 entraîne une augmentation de la concentration, de la mobilité et de la réactivité de l'oxygène de réseau. Ainsi, l'augmentation de la concentration en lacune cationique ainsi que la présence de Mn_3O_4 entraîne une amélioration de la réductibilité à basse température des matériaux, ce qui se reflète dans les propriétés catalytiques des matériaux pour l'oxydation du formaldéhyde (HCHO): le matériau le plus deficient en La est le matériau le plus actif catalytiquement. Ce matériau, $La_{0.6}Mn$, présente également d'excellentes stabilités sous milieu sec et sous milieu humide pendant 63 heures en réaction.

Abstract

Over the last decades, the deteriorating environmental issues, especially water contamination and air pollution, have triggered worldwide concerns. Hence, it is necessary to develop effective advanced techniques to remove pollutants either from wastewater or from gas phase.

Advanced oxidation processes (AOPs), based on the formation of highly reactive species such as hydroxyl radicals ($HO^\bullet$) and sulfate radicals ($SO_4^{\bullet-}$), have gained popularity due to their high oxidative capacity allowing to degrade a wide variety of refractory chemical molecules in wastewater. In addition to the conventional oxidant H_2O_2, ozone is also a good source of hydroxyl radicals. Meanwhile, the peroxymonosulfate (PMS, HSO_5^-) with similar structure to H_2O_2 can be decomposed to form sulfate radical, another kind of highly active species that can degrade organic contaminants. Classical ozonation or peroxymonosulfate catalytic systems based on transition metal ions redox cycles (Fe^{2+}, Cu^+, Co^{2+}, etc.) usually suffer from some intrinsic drawbacks. To resolve these issues, heterogeneous catalytic processes were applied for the removal of organic pollutants. Similar problematics are identified for gas phase depollution. Though adsorption processes are widely used in industrial plants to remove volatile organic compounds (VOCs) from exhaust gases, the relatively short lifetime of adsorbents or requirements of adsorbent regeneration are also a problem. In contrast, heterogeneous catalysis is proposed as an efficient and economically viable process for the removal of VOCs by complete combustion into CO_2 and H_2O.

The search for low-cost catalysts based on readily available elements has brought the materials such as spinels and perovskites to the forefront. Spinel type oxides with a general formula AB_2O_4, and perovskites with a general formula ABO_3 (where A and B are metal ions), have received particular attention due to their availability and low cost.

Some properties such as numerous compositions, valence states, morphologies and surface defects have demonstrated good catalytic performances in various research fields (i.e. energy, automotive depollution). Therefore, application of these oxides to efficiently activate ozone or PMS in water or for heterogeneous catalytic oxidation of toxic hydrocarbons in air is attractive. These will contribute to a gain in efficiency of the depollution processes in water or air, favouring their industrial development in a near future.

In this work, two kinds of spinels ($CuAl_2O_4$ and $CuFe_2O_4$) were evidenced as active catalysts for ozone and peroxymonosulfate activation, respectively, into reactive oxygen species to degrade azo dyes and bisphenol A in water, while the perovskites (raw $LaMnO_3$ and its modified oxides) were first studied to oxidize formaldehyde (HCHO) in gas totally at mild temperatures. Results indicated that many factors are affecting the heterogeneous catalytic system. Some are related to the surface properties of solids owing to the surface reaction occurring on materials surface, while others are related to the operating conditions. This PhD manuscript is constituted of five experimental studies:

First study: $CuAl_2O_4$ based mixed oxides were used as heterogeneous catalysts for ozone activation to degrade organics in aqueous solutions. The solids were thoroughly characterized by SEM/EDS, N_2 physisorption, XRD, FTIR, Pyridine-FTIR, TEM and XPS. We demonstrated that the solid precursor calcined at 300 °C exhibited the best catalytic ozonation activity with respect to $CuAl_2O_4$ spinel phase obtained at higher temperatures. Such performance was attributed to the better textural properties and a higher density of active sites (hydroxyl groups and Lewis acidity). Specifically, the mixed oxide/O_3 process allows to reach a near complete color removal of the dye solution (100 mg L^{-1}) within 25 minat neutral pH. Corresponding reaction rate value

was determined as 0.112 min^{-1} and was clearly higher compared to the single oxide ozonation process (0.071 min^{-1} for CuO/O$_3$ and 0.074 min^{-1} for Al$_2$O$_3$/O$_3$). Then, we proposed that such catalytic performance was related to a synergistic effect between $\equiv$Cu^{2+} and $\equiv$Al^{3+}, which took part in the mechanism of radical formation. In such mechanism, $\equiv$Al^{3+} could act as a reservoir for surface active sites such as hydroxyl groups and Lewis acid sites, while $\equiv$Cu^{2+} could provide the possibility of electron transfer with ozone for the enhancement of radical generation. We suggested that the interaction between chemisorbed ozone and surface hydroxyl groups initially stabilized on $\equiv$Al^{3+} initiated the generation of reactive radical species. This interaction led as well to the formation of surface adsorbed HO$^{\bullet}$ and few O$_2^{\bullet-}$ on $\equiv$Cu^{2+} Lewis acid sites. Besides, the interfacial redox reaction with ozone is favored by the presence of $\equiv$Cu^{2+}following the sequence of $\equiv$Cu^{2+}/$\equiv$Cu^{+}/$\equiv$Cu^{2+} redox cycles.

Second study: The removal of bisphenol A (BPA) in aqueous solution by an oxidation process involving peroxymonosulfate (PMS) activated by CuFe$_2$O$_4$ magnetic nanoparticles (MNPs) is reported herein. Results indicate that nearly complete removal of BPA (50 mg/L) within 60 min and 84.0% total organic carbon (TOC) removal in 120 min could be achieved at neutral pH by using 0.6 g/LCuFe$_2$O$_4$ MNPs and 0.3 g/L PMS. The generation of reactive radicals (mainly hydroxyl radicals) was confirmed using electron paramagnetic resonance (EPR). Possible mechanisms on the radical generation from CuFe$_2$O$_4$/PMS system are proposed based on the results of radical identification tests and XPS analysis. The lack of inhibition of the reaction by free radical scavengers such as methanol and *tert*-butyl alcohol suggests that these species may not be generated in the bulk solution, and methylene blue probe experiments confirm that this process does not involve free radical generation. Surface-bound, rather than free radicals generated by a surface catalyzed-redox cycle involving both Fe(III) and Cu(II),

are postulated to be responsible for the mineralization of bisphenol A.

Third study: A simple template-free method, based on a mineral acid etching process using perovskite as precursors, was successfully developed to obtain a series of 3D meso/macro-porous materials. The manganite perovskite ($LaMnO_3$) transformation was fully investigated using XRD, N_2 physisorption, SEM, TEM/EDS, ICP, XPS and TPR. This transformation proceeds through a soft-chemical process involving the dissolution of trivalent lanthanum and manganese from the perovskite structure and dismutation of Mn^{3+} cations into MnO_2 and Mn^{2+} species. Strength and oxidizing properties of the acid used as modifying agent strongly impact textural and redox surface properties of the resulting materials. Specifically, extending the acid etching duration promotes the surface area and pore volume of the materials while developing interconnected macro-mesoporous networks. In our case, this soft process allowed us to obtain the ε-MnO_2 phase with hierarchical porosity without any templates. Superior catalytic properties of ε-MnO_2 were observed toward HCHO oxidation as well as an excellent catalytic stability with respect to other macro-mesoporous counterparts. In the light of the experimental results, such performances can be related to cumulated effects associated to the formation of a meso/macro-porous morphology, surface area, surface redox ability and a higher density of active surface oxygen species compared to the perovskite precursors.

Fourth study: Alkali and alkaline earth metals-promoted $LaMnO_3$ (LMO) perovskites were prepared following addition of metal salts during the synthesis ($La_{0.8}A_{0.2}MnO_3$ with A = K, Na, Sr, Ca), post-synthesis impregnation (LMO-Na) and alkali treatment (LMO-OH). TPR and XPS characterizations revealed that low temperature reducibility was promoted by the substituted elements (Sr, Na, K), while the related perovskites show higher oxidation state ion at B-site (Mn) and higher

formation of adsorbed oxygen species, as well as oxygen vacanices on the surface. These results were corroborated by catalytic oxidation of formaldehyde (HCHO), with a remarkable effect of the substituted elements (K, Na, Sr) on the catalytic activity. In comparison, LMO-Na and LMO-OH activities were similar to LMO. Based on the T50 (corresponding to HCHO conversions of 50%), the overall catalyst ranking in terms of the catalytic activity was $La_{0.8}K_{0.2}MnO_3 > La_{0.8}Na_{0.2}MnO_3 > La_{0.8}Sr_{0.2}MnO_3 > LaMnO_3 \approx La_{0.8}Ca_{0.2}MnO_3 \approx$ LMO-OH $\approx$ LMO-Na. Stability tests, under humid and dry conditions, were conducted on the catalysts and a gradual deactivation of the substituted perovskites (K, Na, Sr) was observed, which may due to the loss of surface active oxygen species and high-valence Mn (Mn^{4+}). Besides, owing to the blocking effects caused by the adsorbed oxidation intermediates, the inhibition of adsorption and activation of molecule oxygen on catalyst surface might be also considered as the reason of deactivation. This phenomenon is critical to consider for the further development of alkali-modified perovskite catalysts. Consequently, this work provides new insights for the design of cost-effective perovskite-based catalysts for mild-temperature catalytic oxidation of HCHO.

Fifth study: A series of La-deficient $La_{1-x}MnO_{3+\delta}$ perovskites (with x = 0, 0.1, 0.2, 0.3 and 0.4) was directly synthesized to investigate the effect of cation vacancies on their physico-chemical properties. Experimental results revealed that La-deficiency induces perovskites with La and Mn vacancies for La/Mn atomic ratio between 1.0 and 0.8, and thus increases the concentration of active oxygen species at their surface. Further deficiency of lanthanum ($La_{0.6}Mn$ and $La_{0.7}Mn$) resulted however in the formation of La-deficient perovskites together with Mn_3O_4 as a secondary crystalline phase. The presence of Mn_3O_4 increases the concentration, the mobility and reactivity of the active (lattice) oxygen species. Additionally, both cation vacancy and the

presence of Mn_3O_4 improved the low-temperature reducibility of the materials. These characteristics were correlated to their catalytic activity for the oxidation of formaldehyde (HCHO), with the most La-deficient perovskite-based materials being the most active. The leading material ($La_{0.6}Mn$) could retain its high activity for 63 hours, either under dry or humid air.

Table of content

Chapter 1 Introduction

1.1 Background

In recent centuries, the expansion of human society along with the rapid industrialization has severely impacted the ecosystem, and has interrupted the harmony between human beings and the nature that has lasted for thousands of years. Today, numerous efforts are done to limit the impact of industrial chemical processes on the environment, including water resources and air quality, since there has been an increasing use of hazardous organic pollutants in multiple industrial areas such as the textile, leather goods, pharmaceutical industries, agriculture, food manufacture and other chemical usages [1-3]. Unfortunately, due to the characteristic of pollutants (biological resistance, chemical stability and limited biodegradability), they can hardly be removed efficiently using conventional waste treatments.

During the past few years, researchers never stopped the race to develop state-of-the-art technologies for water treatment, to provide clean drinking water for households and to deal with the polluted water bodies. Advanced oxidation processes (AOPs), based on the formation of highly reactive species such as hydroxyl radicals (HO$^{\bullet}$) and sulfate radicals (SO$_4^{\bullet-}$), have been recognized as effective methods for the removal of organic contaminants from groundwater or wastewaters due to their high oxidative capacity [4-7].

Generally, sulfate radicals possess higher redox potential (E^0= 2.5-3.1 V) than hydroxyl radicals (E^0 = 2.7 V) and are more desirable for organic removal [8, 9]. In comparison with H$_2$O$_2$, peroxymonosulfate (PMS, HSO$_5^-$, E^0 = 1.82 V) is relatively stable and facilitates storage and transportation [10]. Sulfate radicals can be generated by activating PMS using transition metals [8, 11]. However, this process being homogeneous, it may generate large amounts of sludge requiring ulterior separation and acidic conditions (pH 3-4). Consequently, search for alternative heterogeneous catalysts

3

(e.g., metal oxides) to efficiently activate PMS is of necessity and importance. The use of such solid ensures an easy recycling/separation of the catalyst from solution, limited water contamination, and no final sludge to be treated at the end of the process.

Ozone is also a powerful molecule and popular reagent, widely applied for the removal of various organic pollutants in water [12-14]. Usually organic compounds can be oxidized through direct reaction with ozone, and also via radical-mediated oxidation. To overcome the disadvantages of high selectivity and low reaction rate of sole ozonation, ozone can be combined with solid catalysts [14-18]. This way, ozone can be efficiently activated into HO$^{\bullet}$, which is the most reactive radical and is capable of unselectively reacting with almost all types of organics in water. This combination can not only increase the O_3 utilization rate but also enhance the mineralization of pollutants.

Formaldehyde (HCHO) is one of the dominating volatile organic compounds (VOCs) which are regarded as the most important indoor air pollutants [19, 20]. HCHO is a colorless gas that is flammable and highly reactive, mainly stemming from various building materials and household products such as paints, adhesives, pressed-wood products and other decorating materials [19-21]. The primary effects of acute exposure to HCHO are irritation of the eyes and the upper respiratory tract mucosa [21]. In 2004, the International Agency for Research on Cancer (IARC) classified HCHO as carcinogenic for humans (Group 1).

Heterogeneous catalytic oxidation is also considered as an attractive technology for VOCs (e.g., HCHO) abatement [22-24]. High oxidation efficiency, low energy needs, and easy setting make it promising in the field of indoor air purification. It overcomes disadvantages of a relatively short lifetime of adsorbent [25], and extra apparatus and additional operating cost of plasma technology [26] and photocatalytic oxidation [27]. Currently, the catalytic materials used for the catalytic oxidation of

HCHO are mainly metal oxide-supported noble metal (Pt, Pd, Rh, Au and Ag) catalysts [28]. However, their upscaling is restricted owing to their high cost. Thus, transition metal based catalysts are proposed to efficiently substitute these active noble metals in catalytic oxidation processes.

Spinel-type oxide AB_2O_4, in which A and B are transition metals [29], and perovskite-type oxides ABO_3, in which A is a rare earth and B is a transition metal [30], have demonstrated intrinsic magnetic, optical, electrical and catalytic properties, owing to their multiple compositions, electron configurations, exceptional thermal stability, electron mobility, and redox behavior [29-31]. In this work, in one hand, heterogeneous catalytic processes in the presence of different oxidants (ozone and PMS) and spinel-based catalysts were studied for water treatment. Aims of the study were evaluating the methods to overcome some disadvantages of the homogenous process, and it is very meaningful to insight into the mechanism of these processes using typical metal oxide spinel. As two types of common contaminants, azo dye C. I. Acid Orange 7 (AO7) and phenolic substance Bisphenol A (BPA) were selected as refractory probes to evaluate the catalytic activity of solids. On the other hand, manganese based perovskites ($LaMnO_3$ and its modified solids) were applied in indoor air purification, that is, mild temperature catalytic oxidation catalytic oxidation of HCHO in gas phase. This study is focused on the discovery of highly active materials *via* kinds of modifications for enhancing the catalytic activity of these materials in environmental application.

1.2 Motivation of this PhD work

In order to eliminate the impact of organic sewage and formaldehyde exhaust gas efficiently, a large number of physical, chemical or biological methods have been tried

to slove these environmental pollution problems. Among them, heterogeneous catalytic oxidation technology is more attractive due to its facility and high efficiency.

Currently, most catalysts used in modern technology and chemical industry are based on mixed metal oxides. The synthesis of specific tailor-made mixed oxides able to meet specific reactions is one of the main topics of research in heterogeneous catalysis. Achieving complex catalytic reactions requires a polyfunctional material with appropriate solid state, surface, and morphological properties.

As two typical composite metal oxides, spinel and perovskite might represent the most studied mixed-oxide structures, owing to their exceptional thermal stability, ionic conductivity, electronic structure, electron mobility, and redox behavior. In addition, their properties can be adjusted by controlling their structure, phase, composition, valence, morphology, and defects. In recent decades, some spinel and perovskite compounds have demonstrated their great potential in environmental pollution control and exhibited good catalytic activities. Therefore, it is essiental to further investigate their solid state surface chemistry as well as their catalytic performance, and importantly insight into their structure-activity relationship, which are the crucial points in heterogeneous catalytic oxidation.

This PhD work will carry out research on the application of composite oxides (spinel and perovskite) in heterogeneous catalytic systems for water and air treatment, aiming to provide more knowledge on the correlation between surface physicochemical properties and catalytic performance in the field of heterogeneous catalysis. These may be usefully applied in the design and the engineering of new high performance materials in the future.

1.3 Research goals and objective

The objective of this work was to investigate the removal of representative organic

pollutants following catalytic oxidation reactions using two types of catalysts –metal oxide spinels in aqueous phase and modified perovskites in gas phase. For water treatment, the effect of reaction parameters on oxidation effectiveness was evaluated and the AOP reaction mechanisms (catalytic ozonation and persulfate oxidation) were also clarified. For toxic gas remediation, the surface properties of modified perovskites and their performances in catalytic oxidation of HCHO were investigated. Also, emphasis was made on the structure-function relationship.

To meet these goals, the following specific goals were defined:

1. To elucidate the role of copper (Cu) and aluminium (Al) species in $CuAl_2O_4$ during the catalytic ozonation reaction, and to investigate the mechanism of this process as well as the effect of operation parameters.

2. To study the degradation and mineralization of BPA by a heterogeneous oxidation process ($CuFe_2O_4$/PMS) and to identify the main active species affecting the oxidation efficiency. Moreover, the influence of operation parameters and the role of copper (Cu) and iron (Fe) will be investigated, and the acute toxicity of BPA degradation products will be verified during catalytic oxidation.

3. To investigate the mechanism of acid etching on modified lanthanum manganite perovskite ($LaMnO_3$). The morphological, textural, structural, surface and redox properties of these solids along with their catalytic activities for HCHO oxidation will be explored.

4. To prepare alkali and alkaline earth metals-modified perovskites. The textural and redox properties of these solids and their catalytic activities on the oxidation of HCHO will be extensively examined. Moreover stability tests under humid and dry conditions will also be conducted on these catalysts.

5. To synthesize La-deficient $La_{1-x}MnO_{3+\delta}$ perovskites. The chemical and surface

properties of these oxides will be characterized and their catalytic activity for the oxidation of formaldehyde (HCHO) will be tested, with emphasis on the relationships between catalytic performances and surface properties.

1.4 Structure of the thesis

The whole thesis is divided into eight chapters, including the current introductive chapter.

Chapter 2 presents a review of recent research related to this work. Three parts are described:

2.1 Organic pollutants in the environment

2.2 Treatment methods in water and air

2.3 Oxides in heterogeneous catalysis – application in AOPs and oxidation

Chapter 3 and **Chapter 4** focus on heterogeneous AOPs in water.

Chapter 3 is entitled "Heterogeneous catalytic ozonation by spinel-type $CuAl_2O_4$ and its precursor". $CuAl_2O_4$ based mixed oxides were synthesized as catalysts for ozone activation to degrade organics in water. The solid precursor was found to show higher catalytic activity compared to $CuAl_2O_4$ spinel phase. Such performance was demonstrated to relate to the better textural properties and a higher density of active sites (hydroxyl groups and Lewis acidity). Based on the obtained experiments, the roles of $\equiv Al^{3+}$ and $\equiv Cu^{2+}$ for the enhancement of radical generation were further studied.

Chapter 4 is entitled "High-efficiency oxidation process involving peroxymonosulfate activated by $CuFe_2O_4$ magnetic nanoparticles". The removal of BPA in aqueous solution by an oxidation process involving PMS activated by $CuFe_2O_4$ was investigated. The effects of different operation parameters and the change of acute toxicity during the treatment were investigated. Additionally, possible mechanisms on the radical generation from $CuFe_2O_4$/PMS system are proposed based on the results of

radical identification tests and XPS analysis.

Chapter 5 to **Chapter 7** relate to heterogeneous catalytic oxidation in air.

Chapter 5 is entitled "Perovskite conversion into hierarchical porous ε-MnO2 via acid treatment: application to the formaldehyde total oxidation". This part focused on a simple acid etching modification successfully developed to obtain a series of 3D meso/macro-porous materials including perovskite, ε-MnO$_2$/perovskite and pure ε-MnO$_2$ utilizing LaMnO$_3$ perovskites as precursors. Their transformation was investigated comprehensively. The textural and redox properties of the resulting materials were also investigated. The final MnO$_2$ materials exhibited a superior catalytic activity on HCHO oxidation and an excellent catalytic stability, which were explained owing to cumulated effects of several factors.

Chapter 6 is entitled "Alkali and alkaline earth-promoted perovskites for formaldehyde total oxidation". In this part, alkali and alkaline earth metals-promoted LaMnO$_3$ perovskites were prepared to promote the catalytic activity of catalysts in oxidation of HCHO. Their reducibility, oxidation state of ion at B-site (Mn) and adsorbed oxygen species were quantified. Stability tests in catalytic oxidation of HCHOwere conducted on the catalysts.A gradual deactivation of the substituted perovskites (K, Na, Sr) was observed and the reason for this deactivation was also tentatively proposed.

Chapter 7 is entitled "La-deficient lanthanum manganite perovskites for catalytic oxidation of formaldehyde: impact of cationic vacancy?". In this study, a series of La-deficient La$_{1-x}$MnO$_{3+\delta}$ perovskites (with x = 0.1, 0.2, 0.3 and 0.4) was synthesized and applied for the catalytic oxidation of HCHO. The chemical compositionand surface properties of these oxides were studied. Results revealed that the cations (La and Mn) vacancy would induce more active oxygen species on the catalyst surface. In addition,

further deficiency of lanthanum (e.g., x = 0.3 or 0.4) was found to result in the formation of perovskite together with Mn_3O_4. The surface Mn_3O_4 might further increase the reactivity of the active (lattice) oxygen species. These observations correlated well with the evolution of catalytic activity for HCHO conversion.

Finally, **Chapter 8** is the "General conclusion and perspectives". Firstly, the overall results of this thesis are discussed and the conclusions are given. Then, perspectives of this work are proposed.

References

[1] Y.Q. Huang, C.K.C. Wong, J.S. Zheng, H. Bouwman, R. Barra, B. Wahlström, L. Neretin, M.H. Wong, Bisphenol A (BPA) in China: A review of sources, environmental levels, and potential human health impacts, Environment International, 42 (2012) 91-99.

[2] I.C. Yadav, N.L. Devi, J.H. Syed, Z. Cheng, J. Li, G. Zhang, K.C. Jones, Current status of persistent organic pesticides residues in air, water, and soil, and their possible effect on neighboring countries: A comprehensive review of India, Science of The Total Environment, 511 (2015) 123-137.

[3] T. Robinson, G. McMullan, R. Marchant, P. Nigam, Remediation of dyes in textile effluent: a critical review on current treatment technologies with a proposed alternative, Bioresource Technology, 77 (2001) 247-255.

[4] S. Yang, P. Wang, X. Yang, L. Shan, W. Zhang, X. Shao, R. Niu, Degradation efficiencies of azo dye acid orange 7 by the interaction of heat, UV and anions with common oxidants: Persulfate, peroxymonosulfate and hydrogen peroxide, Journal of Hazardous Materials, 179 (2010) 552-558.

[5] G.P. Anipsitakis, D.D. Dionysiou, M.A. Gonzalez, Cobalt-mediated activation of peroxymonosulfate and sulfate radical attack on phenolic compounds. Implications of chloride Ions, Environmental Science & Technology, 40 (2006) 1000-1007.

[6] G.P. Anipsitakis, T.P. Tufano, D.D. Dionysiou, Chemical and microbial decontamination of pool water using activated potassium peroxymonosulfate, Water Research, 42 (2008) 2899-2910.

[7] S. Miralles-Cuevas, D. Darowna, A. Wanag, S. Mozia, S. Malato, I. Oller, Comparison of UV/H_2O_2, UV/$S_2O_8^{2-}$, solar/Fe(II)/H_2O_2 and solar/Fe(II)/$S_2O_8^{2-}$ at pilot plant scale for the elimination of micro-contaminants in natural water: An economic assessment, Chemical Engineering Journal, 310 (2017) 514-524.

[8] G.P. Anipsitakis, D.D. Dionysiou, Degradation of organic contaminants in water with sulfate radicals generated by the conjunction of peroxymonosulfate with cobalt, Environmental Science & Technology, 37 (2003) 4790-4797.

[9] H. Sun, C. Kwan, A. Suvorova, H.M. Ang, M.O. Tadé, S. Wang, Catalytic oxidation of organic pollutants on pristine and surface nitrogen-modified carbon nanotubes with sulfate radicals, Applied Catalysis B: Environmental, 154-155 (2014) 134-141.

[10] T. Zhang, Y. Chen, Y. Wang, J. Le Roux, Y. Yang, J.-P. Croué, Efficient peroxydisulfate activation process not relying on sulfate radical generation for water pollutant degradation, Environmental Science & Technology, 48 (2014) 5868-5875.

[11] C. Liang, C.F. Huang, Y.J. Chen, Potential for activated persulfate degradation of BTEX contamination, Water Research, 42 (2008) 4091-4100.

[12] Y. Lee, U. von Gunten, Advances in predicting organic contaminant abatement during ozonation of municipal wastewater effluent: reaction kinetics, transformation products, and changes of biological effects, Environmental Science: Water Research & Technology, 2 (2016) 421-442.

[13] J. Nawrocki, B. Kasprzyk-Hordern, The efficiency and mechanisms of catalytic ozonation, Applied Catalysis B: Environmental, 99 (2010) 27-42.

[14] B. Kasprzyk-Hordern, M. Ziółek, J. Nawrocki, Catalytic ozonation and methods of enhancing molecular ozone reactions in water treatment, Applied Catalysis B: Environmental, 46 (2003) 639-669.

[15] S. Afzal, X. Quan, J. Zhang, High surface area mesoporous nanocast LaMO$_3$ (M=Mn, Fe) perovskites for efficient catalytic ozonation and an insight into probable catalytic mechanism, Applied Catalysis B: Environmental, 206 (2017) 692-703.

[16] Y. Wang, Y. Xie, H. Sun, J. Xiao, H. Cao, S. Wang, Efficient Catalytic ozonation over reduced graphene oxide for p-hydroxylbenzoic acid (PHBA) destruction: Active site and mechanism, ACS Applied Materials & Interfaces, 8 (2016) 9710-9720.

[17] J. Bing, C. Hu, L. Zhang, Enhanced mineralization of pharmaceuticals by surface oxidation over mesoporous γ-Ti-Al$_2$O$_3$ suspension with ozone, Applied Catalysis B: Environmental, 202 (2017) 118-126.

[18] F. Qi, Z. Chen, B. Xu, J. Shen, J. Ma, C. Joll, A. Heitz, Influence of surface texture and acid–base properties on ozone decomposition catalyzed by aluminum (hydroxyl) oxides, Applied Catalysis B: Environmental, 84 (2008) 684-690.

[19] B. Bai, Q. Qiao, J. Li, J. Hao, Progress in research on catalysts for catalytic oxidation of formaldehyde, Chinese Journal of Catalysis, 37 (2016) 102-122.

[20] J. Quiroz Torres, S. Royer, J.P. Bellat, J.M. Giraudon, J.F. Lamonier, Formaldehyde: Catalytic oxidation as a promising soft way of elimination, ChemSusChem, 6 (2013) 578-592.

[21] T. Salthammer, S. Mentese, R. Marutzky, Formaldehyde in the indoor environment, Chemical Reviews, 110 (2010) 2536-2572.

[22] J. Quiroz, J.M. Giraudon, A. Gervasini, C. Dujardin, C. Lancelot, M. Trentesaux, J.F. Lamonier,

Total oxidation of formaldehyde over MnO_x-CeO_2 catalysts: The effect of acid treatment, ACS Catalysis, 5 (2015) 2260-2269.

[23] X. Tang, Y. Li, X. Huang, Y. Xu, H. Zhu, J. Wang, W. Shen, MnO_x-CeO_2 mixed oxide catalysts for complete oxidation of formaldehyde: Effect of preparation method and calcination temperature, Applied Catalysis B: Environmental, 62 (2006) 265-273.

[24] J. Zhang, Y. Li, L. Wang, C. Zhang, H. He, Catalytic oxidation of formaldehyde over manganese oxides with different crystal structures, Catalysis Science & Technology, 5 (2015) 2305-2313.

[25] J.-P. Bellat, I. Bezverkhyy, G. Weber, S. Royer, R. Averlant, J.M. Giraudon, J.F. Lamonier, Capture of formaldehyde by adsorption on nanoporous materials, Journal of Hazardous Materials, 300 (2015) 711-717.

[26] W.J. Liang, J. Li, J.X. Li, T. Zhu, Y.Q. Jin, Formaldehyde removal from gas streams by means of NaNO2 dielectric barrier discharge plasma, Journal of Hazardous Materials, 175 (2010) 1090-1095.

[27] T. Noguchi, A. Fujishima, P. Sawunyama, K. Hashimoto, Photocatalytic degradation of gaseous formaldehyde using TiO_2 film, Environmental Science & Technology, 32 (1998) 3831-3833.

[28] L. Nie, J. Yu, M. Jaroniec, F.F. Tao, Room-temperature catalytic oxidation of formaldehyde on catalysts, Catalysis Science & Technology, 6 (2016) 3649-3669.

[29] Q. Zhao, Z. Yan, C. Chen, J. Chen, Spinels: Controlled preparation, oxygen reduction/evolution reaction application, and beyond, Chemical Reviews, 117 (2017) 10121-10211.

[30] S. Royer, D. Duprez, F. Can, X. Courtois, C. Batiot-Dupeyrat, S. Laassiri, H. Alamdari, Perovskites as substitutes of noble metals for heterogeneous catalysis: Dream or reality, Chemical Reviews, 114 (2014) 10292-10368.

[31] M.A. Peña, J.L.G. Fierro, Chemical structures and performance of perovskite oxides, Chemical Reviews, 101 (2001) 1981-2018.

Chapter 2 Literature review

2.1 Organic pollutants in the environment

Over recent decades, the increasing worldwide contamination of ecosystem with thousands of chemicals generated from industries becomes the key environmental problems facing humanity [1-4]. Between 1930s and 2000s, global production of artificial chemicals increased from 1 million to 400 millions tons each year [5]. The world has undergone the adverse consequences of uncontrolled development of human activities in industry, agriculture, transport and urbanization. The increase in consumer demand of living has enhanced pollution of water with a wide range of chemicals, such as pesticides, cosmetics, personal and household care products, pharmaceuticals, leachates, oil spills, among others [5-7], and of the air with VOCs, NO_x, SO_2, O_3, CO_2 and other greenhouse gases, and particulate matter [8,9]. Briefly, the growing environmental problems especially water and air pollution have aroused worldwide concerns.
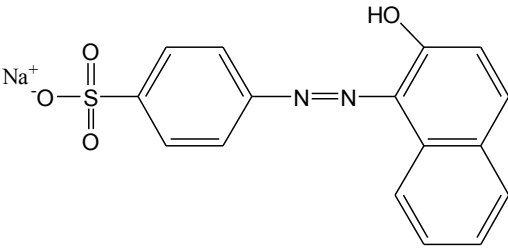
2.1.1 Refractory organic compounds in water - case of C. I. Acid Orange 7

Synthetic dyes are widely used in different fields, such as, in various kinds of the textile, paper, leather tanning, food processing, rubber, cosmetics, plastics and printing industries [10-12]. The environmental problems related with the textile industry have received increased attention for several decades, as it is one of the largest generators of contaminated effluents [13]. Worldwide, more than 100,000 commercial dyes are known with an annual production of over 7×10^5 metric tons [14]. Among those, about 10-15% of textile dyes are discharged in textile industrial effluents every year [15]. Dyes contained in wastewater usually have adverse impacts on Chemical Oxygen Demand (COD), Biological Oxygen Demand (BOD), Total Organic Carbon (TOC), colour, and lead to a wide rangeof pH (5-12). Moreover, the recalcitrance of some of those dyes, and in particular azo dyes, is of high concern. Basic dyes are greatly visible

with high intensity of colours evenin very little concentration [12, 16]. Dyes may affect the photo synthetic activity in aquatic life due to the decrease of light penetration, and also be toxic to some aquatic life due to the presence of aromatics, etc. In addition, dyes can also cause severe damage to human beings such as dys function of the kidney, reproductive system, brain and central nervous system [17].

Azo dyes are the most widely used dyes and represent over 60% of the total dyes [18]. Due to their large degree of aromaticity, they have a high degree of chemical, biological and photo-catalytic stability and resist break down due to time, exposure to sunlight, micro organisms, and water; that is, azo dyes are difficult to degrade once released into the aquatic systems. For instance, azo dyes are generally persistent in traditional biological processes [19]. Furthermore, the reductive cleavage of azo linkages is responsible for the formation of amines, which are classified as toxic and carcinogenic [12]. They can cause severe ecological and environmental problems [20]. Thus, the removal of dyes from water and wastewaters is important before they are mixed up with unpolluted natural water resources. As one of azo dyes, C. I. Acid Orange 7 (AO7) is a typical case (Table 2-1) [21]. They are characterized by the presence of azo groups ($-N=N-$) in association with aromatic systems and auxochromes, which are extremely stable and resistant to conventional wastewater treatment methods [22-24]. Therefore, the development of more efficient and destructive processes for the degradation of dye in water and wastewater has aroused significant interest.

Table 2-1 Main characteristics of acid orange 7
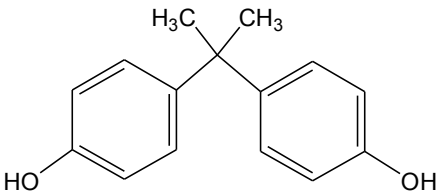
Dye name Abbreviation	Acid Orange 7 AO7
Chemical IUPAC name	Sodium 4-[(2E)-2-(2-oxonaphthalen-1-ylidene)hydrazinyl]benzenesulfonate
Chemical formula	$C_{16}H_{11}N_2NaO_4S$
Chemical structure	
Chromophore	Monoazo
Molecular weight (g/mol)	350.3
Maximum wavelength λ_{max} (nm)	484
Ionization	Acidic
pK_a	pK1, 11.4; pK2, 1.0

2.1.2 Endocrine disruptor (ED) in water - case of bisphenol A

The concept of endocrine disruptor was proposed 25 years ago [25], when various observations of deleterious influences on wildlife or humans were concluded, in association with the intensive use of pesticides in agriculture [26]. The potentially detrimental reproductive effects of these compounds on wildlife or humans werewidely accepted [27, 28]. It refers that synthetic chemical products can affect the operation of the endocrine system by different ways including mimic or block a hormone receptor, generating unexpected harmful effects on animal or human health [26, 29]. In recent years, endocrine disruption has been a major issuein environmental research. Bisphenol A (BPA), a proven endocrine disruptor, is the common name for 2,2 - (4,4′-dihydroxydiphenyl) propane, 4,4′ - isopropyllidenediphenol, alternatively, 2,2′- bis(4-

hydroxyphenyl) propane (Table 2-2) [28,30]. It has some important properties, such as low vapor pressure, moderate water solubility, and low volatility.

Table 2-2 Main characteristics of Bisphenol A

Dye name	Bisphenol A
Abbreviation	BPA
Chemical IUPAC name	2,2-(4,4′-dihydroxydiphenyl) propane, 4,4′-isopropyllidenediphenol
Chemical formula	$C_{15}H_{16}O_2$
Chemical structure	
Molecular weight (g/mol)	228.3
Solubility in water at 298K (mg/L)	120
Melting point (K)	330.4
Aquatic toxicity on algae (selenastrum capricornutum) (EC/LC_{50}) (mg/L)	2.7-3.1
pK_a	pK1, 9.59; pK2, 10.2

BPA was first reported in 1891 and then synthesized by Zincke in 1905, from phenol and acetone [30, 31]. Being an important industrial chemical in the manufacture of polycarbonate (e.g., plastics) and epoxy resins, BPA is widely used in various products of daily life, including digital media (typically CDs and DVDs), automobiles, electronic equipment, sports safety equipment, construction glazing, tableware, reusable bottles (e.g., baby bottles) and food storage containers [29, 31], and also used in the internalcoating of food and beverage cans. Especially, children's toys may contain BPA, beingused as an additive in other types of plastic [30]. More than 3.6×10^6 ton of BPA are produced annually and approximately 100 tons, may be released into the environment every year [47, 48]. BPA is considered as one of the highest amounts of chemicals produced in the world [31].

Due to the massive scale of its utilization, BPA contamination is detected in various environmental matrices such as groundwater, surface water, soil, sediments, and air [29, 34]. There are various harmful impacts of the BPA exposure onto the living biota [29]. In case of human, BPA can disrupt normal cell function by acting as an estrogen agonist [35], as well as an androgen antagonist [36]. BPA may affect human development throughout the fetal period [37]. Higher BPA exposure in humans could even induce carcinogenesis and epigenetic modifications [38]. Consequently, it is necessary to remove BPA from wastewaters, before it is discharged into surface waters. There are various conventional approaches that have been used in the removal of BPA. However, the overall efficiency and feasibility were constantly compromised by using conventional biological, physical and chemical methods [39,40]. As emerging methods, advanced oxidation processes (AOP) are considered good alternatives for treating waters with biorefractory organic pollutants.

2.1.3 Volatile organic compounds in air - case of formaldehyde

Volatile organic compounds (VOCs) are organic compounds with vapor pressure of over 10.3 Pa at normal temperature (293.15 K) and pressure (101.325 kPa) [41]. VOCs are among the most common air pollutants emitted from a wide range of outdoor and indoor sources, together with sulphur oxides, nitrogen oxides, carbon monoxide and particulate matters (PM). Outdoor sources include but are notlimited to chemical industries, food processing, paper production, petroleum refineries, transportation, automobile manufacturers, textile manufacturers, solvents, electronic component plants, and cleaning products [41]. Indoor sources include household products, office supplies, insulating materials, pressed woods, woodstoves, and leaks from piping [42-44].

Formaldehyde (HCHO) is one of the dominating VOCs, which isregarded as the most important indoor air pollutants.The primaryeffects of acute exposure to HCHO

are irritations of the eyes and mucosa of the upper respiratory tract [45]. The high solubility of HCHO in water causes rapid absorption in gas trointestinal and respiratory tracts [46]. In 2004, the International Agency for Research on Cancer (IARC) has classified HCHO as carcinogenic for humans (Group 1). Industrially, HCHO is produced on a large scale by the selective catalytic oxidation of methane or methanol [47]. More than 65 % of the total HCHO is used to formulate resins. HCHO also finds applications in the manufacture of disinfectants, antiseptics, dyes, artificial silk, glass mirrors, explosives, and textiles. In our environment (air or water) HCHO usually stems from natural and anthropogenic sources. For instance, the plants combustion is the main source of bio-based HCHO and vehicles exhausts (gasoline and diesel) produce most of the emissions from human activities. Although the associated quantities of HCHO are small, cigarettes moke, the use of wood stoves emitting biomass fuel smoke, and some residential cooking methods constitute sources of indoor air contamination [46]. It is noteworthy that HCHO can be emitted from various building materials and household products such as paints, textiles, adhesives, pressed-wood products (plywood, fiber board and particle board) and other decorating materials [47, 48].
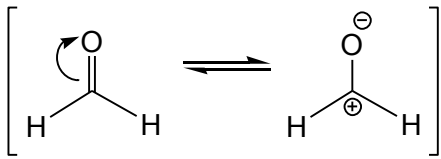
The main physical and chemical properties of HCHO are shown in Table 2-3 [46]. Formaldehyde has a dipolar resonance structure, which makes the moleculea typical electrophile. At room temperature, HCHO is a colorless gas with a strong, pungent, suffocating, and irritating odour. In addition, it is flammable with ignition temperature of 430 °C, highly reactive and can form explosive mixtures with air [49]. HCHO is soluble in water, alcohols, diethyl ether, acetone and other polar solvents. In aqueous solution, methyleneglycol $[CH_2(OH)_2]$ and polymethylene glycols $[H(CH_2O)_nOH]$ are readily formed [50]. Apart from polymerization, there are also some important reactions involving HCHO [50, 51], such asreaction with ammonia to form hexamethylene

tetramine (Eq. 2-1), Cannizzaro reaction (Eq. 2-2), aldol reaction (Eq. 2-3) and Tischenko reaction (Eq. 2-4).

$$6HCHO + 4NH_3 \rightarrow (CH_2)_6N_4 + 6H_2O \qquad (2-1)$$

$$2HCHO + H_2O \rightarrow CH_3OH + HCOOH \qquad (2-2)$$

$$2HCHO \rightarrow HOCH_2CHO \qquad (2-3)$$

$$2HCHO \rightarrow HCOOCH_3 \qquad (2-4)$$

In the gas phase, HCHO can undergo various reaction pathways. The lifetimes of HCHO (τ) against several reactions were calculated [52] with respect to photolysis ($\tau = 4$ h), reaction with HO$^\bullet$ radical ($\tau = 1.2$ days), reaction with the NO$_3^\bullet$ radical ($\tau = 80$ days), and reaction with O$_3$ ($\tau > 4.5$ years).

Table 2-3 Physical and Chemical Properties of formaldehyde

Chemical IUPAC* name	Formaldehyde
Synonyms	methanal, methyl aldehyde, methyl oxide
Chemical formula	HCHO, CH$_2$O
Chemical structure	
Molecular weight (g/mol)	30.03
Solubility	soluble in water, ethanol, ether, acetone
Melting point (°C)	-92
Boiling point (°C)	-21
Henry's law constant at 25 °C (M atm^{-1})	2.5×10^3
Vapor pressure at 25 °C (mmHg)	3.883
conversion factor	0.1ppm = 124.8μg m^{-3} (293 K, 1013mbar) 1μg m^{-3}= 0.815 ppb (293 K, 1013 mbar)

*IUPAC:International Union for Pure and Applied Chemistry.

2.2 Treatment methods in water and air

2.2.1 Advanced oxidation processes (AOPs) in water

Nowadays, advanced oxidation processes (AOPs) have attracted intensive attention in wastewater treatment and soil remediation owing totheir high efficiencies and intrinsic superiority for the complete degradation of organic pollutants over other traditional treatment processes [53-57]. Fenton or Fenton-like reactions as one of AOPs can remove pollutants efficiently due to the production of hydroxyl radicals.

The classical Fenton reaction describes a catalytic process for the generation of hydroxyl radicals (HO$^{\bullet}$) from hydrogen peroxide (H$_2$O$_2$) and isbased on an electron transfer between H$_2$O$_2$ and iron ionsacting as homogeneous catalyst [58].

$$Fe^{2+} + H_2O_2 \rightarrow Fe^{2+} + HO^{\bullet} + OH^- \qquad k = 63{\sim}76 \ M^{-1}s^{-1} \qquad (2\text{-}5)$$

$$Fe^{3+} + H_2O_2 \rightarrow Fe^{2+} + HO_2^{\bullet} + H^+ \qquad k = 0.001{\sim}0.01 \ M^{-1}s^{-1} \qquad (2\text{-}6)$$

The further reaction of HO$^{\bullet}$ with an organic substrate (R-H) forms an organic radical (R$^{\bullet}$), which subsequently undergoes different chemical reaction to form aseries of oxidation products [59]. The HO$^{\bullet}$ reacts in well-known ways withorganic compounds, always by abstracting H from C-H, N-H, or O-H bonds, adding to C=C bonds, or adding to aromatic rings [60]. The organic intermediates generated in the first stage of the oxidation may react further with HO$^{\bullet}$ and O$_2$ (reaction of R$^{\bullet}$ with O$_2$ is very fast at rate constant of ${\sim}10^9 \ M^{-1}s^{-1}$), with the overall process resulting in the oxidation of all organics into CO$_2$, H$_2$O, and inorganic acids [56].

In recent decades, ozone based AOPs are widely applied for the removal of various organic micropollutants in water and wastewatertreatment. Furthermore, ozonation has been intensively tested as an advanced wastewater treatment technology in laboratory-, pilot- and full-scale studies [55, 61-63]. Ozone, as one of the powerful oxidants (2.07 V), can oxidize or degrade organic pollutants through two ways: (1) direct electrophilic

attack by molecular ozone; (2) indirect attack by HO$^{\bullet}$ radicals, which were generated via a chain reaction mechanism during ozone decomposition process [63]. Ozonation alone has several disadvantages which limit its application [55, 63]. Firstly, the reactions between O_3 and pollutants are selective, and most of oxidation process is slow and incomplete; secondly, the O_3 is unstable in water with relatively low solubility, resulting in low utilization rate.

In order to solve these problems, catalytic ozonation (homogeneous *vs* heterogeneous) has received increasing attention, especially for the degradation of refractory organic pollutants. Ozone can be catalytically converted into HO$^{\bullet}$, which is the most reactive radical and is capable of unselectively reacting with almost all types of organics in water. The catalysts proposed for homogeneous catalytic ozonation process are transition metals including Fe^{2+}, Mn^{2+}, Ni^{2+}, Co^{2+}, Cu^{2+}, Ag^+, Zn^{2+}. The reaction rate, the selectivity and O_3 consumption in this process are determined by the nature of transition metal [61]. Generally, two main processes about the mechanism of homogeneous catalytic ozonation have been proposed: the free radicals were generated due to the ozone decomposition activated by active metal ions, and complexes formation between the catalyst and organics and final oxidation of the complex. Although the catalytic process using homogeneous catalyst is highly efficient for destruction of organic compounds, it also has some drawbacks such as metal leaching, generation of sludge and pH limits (requirement of pH $\sim$ 3). Consequently, the heterogeneous catalytic ozonation process with the use of solid catalysts is more promising.

Catalysts used in heterogeneous catalytic ozonation mainly include carbon materials (activated carbon, carbon nanotube, grapheme and so on) [64,65], metal oxides, metals/metal oxides on supports and natural minerals [55]. Among these

catalysts, metal-based catalysts, such as MgO [66], CuO [67], FeOOH [68], manganese oxide [69], cobalt oxide [70], and alumina oxides [71] and so on, were mostly studied in the catalytic ozonation process. However, we found that the catalytic activity of sole metal oxides (CuO, Fe_2O_3, Al_2O_3, etc.) was not effective in removing organic pollutants. To enhance the efficiency of reactive radicals generation, search for alternative more efficient heterogeneous catalysts to activate ozone is of necessity.

As an alternative to the hydroxyl radicals (HO$^{\bullet}$), the sulfate radicals (SO$_4^{\bullet-}$) based AOPs have received increasing interest in both research and application for the remediation of organic contaminants in groundwater or wastewaters [57]. Generally, sulfates radicals possess higher redox potential ($E_0 = 2.5\text{-}3.1$ V) than hydroxyl radicals ($E_0 = 2.7$ V) and are thus more desirable for organics removal [58]. Sulfate radicals can be generated by activating peroxymonosulfate (PMS, HSO_5^-). Potassium salt of PMS is stabled in triple salt (Oxone, $2KHSO_5 \cdot KHSO_4 \cdot K_2SO_4$) [73]. PMS is a white solid powder applied to energy storage and transportation. It is relatively stable when pH is less than 6. However, at pH 9, it showed the poorest stability wherehalf of HSO_5^- transfers to SO_5^{2-} [57]. PMS can be easily dissolved in water and the water solution becomes acidic. As shown in Table 2-4, it has asymmetrical structure with the distance of O-O bond of 1.453 Å. The bond energy is estimated to be in the range of 140-213.3 kJ/mol [57, 74, 75].

Table 2-4 Characteristics of peroxymonosulfate (PMS)

Chemical name	Peroxymonosulfate
Synonyms	Coroat, monopersulfate, Oxone, Curex
Chemical formula	HSO_5^-
CAS Number	10058-23-8
Chemical structure	

Molecular weight (g/mol)	113.07 (614.7 as Oxone)
Solubility at 20 °C (g/L)	> 250
Physical description	white crystallline solid
Redox potential (V)	1.82
pK$_a$	pK1, nearly 0; pK2, 9.4

Sulfate radicals can be generated by activating PMS using heat [76], alkaline ions [77], ultraviolet [78], transition metal ions [53], carbon based materials [79], metal oxides including metal oxide-supported materials [80-82] and hybrid activation [83, 84]. In 1956, Ball and Edwards reported the decomposition of PMS by cobalt ions for the first time [85]. Until 2003, Anipsitakis and Dionysiou first reported a Co^{2+}/PMS process successfully used to generate sulfate radicals for the degradation of organic compounds [53]. In addition, a lot of different transition metals (Ni^{2+}, Fe^{3+}, Mn^{2+}, V^{3+}, Ce^{3+}, Fe^{2+}, Ru^{3+}) for PMS activation have been also found [54]. For instance, the following reaction of Co^{2+} with PMS is suggested to generate sulfate radicals according to Eq. (2-7).

$$Co^{2+} + HSO_5^- \rightarrow Co^{3+} + SO_4^{\bullet-} + OH^- \qquad (2\text{-}7)$$

After these basic studies by Dionysiou's group, lots of researchers have attempted to clarifydifferent aspects of PMS activation by transition metals for degradation of organic pollutants.The mechanism of PMS activation by homogenous metal catalysts isschematically illustrated as following [86].
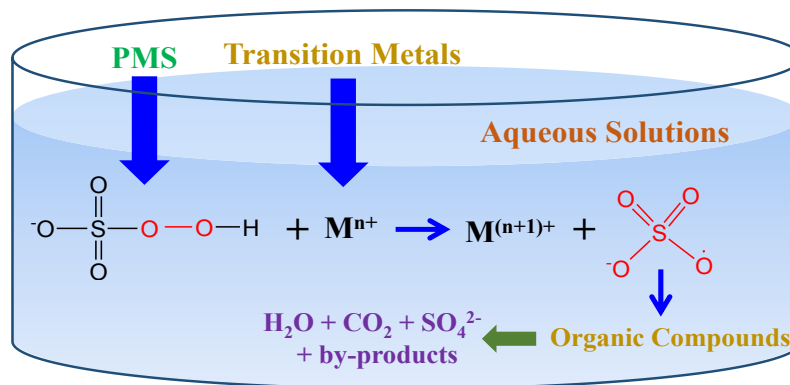
Figure 2-1 The scheme of PMS activation by transition metals as homogeneous catalyst

Similar to other homogeneous processes in Fenton and ozonation systems, some limitations exist when applying homogenous catalysts herein. For example, this process may lead to the formation of large amounts of metal ion sludge, it requires acidic condition ($pH \leq 4$), the catalyst recovery is difficult and it could form secondary pollutants. Comparatively, the solid catalyst can be readily separated from liquid phase and it is less harmful to the environment. For PMS activation, various heterogeneous catalysts have been applied based on different carbon catalysts and transition metals catalysts. In heterogeneous catalytic process, the surface of the catalyst plays an important role as reactions occur at the surface. Briefly, the development of efficient solid catalysts, as well as the investigation of activation mechanism are always deserved to investigate.

2.2.2 Catalytic oxidation of formaldehyde in air

Indoor air purification is of particular important for human health, comfort and productivity, because people spend >80% of their time indoors, including living and working places such as houses, offices, and workshops [87]. There are different international guidelines and recommended thresholds for indoor air HCHO concentrations [46]. The World Health Organization (WHO) proposes a short-term (30 min) HCHO exposure limit of 0.1 μg/L for the avoidance of sensory irritation and a long-term exposure limit of 0.2 μg/L for protection against health effects [88]. To meet

the rigorous requirement of environmental regulations, many techniques have been developed to remove HCHO, improving indoor air quality and safeguarding human health, for instance, adsorption [89], plasma technology [90], photocatalytic oxidation [91] and thermal catalytic oxidation [92].

Adsorption processes require adsorbent regeneration as an additional step, and consequently a final degradation step is needed. For plasma technology and photocatalytic oxidation, large equipment such as a light source, plasma equipment is needed, making it a quite complicated processes and largely increases costs [93]. In contrast, catalytic oxidation is a promising technique, and has advantages such as high removal efficiency, simple equipment, wide application scope, and no secondary pollution. HCHO can be totally oxidized to CO_2 and H_2O.

The catalytic materials for HCHO oxidation are divided into two main types: supported noble metals (e.g., Pt, Pd, Au and Ag), and supported or unsupported transition- metal oxide catalyst systems [48]. Noble metal materials attract much attention because of their excellent low- temperature oxidation activities. They are usually loaded on supports (TiO_2, SiO_2, Al_2O_3, CeO_2, ZrO_2, ZSM-5, SBA-15 etc.) because precious metals themselves are easily volatilized, oxidized, and sintered [47, 48, 93].

There is no general mechanism for oxidation of VOCs due to the different properties of pollutants and reaction conditions [95]. However, literatures concerning the oxidation of VOCs over supported noble metals report the following three typical mechanisms [43, 93, 96] (Fig. 2-2). (i) Langmuir-Hinshelwood (L-H), (ii) Eley-Rideal (E-R) and (iii) Mars-Van Krevelen (MVK) mechanisms. According to the L-H mechanism, the surface reaction occurs between two adsorbed reactant molecules on analogous active sites. In the E-R mechanism, adsorbed oxygen species react with a

pollutant molecule in the gas phase. In the MVK mechanism, a two-stage redox process occurs: (1) the catalyst is partially oxidized by O_2 from the gas phase (it is a nonequilibrium dissociative adsorption of O_2 on the surface) to form surface oxygen (O*), and then (O*) reacts with the gaseous organics and/or the organics weakly adsorbed on the surface, and (2) meanwhile the oxidized catalyst is reduced by the organic molecule [97-99].
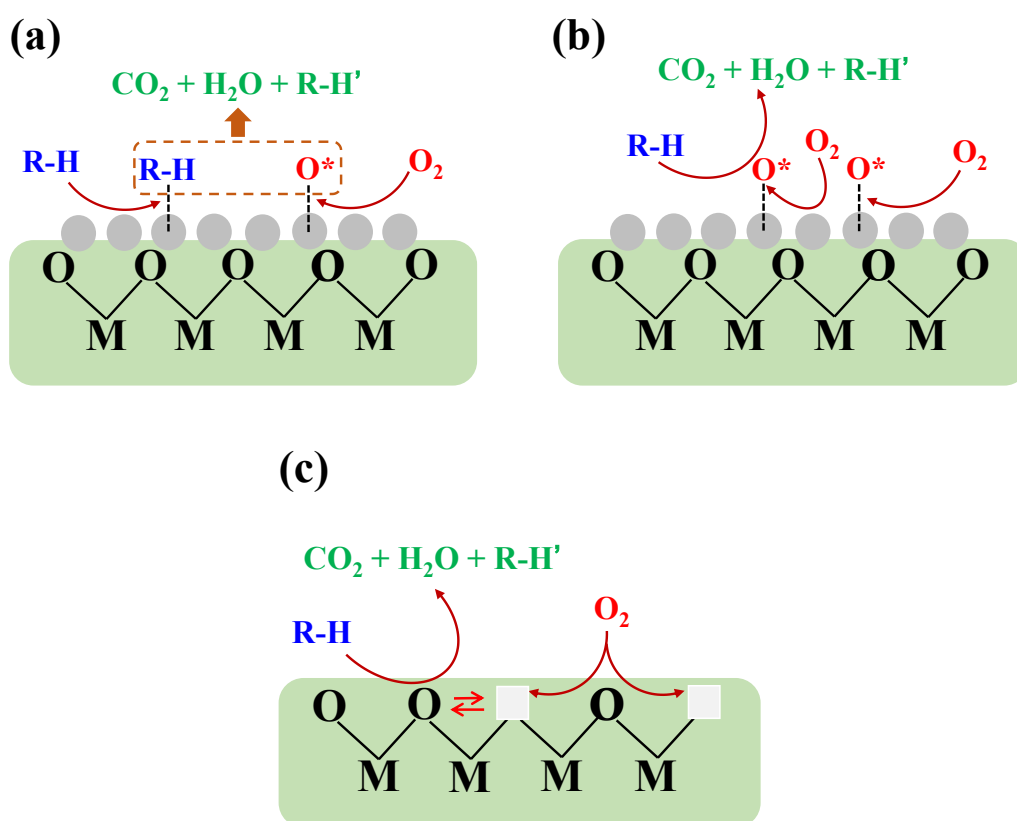
Figure 2-2 Schematic diagram of (a) L-H mechanism, (b) E-R mechanism, (c) MVK mechanism

Though the activity of noble metal catalysts is higher (Table 2-5), their industrial applications are restricted by their high costs, limited resources, and poor thermal stabilities [100]. Instead, transition metal oxides were highlighted as very powerful systems for mild temperature oxidation reactions. Some conventional transition metal-based catalysts have been reported to show good catalytic activities for HCHO oxidation (Table 2-6). For example, Sekine first reported the catalytic oxidation of

HCHO over metal oxide catalysts at room temperature [101], including CoO, MnO$_2$, TiO$_2$, CeO$_2$, and Mn$_3$O$_4$. Besides, MnO$_2$ was described to exhibit the highest catalytic activity. Mn based oxide is one of the most widely studied transition metal catalyst for the oxidation of HCHO [102], owing to its high catalytic activity, existence in various crystal morphologies such as α-, β-, γ-, and δ-MnO$_x$ [103] and different tunnel assemblies (1D tunnels, layered structures such as birnessite and buserite and 3D spinel tunnel structures) [104].

Table 2-5 Survey of the conditions for catalytic oxidation of HCHO on noble metal catalysts

Catalyst	Reaction conditions	T50 (°C)	Ref.
Pt/TiO$_2$	100 ppm of HCHO, GHSV (gas hourly space velocity): 50000~200000 h^{-1}, 20 vol% O$_2$	R.T.	[105,106]
Rh/TiO$_2$		50	
Pd/TiO$_2$		70	
Au/TiO$_2$		90	
Pd/Beta	40 ppm of HCHO, GHSV: 50000 h^{-1}, 20 vol% O$_2$, 3% H$_2$O	< 40	[107]
Pd/USY		< 40	
Pd/ZSM-5		70	
Pd/HM10		> 140	
Pd/Zeo-13X		< 40	
Pd/Al$_2$O$_3$		< 40	
Ag/SBA-15	1000 ppm of HCHO, GHSV: 15000 mL g$_{cat}^{-1}$ h^{-1}, 15 vol% O$_2$	50	[108]
Ag/MnO$_x$-CeO$_2$	580 ppm of HCHO, GHSV: 30000 mL g$_{cat}^{-1}$ h^{-1}, 18 vol% O$_2$	70	[109]
Ag/CeO$_2$		90	
Ag/MnO$_x$		115	
Au/CeO$_2$	0.06% HCHO, GHSV: 32000 mL g$_{cat}^{-1}$ h^{-1}	90	[110]
Pt/Fe$_2$O$_3$	100-500 ppm of HCHO, GHSV: 60000 mL g$_{cat}^{-1}$ h^{-1}	R.T.	[111]
2D Au/Co$_3$O$_4$-CeO$_2$	200 ppm of HCHO, GHSV: 55000 h^{-1}, 22 vol% O$_2$	R.T.	[112]
2D Au/Co$_3$O$_4$		R.T.	
2D Au/CeO$_2$		-	
Ag/CeO$_2$ nanosperes	810 ppm of HCHO, GHSV: 84000 h^{-1}, 20 vol% O$_2$	90	[113]

Ag/CeO$_2$ bulk particles		140	
Ag/CeO$_2$ (50:50)	0.42% HCHO, 0.074% CH$_3$OH GHSV: 21000 h^{-1}, 19.9% H$_2$O, 62.7% N$_2$, 16.9% O$_2$	< 150	[114]
Ag/CeO$_2$ (20:80)		< 150	
Ag/CeO$_2$ (10:90)		< 150	
Ag/CeO$_2$ (5:95)		< 150	
Pt-Ag/HZSM-5 (nanoscale HZSM, Pt:Ag = 1:1)		R.T.	[115]
Pt-Ag/HZSM-5 (medium scale HZSM, Pt:Ag = 1:1)		~40	
Pt-Ag/HZSM-5 (microscale HZSM, Pt:Ag = 1:1)		~120	
Pt-Ag/HZSM-5 (nanoscale HZSM, Pt:Ag = 1:3~3:1)		R.T.	
Ag/HZSM-5 (nanoscale HZSM)		> 200	

Catalytic redox processes on metal oxides are often described in terms of a redox mechanism, consisting of two successive steps [47]:

$$\text{RED}_{(s)}\text{-O} + \text{HC} \rightarrow \text{RED}_{(s)}\text{-}\square + \text{oxidized products} \tag{2-8}$$

$$\text{RED}_{(s)}\text{-}\square + 0.5\ \text{O}_2\ (g) \rightarrow \text{RED(s)-O} \tag{2-9}$$
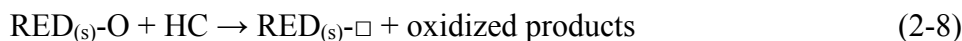
In this cyclic mechanism, the surface of oxidic catalyst ($\text{RED}_{(s)}$-O) is reduced with the oxidation of hydrocarbon (HC) (Eq. (2-8)). The so-formed reduced site ($\text{RED}_{(s)}$-$\square$) can return to its initial state via re-oxidation through consumption of gaseous O$_2$ (Eq. (2-9)) or through diffusion of oxygen ions from the bulk to the surface. That is, the reduction and re-oxidation of oxides occur simultaneously by providing surface oxide ions and taking up oxygen from the gas phase. A common feature of these oxides is the presence of multiple oxidation states in the structure, leading to the ability of the cation to undergo reversible oxidation and reduction. Of note, the activity of the catalyst for deep oxidation depends on the type of oxygen involved in the reaction. Various oxygen

species may be present on the oxide surfaces [47]: O_2 (adsorbed molecule), O (adsorbed neutral atom), O_2^- (superoxide anion), O_2^{2-} (peroxide anion), O_3^- (ozonide), or O^- (ion radical). Some of these aspects, as well as the redox mechanisms developed by M-K mechanism [98], are discussed above.

Due to inferior surface properties, metal oxides in the conventional bulk form always possess relatively low catalytic activity for HCHO oxidation. Interestingly, nanostructured transition metal oxide catalysts with similar compositions to their bulk counterparts exhibit improved morphologies and surface properties and hence higher activities for HCHO oxidation (Table 2-6). Thus, current investigations on transition metal-based catalysts are focused on developing materials with enhanced morphologies, structures or improved surface properties.

Table 2-6 Survey of the conditions for catalytic oxidation of HCHO on transition metal catalysts

Catalyst	Reaction conditions	T50 (°C)	Ref.
Pyrolusite (β-MnO$_x$ with 1×1 tunnel)	400 ppm of HCHO, GHSV: 18000 h^{-1}, 10 vol% O$_2$, N$_2$ balance	150	[116]
Cryptomelane (α-MnO$_x$ with 2×2 tunnel)		110	
Todorokite (3×3 tunnel)		140	
Cocoon-like MnO$_2$	460 ppm of HCHO, GHSV: 20000 mL g$_{cat}^{-1}$ h^{-1}	130	[117]
Urchin-like MnO$_2$		120	
Nest-like MnO$_2$		110	
α-MnO$_x$	170 ppm of HCHO, GHSV: 100000 mL g$_{cat}^{-1}$ h^{-1}, 20 vol% O$_2$, 25% Relative humid with N$_2$ balance	~90	[103]
β-MnO$_x$		~140	
γ-MnO$_x$		~125	
δ-MnO$_x$		~60	
3D-Co$_3$O$_4$	400 ppm of HCHO, GHSV: 30000 mL g$_{cat}^{-1}$ h^{-1}, 20 vol% O$_2$	< 110	[118]
2D-Co$_3$O$_4$		< 130	
Co$_3$O$_4$ nanopaticles		< 210	

CeO₂ nanospheres	810 ppm of HCHO, GHSV: 84000 h⁻¹, 20 vol% O₂	175	[119]
CeO₂ bulk particles		> 250	
CeO₂	580 ppm of HCHO, 20 vol% O₂	225	[120]
CeMn10		150	
CeMn30		125	
CeMn50		100	
CeMn80		80	
MnOₓ		75	

2.3 Oxides in heterogeneous catalysis – application in AOPs and oxidation

Catalysis is central to efficiently address some ofthe most pressing societal and environmental challenges, including the reduction of fossil fuel emissions, the production of sustainable fuels and the purification of pollutants in water or air [121, 122].

2.3.1 Spinel oxide in environmental catalysis

Spinels have been initially employed as precious stones, such as red spinels containing Cr^{3+} and blue spinels containing Fe^{2+} [123]. Spinels classically present the composition AB_2O_4 (where A and B aremetal ions) (Fig. 2-3), where A and B are metallic cations positioned at two different crystallographic sites, tetrahedral (A sites) and octahedral (B sites) [124]. The cations of both positions are tetrahedrally and octahedrally coordinated to oxygen atoms, respectively. Depending on their situations of cation distribution, spinels can be classified into three types: normal, inverse, and complex spinels. In a more accurate formula $A_{1-\lambda}B_{\lambda}(A_{\lambda}B_{2-\lambda})O_4$, $\lambda = 0$ is regarded as the normal spinel structure, $\lambda = 1$ is the inverse spinel structure, and $0 < \lambda < 1$ reflects the complex spinels. $ZnFe_2O_4$ is an example of normal spinel ferrite, $NiFe_2O_4$ (e.g., $Fe(NiFe)O_4$) is common example for inverse spinel ferrite while $MnFe_2O_4$ is a good

example for complex spinel such as $Mn_{0.8}Fe_{0.2}(Mn_{0.2}Fe_{1.8})O_4$ [125]. Several factors such as the cation radius, coulomb interactions between the cations, and crystal field effects of the octahedral site preference energy (OSPE) of cations, can determine the distribution of cations in spinels [124]. Owing to their manifold compositions, electron configurations, and valence states, spinels possess intrinsic optical [126], electrical [127], magnetic [128], and catalytic properties [129].
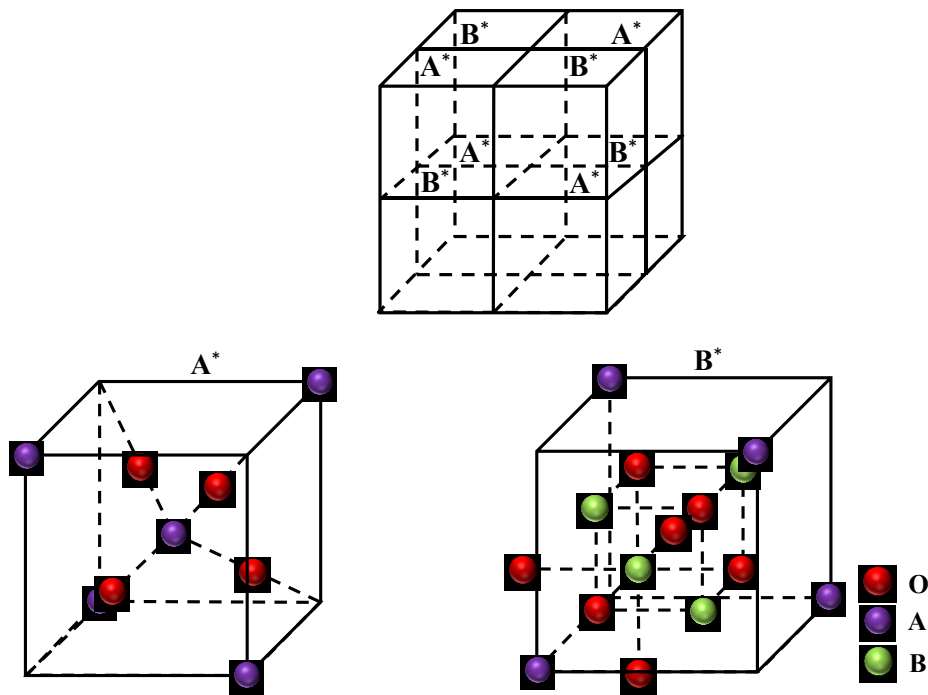
Figure 2-3 Schematic diagram of spinel (AB_2O_4) structure

Recently, research has clearly shown the extensive applications of spinel and their composites in water and wastewater treatments (Table 2-7). More precisely, spinels have been applied for the adsorption of pollutants [30], photocatalytic degradation of organic contaminants [131], pathogen disinfection [132], membrane modification [133], analyte extraction [134], and so on. Particularly, Fe_3O_4 or γ-Al_2O_3 have been widely applied [71, 135, 136]. This may be mainlydue to ease of synthesis and availability of the precursors relative to other spinels. Of note, Fe_3O_4 and γ-Al_2O_3 are one kind of spinels with only one element in the structure. The inverse spinel Fe_3O_4 can be expressed as $Fe^{3+}(Fe^{3+}Fe^{2+})O_4$ [137]. In contrast, the spinel γ-Al_2O_3 displays Al

vacancies in the B site (octahedral interstices), which can be expressed as $(Al^{3+})(Al^{3+}_{5/3}V_{1/3})O_4$ (V corresponds to the vacancy) [138, 139]. In the preliminary experiments, we found that the catalytic activity of single metal oxide (Fe_3O_4, Al_2O_3, etc.) was not very effective for degrading organic compounds in water. Thus, the search for efficientbimetallicspinel ($CoFe_2O_4$, $CuFe_2O_4$ and $ZnFe_2O_4$ etc.) catalysts for wastewater treatment is required, as reported in literatures (Table 2-7). The coexistence of tetrahedral and octahedral sites provides multiplesites to accommodate different metal cations with various valence states, which are considered to be beneficial for the redox of transition metals involved in catalytic oxidation process, further improving the catalytic activity of catalysts.

Table 2-7 Survey of recent studies on spinel particles for water treatment

Catalyst	Organic pollutants	Reaction conditions	Treatment efficiency	Ref.
$NiFe_2O_4$	Eriochrome black-T (EBT)	[EBT]: 10 mg L^{-1}, [catalyst]: 0.02 g L^{-1}, pH : 6	86.7% EBT removal in 10 min	[130]
$ZnFe_2O_4$	Phenol	[phenol]: 20 g L^{-1}, UV irradiation, [catalyst]: 20 mg L^{-1}, Temperature: 35 °C	73% phenol removal in 360 min	[131]
Fe_3O_4 powder with particles size of μm	Acetaminophen (APAP)	[APAP]: 10.0 mg L^{-1}, [catalyst]: 0.8 g L^{-1}, [PMS]: 0.2 mM, pH: 4.3	15.8% APAP removal in 120 min	[135]
Fe_3O_4 (magnetic nano-particles about 100–300 nm)			31.7% APAP removal in 120 min	
Fe_3O_4 (nano-particles about 20 nm)			98.1% APAP removal in 120 min	
Fe_3O_4 (magnetic nano-particles about 20 nm)			74.7% APAP removal in 120 min	
γ-Al_2O_3	Phenol	[phenol]: 100 mg L^{-1}, [catalyst]: 1.0 g L^{-1}, [O_3]: 8 mg min^{-1}, pH: 6.5,	50% Phenol removal in 90 min	[136]
γ-Al_2O_3	2,4-dimethylphenol (2,4-DMP)	[2,4-DMP]: 50 mg L^{-1}; [catalyst]: 2 g L^{-1}, [O_3]: 2 g Nm^{-3}, O_3 flow rate: 40 L h^{-1}	75% COD removal in 5h	[71]
$ZnFe_2O_4$	Di-n-butyl phthalate (DBP)	[DBP]: 2 mol L^{-1}, [catalyst]: 0.1 g L^{-1}, [PMS]: 0.02 mmol	81% DBP removal in 30	[140]

		L^{-1}	min	
MnFe$_2$O$_4$			42.3% DBP removal in 30 min	
CuFe$_2$O$_4$			62.3% DBP removal in 30 min	
CoFe$_2$O$_4$			30% DBP removal in 30 min	
NiFe$_2$O$_4$	Phenol	[phenol]: 300 mg L^{-1}, [catalyst]: 1 g L^{-1}, [O$_3$]: 0.75 mg min^{-1}, pH: 6.5 ± 0.1	55.2% phenol removal in 60 min	[141]
MgFe$_2$O$_4$	Acid Orange 7 (AO7)	[AO7]: 50 mg L^{-1}, [catalyst]: 0.1 g L^{-1}, [O$_3$]: 0.5 mg min^{-1}, pH: 6.36	94.1% AO7 removal in 40 min	[142]
CuFe$_2$O$_4$	Phenacetin (PNT)	[PNT]: 0.2 mM, [catalyst]: 2 g L^{-1}, [O$_3$]: 0.36 mg L^{-1}, flow rate: 1 L h^{-1}, pH: 7.72	70% PNT removal in 180 min	[143]
CuCo$_2$O$_4$	Sulfamethazine (SMZ)	[SMZ]: 5 mg L^{-1}, [catalyst]: 0.01 g L^{-1}, [PMS]: 20 mg L^{-1}, pH 6.3, 0.01 M NaClO$_4$	87.2% removal efficiency in 20 min	[144]
CuFe$_2$O$_4$	P-Nitrophenol (PNP)	[PNP]: 50 mg L^{-1}, [catalyst]: 30 g L^{-1}, [PS]: 8 mM, pH 6.0	89% removal efficiency in 60 min	[145]
MnFe$_2$O$_4$	Acid Orange 7 (AO7)	[AO7]: 50 mgL^{-1}, [catalyst]: 0.2 g L^{-1}, [PMS]: 2 mM, pH: 5.42	97.3% AO7 removal in 30 min	[146]
CoMn$_2$O$_4$	Rhodamine B (RhB)	[RhB]: 30 mg L^{-1}, [catalyst]: 0.02 g L^{-1}, [PMS]: 0.2 g L^{-1}, pH 6.3	> 95% removal efficiency in 10 min	[147]
CuBi$_2$O$_4$	Bisphenol A (BPA)	[BPA]: 5 mg L^{-1}, [catalyst]: 0.2 g L^{-1}, [PMS]: 0.36 g L^{-1}, pH 7.0 ± 0.2,	~80% removal efficiency in 60 min	[148]

2.3.2 Perovskite oxide in environmental catalysis (manganese based-)

Perovskite can be expressed with a general formula ABO$_3$, where the A-site cation is 12-fold coordinated with the oxygen, while the B-site cation is 6-fold coordinated with the oxygen. The A cation can be a lanthanide, alkaline, or alkaline-earth cation while the B cation is a metallic element from the 3d, 4d, or 5d configuration [121, 149]. In the ideal structure of perovskite, the A-O distance is (a/√2) (a is the cubic unit cell parameter) while the B-O distance is equal to a/2. Their ionic radii have the following relationship: $t = (r_A + r_O)/(\sqrt{2}r_B + r_O) = 1$, where t expresses the tolerance factor.
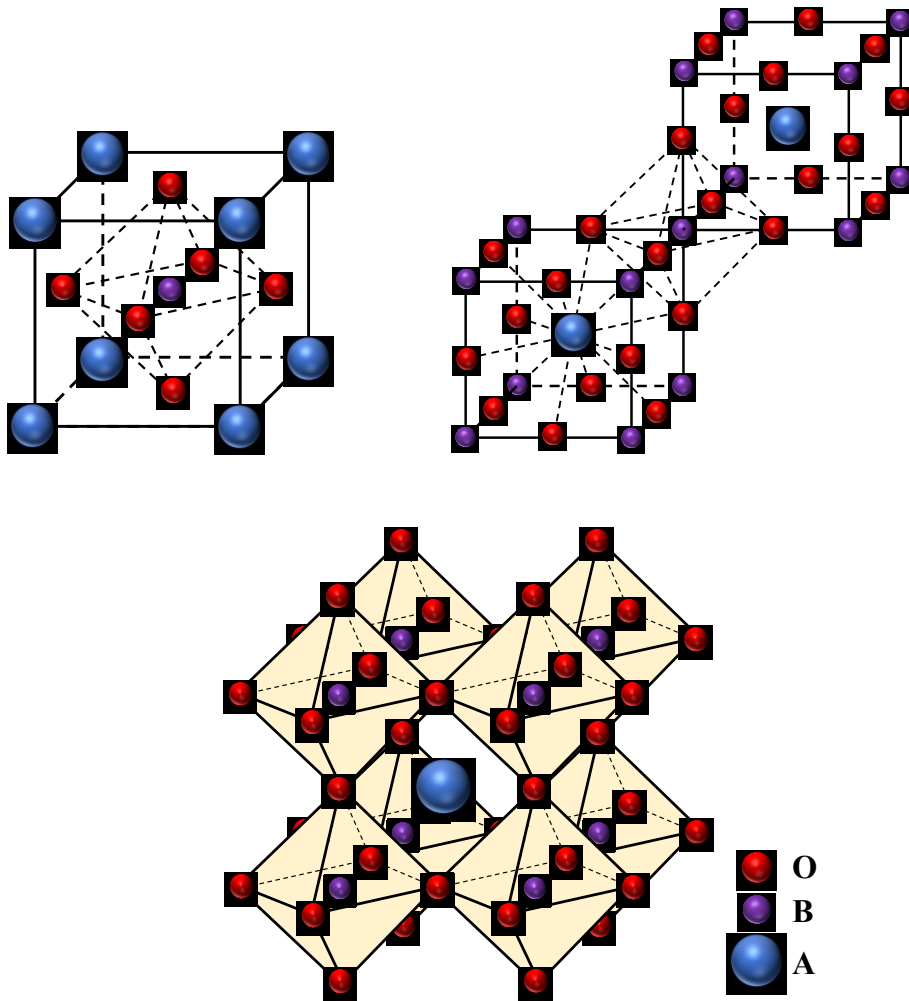
Figure 2-4 Ideal structure of perovskite (ABO$_3$)

Perovskites have emerged as an important class of mixed-oxides and represent the most studied mixed-oxide system due to their exceptional thermal stability, ionic conductivity, electronic structure, electron mobility, and redox behavior [150]. Especially, they are applied to a wide range of industrial applications, primarily in heterogeneous catalysis.

As a benefit of a wide range of possible substitutions and doping at both A and B sites, resulting in a general formula of $A_{1-x}A'_xB_{1-y}B'_xO_{3\pm\delta}$, perovskites offer great flexibility allowing tailoring their physical-chemical properties to better target their applications. For instance, substituting B cations with a reducible early transition metal (e.g., Co, Mn, or Fe) provides redox active sitesto facilitate catalytic reactions, including CO oxidation [151], CH$_4$ oxidation [152], steric acid oxidation [153] and NO

oxidation [154]. Following partial substitution of A or B cations with elements like Sr or Ce, oxygen vacancies may be introduced to the structure to facilitate oxygen transfer, thus increasing oxygen mobility [152, 155, 156]. Around 90% ofthe metallic elements in the periodic table can be used in synthesizing perovskite oxides, providing a broad possibility for tunable catalytic performance. Besides, most of the recently published works on catalytic oxidation reactions have been dealing with manganese-based perovskites and particularly lanthanum manganite of formula $LaMnO_{3+\delta}$ [157].

Manganese-based perovskites are emphasized as possible alternatives for noble metal-based catalysts (Pt, Rh, Pd) in many catalyticapplications particularly in automotive exhaust catalytic converters, mainly due to their relatively low cost, good thermal stability at high temperature and ease of preparation. For instance, lanthanum manganite perovskites (A=La; B=Mn) provide redox active sites to facilitate a wide variety of catalytic reactions [150, 152, 153, 155]. It is believed that the crystallinity, morphology, microstructures and surface/interface chemical states all may have critical effects on its catalytic activity. In order to improve the catalytic activity of stoechiometric perovskites, researchers made many strategies to improve their performance to meet the increasing requirement, such as increasing the specific surface area, doping with transition metal, surface properties and morphologies controlling, and process optimization.

Perovskites tend to present limited performances owing to their low surface area, and their nativesurfaces are preferentially A-sites-rich, inhibiting the role of catalytically active B-sites.Thus, the B-sites enrichment of perovskite surfaces *via* simple post-modification methods is highly interesting. Acid etching is a soft chemical method commonly used to modify the structure of materials [158, 159], improving the catalytic activity [160] or some functions like their conductivity [161]. For example, an

acidic treatment was reported to preferentially dissolve silver from a silver-gold alloy, leaving behind pure gold with a higher surface area [158]. Kudo *et al.* [159] and Sugimoto *et al.* [162] have reported the conversion of an Aurivillius phase, $Bi_2W_2O_9$ and $Bi_2O_2[SrNaNb_3O_{10}]$, into $H_2W_2O_7$ and $H_{1.8}[Bi_{0.21}Sr_{0.80}Na_{0.95}Nb_3O_{10}]$ respectively by hydrochloric acid treatment. Selective dealumination was also reported when etching a microporous aluminosilicate H-Y (FAU) zeolite with hydrochloric acid, leading to the formation of a micro/meso-porous USY zeolite with improved stability and catalytic activity [163].

In contrast, alkali modification of material seems to alter their function e.g. catalytic performance via different ways. The positive effect of alkali metals in heterogeneous catalysishas been studied in the past few decades. It was reported that oxide catalysts need alkali metal promotion to attain desired activity and selectivity. For example, the addition of alkali ion (Na^+ or K^+) is beneficial to the synthesis of ammonia [164], olefin production [165], and conversion of CO_2 to gasoline-range (C_5-C_{11}) hydrocarbons [166]. Previous studies proposed that the alkali promotion effect is related to the change in the electronic features of metallic components, to co-adsorbed molecules, or to the crystallographic orientation [167], thus enhancing their catalytic performance.

Also, it has been reported that the introduction of alkali metal ions can enhance the catalytic oxidation of VOCs such as ethanol [168], benzene [169], CO oxidation [170] and HCHO [171]. Avgouropoulos et al. [168] prepared K-promoted Pt/Al_2O_3catalyst, which could enhance the ethanol oxidation activity at lowtemperature and the performance is better than that of Na-promoted Pt/Al_2O_3. For HCHO oxidation, Zhang et al. [171] first reported that addition of a small amount of Na^+ to supported Pt catalyst can decrease the activation energy of the reaction, stabilize the hydroxyl species

in close to proximityto Na-O-Pt sites, and therefore enhance catalytic activity of HCHO oxidation. Recently, similar observations were reported in the case of Na^+-modified Pd/TiO_2 catalyst [172] and K^+-modified Ag/Co_3O_4 catalyst [173]. Nie et al. also investigated the HCHO oxidation reaction using a Pt/TiO_2 catalyst prepared using a combined NaOH-assisted impregnation method, and found that the catalyst prepared with NaOH had higher HCHO oxidation activity than the unimpregnated catalyst due to the introduction of additional surface OH^- species and the improved adsorption capacity toward HCHO [174]. Most of these phenomena were observed on the supported noble metal oxides, as well as on a few of pure MnO_2 (Table 2-8). The effect ofalkali (or alkali earth) metals on the catalytic activity of noble free oxides in especial perovskite is rarely discussed.

Table 2-8 Survey of recent studies on alkali modified material for catalytic oxidation of HCHO

Catalyst	Reaction conditions	T50 (°C)	Ref.
1wt%Pt/TiO$_2$	600 ppm of HCHO, Relative humidity: ~50%, GHSV: 120000 h^{-1}, 20 vol% O$_2$, He balance	~120	[171]
1~2wt%Na-1wt%Pt/TiO$_2$		R.T.	
Ag/Co$_3$O$_4$	100 ppm of HCHO, GHSV: 30000 h^{-1}, 20 vol% O$_2$, H$_2$ balance	~72	[173]
0.9%K-Ag/Co$_3$O$_4$		~60	
1.7%K-Ag/Co$_3$O$_4$		R.T.	
1wt%Pd/TiO$_2$	140 ppm of HCHO, Relative humidity: 25%, GHSV: 95000 h^{-1}, 20 vol% O$_2$, He balance	R.T. (~55%)	[172]
2wt%Na-1wt%Pd/TiO$_2$		R.T. (~100%)	
1wt%Pt/TiO$_2$	253 ppm of HCHO, Relative humidity: 25%, GHSV: 95000 h^{-1}, 20 vol% O$_2$, He balance	HCHO concentration decreased to 59 ppm after 60 min	[174]
1wt%Pt/TiO$_2$ prepared with the assistance of NaOH		HCHO concentration decreased to 15 ppm after 60 min	
MnO$_2$	100 ppm of HCHO, Relative humidity: 70% (at 27 °C), GHSV: ~90 L g$_{cat}^{-1}$ h^{-1}, 21 vol% O$_2$, N$_2$ balance	68	[175]

1K/MnO$_2$		56	
2.5K/MnO$_2$		61	
5K/MnO$_2$		78	
8K/MnO$_2$		86	
Hollandite manganese oxide (HMO)		~120	[176]
Ag/HMO, [Ag/Mn]$_{atomic ratio}$ = 0.15	140 ppm of HCHO, GHSV: 92000 h^{-1}, 10 vol% O$_2$, N$_2$ balance	~110	
Na/HMO, [Na/Mn]$_{atomic ratio}$ = 0.18		~95	

The doping with various transition metals is an common efficient strategy for improving the catalytic property of catalyst. For example, aliovalent substitutions on A or B sites using cations of different valencies were reported. To meet the principle of electron neutrality, this substitution was suggested to either change the oxidation state of the transition metal cation or to introduce oxygen vacancies, facilitating oxygen transfer and thus increasing oxygen mobility. As a kind of surface defect, oxygen vacancies have been widely reported to act as adsorption and active sites in heterogeneous catalytic reactions. In contrast, cation vacancies are another kind of important defect, which receive little attention. For instance, as-prepared MnO$_2$ often tend to exhibit Mn vacancies (with 2.8~ 11.1 mol%) [177], and these vacancies can directly affect their electronic structures and photo-conductivities [178], which can be significantly changed even with very low vacancy or dopant concentrations. Thus, it is very interesting to evaluate the possible effect of cationic vacancies on the surface physicochemical properties, as well catalytic performances of perovskite. In this work, three modified approaches will be used to promote the surface physicochemical properties and the catalytic performance of perovskite-based materials. Additional, no perovskite-based materials (*via* acid or alkali modification or cationic vacancies) have been successfully used before for formaldehyde oxidation though perovskite materials

have been widely used for VOCs combustion.

References

[1] R.P. Schwarzenbach, B.I. Escher, K. Fenner, T.B. Hofstetter, C.A. Johnson, U. von Gunten, B. Wehrli, The challenge of micropollutants in aquatic systems, Science, 313 (2006) 1072.

[2] D.K. Nordstrom, Worldwide Occurrences of Arsenic in Ground Water, Science, 296 (2002) 2143.

[3] R. Dris, H. Imhof, W. Sanchez, J. Gasperi, F. Galgani, B. Tassin, C. Laforsch, Beyond the ocean: contamination of freshwater ecosystems with (micro-)plastic particles, Environmental Chemistry, 12 (2015) 539-550.

[4] F.A. Pitten, J. Bremer, A. Kramer, Air pollution by volatile organic compounds (VOC) and health complaints, Dtsch Med Wochenschr, 125 (2000) 545-550.

[5] M. Gavrilescu, K. Demnerová, J. Aamand, S. Agathos, F. Fava, Emerging pollutants in the environment: present and future challenges in biomonitoring, ecological risks and bioremediation, New Biotechnology, 32 (2015) 147-156.

[6] R.J. Slack, J.R. Gronow, N. Voulvoulis, Household hazardous waste in municipal landfills: contaminants in leachate, Science of The Total Environment, 337 (2005) 119-137.

[7] N. Warren, I.J. Allan, J.E. Carter, W.A. House, A. Parker, Pesticides and other micro-organic contaminants in freshwater sedimentary environments-a review, Applied Geochemistry, 18 (2003) 159-194.

[8] C.H. Ao, S.C. Lee, S.C. Zou, C.L. Mak, Inhibition effect of SO_2 on NO_x and VOCs during the photodegradation of synchronous indoor air pollutants at parts per billion (ppb) level by TiO_2, Applied Catalysis B: Environmental, 49 (2004) 187-193.

[9] J. Madureira, I. Paciência, J. Rufo, M. Severo, E. Ramos, H. Barros, E. de Oliveira Fernandes, Source apportionment of CO_2, PM10 and VOCs levels and health risk assessment in naturally ventilated primary schools in Porto, Portugal, Building and Environment, 96 (2016) 198-205.

[10] J. Sokolowska-Gajda, H.S. Freeman, A. Reife, Synthetic dyes based on environmental considerations. Part 2: Iron complexes formazan dyes, Dyes and Pigments, 30 (1996) 1-20.

[11] D. Wróbel, A. Boguta, R.M. Ion, Mixtures of synthetic organic dyes in a photoelectrochemical cell, Journal of Photochemistry and Photobiology A: Chemistry, 138 (2001) 7-22.

[12] M.T. Yagub, T.K. Sen, S. Afroze, H.M. Ang, Dye and its removal from aqueous solution by adsorption: A review, Advances in Colloid and Interface Science, 209 (2014) 172-184.

[13] T. Robinson, G. McMullan, R. Marchant, P. Nigam, Remediation of dyes in textile effluent: a critical review on current treatment technologies with a proposed alternative, Bioresource Technology, 77 (2001) 247-255.

[14] T.K. Sen, S. Afroze, H.M. Ang, Equilibrium, Kinetics and Mechanism of Removal of Methylene Blue from Aqueous Solution by Adsorption onto Pine Cone Biomass of Pinus radiata, Water, Air, & Soil Pollution, 218 (2011) 499-515.

[15] X.-C. Jin, G.-Q. Liu, Z.-H. Xu, W.-Y. Tao, Decolorization of a dye industry effluent by aspergillus fumigatus XC6, Applied Microbiology and Biotechnology, 74 (2007) 239-243.

[16] I.M. Banat, P. Nigam, D. Singh, R. Marchant, Microbial decolorization of textile-dyecontaining effluents: A review, Bioresource Technology, 58 (1996) 217-227.

[17] K. Kadirvelu, M. Kavipriya, C. Karthika, M. Radhika, N. Vennilamani, S. Pattabhi, Utilization of various agricultural wastes for activated carbon preparation and application for the removal of dyes and metal ions from aqueous solutions, Bioresource Technology, 87 (2003) 129-132.

[18] Y. Fu, T. Viraraghavan, Fungal decolorization of dye wastewaters: a review, Bioresource Technology, 79 (2001) 251-262.

[19] S.M. Ghoreishi, R. Haghighi, Chemical catalytic reaction and biological oxidation for treatment of non-biodegradable textile effluent, Chemical Engineering Journal, 95 (2003) 163-169.

[20] K.-T. Chung, Azo dyes and human health: A review, Journal of Environmental Science and Health, Part C, 34 (2016) 233-261.

[21] B. Abdollahi, A. Shakeri, S. Aber, M. Sharifi Bonab, Simultaneous photodegradation of acid orange 7 and removal of Pb^{2+} from polluted water using reusable clinoptilolite-TiO_2 nanocomposite, Research on Chemical Intermediates, 44 (2018) 1505-1521.

[22] F.I. Vacchi, A.F. Albuquerque, J.A. Vendemiatti, D.A. Morales, A.B. Ormond, H.S. Freeman, G.J. Zocolo, M.V.B. Zanoni, G. Umbuzeiro, Chlorine disinfection of dye wastewater: Implications for a commercial azo dye mixture, Science of The Total Environment, 442 (2013) 302-309.

[23] S. Hammami, N. Bellakhal, N. Oturan, M.A. Oturan, M. Dachraoui, Degradation of Acid Orange 7 by electrochemically generated •OH radicals in acidic aqueous medium using a boron-

doped diamond or platinum anode: A mechanistic study, Chemosphere, 73 (2008) 678-684.

[24] A. Özcan, M.A. Oturan, N. Oturan, Y. Şahin, Removal of Acid Orange 7 from water by electrochemically generated Fenton's reagent, Journal of Hazardous Materials, 163 (2009) 1213-1220.

[25] T. Colborn, F.S. vom Saal, A.M. Soto, Developmental effects of endocrine-disrupting chemicals in wildlife and humans, Environmental Health Perspectives, 101 (1993) 378-384.

[26] P. Fenichel, N. Chevalier, F. Brucker-Davis, Bisphenol A: An endocrine and metabolic disruptor, Annales d'Endocrinologie, 74 (2013) 211-220.

[27] E.J. Routledge, J.P. Sumpter, Estrogenic activity of surfactants and some of their degradation products assessed using a recombinant yeast screen, Environmental Toxicology and Chemistry, 15 (1996) 241-248.

[28] M. Neamţu, F.H. Frimmel, Degradation of endocrine disrupting bisphenol A by 254nm irradiation in different water matrices and effect on yeast cells, Water Research, 40 (2006) 3745-3750.

[29] A. Bhatnagar, I. Anastopoulos, Adsorptive removal of bisphenol A (BPA) from aqueous solution: A review, Chemosphere, 168 (2017) 885-902.

[30] C.A. Staples, P.B. Dome, G.M. Klecka, S.T. Oblock, L.R. Harris, A review of the environmental fate, effects, and exposures of bisphenol A, Chemosphere, 36 (1998) 2149-2173.

[31] Y.Q. Huang, C.K.C. Wong, J.S. Zheng, H. Bouwman, R. Barra, B. Wahlström, L. Neretin, M.H. Wong, Bisphenol A (BPA) in China: A review of sources, environmental levels, and potential human health impacts, Environment International, 42 (2012) 91-99.

[32] B.S. Rubin, Bisphenol A: An endocrine disruptor with widespread exposure and multiple effects, The Journal of Steroid Biochemistry and Molecular Biology, 127 (2011) 27-34.

[33] N. Vandenberg Laura, I. Chahoud, J. Heindel Jerrold, V. Padmanabhan, J.R. Paumgartten Francisco, G. Schoenfelder, Urinary, Circulating, and Tissue Biomonitoring Studies Indicate Widespread Exposure to Bisphenol A, Environmental Health Perspectives, 118 (2010) 1055-1070.

[34] P. Fu, K. Kawamura, Ubiquity of bisphenol A in the atmosphere, Environmental Pollution, 158 (2010) 3138-3143.

[35] A.L. Wozniak, N.N. Bulayeva, C.S. Watson, Xenoestrogens at picomolar to nanomolar concentrations trigger membrane estrogen receptor-alpha-mediated Ca^{2+} fluxes and prolactin release in GH3/B6 pituitary tumor cells, Environmental health perspectives, 113 (2005) 431-439.

[36] H.J. Lee, S. Chattopadhyay, E.-Y. Gong, R.S. Ahn, K. Lee, Antiandrogenic Effects of Bisphenol A and Nonylphenol on the Function of Androgen Receptor, Toxicological Sciences, 75 (2003) 40-46.

[37] B.S. Rubin, A.M. Soto, Bisphenol A: Perinatal exposure and body weight, Molecular and Cellular Endocrinology, 304 (2009) 55-62.

[38] D. Cuomo, I. Porreca, G. Cobellis, R. Tarallo, G. Nassa, G. Falco, A. Nardone, F. Rizzo, M. Mallardo, C. Ambrosino, Carcinogenic risk and Bisphenol A exposure: A focus on molecular aspects in endoderm derived glands, Molecular and Cellular Endocrinology, 457 (2017) 20-34.

[39] C. Zhang, G. Zeng, L. Yuan, J. Yu, J. Li, G. Huang, B. Xi, H. Liu, Aerobic degradation of bisphenol A by Achromobacter xylosoxidans strain B-16 isolated from compost leachate of municipal solid waste, Chemosphere, 68 (2007) 181-190.

[40] G. Liu, J. Ma, X. Li, Q. Qin, Adsorption of bisphenol A from aqueous solution onto activated carbons with different modification treatments, Journal of Hazardous Materials, 164 (2009) 1275-1280.

[41] M.S. Kamal, S.A. Razzak, M.M. Hossain, Catalytic oxidation of volatile organic compounds (VOCs) – A review, Atmospheric Environment, 140 (2016) 117-134.

[42] M. Drobek, A. Figoli, S. Santoro, N. Navascués, J. Motuzas, S. Simone, C. Algieri, N. Gaeta, L. Querze, A. Trotta, G. Barbieri, R. Mallada, A. Julbe, E. Drioli, PVDF-MFI mixed matrix membranes as VOCs adsorbers, Microporous and Mesoporous Materials, 207 (2015) 126-133.

[43] L.F. Liotta, Catalytic oxidation of volatile organic compounds on supported noble metals, Applied Catalysis B: Environmental, 100 (2010) 403-412.

[44] S. Scirè, L.F. Liotta, Supported gold catalysts for the total oxidation of volatile organic compounds, Applied Catalysis B: Environmental, 125 (2012) 222-246.

[45] N. Gilbert, Proposed residential indoor air quality guidelines for formaldehyde, Health Canada,

Ottawa, ON (Canada), Canada, 2005.

[46] T. Salthammer, S. Mentese, R. Marutzky, Formaldehyde in the Indoor Environment, Chemical Reviews, 110 (2010) 2536-2572.

[47] J. Quiroz Torres, S. Royer, J. P. Bellat, J. M. Giraudon, J. F. Lamonier, Formaldehyde: Catalytic Oxidation as a Promising Soft Way of Elimination, ChemSusChem, 6 (2013) 578-592.

[48] B. Bai, Q. Qiao, J. Li, J. Hao, Progress in research on catalysts for catalytic oxidation of formaldehyde, Chinese Journal of Catalysis, 37 (2016) 102-122.

[49] A.W. Franz, H. Kronemayer, D. Pfeiffer, R.D. Pilz, G. Reuss, W. Disteldorf, A.O. Gamer, A. Hilt, Formaldehyde, Ullmann's Encyclopedia of Industrial Chemistry, (2016).

[50] E. Roffael, Formaldehyde Release from Particleboard and Other Wood Based Panel; Forest Research Institute Malaysia, Kuala Lumpur, (1993).

[51] J.F. Walker, Formaldehyde, Reinhold Publishing Corporation: New York, (1964).

[52] R. Atkinson, Atmospheric chemistry of VOCs and NOx, Atmospheric Environment, 34 (2000) 2063-2101.

[53] G.P. Anipsitakis, D.D. Dionysiou, Degradation of Organic Contaminants in Water with Sulfate Radicals Generated by the Conjunction of Peroxymonosulfate with Cobalt, Environmental Science & Technology, 37 (2003) 4790-4797.

[54] G.P. Anipsitakis, D.D. Dionysiou, Radical Generation by the Interaction of Transition Metals with Common Oxidants, Environmental Science & Technology, 38 (2004) 3705-3712.

[55] S.P. Ghuge, A.K. Saroha, Catalytic ozonation for the treatment of synthetic and industrial effluents - Application of mesoporous materials: A review, Journal of Environmental Management, 211 (2018) 83-102.

[56] J.J. Pignatello, E. Oliveros, A. MacKay, Advanced Oxidation Processes for Organic Contaminant Destruction Based on the Fenton Reaction and Related Chemistry, Critical Reviews in Environmental Science and Technology, 36 (2006) 1-84.

[57] J. Wang, S. Wang, Activation of persulfate (PS) and peroxymonosulfate (PMS) and application for the degradation of emerging contaminants, Chemical Engineering Journal, 334 (2018) 1502-1517.

[58] A. Babuponnusami, K. Muthukumar, A review on Fenton and improvements to the Fenton process for wastewater treatment, Journal of Environmental Chemical Engineering, 2 (2014) 557-572.

[59] E. Neyens, J. Baeyens, A review of classic Fenton's peroxidation as an advanced oxidation technique, Journal of Hazardous Materials, 98 (2003) 33-50.

[60] G.V. Buxton, C.L. Greenstock, W.P. Helman, A.B. Ross, Critical Review of rate constants for reactions of hydrated electrons, hydrogen atoms and hydroxyl radicals ($\cdot$OH/$\cdot$O$^-$ in Aqueous Solution, Journal of Physical and Chemical Reference Data, 17 (1988) 513-886.

[61] B. Kasprzyk-Hordern, M. Ziółek, J. Nawrocki, Catalytic ozonation and methods of enhancing molecular ozone reactions in water treatment, Applied Catalysis B: Environmental, 46 (2003) 639-669.

[62] J. Nawrocki, Catalytic ozonation in water: Controversies and questions. Discussion paper, Applied Catalysis B: Environmental, 142-143 (2013) 465-471.

[63] J. Wang, Z. Bai, Fe-based catalysts for heterogeneous catalytic ozonation of emerging contaminants in water and wastewater, Chemical Engineering Journal, 312 (2017) 79-98.

[64] R. Yin, W. Guo, J. Du, X. Zhou, H. Zheng, Q. Wu, J. Chang, N. Ren, Heteroatoms doped graphene for catalytic ozonation of sulfamethoxazole by metal-free catalysis: Performances and mechanisms, Chemical Engineering Journal, 317 (2017) 632-639.

[65] A.G. Gonçalves, J.J.M. Órfão, M.F.R. Pereira, Catalytic ozonation of sulphamethoxazole in the presence of carbon materials: Catalytic performance and reaction pathways, Journal of Hazardous Materials, 239-240 (2012) 167-174.

[66] G. Moussavi, M. Mahmoudi, Degradation and biodegradability improvement of the reactive red 198 azo dye using catalytic ozonation with MgO nanocrystals, Chemical Engineering Journal, 152 (2009) 1-7.

[67] X. Liu, Z. Zhou, G. Jing, J. Fang, Catalytic ozonation of Acid Red B in aqueous solution over a Fe-Cu-O catalyst, Separation and Purification Technology, 115 (2013) 129-135.

[68] J.-S. Park, H. Choi, J. Cho, Kinetic decomposition of ozone and para-chlorobenzoic acid (pCBA) during catalytic ozonation, Water Research, 38 (2004) 2285-2292.

[69] Y. Wang, Y. Xie, H. Sun, J. Xiao, H. Cao, S. Wang, 2D/2D nano-hybrids of γ-MnO$_2$ on reduced

graphene oxide for catalytic ozonation and coupling peroxymonosulfate activation, Journal of Hazardous Materials, 301 (2016) 56-64.

[70] Z. Xu, Z. Chen, C. Joll, Y. Ben, J. Shen, H. Tao, Catalytic efficiency and stability of cobalt hydroxide for decomposition of ozone and p-chloronitrobenzene in water, Catalysis Communications, 10 (2009) 1221-1225.

[71] J. Vittenet, W. Aboussaoud, J. Mendret, J. S. Pic, H. Debellefontaine, N. Lesage, K. Faucher, M.-H. Manero, F. Thibault-Starzyk, H. Leclerc, A. Galarneau, S. Brosillon, Catalytic ozonation with γ-Al₂O₃ to enhance the degradation of refractory organics in water, Applied Catalysis A: General, 504 (2015) 519-532.

[73] S. Wacławek, K. Grübel, M. Černík, Simple spectrophotometric determination of monopersulfate, Spectrochimica Acta Part A: Molecular and Biomolecular Spectroscopy, 149 (2015) 928-933.

[74] S. Yang, P. Wang, X. Yang, L. Shan, W. Zhang, X. Shao, R. Niu, Degradation efficiencies of azo dye Acid Orange 7 by the interaction of heat, UV and anions with common oxidants: Persulfate, peroxymonosulfate and hydrogen peroxide, Journal of Hazardous Materials, 179 (2010) 552-558.

[75] J. Flanagan, W.P. Griffith, A.C. Skapski, The active principle of Caro's acid, HSO5–: X-ray crystal structure of KHSO5·H2O, Journal of the Chemical Society, Chemical Communications, (1984) 1574-1575.

[76] H. Hori, Y. Nagaoka, M. Murayama, S. Kutsuna, Efficient Decomposition of Perfluorocarboxylic Acids and Alternative Fluorochemical Surfactants in Hot Water, Environmental Science & Technology, 42 (2008) 7438-7443.

[77] C. Qi, X. Liu, J. Ma, C. Lin, X. Li, H. Zhang, Activation of peroxymonosulfate by base: Implications for the degradation of organic pollutants, Chemosphere, 151 (2016) 280-288.

[78] J. Sharma, I.M. Mishra, D.D. Dionysiou, V. Kumar, Oxidative removal of Bisphenol A by UV-C/peroxymonosulfate (PMS): Kinetics, influence of co-existing chemicals and degradation pathway, Chemical Engineering Journal, 276 (2015) 193-204.

[79] Q. Zhao, Q. Mao, Y. Zhou, J. Wei, X. Liu, J. Yang, L. Luo, J. Zhang, H. Chen, H. Chen, L. Tang, Metal-free carbon materials-catalyzed sulfate radical-based advanced oxidation processes: A review on heterogeneous catalysts and applications, Chemosphere, 189 (2017) 224-238.

[80] Q. Yang, N. Jia, C. Shen, J. Ma, Y. Wen, Activation of peroxymonosulfate by Fe-N complexes embedded within SBA-15 for removal of organic contaminants via production of singlet oxygen, Environmental Science and Pollution Research, 25 (2018) 34190-34199.

[81] L. Chen, X. Zuo, L. Zhou, Y. Huang, S. Yang, T. Cai, D. Ding, Efficient heterogeneous activation of peroxymonosulfate by facilely prepared Co/Fe bimetallic oxides: Kinetics and mechanism, Chemical Engineering Journal, 345 (2018) 364-374.

[82] J. Du, J. Bao, Y. Liu, S.H. Kim, D.D. Dionysiou, Facile preparation of porous Mn/Fe₃O₄ cubes as peroxymonosulfate activating catalyst for effective bisphenol A degradation, Chemical Engineering Journal, (2018).

[83] C. Cai, H. Zhang, X. Zhong, L. Hou, Ultrasound enhanced heterogeneous activation of peroxymonosulfate by a bimetallic Fe-Co/SBA-15 catalyst for the degradation of Orange II in water, Journal of Hazardous Materials, 283 (2015) 70-79.

[84] H. Lin, X. Zhong, C. Ciotonea, X. Fan, X. Mao, Y. Li, B. Deng, H. Zhang, S. Royer, Efficient degradation of clofibric acid by electro-enhanced peroxydisulfate activation with Fe-Cu/SBA-15 catalyst, Applied Catalysis B: Environmental, 230 (2018) 1-10.

[85] L.C.D.L.B. Campos, J.O. Edwards, The Kinetics and Mechanism of the Decomposition of Caro's Acid. I, Journal of the American Chemical Society, 78 (1956) 1125-1129.

[86] F. Ghanbari, M. Moradi, Application of peroxymonosulfate and its activation methods for degradation of environmental organic pollutants: Review, Chemical Engineering Journal, 310 (2017) 41-62.

[87] J. Yu, X. Li, Z. Xu, W. Xiao, NaOH-Modified Ceramic Honeycomb with Enhanced Formaldehyde Adsorption and Removal Performance, Environmental Science & Technology, 47 (2013) 9928-9933.

[88] W.H. OrganizationWHO, WHO Guidelines for Indoor Air Quality: Selected Pollutants, Copenhagen, (2010).

[89] Z. Xu, J. Yu, J. Low, M. Jaroniec, Microemulsion-Assisted Synthesis of Mesoporous

Aluminum Oxyhydroxide Nanoflakes for Efficient Removal of Gaseous Formaldehyde, ACS Applied Materials & Interfaces, 6 (2014) 2111-2117.

[90] W.-J. Liang, J. Li, J.-X. Li, T. Zhu, Y.-Q. Jin, Formaldehyde removal from gas streams by means of $NaNO_2$ dielectric barrier discharge plasma, Journal of Hazardous Materials, 175 (2010) 1090-1095.

[91] J. Yu, S. Wang, J. Low, W. Xiao, Enhanced photocatalytic performance of direct Z-scheme g-C_3N_4-TiO_2 photocatalysts for the decomposition of formaldehyde in air, Physical Chemistry Chemical Physics, 15 (2013) 16883-16890.

[92] H. Huang, D.Y.C. Leung, D. Ye, Effect of reduction treatment on structural properties of TiO_2 supported Pt nanoparticles and their catalytic activity for formaldehyde oxidation, Journal of Materials Chemistry, 21 (2011) 9647-9652.

[93] L. Nie, J. Yu, M. Jaroniec, F.F. Tao, Room-temperature catalytic oxidation of formaldehyde on catalysts, Catalysis Science & Technology, 6 (2016) 3649-3669.

[94] J. Quiroz, J.-M. Giraudon, A. Gervasini, C. Dujardin, C. Lancelot, M. Trentesaux, J.-F. Lamonier, Total Oxidation of Formaldehyde over MnO_x-CeO_2 Catalysts: The Effect of Acid Treatment, ACS Catalysis, 5 (2015) 2260-2269.

[95] J.J. Spivey, Complete catalytic oxidation of volatile organics, Industrial & Engineering Chemistry Research, 26 (1987) 2165-2180.

[96] S. Ordóñez, L. Bello, H. Sastre, R. Rosal, F.V. Díez, Kinetics of the deep oxidation of benzene, toluene, n-hexane and their binary mixtures over a platinum on γ-alumina catalyst, Applied Catalysis B: Environmental, 38 (2002) 139-149.

[97] N. Radic, B. Grbic, A. Terlecki-Baricevic, Kinetics of deep oxidation of n-hexane and toluene over Pt/Al_2O_3 catalysts: Platinum crystallite size effect, Applied Catalysis B: Environmental, 50 (2004) 153-159.

[98] P. Mars, D.W. van Krevelen, Oxidations carried out by means of vanadium oxide catalysts, Chemical Engineering Science, 3 (1954) 41-59.

[99] T.F. Garetto, C.R. Apesteguía, Oxidative catalytic removal of hydrocarbons over Pt/Al_2O_3 catalysts, Catalysis Today, 62 (2000) 189-199.

[100] A. Yusuf, C. Snape, J. He, H. Xu, C. Liu, M. Zhao, G.Z. Chen, B. Tang, C. Wang, J. Wang, S.N. Behera, Advances on transition metal oxides catalysts for formaldehyde oxidation: A review, Catalysis Reviews, 59 (2017) 189-233.

[101] Y. Sekine, Oxidative decomposition of formaldehyde by metal oxides at room temperature, Atmospheric Environment, 36 (2002) 5543-5547.

[102] L. Miao, J. Wang, P. Zhang, Review on manganese dioxide for catalytic oxidation of airborne formaldehyde, Applied Surface Science, 466 (2019) 441-453.

[103] J. Zhang, Y. Li, L. Wang, C. Zhang, H. He, Catalytic oxidation of formaldehyde over manganese oxides with different crystal structures, Catal. Sci. Technol. 5 (2015) 2305-2313.

[104] Q. Feng, H. Kanoh, K. Ooi, Manganese oxide porous crystals, Journal of Materials Chemistry, 9 (1999) 319-333.

[105] C. Zhang, H. He, K. I. Tanaka, Catalytic performance and mechanism of a Pt/TiO_2 catalyst for the oxidation of formaldehyde at room temperature. Applied Catalysis B: Environmental, 65 (2006) 37-43

[106] C. Zhang, H. He, A comparative study of TiO_2 supported noble metal catalysts for the oxidation of formaldehyde at room temperature. Catalysis Today, 126 (2007) 345-350.

[107] S. J. Park, I. Bae, I. S. Nam, B. K. Cho, S. M. Jung, J. H. Lee, Oxidation of formaldehyde over Pd/Beta catalyst. Chemical engineering journal, 195 (2012) 392-402.

[108] Z. Qu, S. Shen, D. Chen, Y. Wang, Highly active Ag/SBA-15 catalyst using post-grafting method for formaldehyde oxidation. Journal of Molecular Catalysis A: Chemical, 356 (2012) 171-177.

[109] X. Tang, J. Chen, Y. Li, Y. Li, Y. Xu, W. Shen, Complete oxidation of formaldehyde over Ag/MnO_x-CeO_2 catalysts. Chemical Engineering Journal, 118 (2006) 119-125.

[110] Y. Shen, X. Yang, Y. Wang, Y. Zhang, H. Zhu, L. Gao, M. Jia, The states of gold species in CeO_2 supported gol d catalyst for formaldehyde oxidation. Applied Catalysis B: Environmental, 79 (2008) 142-148.

[111] N. An, Q. Yu, G. Liu, S. Li, M. Jia, W. Zhang, Complete oxidation of formaldehyde at ambient temperature over supported Pt/Fe_2O_3 catalysts prepared by colloid-deposition method. Journal of hazardous materials, 186 (2011) 1392-1397.

[112] C. Ma, D. Wang, W. Xue, B. Dou, H. Wang, Z. Hao, Investigation of formaldehyde oxidation over Co_3O_4-CeO_2 and Au/Co_3O_4-CeO_2 catalysts at room temperature: effective removal and determination of reaction mechanism. Environmental science & technology, 45 (2011) 3628-3634.

[113] L. Ma, D. Wang, J. Li, B. Bai, L. Fu, Y. Li, Ag/CeO_2 nanospheres: Efficient catalysts for formaldehyde oxidation. Applied Catalysis B: Environmental, 148 (2014) 36-43.

[114] S. Imamura, D. Uchihori, K. Utani, T. Ito, Oxidative decomposition of formaldehyde on silver-cerium composite oxide catalyst. Catalysis Letters, 24 (1994) 377-384.

[115] Y. Wang, C. Dai, B. Chen, Y. Wang, C. Shi, X. Guo, Nanoscale HZSM-5 supported PtAg bimetallic catalysts for simultaneous removal of formaldehyde and benzene. Catalysis Today, 258 (2015) 616-626.

[116] T. Chen, H. Dou, X. Li, X.Tang, J. Li, J. Hao, Tunnel structure effect of manganese oxides in complete oxidation of formaldehyde. Microporous and Mesoporous Materials, 122 (2009) 270-274.

[117] X. Yu, J. He, D. Wang, Y. Hu, H. Tian, Z. He, Facile controlled synthesis of Pt/MnO_2 nanostructured catalysts and their catalytic performance for oxidative decomposition of formaldehyde. The Journal of Physical Chemistry C, 116 (2011) 851-860.

[118] B. Bai, H. Arandiyan, J. Li, Comparison of the performance for oxidation of formaldehyde on nano-Co_3O_4, 2D-Co_3O_4, and 3D-Co_3O_4 catalysts. Applied Catalysis B: Environmental, 142 (2013) 677-683.

[119] L. Ma, D. Wang, J. Li, B. Bai, L. Fu, Y. Li, Ag/CeO_2 nanospheres: Efficient catalysts for formaldehyde oxidation. Applied Catalysis B: Environmental, 148 (2014) 36-43.

[120] X. Liu, J, Lu, Q, Kun, W. X. Huang, M. Luo, A comparative study of formaldehyde and carbon monoxide complete oxidation on MnO_x-CeO_2 catalysts. Journal of rare earths, 27 (2009) 418-424.

[121] S. Royer, D. Duprez, F. Can, X. Courtois, C. Batiot-Dupeyrat, S. Laassiri, H. Alamdari, Perovskites as substitutes of noble metals for heterogeneous catalysis: Dream or Reality, Chemical Reviews, 114 (2014) 10292-10368.

[122] J. Hwang, R.R. Rao, L. Giordano, Y. Katayama, Y. Yu, Y. Shao-Horn, Perovskites in catalysis and electrocatalysis, Science, 358 (2017) 751.

[123] F.L. Sutherland, K. Zaw, S. Meffre, G. Giuliani, A.E. Fallick, I.T. Graham, G.B. Webb, Gem-corundum megacrysts from east Australian basalt fields: trace elements, oxygen isotopes and origins, Australian Journal of Earth Sciences, 56 (2009) 1003-1022.

[124] Q. Zhao, Z. Yan, C. Chen, J. Chen, Spinels: Controlled Preparation, Oxygen Reduction/Evolution Reaction Application, and Beyond, Chemical Reviews, 117 (2017) 10121-10211.

[125] K.K. Kefeni, B.B. Mamba, T.A.M. Msagati, Application of spinel ferrite nanoparticles in water and wastewater treatment: A review, Separation and Purification Technology, 188 (2017) 399-422.

[126] T.J. Mroz, T.M. Hartnett, J.M. Wahl, L.M. Goldman, K. James, W.R. Lindberg, Recent advances in spinel optical ceramic, 5786 (2005) 66-71.

[127] K. Miura, A. Yamada, M. Tanaka, Electric states of spinel $LixMn_2O_4$ as a cathode of the rechargeable battery, Electrochimica Acta, 41 (1996) 249-256.

[128] K. Ounnunkad, S. Phanichphant, Cellulose-precursor synthesis of nanocrystalline $Co_{0.5}Cu_{0.5}Fe_2O_4$ spinel ferrites, Materials Research Bulletin, 47 (2012) 473-477.

[129] P. Liu, H. He, G. Wei, X. Liang, F. Qi, F. Tan, W. Tan, J. Zhu, R. Zhu, Effect of Mn substitution on the promoted formaldehyde oxidation over spinel ferrite: Catalyst characterization, performance and reaction mechanism, Applied Catalysis B: Environmental, 182 (2016) 476-484.

[130] F. Moeinpour, A. Alimoradi, M. Kazemi, Efficient removal of Eriochrome black-T from aqueous solution using $NiFe_2O_4$ magnetic nanoparticles, Journal of Environmental Health Science and Engineering, 12 (2014) 112.

[131] S. W. Cao, Y. J. Zhu, G. F. Cheng, Y. H. Huang, $ZnFe_2O_4$ nanoparticles: Microwave-hydrothermal ionic liquid synthesis and photocatalytic property over phenol, Journal of Hazardous Materials, 171 (2009) 431-435.

[132] S. Singh, K.C. Barick, D. Bahadur, Surface engineered magnetic nanoparticles for removal of toxic metal ions and bacterial pathogens, Journal of Hazardous Materials, 192 (2011) 1539-

1547.

[133] H.H. Himstedt, Q. Yang, L.P. Dasi, X. Qian, S.R. Wickramasinghe, M. Ulbricht, Magnetically activated micromixers for separation membranes, Langmuir, 27 (2011) 5574-5581.

[134] J. Xie, T. Liu, G. Song, Y. Hu, C. Deng, Simultaneous analysis of organophosphorus pesticides in water by magnetic solid-phase extraction coupled with GC-MS, Chromatographia, 76 (2013) 535-540.

[135] C. Tan, N. Gao, Y. Deng, J. Deng, S. Zhou, J. Li, X. Xin, Radical induced degradation of acetaminophen with Fe_3O_4 magnetic nanoparticles as heterogeneous activator of peroxymonosulfate. Journal of hazardous materials, 276 (2014) 452-460.

[136] Y. Wang, Yang, W., Yin, X., & Liu, Y. The role of Mn-doping for catalytic ozonation of phenol using $Mn/\gamma-Al_2O_3$ nanocatalyst: performance and mechanism. Journal of environmental chemical engineering, 4 (2016) 3415-3425.

[137] G.K. Rozenberg, Y. Amiel, W.M. Xu, M.P. Pasternak, R. Jeanloz, M. Hanfland, R.D. Taylor, Structural characterization of temperature- and pressure-induced inverse-normal spinel transformation in magnetite, Physical Review B, 75 (2007) 020102.

[138] M. Sun, A.E. Nelson, J. Adjaye, Examination of Spinel and Nonspinel Structural Models for $\gamma-Al_2O_3$ by DFT and Rietveld Refinement Simulations, The Journal of Physical Chemistry B, 110 (2006) 2310-2317.

[139] G. Gutiérrez, A. Taga, B. Johansson, Theoretical structure determination of $\gamma-Al_2O_3$, Physical Review B, 65 (2001) 012101.

[140] Y. Ren, L. Lin, J. Ma, J. Yang, J. Feng, Z. Fan, Sulfate radicals induced from peroxymonosulfate by magnetic ferrospinel MFe_2O_4 (M=Co, Cu, Mn, and Zn) as heterogeneous catalysts in the water, Applied Catalysis B: Environmental, 165 (2015) 572-578.

[141] H. Zhao, Y. Dong, G. Wang, P. Jiang, J. Zhang, L. Wu, K. Li, Novel magnetically separable nanomaterials for heterogeneous catalytic ozonation of phenol pollutant: $NiFe_2O_4$ and their performances. Chemical Engineering Journal, 219 (2013) 295-302.

[142] J. Lu, X. Wei, Y. Chang, S. Tian, Y. Xiong, Role of Mg in mesoporous $MgFe_2O_4$ for efficient catalytic ozonation of Acid Orange II. Journal of Chemical Technology & Biotechnology, 91 (2016) 985-993.

[143] Qi, F., Chu, W., & Xu, B. (2015). Ozonation of phenacetin in associated with a magnetic catalyst CuFe2O4: the reaction and transformation. Chemical engineering journal, 262, 552-562.

[144] Y. Feng, J. Liu, D. Wu, Z. Zhou, Y. Deng, T. Zhang, K. Shih, Efficient degradation of sulfamethazine with $CuCo_2O_4$ spinel nanocatalysts for peroxymonosulfate activation. Chemical Engineering Journal, 280 (2015) 514-524.

[145] J. Li, Y. Ren, F. Ji, B. Lai, Heterogeneous catalytic oxidation for the degradation of p-nitrophenol in aqueous solution by persulfate activated with $CuFe_2O_4$ magnetic nano-particles. Chemical Engineering Journal, 324 (2017) 63-73.

[146] J. Deng, S. Feng, X. Ma, C. Tan, H. Wang, S. Zhou, J. Li, Heterogeneous degradation of Orange II with peroxymonosulfate activated by ordered mesoporous $MnFe_2O_4$. Separation and Purification Technology, 167 (2016) 181-189.

[147] Y. Yao, Y. Cai, G. Wu, F. Wei, X. Li, H. Chen, S. Wang, Sulfate radicals induced from peroxymonosulfate by cobalt manganese oxides ($Co_xMn_{3-x}O_4$) for Fenton-like reaction in water. Journal of hazardous materials, 296 (2015) 128-137.

[148] W. D. Oh, Z. Dong, Z. T. Hu, T. T. Lim, A novel quasi-cubic $CuFe_2O_4-Fe_2O_3$ catalyst prepared at low temperature for enhanced oxidation of bisphenol A via peroxymonosulfate activation. Journal of Materials Chemistry A, 3 (2015) 22208-22217.

[149] M.A. Peña, J.L.G. Fierro, Chemical Structures and Performance of Perovskite Oxides, Chemical Reviews, 101 (2001) 1981-2018.

[150] H. Zhu, P. Zhang, S. Dai, Recent Advances of Lanthanum-Based Perovskite Oxides for Catalysis, ACS Catalysis, 5 (2015) 6370-6385.

[151] S. Royer, D. Duprez, Catalytic Oxidation of Carbon Monoxide over Transition Metal Oxides, ChemCatChem, 3 (2010) 24-65.

[152] S. Royer, H. Alamdari, D. Duprez, S. Kaliaguine, Oxygen storage capacity of $La_{1-x}A'_xBO_3$ perovskites (with A′=Sr, Ce; B=Co, Mn)-relation with catalytic activity in the CH_4 oxidation reaction, Applied Catalysis B: Environmental, 58 (2005) 273-288.

[153] S. Royer, B. Levasseur, H. Alamdari, J. Barbier, D. Duprez, S. Kaliaguine, Mechanism of

stearic acid oxidation over nanocrystalline $La_{1-x}A'_xBO_3$ (A'=Sr, Ce; B=Co, Mn): The role of oxygen mobility, Applied Catalysis B: Environmental, 80 (2008) 51-61.

[154] C.H. Kim, G. Qi, K. Dahlberg, W. Li, Strontium-doped perovskites rival platinum catalysts for treating NO_x in simulated diesel exhaust, Science, 327 (2010) 1624.

[155] T. Nitadori, S. Kurihara, M. Misono, Catalytic properties of $La_{1-x}A'_xMnO_3$ (A' = Sr, Ce, Hf), Journal of Catalysis, 98 (1986) 221-228.

[156] Y. Zhang-Steenwinkel, J. Beckers, A. Bliek, Surface properties and catalytic performance in CO oxidation of cerium substituted lanthanum-manganese oxides, Applied Catalysis A: General, 235 (2002) 79-92.

[157] H. Najjar, H. Batis, Development of Mn-based perovskite materials: Chemical structure and applications, Catalysis Reviews, 58 (2016) 371-438.

[158] J. Erlebacher, M.J. Aziz, A. Karma, N. Dimitrov, K. Sieradzki, Evolution of nanoporosity in dealloying, Nature, 410 (2001) 450.

[159] M. Kudo, H. Ohkawa, W. Sugimoto, N. Kumada, Z. Liu, O. Terasaki, Y. Sugahara, A Layered Tungstic Acid $H_2W_2O_7 \cdot nH_2O$ with a Double-Octahedral Sheet Structure: Conversion Process from an Aurivillius Phase $Bi_2W_2O_9$ and Structural Characterization, Inorganic Chemistry, 42 (2003) 4479-4484.

[160] K. Huang, X. Chu, L. Yuan, W. Feng, X. Wu, X. Wang, S. Feng, Engineering the surface of perovskite $La_{0.5}Sr_{0.5}MnO_3$ for catalytic activity of CO oxidation, Chemical Communications, 50 (2014) 9200-9203.

[161] H.-Z. Geng, K.K. Kim, K.P. So, Y.S. Lee, Y. Chang, Y.H. Lee, Effect of acid treatment on carbon nanotube-based flexible transparent conducting films, Journal of the American Chemical Society, 129 (2007) 7758-7759.

[162] W. Sugimoto, M. Shirata, Y. Sugahara, K. Kuroda, New conversion reaction of an aurivillius phase into the protonated form of the layered perovskite by the selective leaching of the bismuth oxide sheet, J. Am. Chem. Soc. 121 (1999) 11601-11602.

[163] A.H. Janssen, A.J. Koster, K.P. de Jong, Three-dimensional transmission electron Microscopic observations of mesopores in dealuminated Zeolite Y, Angew. Chem. Int. Edit. 40 (2001) 1102-1104.

[164] G. Ertl, S.B. Lee, M. Weiss, Adsorption of nitrogen on potassium promoted Fe(111) and (100) surfaces, Surface Science, 114 (1982) 527-545.

[165] Z. Li, L. Zhong, F. Yu, Y. An, Y. Dai, Y. Yang, T. Lin, S. Li, H. Wang, P. Gao, Y. Sun, M. He, Effects of Sodium on the Catalytic Performance of CoMn Catalysts for Fischer-Tropsch to Olefin Reactions, ACS Catalysis, 7 (2017) 3622-3631.

[166] J. Wei, Q. Ge, R. Yao, Z. Wen, C. Fang, L. Guo, H. Xu, J. Sun, Directly converting CO_2 into a gasoline fuel, Nature Communications, 8 (2017) 15174.

[167] S.J. Jenkins, D.A. King, A Role for Induced Molecular Polarization in Catalytic Promotion: CO Coadsorbed with K on Co{1010}, Journal of the American Chemical Society, 122 (2000) 10610-10614.

[168] G. Avgouropoulos, E. Oikonomopoulos, D. Kanistras, T. Ioannides, Complete oxidation of ethanol over alkali-promoted Pt/Al_2O_3 catalysts, Applied Catalysis B: Environmental, 65 (2006) 62-69.

[169] J. Hou, L. Liu, Y. Li, M. Mao, H. Lv, X. Zhao, Tuning the K^+ Concentration in the Tunnel of OMS-2 Nanorods Leads to a Significant Enhancement of the Catalytic Activity for Benzene Oxidation, Environmental Science & Technology, 47 (2013) 13730-13736.

[170] D.-Q. Han, C.-Q. Zhou, H.-M. Yin, D.-J. Zhang, X.-H. Xu, Reactivity of the Alkaline Pretreated Nanoporous Gold for the CO Oxidation, Catalysis Letters, 141 (2011) 1026-1031.

[171] C. Zhang, F. Liu, Y. Zhai, H. Ariga, N. Yi, Y. Liu, K. Asakura, M. Flytzani-Stephanopoulos, H. He, Alkali-Metal-Promoted Pt/TiO_2 Opens a More Efficient Pathway to Formaldehyde Oxidation at Ambient Temperatures, Angewandte Chemie International Edition, 51 (2012) 9628-9632.

[172] C. Zhang, Y. Li, Y. Wang, H. He, Sodium-Promoted Pd/TiO_2 for Catalytic Oxidation of Formaldehyde at Ambient Temperature, Environmental Science & Technology, 48 (2014) 5816-5822.

[173] B. Bai, J. Li, Positive Effects of K^+ Ions on Three-Dimensional mesoporous Ag/Co_3O_4 catalyst for HCHO oxidation, ACS Catalysis, 4 (2014) 2753-2762.

[174] L. Nie, J. Yu, X. Li, B. Cheng, G. Liu, M. Jaroniec, Enhanced Performance of NaOH-Modified

Pt/TiO$_2$ toward Room Temperature Selective Oxidation of Formaldehyde, Environmental Science & Technology, 47 (2013) 2777-2783.

[175] S. Rong, K. Li, P. Zhang, F. Liu, J. Zhang, Potassium associated manganese vacancy in birnessite-type manganese dioxide for airborne formaldehyde oxidation, Catalysis Science & Technology, 8 (2018) 1799-1812.

[176] Y. Chen, J. Gao, Z. Huang, M. Zhou, J. Chen, C. Li, Z. Ma, J. M. Chen, X. F. Tang, Sodium rivals silver as single-atom active centers for catalyzing abatement of formaldehyde. Environmental science & technology, 51 (2017) 7084-7090.

[177] H. Wang, J. Zhang, X. Hang, X. Zhang, J. Xie, B. Pan, Y. Xie, Half- Metallicity in Single-layered manganese dioxide nanosheets by defect engineering, Angew. Chem. Int. Edit. 127 (2015) 1211-1215.

[178] K.D. Kwon, K. Refson, G. Sposito, Defect-induced photoconductivity in layered manganese oxides: A density functional theory study, Phys. Rev. lett. 100 (2008) 146601.

Chapter 3 Heterogeneous catalytic ozonation by spinel-type CuAl$_2$O$_4$ and its precursor

Example of C. I. Acid Orange 7 degradation over spinel in water

3.1 Introduction

Over the past two decades, heterogeneous catalytic ozonation has been extensively studied for the degradation of refratory organic pollutants in wastewater [1-3]. Various classes of catalytic solids were studied for ozone activation into reactive oxygen species (ROS), the key step to degradation reaction. For instance, mono or mixed metal oxides [4-9], supported metals [10-15] and metal-free materials [16-18] have been reported to be effective catalysts in accelerating ozone decomposition to generate reactive radicals. Hence, heterogeneous catalytic ozonation can be envisaged as a highly efficient process for degradation and mineralization of organic pollutants.

To our knowledge, most of the research groups assume that reactive radicals are produced if a catalytic effect is observed [4, 19, 20]. In many classes of solid materials, catalytic ozonation activities were related to the generation of hydroxyl radicals [9, 21], superoxide radical ($O_2^{\bullet-}$) and singlet oxygen ($^1O_2$) as dominant ROS for pollutant degradation [18]. To note, Zhang *et al.*[22, 23] revealed that catalytic ozonation could follow a non-hydroxyl radical oxidation pathway. Now, an interesting study from Bing et al. [13], who prepared a combination of two single oxides (Fe_2O_3 and Al_2O_3) supported on SBA-15, was conducted toward ibuprofen degradation by catalytic ozonation. They observed an increase of lewis acid sites where ozone could substitute the surface OH groups stabilized on Fe^{3+} or either Al^{3+}, improving the production of HO$^{\bullet}$ and $O_2^{\bullet-}$active radicalswhich were beneficial for the catalytic improvement of ibuprofen degradation. In this line, hydroxyl sites and Lewis acid sites are usually found on Al_2O_3 and CuO surfaces but some controversies still exist in literature over the reaction mechanisms occurring on such single oxides, i.e. the generation of reactive radicals, the location of active sites, and the roles of catalyst surface and water. For instance, Al_2O_3 materials can be reported as an active catalyst for ozone decomposition

[20, 24] while some authors proposed that ozone was not decomposed by Al_2O_3 in water [25], suggesting that pollutant abatement may originate from the adsorption of organic molecules on alumina surface [26, 27]. In contrast, only few works on single copper based materials (bulk CuO or supported CuO) were reported for catalytic ozonation processes. In those studies, reaction mechanisms over Cu-based oxides were not fully described [7, 10, 28-30] and the lack of information on the determination of the copper valence state involved in the ozone activation process deserved to be investigated. As monometallic CuO usually presents low catalytic activity and stability compared with bimetallic oxides [31, 32], the addition of aluminum in the presence of copper oxide may be beneficial for the improvement of the catalytic ozonation reaction.

Spinel type oxides, briefly described as AB_2O_4 (where A and B are metal ions), have received particular attention due to their availability and low cost, numerous compositions, valence states, morphologies and surface defects. Such properties have demonstrated that their good catalytic performances in various research fields (i.e. energy, automotive depollution and pollutants oxidation), could be potentially competitive with respect to noble metal based catalysts [33]. Copper aluminate solid materials with a homogeneous spinel phase ($CuAl_2O_4$) can be easily synthesized via common approaches such as the sol-gel technique [34]. Herein, we focused our efforts on the preparation of different $CuAl_2O_4$ solid materials applied to the catalytic ozonation reaction for water depollution. As one of the common azo dyes, C. I. Acid Orange 7 (AO7) was selected as a refractory probe to evaluate the catalytic activity of $CuAl_2O_4$ solids. Degradation kinetics and stability of the catalyst were studied, together with the detection of liquid phase by-products (NO_2^-, NO_3^- and NH_4^+) along with AO7 degradation. Reactive species generated from the catalytic ozonation were identified by electron spin resonance (ESR), fluorescence spectra analysis and quenching tests. The

mechanism of catalytic ozonation at the liquid-solid interface of the present system was proposed and discussed with results from literature.

3.2 Experimental section

3.2.1 Chemicals

AO7 (reagent purity grade, $C_{16}H_{11}N_2NaO_4S$), 4-Chlorobenzoic acid (pCBA: $C_7H_5ClO_2$), coumarin ($C_9H_6O_2$), *tert*-butyl alcohol (TBA), benzoquinone, nitrobenzene, $Cu(NO_3)_2 \cdot 3H_2O$ (99.0~102.0%), $Al(NO_3)_3 \cdot 9H_2O$ (99.0%) and citric acid ($C_6H_8O_7 H_2O$, 99.0%) were purchased from Sinopharm Chemical Reagent Co., Ltd. (Shanghai, China) and were of analytical grade. 5,5-Dimethyl-1-pyrrolidine N-oxide (DMPO, 97.0%) was purchased from Aladdin Chemistry Co. Ltd. (Shanghai, China). Other chemicals used in the experiment were analytical grade reagents. All of them were used without any additional purification. The aqueous solutions were freshly prepared with the milli-Q water.

3.2.2 Synthesis of catalysts and characterization

$CuAl_2O_4$ was prepared by a conventional citric acid complexation method starting from the metal nitrates precursors: $Cu(NO_3)_2 \cdot 3H_2O$ (99.0~102.0%, Sinopharm), $Al(NO_3)_3 \cdot 9H_2O$ (99.0%, Sinopharm), and citric acid ($C_6H_8O_7 H_2O$, 99%, Sinopharm). For the synthesis, a molar ratio ($n_{Cu} + n_{Al}$)/$n_{citric acid}$ of 1 is applied. Copper nitrate and aluminum nitrate, weighted to obtain a final mass of spinel of 5.5 g are dissolved in 100 mL of distilled water. 12.6 g of citric acid is dissolved in 100 mL of distilled water, and is drop-wise added to the solution containing metal precursors under magnetic stirring. The resulting homogeneous solution was stirred for 2 h at 60 °C, and the temperature of the solution is increased to 80 °C for water evaporation. The obtained gel was calcined at different temperatures, from 200 °C to 700 °C for 4h. The calcined particles were finely ground after calcination, washed several times with water until the pH

reached neutral and further dried at 100°C for 24h. Pure CuO and Al_2O_3 were also prepared by the same method.

Appropriate characterization of the solids was assessed by differential thermal analysis (DTA) and thermogravimetric analysis (TGA), X-ray diffraction (XRD), N_2 physisorption, Fourier transform infrared spectroscopy (FTIR), Infrared spectra of chemisorbed pyridine (Pyridine-FTIR), Transmission electron microscopy (TEM, JEM-2100 microscope), scanning electron microscope (Zeiss SIGMA FESEM, Germany) coupled with an EDS microanalysis (EDAX Genesis, USA), and X-ray Photoelectron Spectroscopy (XPS). pH_{pzc} (pzc: point of zero charge) was determined with acid-base titration. Differential thermal and thermogravimetric analyses were performed approximatively 5.0 mg of solid in air flow (50 mL/min) in the range of 20-800 °C with a rate of 5 °C min^{-1} using a DSC-TGA equipment (SDT Q600 V 20.9 Build 20). X-ray diffraction (XRD) was analyzed from Cu Kα radiation (λ = 1.5406 Å) operating at 36 kV and 30 mA (XPert Pro, Netherlands). X-ray diffractograms were recorded in the 2θ values range 10-80° with a rate of 0.03°/1s. The Brunauer-Emmett-Teller (BET) surface area was measured on N_2 adsorption at 77 K on an ASAP2020 analyzer (USA). Before analysis, about 0.3 g of sample was put in the analysis cell and first outgassed under vacuum at 423 K for 10 h. After cooling at room temperature, the cell was transferred to the analysis port of the instrument to obtain the adsorption/desorption isotherms.

The Fourier transform infrared spectroscopy (FTIR) analyzer was employed to determine the functional groups present for understanding the chemistry of the samples. The infrared spectrum of the dry samples supported on KBr pellets at a fixed amount of sample (1 wt%), which was recorded over the 4000-400 cm^{-1} range on a Nicolet 5700 FTIR spectrophotometer (USA). Infrared spectra of chemisorbed pyridine

(Pyridine-FTIR) were obtained on a Frontier FT-IR Spectrometer. The self-supported sample wafers were evacuated in a vacuum cell at 250 °C for 1 h prior to pyridine adsorption. After the adsorption of pyridine at room temperature, the samples were out-gassed at 40 °C and 150 °C, and then the spectra were recorded.

Morphological properties and the atomic composition of samples were observed on a transmission electron microscope (TEM, JEM-2100 (HR) microscope operatedat 200 kV equipped with a LaB_6 crystal) and a field-emission scanning electron microscope (Zeiss SIGMA FESEM, German) with an EDS microanalysis (EDAX Genesis, USA). X-ray Photoelectron Spectroscopy (XPS) was performed on a ESCALAB 250Xi spectrometer (Thermo Fisher, USA) equipped with Al Kα X-ray source.High resolution spectra were collected in the constant analysis energy mode(CAE = 30 eV) and the binding energy was calibrated with the C1s (284.8 eV). pH_{pzc} (pH at which the surface is zero-charged) was determined with acid-base titration. The oxide (10 g/L) with ionic strength of 50 mM NaCl was first placed in the shaker (30mL) for 24 h at roomtemperature. Then titrations were carried out by using 0.1 M hydrochloride acid and 0.1 M sodium hydroxide, respectively, and the pH and the volume of acid or base needed was recorded throughout the titration process.The quantity of surface OH sites is determined as follows [35-37]: 0.2 g of the oxide was dispersed in 35 mL NaOH solution (0.05M) at room temperature. The suspensions were shaken for 4 h at room temperature. Then the catalyst was separated from the solution by filtration with 0.45 μm acetate membrane. Later the supernatants were titrated with an HCl standard solution (0.1M) to determine the residual NaOH. As the acid hydroxyl groups (-OH) can react with NaOH, their density can be quantified by the NaOH consumption. Based on the principle of charge balance, the acid and base hydroxyl groups are quantitatively equal. Therefore, the total density of the surface hydroxyl

groups is two times that of the acid ones.

3.2.3 Experimental procedure and analytical methods

Experiments were performed in a 250 mL glass beaker (internal diameter = 70 mm; height = 99 mm), under vigorous stirring (450 rpm) using a mechanical stirrer (RW 20, IKA, Germany). A fresh solution of AO7 (200 mL) was prepared at an initial concentration (C_0) of 100 mg L^{-1} before each run. The pH value of the solution was adjusted by sulfuric acid or sodium hydroxide solution, and measured with a Mettler-Toledo FE20 pH-meter (Mettler-Toledo Instruments Co., Ltd., Shanghai). Bubbling of ozone gas into the AO7 solution started as soon as a known amount of catalyst was added into the solution. At determined time intervals, samples were withdrawn and immediately filtered through 0.45 μm membrane (Millipore Co.) for chemical analysis. Residual aqueous ozone in the samples was quenched by 1 mL $Na_2S_2O_3$ solution (1.0 M).

Ozone was provided by electric discharge using 99.9% oxygen in an ozone generator (XFZ-5BI, China). Ozone concentration in the liquid and gas phases were monitored bythe indigo method and iodometric method with potassium iodide solution, respectively [38, 39]. A Rayleigh UV-9100 spectrophotometer (Rayleigh Co., China) was employed to measure the concentration of AO7 at its maximum absorption wavelength (485 nm). The 4-chlorobenzoic acid (pCBA) concentration was measured using a HPLC system consisting of a SPDM20A chromatograph equipped with a C-18 column (Shim-PackVP-ODS-C8) and a UV detector (wavelength of pCBA, 236 nm). COD (Chemical Oxygen Demand) was measured by a closed reflux spectrophotometric method based on the Standard of the People's Republic of China for Environmental Protection (HJ-T 399-2007). The concentration of ammonium, nitrite, nitrate and sulphate ions released during oxidation was measured using a Dionex ICS 2500 ion

chromatograph, equiped with a Ion Pas AS11-HC column and a ED50 conductance detector. Finally, the concentration of dissolved metal ions in the solution was measured by Atomic Absorption Spectroscopy (AAS, Perkin Elmer A Analyst 800).

Coumarin (1 mM) was used as a chemical probe for hydroxyl radical (HO•) formation. The concentration in 7-Hydroxycoumarin, product of the reaction between coumarin and hydroxyl radical, was determined by measuring the fluorescence emission at 452 nm under excitation at 332 nm using a spectrofluorometer (Shimadzu F-4500 FL Spectrophotometer). Electron spin resonance (ESR) experiments were performed using DMPO (40 mM) as a spin-trapping agent.ESR signals of radicals trapped by DMPO were recorded at ambient temperatures on a JES-FA200 spectrometer. Electrochemical experiments of cyclic voltammetry scan were performed on an electrochemical analyzer (CS350, CorrTest) with a three-electrode electrochemical cell. A catalyst modified inductive glasses(prepared by dip coating and drying at 80°C in oven) act as working electrode, a platinum wire act as the counter electrode and a saturated calomel electrode act as the reference.

3.3 Results and discussion

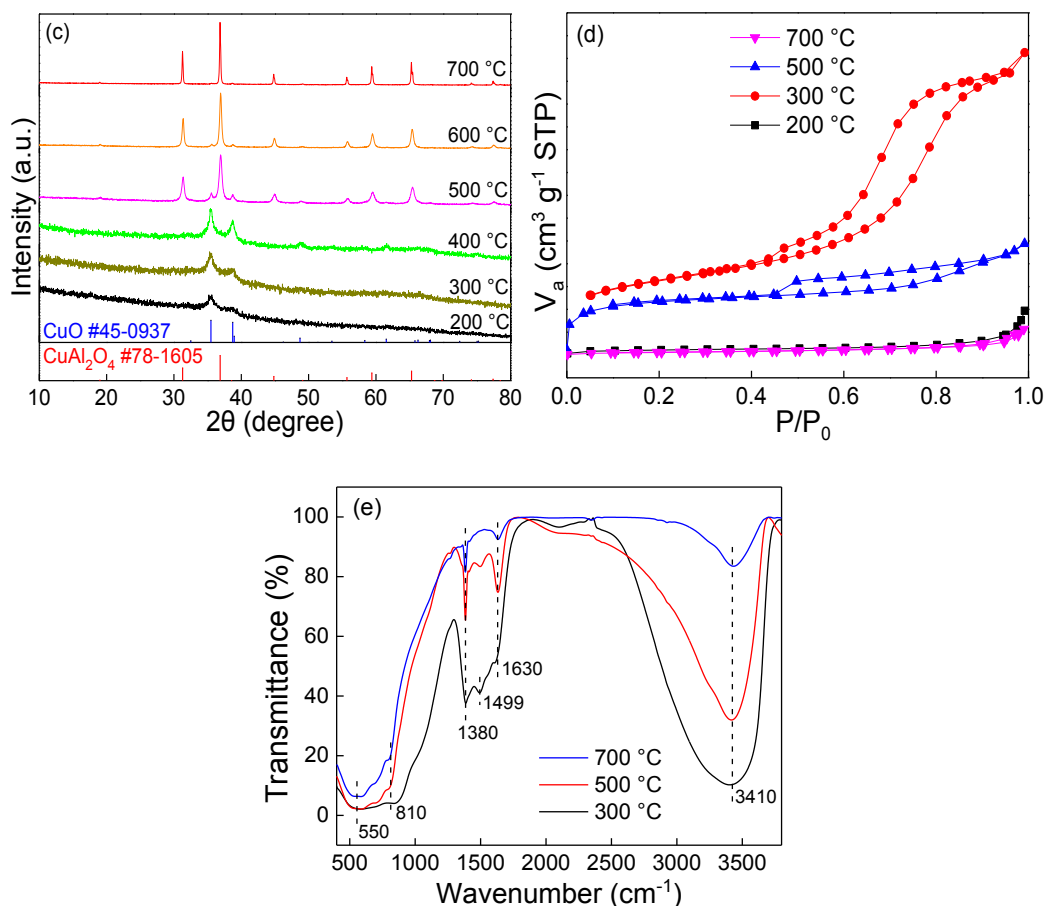### 3.3.1 Characterization of catalysts
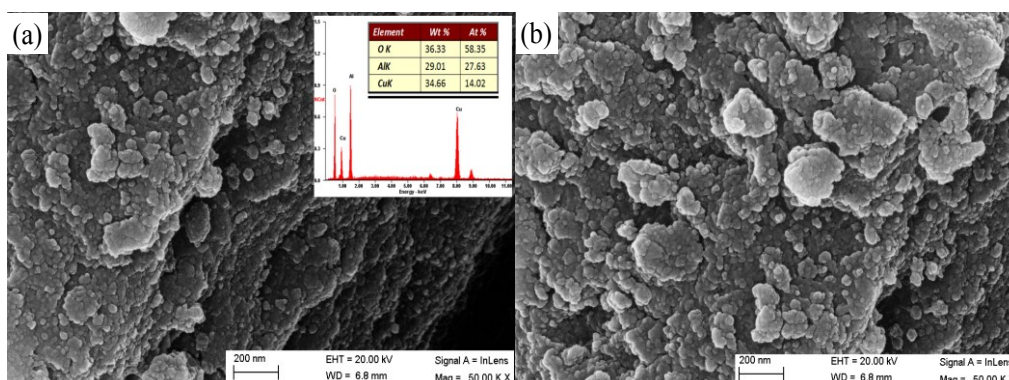
Figure 3-1 Characterization of $CuAl_2O_4$ material (typically calcined at 300 °C): (a and b) SEM images and EDS analysis of the sample; (c) Wide-angle XRD patterns of samples calcined at different temperatures; (d) N_2 physisorption isotherm of samples calcined at different temperatures; (e) FTIR spectra of the samples calcined at three different temperatures

SEM images displayed the surface morphology of spinel particles (Fig. 3-1a,b). Dense and loose agglomerations of particles spanning various sizes were observed at low temperature (300 °C). Representative elemental composition of the particle surface (see the inset of Fig. 3-1a) evidenced the presence of copper and aluminum in a ratio very close to the theoretical value of $CuAl_2O_4$ crystal, the atomic ratio of Cu and Al being close to 1:2. Complementary results from XRD pattern (Fig. 3-1c) show that such agglomerates were amorphous since no peak belonging to spinel structure was observed. XRD patterns of the synthesized $CuAl_2O_4$ treated at different temperatures (from 200 °C to 700 °C) were performed in order to investigate the evolution of the

amorphous structure under heating. As depicted in Fig. 3-1c, it can be seen that the slight increase of temperature up to 400 °C did not allow the formation of the spinel structure. Now, obvious (002), (111) reflection peaks ($2\theta = 35.6°$, $38.7°$) of CuO with monoclinic structure were observed (JCPDS No. 45-0937) in this sample and the one calcined at lower temperature. Reflections of $CuAl_2O_4$ phase (JCPDS No. 78-1605), (220), (311), (400), (422), (511) and (440) appeared at 500 °C and the relative intensity of CuO phase became weaker. Pure and strong spinel peaks of bulk $CuAl_2O_4$ phase were seen at calcination temperature set at 700 °C as reported in literature [34, 40, 41]. These results are in agreement with the TG-DTA profile of the corresponding dried precursor ($CuAl_2O_4$) (Fig. 3-2). The total weight loss was about 70% and there are two weight loss steps in the TG curve. In the first step, mass loss between 100 °C and 200 °C was observed due to desorption of water and dehydration of the precursor. The second weight loss step is from 200 °C to 400 °C, which may be due to the decomposition of organic residuals and dehydration of the gel. Of note, most of organic residuals in the gel would be decomposed after 300 °C during the thermal treatment.
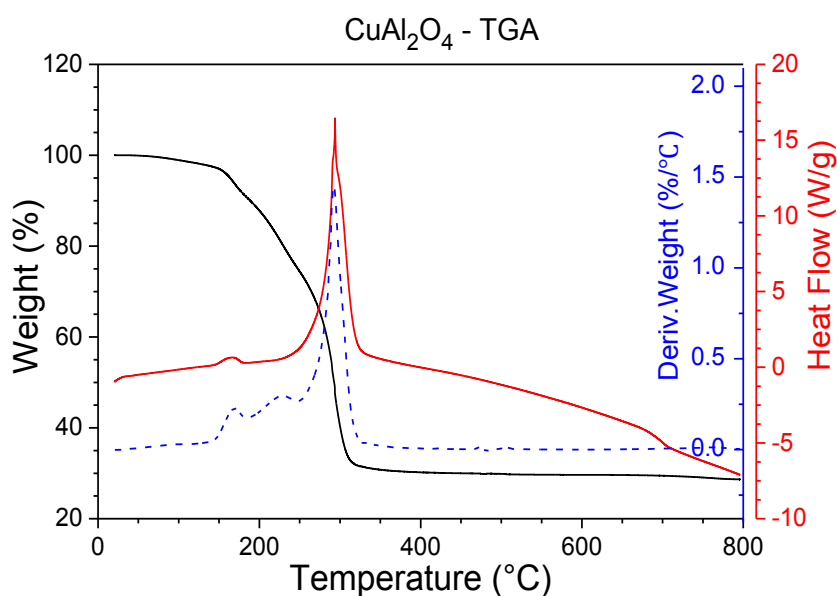

Figure 3-2 TG-DTA curves of dried precursor ($CuAl_2O_4$)

Furthermore, the broadening of the peaks decreased while increasing the temperature up to 700 °C, which indicated a clear crystallite growth. The average grain size of $CuAl_2O_4$ crystal calcined at 500 °C, 600 °C and 700 °C were 14.4 nm, 21.7 nm and 40.7 nm, respectively, according to the calculation roughly estimated from the Sherrer equation with the half-maximum (FWHM) of the main (311) planes ($2\theta = 65.3°$) observed on XRD patterns [40].

The N_2 adsorption/desorption isotherms of $CuAl_2O_4$ at 200 °C, 300 °C, 500 °C and 700 °C are illustrated in Fig. 3-1d. The sample calcined at 200 °C exhibited a low surface area of 4 m^2 g^{-1} with a weak pore volume of 0.01 cm^3 g^{-1}, suggesting that the oxide precursor did not form the pore structure when treated at 200 °C. At this stage, we assumed that the dehydration process was mainly occurring within the oxide precursor (Fig. 3-2). When the calcination temperature increased to 300 °C, the whole precursor would start to break into smaller particles and pores appeared due to the loss of water, anions and organic residuals [42]. $CuAl_2O_4$ calcined at 300 °C developed a specific surface area of 58 m^2 g^{-1} with a pore volume of 0.10 cm^3 g^{-1} (Table 3-1). It can be noticed that the sample calcined at 300 °C exhibited an isotherm of type IV, revealing a main adsorption step due to capillary condensation at relative pressures (P/P_0) ~ 0.45-0.80 typical of mesoporous materials (Fig. 3-1d). Obviously, the agglomeration of smaller particles, with a size estimated around 10-20 nm, led to a wormhole-like but uniform mesoporosity, as indicated by the SEM image and the parallel sorption branches of the solid hysteresis (Fig. 3-1a,b,d). The corresponding pore size distribution curve (data not shown) indicated a clear uniform pore size distribution profile centered at 7.1 nm. However, when the calcination temperature increased above 300 °C, the sample sintering occurred gradually. It is consistent with the transformation of the mixed oxides into the spinel $CuAl_2O_4$ as observed in the XRD analysis (Fig. 3-1c).

These observations were further demonstrated by the assessment of surface area and pore structure of the solids. The sample calcined at 500 °C developed a specific surface area of 41 m^2 g^{-1} with a pore volume of 0.04 cm^3 g^{-1}, while the sample calcined at 700 °C only reached a surface area of 4 m^2 g^{-1} with a pore volume of 0.01 cm^3 g^{-1}. Hence, the surface area of the sample could increase within a temperature window located between 200 and 300 °C and loss of surface area was observed above 300 °C.

Table 3-1 Physicochemical properties of different catalysts typically calcined at 300 °C

Samples	BET (m^2 g^{-1})	Porediameter (nm)	Pore volume (cm^3 g^{-1})	Density of OH groups in water (mmolg^{-1})	pH$_{pzc}$
CuAl$_2$O$_4$	58	7.1	0.10	2.78	8.45
CuO	5	8.6	0.01	1.31	6.61
Al$_2$O$_3$	50	4.4	0.06	2.47	7.17

Fig. 3-1e showed the FTIR spectra of the samples calcined at various temperatures. The absorption peaks at 550-810 cm^{-1} were ascribed to the characteristic vibrations of Cu-O, Al-O, and Cu-O-Al bonds in CuAl$_2$O$_4$ material [34]. The peak at around 1380 cm^{-1} may correspond to the infrared vibration of NO$_3^-$ groups [41], confirming the presence of residual nitrate species.The slight peak at 1499 cm^{-1} might belong to the COO$^-$ stretching vibrations of the citrate ligands. The bending vibrations of the absorbed H$_2$O and the stretching vibrations of -OH groups were observed at around 1630 cm^{-1} and 3410 cm^{-1}, respectively [41]. The decrease of these adsorption peak intensities occurred upon temperature, in the frequency range located between 1380-1630 cm^{-1} and 3410 cm^{-1}. Such results indicate the decomposition of organic residues and nitrate groups as well as removal of surface -OH groups. The results also confirmed the disappearance of the amorphous phase while higher calcination temperatures were applied as reported by XRD results.

To clearly reveal the surface morphology of spinel crystalline phase, the sample calcined at 500 °C was selected as it mainly formed spinel phase with no significant sintering phenomenon (Fig. 3-3). With respect to the morphology of the sample calcined at 300 °C (Fig. 3-1a,b), more uniform globular nanoparticles with a mean diameter of 20-30 nm were identified by SEM at higher calcination temperature (500 °C). Moreover, agglomerates were observed throughout the sample (Fig. 3-3a,b). HRTEM (Fig. 3-3c) evidenced a representative lattice fringe with interplanar spacing of 0.24 nm, corresponding to the (311) plane of spinel $CuAl_2O_4$ [43], further confirming the formation of spinel phase obtained by wide angle XRD.
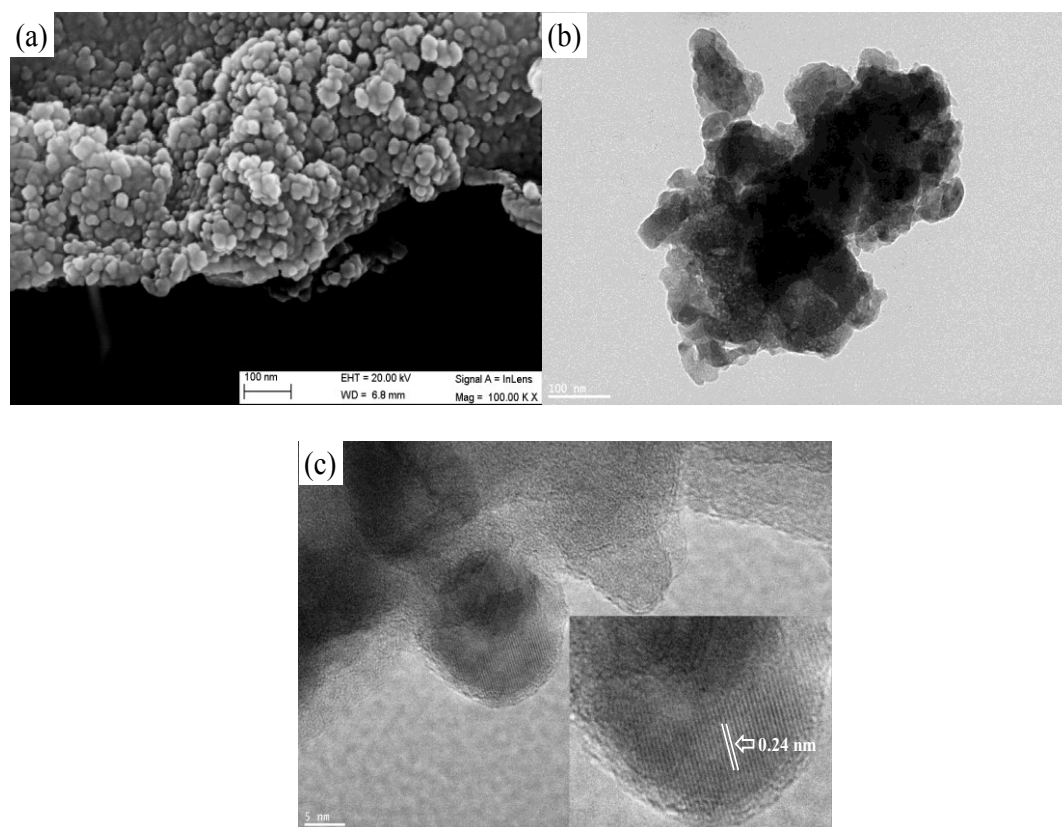

Figure 3-3 (a) SEM and (b and c) TEM images of the sample calcined at 500 °C

3.3.2 Performance of catalytic ozonation under different processes

To investigate the reaction kinetics of dye degradation, a pseudo first-order kinetic was expressed as below:

$$\ln (C/C_0) = -kt \tag{3-1}$$

where k is the apparent reaction constant; C_0 and C are the initial dye concentration and the concentration at time t, respectively.

First, the effect of calcination temperature (100-700 °C) of the catalytic materials was investigated via catalytic ozonation for the degradation of organic compound (AO7) (Fig. 3-4a). The leaching of metal ions from the catalyst was detected in the meantime. From this first material series, the thermal activation at 300 °C led to a catalyst which possessed a high catalytic activity combined with low copper (0.42 mg L^{-1}) and aluminum (less than 0.05 mg L^{-1}) leachings. As seen in Fig. 3-4a, the thermal treatment enhanced the stability of CuAl$_2$O$_4$ and decreased the copper and aluminum leaching from catalyst in the reaction solution. The amount of dissolved copper was as high as 2.59 mg L^{-1} druing 25 min reaction for the as prepared Cu-Al gel. As the gel was calcined at 200 °C and 300 °C, the amount of dissolved copper was decreased from 0.903 mg L^{-1} to 0.436 mg L^{-1}. In addition, the copper and aluminum leaching were remain around 0.4 mg L^{-1} and less than 0.05 mg L^{-1}, respectively, upon calcination at elevated temperatures (300-700 °C). This is possible due to the gradual formation of spinel CuAl$_2$O$_4$ phase, which enhances its stability. With the increase of calcination temperature among 100-300 °C, the catalytic activity of sample increased accordingly and the rate constants were 0.067 min^{-1}, 0.094 min^{-1}and 0.112 min^{-1}, respectively. However, a graducal and slight decrease of catalytic acticity was found with further increasing in calcination temperature. The increased catalytic activity among 100-300 °C is evidently attributed to the enhanced stability of catalyst, while the slight decrease of activity during higher calcination temperature could be ascribed to the loss of specific surface area of particles as well as the intensity of surface active sites such as hydroxyl group at higher sintering temperature.
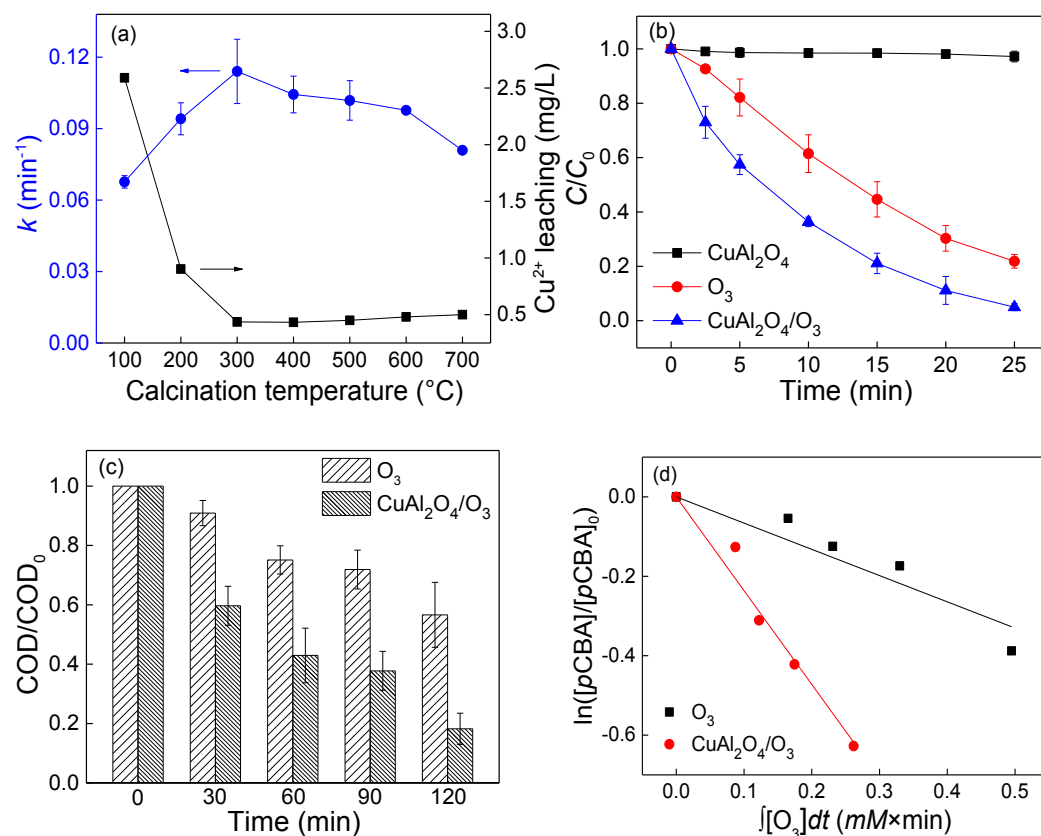
Figure 3-4 Effect of (a)calcination temperature of the samples on the AO7 removal rate; (b and c) degradation of AO7 ([AO7]= 100 mg L^{-1}, Q= 40 L h^{-1}, ozone dosage = 10.06 mg min^{-1}, catalyst dosage = 0.5 gL^{-1}, pH$_0$ 6.54); and (d) change of R$_{ct}$ value in ozonation alone and catalytic ozonation processes

Thus, in the light of these experiments, the catalytic performance of the samples was examined for a calcination temperature fixed at 300 °C. In order to illuminate the reason why the sample calcined at 300 °C exhibited a higher catalytic activity, the surface acidity of the sample was investigated by the pyridine adsorption technique on sample surface with the help of FTIR spectroscopy. The acid sites are thought to be one of the most important activity centers in catalytic ozonation process. Pyridine is the most commonly used basic probe molecule for surface acidity characterization [44]. Fig. 3-5a,b presents the infrared spectra of adsorbed pyridine on the surface of CuAl$_2$O$_4$ after degassing at 40 °C and 150 °C, respectively. At 40 °C, typical IR bands of adsorbed pyridine on catalyst include those related to pyridine adsorbed on (i) Lewis

acid sites (1446, 1597 and 1608 cm^{-1}), (ii) Brønsted acid sites (small peaks at 1540 and 1640 cm^{-1}) [44], and (iii) both Lewis and Brønsted acid sites with a band at 1491 cm^{-1} [13, 45]. The total and medium/strong Lewis acid sites were quantitatively calculated using pyridine adsorption followed by degassing at 40 and 150 °C according to the literature [46]. The total and medium/strong Lewis acid sites were 320.2 and 150.9 μmol g^{-1} on the surface of CuAl$_2$O$_4$ calcined at 300 °C, while those were 224.6 and 139.0 μmol g^{-1} at 500 °C, and 161.7 and 125.8 μmol g^{-1} at 700 °C. Clearly, the amount of Lewis acid sites decreased while increasing the calcination temperature of the sample, which is consistent with the catalytic behavior of the catalysts studied and shed light on the key role of Lewis acid sites during the catalytic ozonation process.
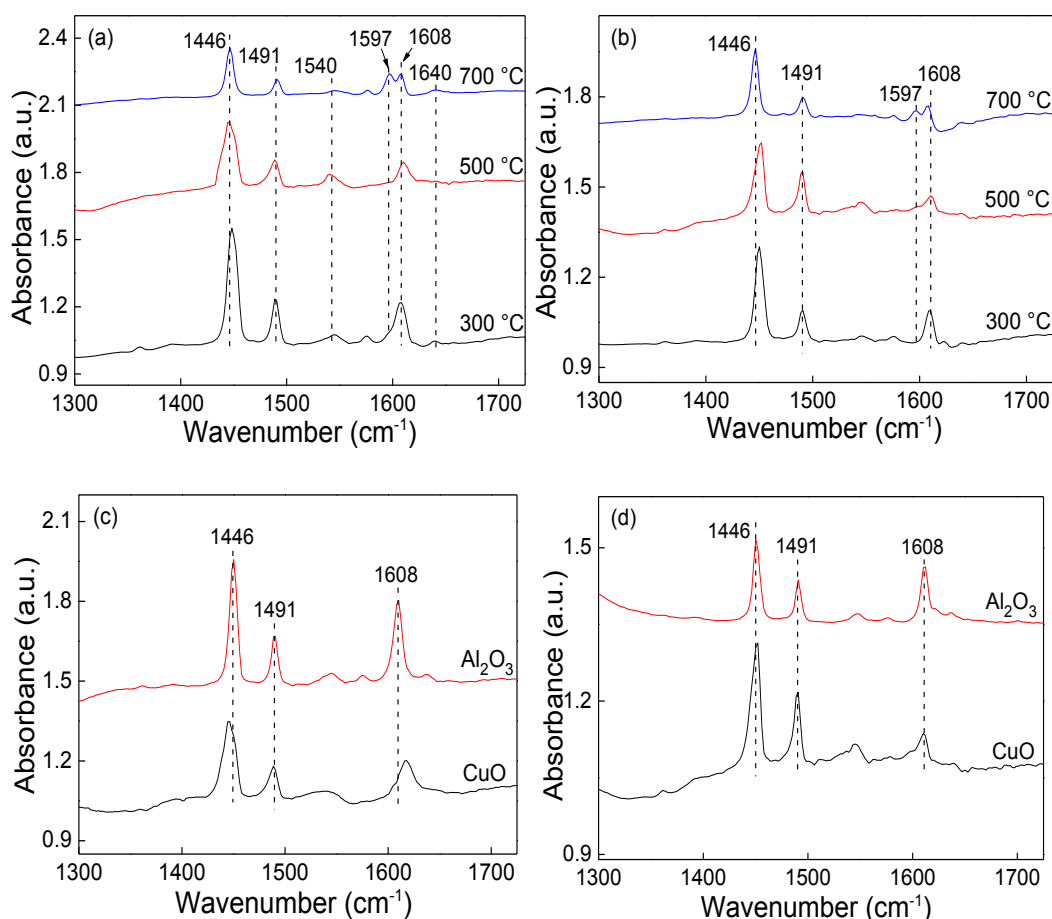

Figure 3-5 Pyridine-FTIR spectra of CuAl$_2$O$_4$ calcined at different temperatures after degassing at (a) 40 °C and (b) 150 °C; and CuO and Al$_2$O$_3$ after degassing at (c) 40 °C and (d) 150 °C

Hence, it is proposed that the better catalytic activity of $CuAl_2O_4$ calcined at 300 °C may arise from the cumulative effect of two main factors. On one hand, $CuAl_2O_4$ calcined at 300 °C presents a mesoporous network and a larger BET surface area/pore volume compared with the catalyst calcined at 200 °C or at temperature above 300 °C. Such properties can favor the diffusion of ozone and supply more active sites. On the other hand, the $CuAl_2O_4$ calcined at 300 °C possesses the largest amount of surface hydroxyl groups and Lewis acid sites. Both hydroxyl groups and Lewis acid sites influence not only the adsorption of organic compounds, but also the ozone decomposition on the catalyst surface [1]. These active sites play a crucial role in the enhancement of the catalytic performance. Therefore, the catalytic activity of $CuAl_2O_4$ with different calcination temperatures can be considered as a function of surface area, surface hydroxyl groups and Lewis acid sites.

As can be seen in Fig. 3-4b, no significant amount of dye was removed on $CuAl_2O_4$ within 25 min, indicating that there is only a weak adsorption of dye on $CuAl_2O_4$. For dye decomposition using ozonation only, 76.4 % of AO7 was decolorized in 25 min with a reaction rate constant of 0.053 min^{-1}, revealing the relatively high oxidation capability of ozone ($E^0 = 2.08$ V). The combination of $CuAl_2O_4$ and ozone enhanced the color removal of dye with an efficiency of 96.0 % reached after 25 min with a reaction rate constant of 0.112 min^{-1}. Obviously, the efficiency of COD removal in catalytic ozonation process is more efficient than that of single ozonation, as indicated in Fig. 3-4c. Ozone itself could only attain about 40% of COD removal within 120 min while the $CuAl_2O_4/O_3$ combination boosted the COD removal up to 87.2%. This implied that catalytic ozonation improved the oxidation performance with respect to ozonation alone for the degradation of organic intermediates, causing more COD removal.

To further confirm the AO7 dye degradation rather than the only decolorization occurring during the catalytic ozonation process, UV-Visible spectrophotometry and ionic chromatography were performed during the catalytic reaction (Fig. 3-6). As seen fromthe UV-visible spectra (Fig. 3-6a), the absorption wavelengths located at 485 nm, 310 nm and 228 nm were gradually faded as the reaction progress during the oxidation process. These absorption bands were related to an azo linkage, benzene and naphthalene ringstructures, respectively. Thus it means the decomposition of azo linkage and aromatic fragment in the parent pollutant dye and its intermediates. In addition, the absorbance of all absorption bands were further decreased over 60 min, which were attributed to the gradual mineralization of intermediates. The quantitative monitoring of inorganic ions, such as SO_4^{2-}, NO_2^-, NO_3^- and NH_4^+ were shown in Fig.3-6b. SO_4^{2-} started to be formed at the beginning of oxidation process and kept positive slope of evolution, indicating the gradual mineralization of dye or $-SO_3$ containing aromatic intermediates. The final concentration of SO_4^{2-} released after 120 min reached a value of 0.2 mM, which is less than the stoichiometric value (0.28 mM, the total sulphur in AO7 molecule). The concentration of $NO_2^-$was almost zero all the time in this catalytic oxidation process. $NO_3^-$and NH_4^+ were generated in the initial stage and followed by the accumulation-destruction cycles. The NO_3^- concentration increased all the time and reached maximum (0.053 mM) at 25 min while NH_4^+ concentration reached maximum (0.519 mM) at 45 min. After that, the concentration of NH_4^+ almost kept unchanged and decreased slightly in the end (120 min). The nitrogen mass balance (the largest nitrogenous detected is 0.557 mM in 45 min) was close tothat expected by the reaction stoichiometry (0.57 mM. The non-equilibrating of the nitrogen mass balance was attributed totransformation of nitrogen to others species such asgas N_2 and/or NH_3. Note that NH_4^+ was not oxidized to NO_3^-in significant extent

even under the strong oxidizing conditions used. The results indicated that the organic AO7 gradually faded with the progress of the reaction [47], which was attributed to the gradual mineralization of intermediates.
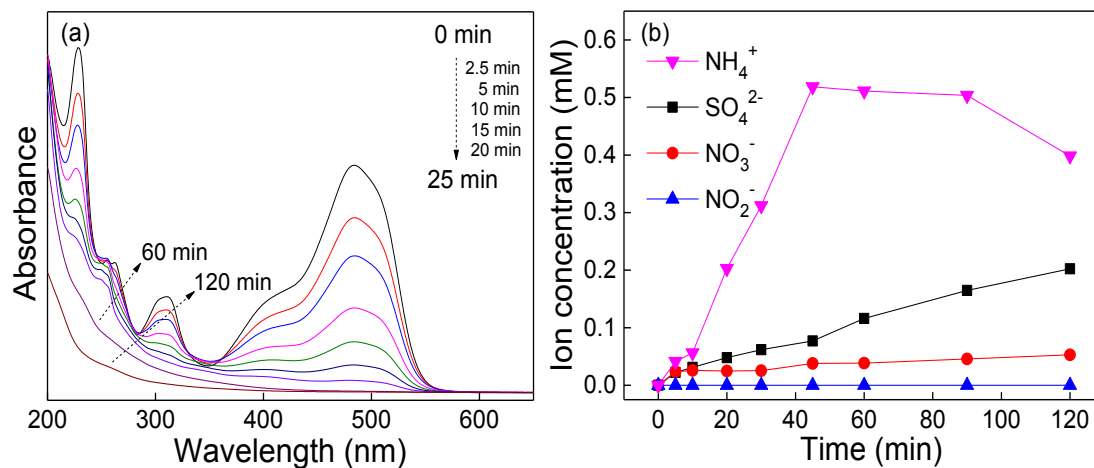

Figure 3-6 UV-visible spectra changes (a) and evolution of inorganic ions (b) with reaction time in catalytic ozonation ([AO7] = 100 mg L^{-1}, Q = 40 L h^{-1}, ozone dosage = 10.06 mg min^{-1}, catalyst dosage = 0.5 g L^{-1}, pH$_0$ 6.54)
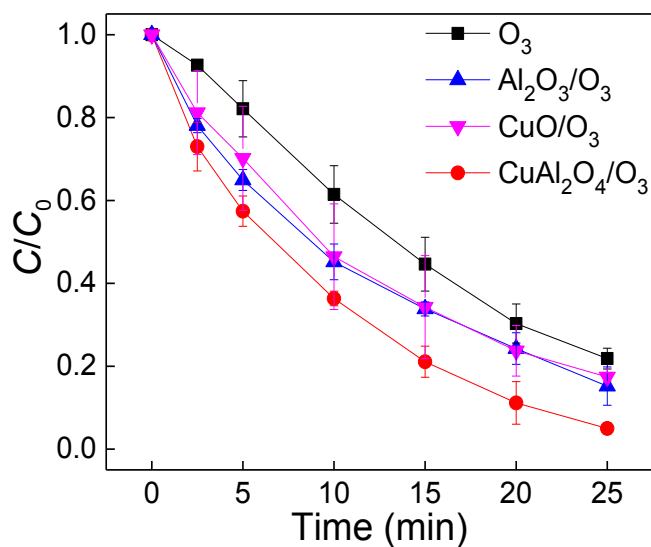

Figure 3-7 Degradation of AO7 with different catalysts in catalytic ozonation ([AO7] = 100 mg L^{-1}, Q = 40 L h^{-1}, ozone dosage = 10.06 mg min^{-1}, catalyst dosage = 0.5 g L^{-1}, pH$_0$ 6.54)
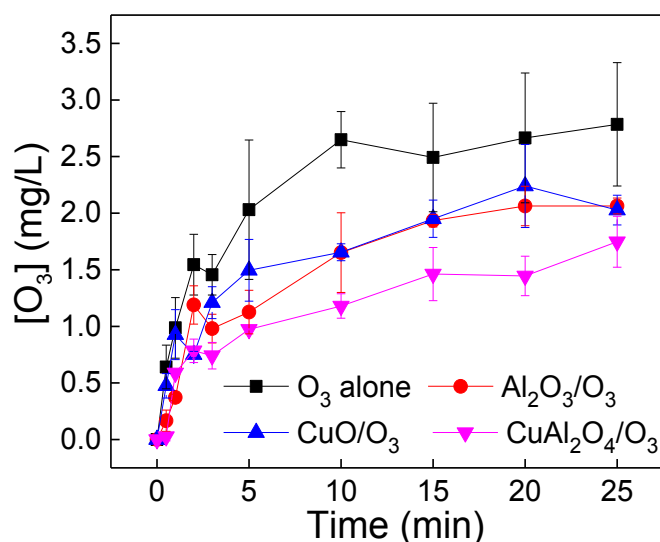
Figure 3-8 The aqueous ozone concentration in catalytic ozonation ($Q = 40$ L h^{-1}, ozone dosage = 10.06 mg min^{-1}, catalyst dosage = 0.5 g L^{-1}, pH$_0$ 6.54)

Under identical experimental conditions, single-metal oxides/ozone combinations (CuO/O$_3$ and Al$_2$O$_3$/O$_3$) exhibit a lower efficiency in dye decolorization with associated rate constants of 0.071 min^{-1} and 0.074 min^{-1} (Fig. 3-7). Thus, the CuAl$_2$O$_4$/O$_3$ catalytic system could efficiently generate more reactive oxygen species (eg.HO$^•$ or O$_2^{•-}$) with respect to CuO/O$_3$ and Al$_2$O$_3$/O$_3$. Besides, the aqueous O$_{3(aq)}$ decomposition in the absence/presence of catalyst was monitored. As shown in Fig. 3-8, the presence of CuAl$_2$O$_4$ significantly reduced aqueous O$_3$ concentration (over 50% in the first 10 min) in comparison with CuO or Al$_2$O$_3$ alone, demonstrating that CuAl$_2$O$_4$ was more active in promoting O$_3$ decomposition. Therefore, the catalytic improvement may arise from a synergic effect between $\equiv$Cu^{2+} and $\equiv$Al^{3+} promoting a higher decomposition rate of aqueous ozone.

On one hand, the high surface area of CuAl$_2$O$_4$ may play an important role in improving the catalytic activity by exposing more reactive sites with respect to single oxides, and accessibility of the actives sites may be easier thanks to the open and uniform mesoporosity of the CuAl$_2$O$_4$ sample (Table 3-1). On the other hand, the density of the surface hydroxyl groups would be affected by the variation of the point

of zero charge (pH$_{pzc}$), then probably affecting theamount of active sites on the catalyst surface and further altering the catalytic activity of catalyst [10]. As seen, the pH$_{pzc}$ values for CuO, Al$_2$O$_3$ and CuAl$_2$O$_4$ were 6.61, 7.17 and 8.45, respectively while the density of surface hydroxyl groups were estimated to be 1.31, 2.47, 2.78 mmol g^{-1}. Thus, it is assumed that more surface Lewis acid sites were formed on the surface of CuAl$_2$O$_4$. In order to confirm this point, the nature and strength of the surface acid sites on single metal oxides (CuO and Al$_2$O$_3$) were also investigated by FTIR spectra of adsorbed pyridine (Fig. 3-5c,d). The respective total and medium/strong Lewis acid sites on the surface of CuO were 245.7 and 145.6 μmol g^{-1}, while those on the surface of Al$_2$O$_3$ were 311.1 and 95.8 μmol g^{-1}. These values are lower than those obtained on the surface of CuAl$_2$O$_4$ with values of 320.2 and 150.9 μmol g^{-1} corresponding to total and medium/strong Lewis acid sites. Notably, the amount of total Lewis acid sites on Al$_2$O$_3$ is close to that of CuAl$_2$O$_4$ and larger than that of CuO. In contrast, a larger amount of medium/strong Lewis acid sites appeared on CuO surface compared with Al$_2$O$_3$. It may indicate that the presence of aluminum increased the total Lewis acid sites, as well as the hydroxyl groups (Table 3-1). Then it can be concluded that aluminum acts as a reservoir for surface active sites, and this is in line with the result of hydroxyl group density (Table 3-1). The loading of copper altered the surface acidity of catalyst surface, especially increased medium/strong Lewis acid sites.

Now, it is interesting to note that albeit strong differences in specific surface areas of CuO and Al$_2$O$_3$ (5 m^2 g^{-1} vs 50 m^2 g^{-1}) were observed (Table 3-1), only little distinction in dye decolorization rate was noticed (0.071 min^{-1} vs 0.074 min^{-1}). Usually, the intrinsic reaction rates in heterogeneous catalytic processes are mediated by available reactive sites, which are directly proportional to the specific surface area of the catalysts. Thus, it is suggested that the catalytic performance of CuO was not only

due to active sites such as the surface hydroxyl groups, but also probably due to the role of electron transfer assigned to a redox couple of copper.

We attempt to estimate the evolution of HO$^{\bullet}$ production with and without the presence of the catalyst. An experimental method has been developed to determine the concentrations of both ozone and HO$^{\bullet}$ during catalytic ozonation process [48]. The method is based on the measurement of the decrease of a probe compound monitored by HPLC. Usually p-chlorobenzoic acid (pCBA) was selected as a probe compound, because of its very weak reactivity with ozone ($k_{ozone/pCBA} \leq 0.15$ M^{-1}s^{-1}), but reacts readily with HO$^{\bullet}$ ($k_{HO\bullet/pCBA} = 5.2\times10^9$M^{-1}s^{-1}). The elimination of the probe compound (pCBA) can be calculated bya second-order kinetic and expressed as a function of ozone exposure in the following equations:

$$\ln\left(\frac{[p\text{CBA}]_t}{[p\text{CBA}]_0}\right) = -(k_{HO\bullet}R_{ct} + k_{ozone})\int_0^t[O_3]\mathrm{d}t \tag{3-2}$$

$$R_{ct} = \frac{\int_0^t[HO\bullet]dt}{\int_0^t[O_3]\mathrm{d}t} \tag{3-3}$$

where the R_{ct} value is defined as the ratio of the HO$^{\bullet}$ concentration to the ozone concentration,which directly reflects the transformation efficiency of ozone into HO$^{\bullet}$.

According to Fig. 3-4d, the R_{ct} values, reflecting the transformation efficiency of ozone into HO$^{\bullet}$, in ozonation alone and catalytic ozonation were calculated to be 2.09×10^{-9} and 7.54×10^{-9}, respectively, indicating that the CuAl$_2$O$_4$/O$_3$ combination enhanced the efficiency of the transformation of ozone into HO$^{\bullet}$. This is in agreement with the degradation efficiency of organic pollutant in ozonation and catalytic ozonation systems.

3.3.3 Investigation of the mechanism - use of organic scavengers

It is known that $tert$-butyl alcohol (TBA) is a prevalent quenching agent for hydroxyl radical at the rate constant of 6.0×10^8 M^{-1}s^{-1} [49]. Moreover, it reacts rather

slowly with O_3 at the rate constant of 3.0×10^{-3} $M^{-1}s^{-1}$ [50]. The quenching tests of TBA were revealed in Fig. 3-9a. The presence of 50 mM TBA suppressed the dye degradation process slightly with the rate constant declining from 0.112 min^{-1} to 0.10 min^{-1}, indicating that the reactive radicals ($HO^{\bullet}$) were generated during the catalytic ozonation. However, the increased concentration of TBA (100 mM or 250 mM) did not inhibit the efficiency of dye removal obviously. Especially, it was found that the reaction rate did not decrease but slightly increase to 0.15 min^{-1} in the presence of 100 mM TBA.
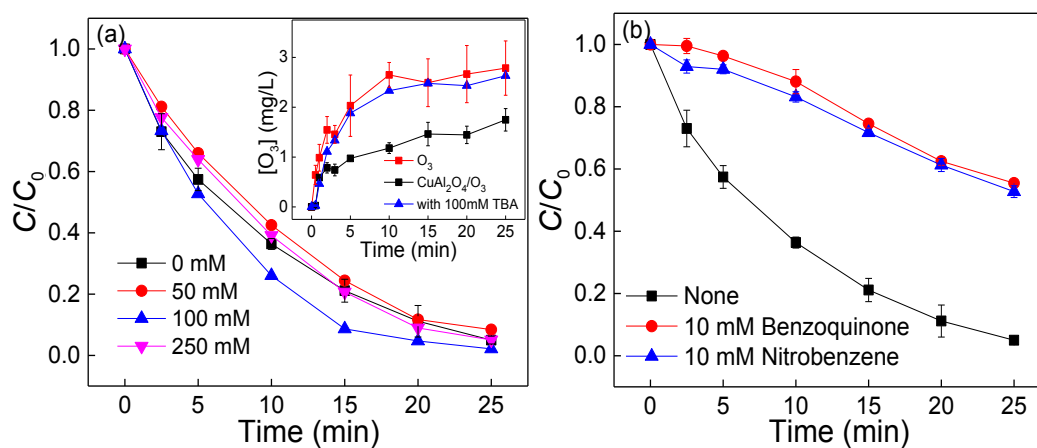

Figure 3-9 Effects of (a) TBA; (b) nitrobenzene (NB) and benzoquinone (BQ) in catalytic ozonation process ([AO7]= 100 mg L^{-1}, Q= 40 L h^{-1}, ozone dosage = 10.06 mg min^{-1}, catalyst dosage = 0.5 g L^{-1}, pH_0 6.54)
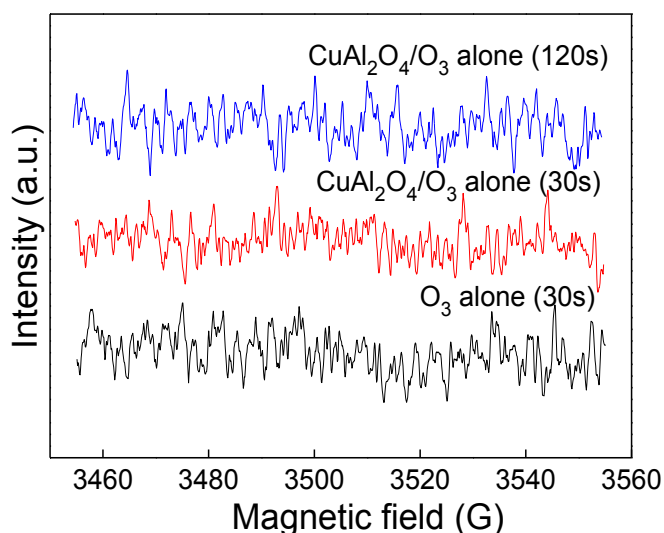
Figure 3-10 ESR spectrums using DMPO as a trapping agent in absolute ethyl alcohol solution

No significant inhibition or even slight positive effect of radical scavenger suggests that the $CuAl_2O_4$ catalytic ozonation of dye may predominantly take place on the catalyst surface, which is in line with previous reports [51-55]. The HO$^\bullet$ generated on the catalyst surface may preferentially react with the target organics adsorbed onto the catalyst. On one hand, the added TBA would improve the stabilization of the dissolved ozone and increase the dissolved ozone concentration, thus rendering more O_3 to diffuse and react within the active sites on the catalyst surface [51, 52, 55]. This can be experimentally confirmed by the increased aqueous O_3 concentration with the presence of TBA in the catalytic ozonation (inset of Fig. 3-9a). On the other hand, as reported in literature [13, 45], TBA with hydrophilic property in bulk solution predominantly scavenged the free radicals in solution rather than to be adsorbed on the catalyst surface [32].

In contrast, unlike hydrophilic compound such as TBA, the hydrophobic quenching agents such as nitrobenzene (NB) and 1,4-benzoquinone (BQ) may approach to the catalyst surface more easily and quench radicals existing both on the catalyst surface as well as in the bulk solution [47]. Hence, quenching tests using nitrobenzene

(NB) and 1,4-benzoquinone (BQ) as quenching agents were also conducted. Nitrobenzene was suggested to be a more effective scavenger for $HO^\bullet$. The observed reaction rate constant of nitrobenzene with O_3 alone was only (0.09 ± 0.02) M^{-1} s^{-1} [50], while nitrobenzene with $HO^\bullet$ reached 3.9×10^9 $M^{-1}s^{-1}$ [49], which was 6.5 times greater with respect to TBA. 1,4-benzoquinone is widely used as a standard scavenger for $O_2^{\bullet-}$ radicals and exhibited a rate constant of 8.0×10^9 M^{-1} s^{-1} [56]. For O_3 alone, the rate was estimated at 2.5×10^3 M^{-1} s^{-1} [57]. As shown in Fig. 3-9b, when 10 mM NB was added, more than 40% decrease in dye removal efficiency was observed. Similarly, the presence of BQ also drastically inhibited the removal efficiency of dye. However, no obvious characteristic spectrum of $DMPO-O_2^-$ was observed in ESR tests (Fig. 3-10). Actually either $O_2^{\bullet-}$ or $HO_2^\bullet$ reacted very slowly with DMPO at rates of 10 and 6.6×10^3 M^{-1} s^{-1}, respectively [58]. Here, instead of pure water, absolute ethyl alcohol was used as a reaction medium to extend the half-life of $O_2^{\bullet-}$. These observation might indicate that the amount of $O_2^{\bullet-}$ was little and the $HO^\bullet$ radicals were the dominant reactive oxygen species responsible for contaminant degradation. Also, it should be noted that though BQ is widely used as a standard scavenger for $O_2^{\bullet-}$, BQ can also rapidly react with $HO^\bullet$ with a rate constant of 1.2×10^9 M^{-1} s^{-1} [49], eliminating part of $HO^\bullet$.

Considering the drastic inhibition with the addition of NB and BQ while almost no inhibition was observed with the presence of TBA, it is further assumed that the hydroxyl radicals within a surface region of the catalyst (this type of radicals is defined as the "adsorbed $HO^\bullet$"), instead of those in the bulk solution, were the main reactive oxygen species.In the heterogeneous catalytic oxidation process, the oxidant needs to directly contact with the catalyst surface on which reactive radicals are formed. The radicals generated on the surface of solid catalyst may diffuse from the catalyst surface

into the bulk solution. Herein, the increased concentration of 50 mM TBA indeed slightly inhibited the efficiency of dye removal. It can be deduced that excessiveHO$^\bullet$ generated on the catalyst surface would also diffuse into the bulk of the aqueous solution and then be scavenged.

3.3.4 Reactive species (HO$^\bullet$) detected by florescence spectroscopy and ESR analysis

The coumarin fluorescence probing technique and ESR/DMPO spin trapping experiment have been used to further confirm the existence of active species.As presented in Fig. 3-11a, the fluorescence intensity at about 452 nm increased gradually as the reaction time was prolonged, suggesting that HO$^\bullet$generation was enhanced with the increase of reaction time in the catalytic ozonation. Compared with ozonation alone, the fluorescence intensity was much higher in the presence of catalyst (Fig. 3-11b), which indicated that the catalyst significantly improved the production of HO$^\bullet$ from ozone decomposition. The generation of same active species was also determined by ESR spin-trap experiments with DMPO, as illustrated in Fig. 3-11c. Two groups of small signals are observed in the presence of O$_3$ alone (30s). The one is the characteristics spectrums of the DMPO-OH adduct (hyperfine splitting constants: a_N= a_H= 14.9 G), demonstrating the generation of HO$^\bullet$ due to self-decomposition of ozone. The other is three-line peak (marked with red dot), which is assigned to the degradation of DMPO to a nitroxide-like radical [59-62]. The typical ESR spectrum of the DMPO-O$_2^-$ (hyperfine splitting constants: a_N= 14.1 G, a_H= 10.8 G, and a_H= 1.4 G) [59] was not observed here, which may due to the conversion of the unstable DMPO-O$_2^-$ adduct [58]. Of note, the nitroxide-like radical is considered to form through cleavage of the N-C bond and ring opening of DMPO-O$_2^-$ adduct [60] or the excessive HO$^\bullet$ oxidation of DMPO-OH [61].
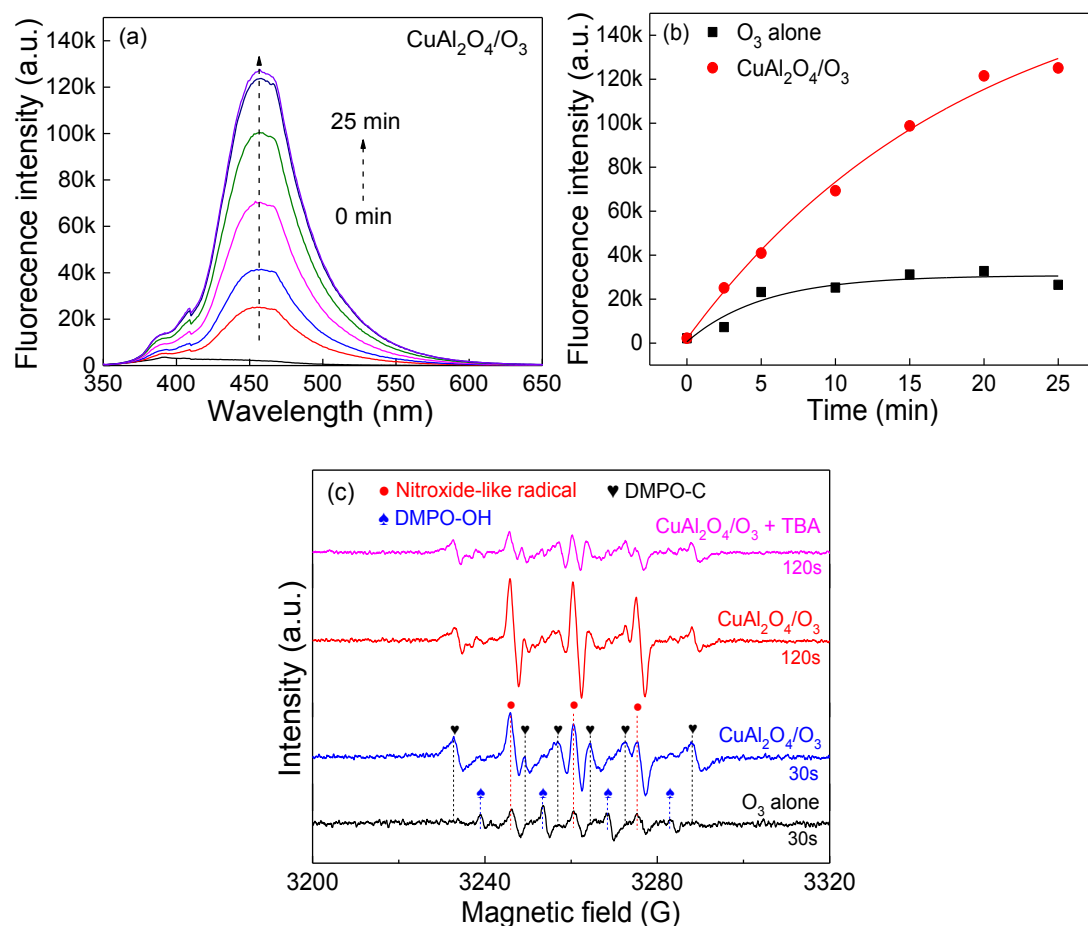
Figure 3-11 Fluorescence spectra changes (a and b) with reaction time in ozonation alone and catalytic ozonation processes; (ozone dosage = 10.06 mg min^{-1}, catalyst dosage = 0.5 g L^{-1}, pH$_0$ 6.54) (c) ESR spectrums using DMPO (40 mM) as a trapping agent

As compared to ozonation alone, the intensity of characteristics spectrums of nitroxide-like radical was obviously enhanced in 120 s, and was not disappeared completely and just decreased with the addition of a quencher TBA (50 mM). These results directly approved the generation of active oxygen species (HO$^{\bullet}$ or O$_2^{\bullet-}$), which were consistent with the result in the radical scavenging experiments. Besides, six new peaks with a ratio intensity of 1:1:1:1:1:1 (Fig. 3-11c), which are thought to be characteristic of carbon-centered radical adduct (DMPO-C) [62-64], were also observed in catalytic ozonation process. The appearance of the carbon-centered radical adduct in catalytic ozonation process can be attributed to two aspects. On one hand, the

DMPO-C adduct could be generated due to the attack ofcarbon containing compounds by HO[63, 64]. As indicatedin Fig. 3-1e, some organic residuals such as COO^- group on catalyst surface can be acted as the carbon source. On the other hand, the DMPO-C adduct might be also formed when DMPO reacted with its oxidized product, which was produced due to the attack of excessive HO[65].
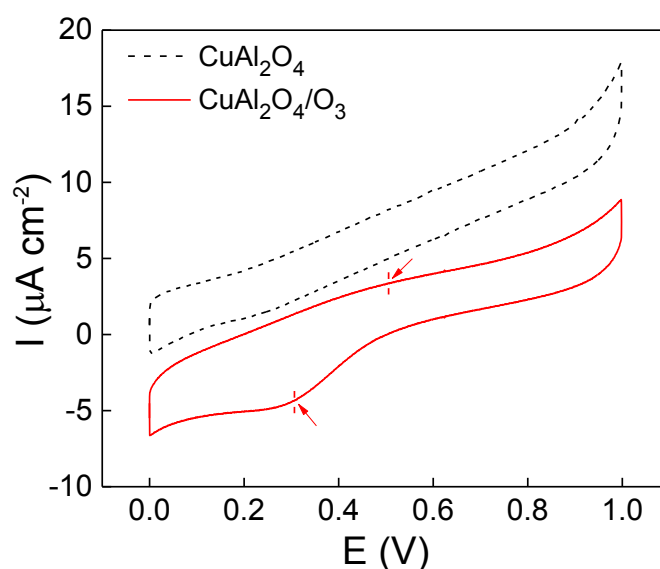
3.3.5 Probing the role of electron transfer process

Figure 3-12 Cyclic voltammetry scans of catalyst with and without ozone in aqueous solutions (scan rate: 50 mV s^{-1}, [NaSO$_4$] = 50 mM)

To clarify the probable role of electron transfer/redox couple of copper, current-voltage scan of the reaction systemwas used to probe the electron transfer process at water-catalyst interface. The cyclic voltammetry (CV) behaviors of $CuAl_2O_4$ were carried out in a 50 mM Na_2SO_4 solution under a saturation air or ozone atmosphere. As indicated in Fig. 3-12, there appeared current at the $CuAl_2O_4$ modified electrode, indicating that there was surface charge on $CuAl_2O_4$. In addition, $CuAl_2O_4$ modified electrode gave stronger current signals in the presence of O_3 than that without O_3, especially for an enhancement in the reduction current. More importantly the obvious redox peak of Cu^+ to Cu^{2+} (around 0.5 V) and Cu^{2+} to Cu^+ (around 0.3 V) [66] in the

CV curve of $CuAl_2O_4/O_3$ process can be observed, indicating the fast redox reaction of $CuAl_2O_4$ in the ozone oxidation solution. The results verify that a reduction process occurred on the surface of $CuAl_2O_4$ during the catalyitc decomposition of O_3. Thus it is believed that the combined action of an interfacial electron transfer and a stronger interaction between the catalyst and O_3 would be responsible for a remarkable enhancement on the catalytic activity.

To further investigate the oxidation state of surface elements before and after ozonation, XPS analysis was carried out. Fig. 3-13a showed that the Al 2p peak region consisted of Al 2p peak of Al^{3+} (around 74 eV) and Cu 3p peaks (around 77 eV) [67]. There was litte difference for these peaks before and after the ozonation reaction. For the XPS spectra of Cu 2p (Fig. 3-13b), the main peak at 934.1 eV was attributed to $\equiv Cu^{2+}$ on the catalyst surface [68]. After ozonation process, it was observed that the peak around 932.6 eV which could be assigned to the formation of Cu^+ [69] with the relative content of 20.6%. It indicated that electrons were transferred from surface $\equiv Cu^{2+}$, which can follow the sequence of $\equiv Cu^{2+} \rightarrow \equiv Cu^+ \rightarrow \equiv Cu^{2+}$ redox reaction during the catalytic ozonation process.
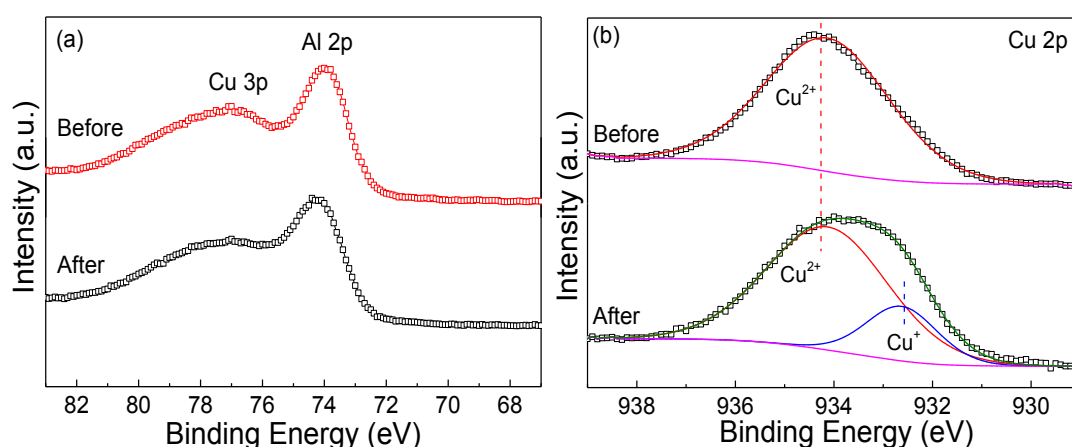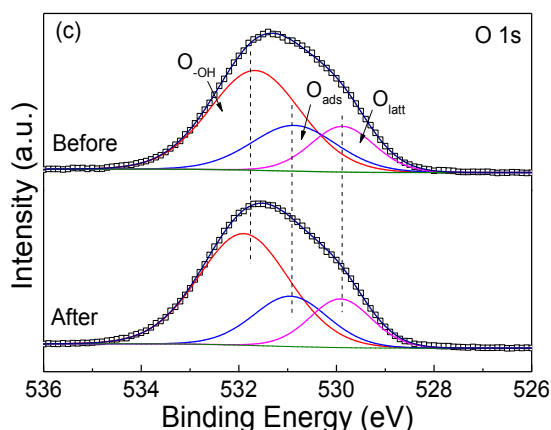
Figure 3-13 XPS spectra of (a) Al 2p and (b) Cu 2p and (c) O 1s before and after ozonation of CuAl$_2$O$_4$ catalyst

Actually the Cu 2p$_{3/2}$ peaks (Fig. 3-13b) of Cu^0 and Cu$^+$ are too close to be differentiated because their binding energies are different by only 0.1 eV. Thus the LMM auger emission spectra were applied to further differentiate between Cu^0 and Cu$^+$. According to previous reports [70-72], the position of Cu LMM Auger peak is around 569.2 eV for Cu^{2+} in CuO, high binding energy 570 eV for Cu$^+$ in Cu$_2$O, and low binding energy 568 eV for Cu^0. As shown in Fig. 3-14, the obvious peak (~572 eV, red arrow) at higher binding energy which can be due to the formation of Cu$^+$ was observed in the spectra of our sample after reaction (Fig. 3-14b) compared with the spectra before reaction (Fig. 3-14a). In addition, no difference was seen in low range of binding energy in both samples. Therefore, it is reasonably concluded that the peak around 932.6 eV in Fig. 3-8b is related to Cu$^+$ in the catalyst.
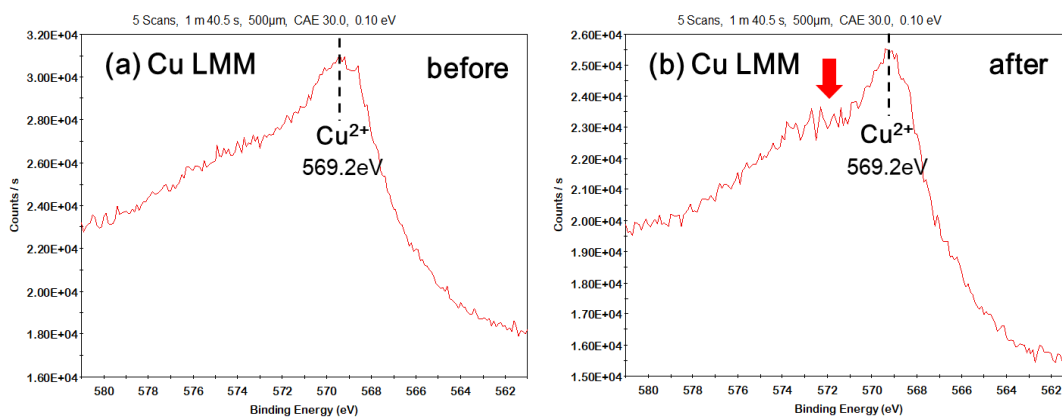
Figure 3-14 XPS Cu LMM spectra of the sample before and after catalytic ozonation

In Fig. 3-13c, the O1s spectra of the catalyst before and after ozonation showed several peaks at 529.9, 530.9 and 531.8 eV, which represented the surface lattice oxygen of metal oxide (O^{2-}, denoted as O_{latt}), surface adsorbed oxygen species (O_2^{2-}/O^-, denatedO_{ads}), and surface hydroxyl species (OH^-, denated O_{-OH}), respectively [73]. It could be found that, after reaction, the relative contents of O_{latt} and O_{ads} decreased slightly from 18.3% to 17.8% and from 24.4% to 22.2%, respectively, while the relative contents of O_{-OH} increased from 57.3% to 60.0%. The slight increase in O_{-OH} content can be ascribed to the formation of hydroxyl groups on the catalyst surface, while the decrease of content in O_{latt} and O_{ads} suggested that the lattice oxygen or surface adsorbed oxygen might be involved in the catalytic reaction. The probable consumption of surface active oxygen including lattice oxygen (O_{latt}) in catalytic ozonation, might also contribute in global copper oxide reduction. In addition, it is remarkable that the oxygen species especially for O_{-OH} on the surface of catalyst could be regenerated via the reaction with water and O_3/O_2 [3], which may be the reason for the increase of surface hydroxyl groups content. This also can be verified from the reactions (Eqs. (3-4)-(3-16)) which are used to illuminate the proposed mechanism of radical generation. Given a little variation of the relative contents of these oxygen species, we further assume that the stable content of oxygen species could be beneficial for the radical generation in the catalytic reaction, as well as the catalyst stability (Fig. 3-17). In contrast, the O1s spectra of CuO were also investigated (Fig. 3-15) and found that the relative contents of surface adsorbed oxygen (O_{ads}) and surface hydroxyl species (O_{-OH}) in $CuAl_2O_4$ oxide (81.7%) were much larger than that in CuO oxide (28.0%). It further confirmed that the present Al can act as a reservoir for surface adsorbed oxygen or surface hydroxyl species which finally contribute to the decomposition of O_3 into reactive radicals.
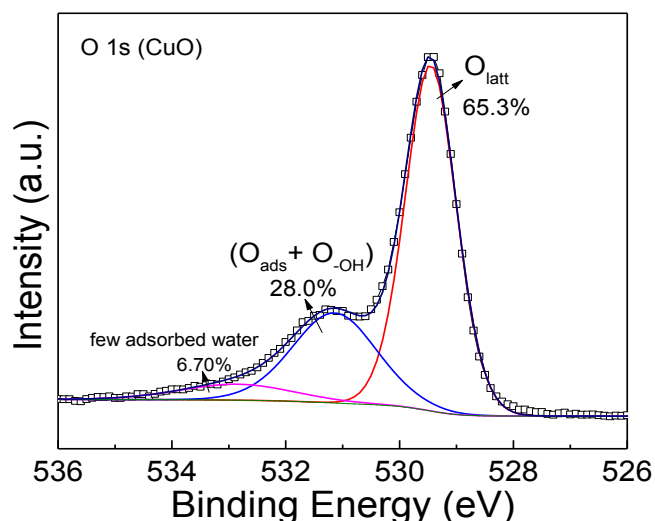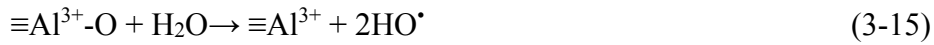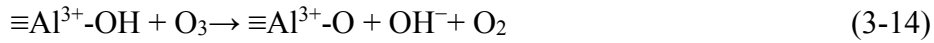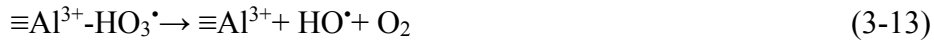
Figure 3-15 XPS spectra of O1s on the surface of CuO oxide

On the basis of the experimental results and the literature [1, 4, 13, 74, 75], a possible mechanism of radical generation (see below) is proposed for the catalytic ozonation process over Cu-Al spinel. First, spontaneous adsorption of water molecules on Lewis acid sites of the metal oxide surface would occur. Slight increase of the adsorbed water molecules acidity would lead to their dissociation and subsequent formation of the surface hydroxyl groups (Eq. (3-4) and Eq. (3-10)). Then, aqueous ozone can easily substitute the surface hydroxyl groups leading to the formation of $O_3^{\bullet-}$ complexing $\equiv Cu^{2+}$ sites at the vicinity, and the parallel release of $HO^{\bullet}$ (Eq. (3-5)). Subsequently, electron charge transfer from $O_3^{\bullet-}$ to $\equiv Cu^{2+}$ site generate the surface Cu(I) oxidation state, with the production of $HO_2^{\bullet}$ (Eq. (3-6)) and molecular O_2. The unstable $HO_2^{\bullet}$ would decompose into H^+ and $O_2^{\bullet-}$ (Eq. (3-7)). Furthermore, ozone may abstract one electron from surface $\equiv Cu^+$ to produce surface $O_3^{\bullet-}$ (Eq. (3-8)). The surface $O_3^{\bullet-}$ could quickly decompose to produce oxygen and $HO^{\bullet}$ (Eq. (3-9)).

Besides, for $\equiv Al^{3+}$ active sites, ozone would react with the surface hydroxyl groups to produce $HO_2^{\bullet}$ with the release of oxygen (Eq. (3-11)), the $HO_2^{\bullet}$ further reacted with ozone to form $HO_3^{\bullet}$ (Eq. (3-12)). Finally the $HO_3^{\bullet}$ decomposed into oxygen and $HO^{\bullet}$ (Eq. (3-13)). Additionally, due to the decomposition of ozone, ozone may react with

the $\equiv Al^{3+}$-OH groups producing surface atomic oxygen (Eq. (3-14)), the active atomic oxygen with a high reduction potential (2.43V) might directly oxidize water to form $HO^\bullet$ (Eq. (3-15)) [45, 76]. It could also react with O_3 to produce $O_2^{\bullet-}$ with the release of oxygen (Eq. (3-16)).

$$\equiv Cu^{2+} + H_2O \rightarrow \equiv Cu^{2+}\text{-}OH + H^+ \tag{3-4}$$

$$\equiv Cu^{2+}\text{-}OH + O_3 \rightarrow \equiv Cu^{2+}\text{-}O_3^\bullet + HO^\bullet \tag{3-5}$$

$$\equiv Cu^{2+}\text{-}O_3^\bullet + OH^- \rightarrow \equiv Cu^+ + HO_2^\bullet + O_2 \tag{3-6}$$

$$HO_2^\bullet \rightarrow H^+ + O_2^{\bullet-} \tag{3-7}$$

$$\equiv Cu^+ + O_3 \rightarrow \equiv Cu^{2+}\text{-}O_3^\bullet \tag{3-8}$$

$$\equiv Cu^{2+}\text{-}O_3^\bullet + H^+ \rightarrow \equiv Cu^{2+} + HO^\bullet + O_2 \tag{3-9}$$

$$\equiv Al^{3+} + H_2O \rightarrow \equiv Al^{3+}\text{-}OH + H^+ \tag{3-10}$$

$$\equiv Al^{3+}\text{-}OH + O_3 \rightarrow \equiv Al^{3+}\text{-}HO_2^\bullet + O_2 \tag{3-11}$$

$$\equiv Al^{3+}\text{-}HO_2^\bullet + O_3 \rightarrow \equiv Al^{3+}\text{-}HO_3^\bullet + O_2 \tag{3-12}$$

$$\equiv Al^{3+}\text{-}HO_3^\bullet \rightarrow \equiv Al^{3+} + HO^\bullet + O_2 \tag{3-13}$$

$$\equiv Al^{3+}\text{-}OH + O_3 \rightarrow \equiv Al^{3+}\text{-}O + OH^- + O_2 \tag{3-14}$$

$$\equiv Al^{3+}\text{-}O + H_2O \rightarrow \equiv Al^{3+} + 2HO^\bullet \tag{3-15}$$

$$\equiv Al^{3+}\text{-}O + O_3 \rightarrow \equiv Al^{3+} + O_2^{\bullet-} + O_2 \tag{3-16}$$
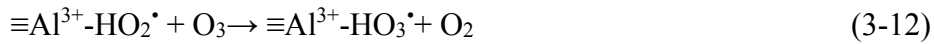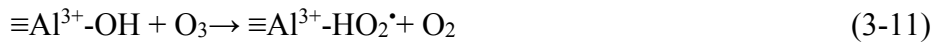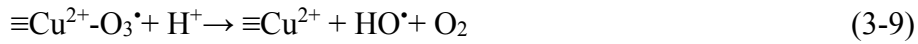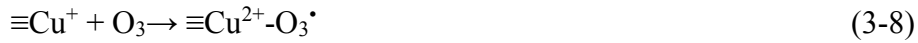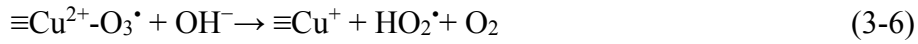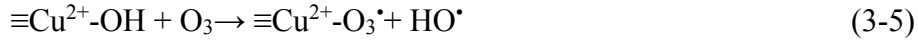
In the Cu-based AOPs, owing to the multiple oxidation states of Cu, the mechanisms are much more complicated [77, 78]. Another potential mechanism of enhanced catalytic ozonation might be also involved in our work, namely, the generation of $\equiv Cu^{3+}$ [79], which is highly unstable and difficult to observe. The electron transfer process may be similar to the $\equiv Cu^{2+}$-oxidant reactions [78, 80]. Although there is no direct evidence to identify the existence of transient high-valent Cu metal on the catalyst surface during ozone-oxide interaction, the $\equiv Cu^{3+}$ species may possibly be formed if an additional electron transfer step (between the $\equiv Cu^{2+}$ and the

undissociated/adsorbed $HO^{\bullet}$) is assumed to follow surface hydroxyl catalysis from the metal-ozone complex $\equiv Cu^{2+}-(OH)O_3$ (to surface absorbed radical $\equiv Cu^{2+}-HO^{\bullet}$) [81]. More studies are needed on the clarification of the Cu(III)-catalyzed mechanism and the nature of complexed Cu(III) species.

3.3.6 Effects of several parameters and stability of the catalyst
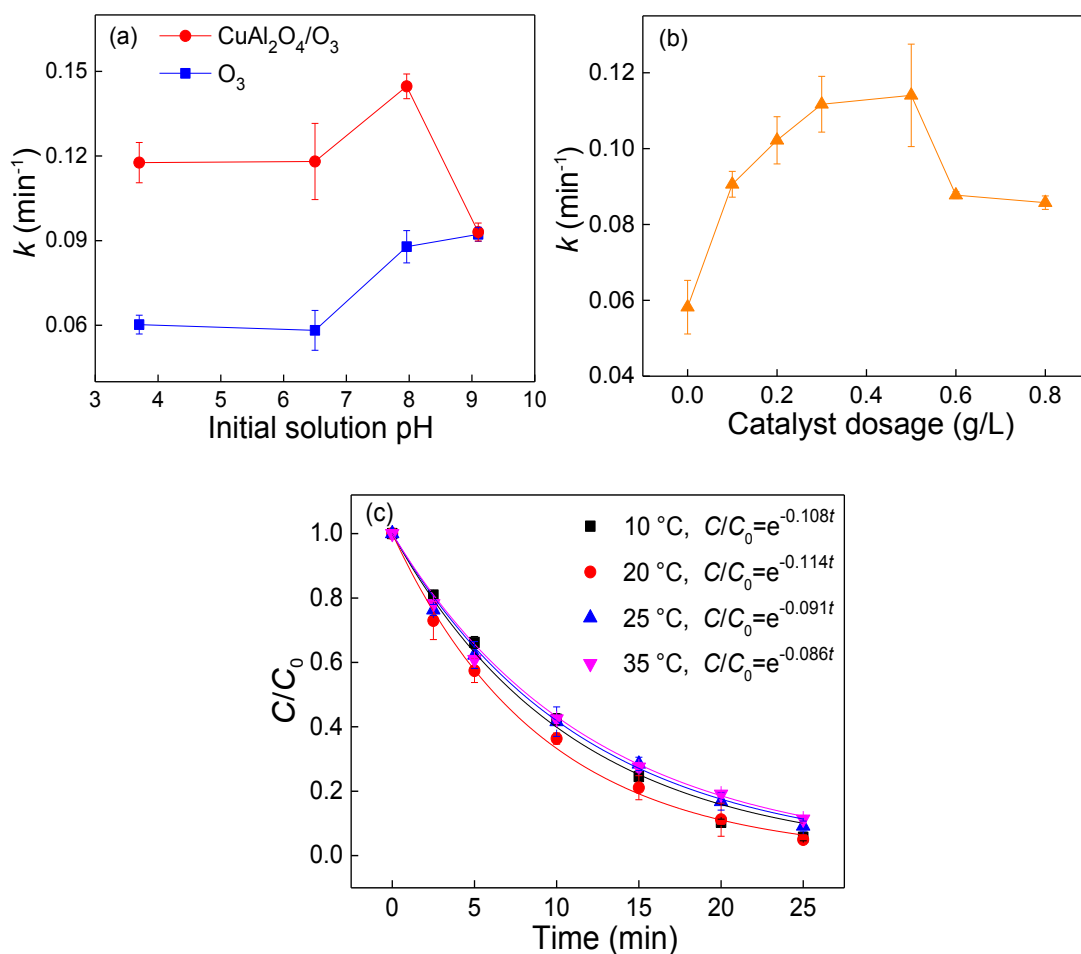
Figure 3-16 Effects of serveral parameters (a) initial pH, (b) catalyst dosage and (c) reaction temperature in catalytic ozonation ([AO7]= 100 mg L^{-1}, Q = 40 L h^{-1}, ozone dosage = 10.06 mg min^{-1}, catalyst dosage = 0.5 g L^{-1}, pH$_0$ 6.54)

To evaluate the suitable conditions for AO7 degradation by CuAl$_2$O$_4$/O$_3$ process, the effect of initial pH, the dosage of catalyst and reaction temperature were investigated. Generally, the solution pH is an important parameter in catalytic ozonation process, which can influence the surface properties of catalyst, charge state of ionizable

organic molecules, and the generation ofreactive radicals. In fact, the effect of pH in ozonation process is not a matter of consensus, especially for the color removal of dye. Silva et al. [82] reported that the initial decolorization rate of AO7 in ozone-based systems was higher at pH 5.0 and pH 9.0,in contrast, the ozone decolorizing was more rapidly in acidic media, as observed by Hsu et al. [83]. The controversial results on the influence of pH on color removal may be attributed to several factors, including the structure of the dye molecule, oxidation mechanism (via O_3 and/or $HO^\bullet$), temperature and others. In our work, compared with neutral condition (pH 6.54) slight enhancement on color removal was observed in the experiments with or without catalyst in acidic media (pH 3.6) (Fig. 3-16a). With increasing pH from 6.5 to 8.0, the dye decolorization rate was increased correspondingly in both processes, which due to the increased decompostion of ozone, resulting in more $HO^\bullet$ formation. However, the color removal rate was greatly decresed at pH 9.0 and the catalyst had no acticity in catalytic ozonation.As the pH_{pzc} of $CuAl_2O_4$ is 8.45, its surfacebecame protonated and more positively charged at pH < pH_{pzc}, whereas, at pH 9.0 (> pH_{pzc}), the surface got deprotonated and negatively charged. It indicated that neutral charged surface (S-OH) and protonated surface ($S\text{-}OH_2^+$) were comparatively more active than deprotonatedsurface ($S\text{-}O^-$). Due to the electrophilic (H) and nucleophilic (O) nature of ozone molecule, it also suggested that O_3 molecule was more likely to combine with H atoms than that of O atoms.

Of note, the catalytic activity washighest at pH 8.0 ~ pH_{pzc} (neutral charged surface). At surface neutral condition, the combination of hydroxyl group and O_3 reached the maximum, which would reinforce ozone decomposition and promote the formation of radicals. Moreover, the protonated and neutral surface were in favour of the adsorption of some organics (eg. organic acid) on the surface of catalyst

(electrostatic attraction), which could influence the oxidation of target compound and its intermediates, especially in aqueous-solid interfacial reaction.

For the influence of catalyst dosage, as inferred from Fig. 3-16b, the dye decolorization rate constant increased with increasing the dosage. The catalyst possess the active sites for catalytic or adsorptive reactions among H_2O, O_3 and organics. The increased catalst dosage provided more available reaction sites for reactions with O_3 to generate reactive radicals. As the catalyst dosage was increased gradually to 0.5 g L^{-1}, the decolorization rate increased slowly, and it sharply declined with the dose above 0.5 g L^{-1}. It indicated that excessive dosage of catalyst above a certain amount would result in more ineffective ozone consumption for the dye degradation.

Fig. 3-16c showed the effect of reaction temperature on the catalytic ozonation in the range of 10-35 °C. It is known that increasing reaction temperature has two opposite effects in the catalytic ozonation process. A higher reaction temperature will raise the reaction rate between oxidant andpollutant, but the solubility of ozone inliquid phase is opposite to the temperature. As indicated in Fig. 3-16c, the result exhibited that the variation of temperature had no obvious tendency on the removal efficiency. The decolorization rate constant increased from 0.108 min^{-1} to 0.114 min^{-1} as the reaction temperature raised from 10 °C to 20 °C.When temperature furtherincreased up to 25 °C and 35 °C, the decolorization rate constants were suppressed.

Therefore, the higher dye decolorization rate in the investigated system could be obtained at pH close to the pH_{pzc} (8.45) of $CuAl_2O_4$ by using 0.5 g L^{-1} of catalyst at the reaction temperature of 20 °C. To test the reusability and stability of the catalytic activities, the same catalyst was used for four successive catalytic runs. As shown in Fig. 3-17, it was found that the dye removal was slightly decreased after the first recycling run, while in the second, third and fourth run, the dye removal rate was similar.

In each recycling experiment, less than 0.28% of Cu ion (<0.5 mg L^{-1}) leaching and nearly zero Al ion (<0.05 mg L^{-1}) leaching was detected, which might be responsible for the slight decrease of catalytic activity. In brief, no significant differences in the surface nature of the catalyst were observed. Hence, we assume that CuAl$_2$O$_4$ possesses a good stability toward catalytic ozonation.
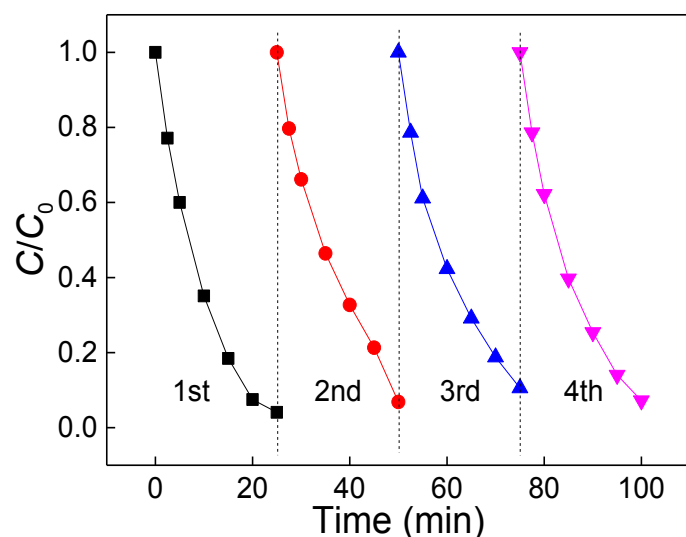
Figure 3-17 Stability of CuAl$_2$O$_4$ catalyst during the cyclic catalytic ozonation ([AO7]= 100 mg L^{-1}, Q= 40 L h^{-1}, ozone dosage = 10.06 mg min^{-1}, catalyst dosage = 0.5 g L^{-1}, pH$_0$ 6.54)

3.4 Conclusions

Spinel-type CuAl$_2$O$_4$ acts as a feasible catalyst to reach an efficient destruction of recalcitrant organic pollutants for water treatment. Combination of Al and Cu was found highly effective to catalyze ozone and form reactive radicals (adsorbed HO$^\bullet$ and few O$_2^{\bullet-}$) for the degradation of organic pollutants. We experimentally obtain almost complete color removal of dye in 25 min and also COD removal of 87.2% in 120 min during the CuAl$_2$O$_4$/O$_3$ process. Of note, the occurrence of nitrobenzene and 1,4-benzoquinone inhibited the catalytic activity of CuAl$_2$O$_4$, while the TBA did not present negative effect on its catalytic activity. Specifically, the superior catalytic activity of CuAl$_2$O$_4$ was attributed to the synergistic effect of surface $\equiv$Cu^{2+} and $\equiv$Al^{3+} active sites.

These findings may pave the way for the development of other spinel type catalysts in order to optimize the catalytic ozonation process for environmental control. Additional study may be needed to clarify the possible Cu(III)-catalyzed mechanism involved in catalytic ozonation and the nature of complexed Cu(III) species.

References

[1] B. Kasprzyk-Hordern, M. Ziółek, J. Nawrocki, Catalytic ozonation and methods of enhancing molecular ozone reactions in water treatment, Appl. Catal. B 46 (2003) 639-669.

[2] J. Nawrocki, B. Kasprzyk-Hordern, The efficiency and mechanisms of catalytic ozonation, Appl. Catal. B99 (2010) 27-42.

[3] J.L. Wang, Z.Y.Bai, Fe-based catalysts for heterogeneous catalytic ozonationof emerging contaminants in water and wastewater, Chem. Eng. J. 312 (2017) 79-98.

[4] M. Ernst, F. Lurot, J.C. Schrotter, Catalytic ozonation of refractory organic model compounds in aqueous solution by aluminum oxide, Appl. Catal. B 47 (2004) 15-25.

[5] T. Zhang, J. Ma, Catalytic ozonation of trace nitrobenzene in water with synthetic goethite, J. Mol. Catal. A-Chem. 279 (2008) 82-89.

[6] W.W. Li, Z.M. Qiang, T. Zhang, F.L. Cao, Kinetics and mechanism of pyruvic acid degradation by ozone in the presence of PdO/CeO_2, Appl. Catal. B113 (2012) 290-295.

[7] F. Qi, W. Chu, B.B. Xu, Comparison of phenacetin degradation in aqueous solutions by catalytic ozonation with $CuFe_2O_4$ and its precursor: surface properties, intermediates and reaction mechanisms, Chem. Eng. J.284 (2016) 28-36.

[8] Y.X. Wang, Y.B. Xie, H.Q. Sun, J.D. Xiao, H.B. Cao, S.B. Wang, 2D/2D nano-hybrids of γ-MnO_2 on reduced graphene oxide for catalytic ozonation and coupling peroxymonosulfate activation, J. Hazard. Mater. 301 (2016) 56-64.

[9] S. Afzal, X. Quan, J.L. Zhang, High surface area mesoporous nanocast $LaMO_3$ (M= Mn, Fe) perovskites for efficient catalytic ozonation and an insight into probable catalytic mechanism, Appl. Catal. B 206 (2017) 692-703.

[10] L. Zhao, Z.Z. Sun, J. Ma, H.L. Liu, Enhancement mechanism of heterogeneous catalytic ozonation by cordierite-supported copper for the degradation of nitrobenzene in aqueous solution, Environ. Sci. Technol. 43 (2009) 2047-2053.

[11] L. Yang, C. Hu, Y.L. Nie, J.H. Qu, Catalytic ozonation of selected pharmaceuticals over mesoporous alumina-supported manganese oxide, Environ. Sci. Technol. 43 (2009) 2525-2529.

[12] R.H. Huang, B.Y. Lan, Z.Y. Chen, H.H. Yan, Q.Y. Zhang, J.S. Bing, L.S. Li, Catalytic ozonation of *p*-chlorobenzoic acid over MCM-41 and Fe loaded MCM-41, Chem. Eng. J. 180 (2012) 19-24.

[13] J.S. Bing, C. Hu, Y.L. Nie, M. Yang, J.H. Qu, Mechanism of catalytic ozonation in Fe_2O_3/Al_2O_3@ SBA-15 aqueous suspension for destruction of ibuprofen, Environ. Sci. Technol. 49 (2015) 1690-1697.

[14] Y.X. Huang, Y. Sun, Z.H. Xu, M.Y. Luo, C.L. Zhu, L. Li, Removal of aqueous oxalic acid by heterogeneous catalytic ozonation with MnOx/sewage sludge-derived activated carbon as catalysts. Sci. Total Environ. 575 (2017) 50-57.

[15] C.M. Chen, X. Yan, B.A. Yoza, T.T. Zhou, Y. Li, Y.L. Zhan, Q.H. Wang, Q.X. Li, Efficiencies and mechanisms of ZSM5 zeolites loaded with cerium, iron, or manganese oxides for catalytic ozonation of nitrobenzene in water. Sci. Total Environ. 612 (2018) 1424-1432.

[16] F.J. Beltrán, F.J. Rivas, L.A. Fernández, P.M. Alvarez, R. Montero-de-Espinosa, Kinetics of catalytic ozonation of oxalic acid in water with activated carbon, Ind. Eng. Chem. Res. 41 (2002) 6510-6517.

[17] A.G. Gonçalves, J.J.M. Órfão, M.F.R. Pereira, Catalytic ozonation of sulphamethoxazole in the presence of carbon materials: catalytic performance and reaction pathways, J. Hazard. Mater. 239 (2012) 167-174.

[18] Y.X. Wang, Y.B. Xie, H.Q. Sun, J.D. Xiao, H.B. Cao, S.B. Wang, Efficient catalytic ozonation over reduced graphene oxide for p-hydroxylbenzoic acid (PHBA) destruction: active site and mechanism,ACS Appl. Mater. Inter. 8 (2016) 9710-9720.

[19] J. Nawrocki, Catalytic ozonation in water: Controversies and questions. Discussion paper, Appl. Catal. B 142 (2013) 465-471.

[20] A. Ikhlaq, D.R. Brown, B. Kasprzyk-Hordern, Catalytic ozonation for the removal of organic contaminants in water on alumina, Appl. Catal. B 165 (2015) 408-418.

[21] L. Zhao, J. Ma, Z. Sun, X.D. Zhai, Mechanism of influence of initial pH on the degradation of nitrobenzene in aqueous solution by ceramic honeycomb catalytic ozonation, Environ. Sci. Technol. 42 (2008) 4002-4007.

[22] T. Zhang, W. Li, J.P. Croué, Catalytic ozonation of oxalate with a cerium supported palladium

oxide: an efficient degradation not relying on hydroxyl radical oxidation, Environ. Sci. Technol.45 (2011) 9339-9346.

[23] T. Zhang, W. Li, J.P. Croué, A non-acid-assisted and non-hydroxyl-radical-related catalytic ozonation with ceria supported copper oxide in efficient oxalate degradation in water, Appl. Catal. B 121 (2012) 88-94.

[24] F. Qi, Z. Chen, B.B. Xu, J.M. Shen, J. Ma, C. Joll, A. Heitz, Influence of surface texture and acid-base properties on ozone decomposition catalyzed by aluminum (hydroxyl) oxides, Appl. Catal. B 84 (2008) 684-690.

[25] B.Kasprzyk-Hordern, U.Raczyk-Stanisławiak, J.Świetlik, J.Nawrocki, Catalytic ozonation of natural organic matter on alumina. Appl. Catal. B 62 (2006) 345-358.

[26] J. Lin, A. Kawai, T. Nakajima, Effective catalysts for decomposition of aqueous ozone, Appl. Catal. B39 (2002) 157-165.

[27] B. Kasprzyk-Hordern, J. Nawrocki, Preliminary results on ozonation enhancement by a perfluorinated bonded alumina phase, Ozone: Sci. Eng. 24 (2002) 63-68.

[28] J.H. Qu, H.Y. Li, H.J. Liu, H. He, Ozonation of alachlor catalyzed by Cu/Al$_2$O$_3$ in water, Catal. Today 90 (2004) 291-296.

[29] A.L. Petre, J.B. Carbajo, R. Rosal, E. Garcia-Calvo, J.A. Perdigon-Melon, CuO/SBA-15 catalyst for the catalytic ozonation of mesoxalic and oxalic acids. Water matrix effects,Chem. Eng. J. 225 (2013) 164-173.

[30] F.X. Deng, S. Qiu, C. Chen, X. Ding, F. Ma, Heterogeneous catalytic ozonation of refinery wastewater over alumina-supported Mn and Cu oxides catalyst, Ozone: Sci. Eng. 37 (2015) 546-555.

[31] T. Zhang, H. Zhu, J.P. Croué, Production of sulfate radical from peroxymonosulfate induced by a magnetically separable CuFe$_2$O$_4$ spinel in water: efficiency, stability, and mechanism, Environ. Sci. Technol.47 (2013) 2784-2791.

[32] Y. Xu, J. Ai, H. Zhang, The mechanism of degradation of bisphenol A using the magnetically separable CuFe$_2$O$_4$/peroxymonosulfate heterogeneous oxidation process, J. Hazard. Mater. 309 (2016) 87-96.

[33] Q. Zhao, Z.H. Yan, C.C. Chen, J. Chen, Spinels: Controlled preparation, oxygen reduction/evolution reaction application, and beyond, Chem. Rev. 117 (2017) 10121-10211.

[34] Y.Y. Jiang, J.G. Li, X.T. Sui, G.L. Ning, C.Y. Wang, X.M. Gu, CuAl$_2$O$_4$ powder synthesis by sol-gel method and its photodegradation property under visible light irradiation, J. Sol-Gel Sci. Techn. 42 (2007) 41-45.

[35] H.P. Boehm, Acidic and basic properties of hydroxylated metal oxide surfaces. Discuss. Faraday Soc. 52 (1971) 264-275.

[36] H.Tamura, A.Tanaka, K.Y. Mita, R.Furuichi, Surface hydroxyl site densities on metal oxides as a measure for the ion-exchange capacity. J. Colloid Interf. Sci. 209 (1999) 225-231.

[37] T. Zhang, C.J. Li, J. Ma, H. Tian, Z.M. Qiang, Surface hydroxyl groups of syntheticα-FeOOH in promoting•OH generation from aqueous ozone: property andactivity relationship, Appl. Catal. B 82 (2008) 131-137.

[38] D.L. Flamm, Analysis of ozone at low concentrations with boric acid bufferedpotassium iodide, Environ. Sci. Technol. 11 (1977) 978-983.

[39] H. Bader, J. Hoingé, Determination of ozone in water by the indigo method, Water Res. 154 (1981) 449-456.

[40] M. Salavati-Niasari, F. Davar, M. Farhadi, Synthesis and characterization of spinel-type CuAl$_2$O$_4$ nanocrystalline by modified sol-gel method, J. Sol-Gel Sci. Techn. 51 (2009) 48-52.

[41] S.A. Hassanzadeh-Tabrizi, R. Pournajaf, A. Moradi-Faradonbeh, S. Sadeghinejad, Nanostructured CuAl$_2$O$_4$: Co-precipitation synthesis, optical and photocatalytic properties, Ceram. Int. 42 (2016) 14121-14125.

[42] X. Cheng, X.Huang, X.Wang, D.Sun, Influence of calcination on the adsorptive removal of phosphate by Zn-Al layered double hydroxides from excess sludge liquor. J. Hazard. Mater. 177 (2010)516-523.

[43] D.W.Ding, M.C.Long, W.M.Cai, Y.H.Wu, D.Wu, C.Chen, In-situ synthesis of photocatalytic CuAl$_2$O$_4$-Cu hybrid nanorod arrays. Chem. Commun. 24 (2009) 3588-3590.

[44] Y.F.Zeng, Z.L.Liu, Z.Z.Qin, Decolorization of molasses fermentation wastewater by SnO$_2$-catalyzed ozonation. J. Hazard. Mater. 162 (2009) 682-687.

[45] J.S. Bing, C.Hu, L.L. Zhang, Enhanced mineralization of pharmaceuticals by surface oxidation

over mesoporous γ-Ti-Al$_2$O$_3$ suspension with ozone. Appl. Catal. B 202 (2017) 118-126.

[46] C.A.Emeis, Determination of integrated molar extinction coefficients for infrared absorption bands of pyridine adsorbed on solid acid catalysts. J. Catal. 141 (1993) 347-354.

[47] Y.Xu, H.Lin, Y.K. Li, H.Zhang, The mechanism and efficiency of MnO$_2$ activated persulfate process coupled with electrolysis. Sci. Total Environ. 609 (2017) 644-654.

[48] M.S. Elovitz, U. von Gunten, Hydroxyl radical/ozone ratios during ozonation processes. I. The R$_{ct}$ concept, Ozone:Sci. Eng. 21 (1999) 239-260.

[49] G.V. Buxton, C.L. Greenstock, W.P. Helman, A.B. Ross, Critical review of rate constants for reactions of hydrated electrons, hydrogen atoms and hydroxyl radicals (•OH/•O$^-$) in aqueous solution, J. Phys. Chem. Ref. Data 17 (1988) 513-886.

[50] J. Hoigné, H. Bader, Rate constants of reactions of ozone with organic and inorganic compounds in water-I: non-dissociating organic compounds, Water Res. 17 (1983) 173-183.

[51] F.J.Rivas, M. Carbajo, F.J. Beltrán, B. Acedo, O. Gimeno, Perovskite catalytic ozonation of pyruvic acid in water: Operating conditions influence and kinetics. Appl. Catal. B 62 (2006) 93-103.

[52] M. Carbajo, F.J. Beltrán, O. Gimeno, B.Acedo, F.J. Rivas, Ozonation of phenolic wastewaters in the presence of a perovskite type catalyst, Appl. Catal. B 74 (2007) 203-210.

[53] R.C.Martins, R.M. Quinta-Ferreira, Catalytic ozonation of phenolic acids over a Mn-Ce-O catalyst. Appl. Catal. B 90 (2009) 268-277.

[54] M.Sui, J.Liu, L.Sheng, Mesoporous material supported manganese oxides (MnO$_x$/MCM-41) catalytic ozonation of nitrobenzene in water. Appl. Catal. B 106 (2011)195-203.

[55] W.W.Li, Z.M.Qiang, T. Zhang, F.L. Cao, Kinetics and mechanism of pyruvic acid degradation by ozone in the presence of PdO/CeO$_2$. Appl. Catal. B113 (2012) 290-295.

[56] P.Neta, R.E.Huie, A.B.Ross, Rate constants for reactions of inorganic radicals in aqueous solution. J. Phys. Chem. Ref. Data 17 (1988) 1027-1284.

[57] E.Mvula, C. von Sonntag, Ozonolysis of phenols in aqueous solution. Org. Biomol. Chem. 1 (2003) 1749-1756.

[58] E.Finkelstein, G.M. Rosen, E.J.Rauckman, Spin trapping. Kinetics of the reaction of superoxide and hydroxyl radicals with nitrones. J. Am. Chem. Soc. 102 (1980) 4994-4999.

[59] C.E. Diaz-Uribe, M.C. Daza, F. Martínez, E.A. Paezmozo, C.L.B. Guedes, E.D. Mauro, Visible light superoxide radical anion generation by tetra (4-carboxyphenyl) porphyrin/TiO$_2$: EPR characterization, J. Photoch. Photobio. A 215 (2010) 172-178.

[60] J. Zhang, Y. Wu, C. Qin, L.P. Liu, Y.Q. Lan, Rapid degradation of aniline in aqueous solution by ozone in the presence of zero-valent zinc, Chemosphere 141 (2015) 258-264.

[61] J.M. Fontmorin, R.C.B. Castillo, W.Z. Tang, M. Sillanpaa, M. Sillanpää, Stability of 5, 5-dimethyl-1-pyrroline-N-oxide as a spin-trap for quantification of hydroxyl radicals in processes based on Fenton reaction, Water Res. 99 (2016) 24-32.

[62] J.M.L. Martínez, M.F.L. Denis, L.L. Piehl, E.R. de Celis, G.Y. Buldain, V.C. Dall' Orto, Studies on the activation of hydrogen peroxide for color removal in the presence of a new Cu (II)-polyampholyte heterogeneous catalyst, Appl. Catal. B 82 (2008) 273-283.

[63] G.H. Dong, Z.H. Ai, L.Z. Zhang, Total aerobic destruction of azo contaminants with nanoscale zero-valent copper at neutral pH: promotion effect of in-situ generated carbon center radicals, Water Res. 66 (2014) 22-30.

[64] B.Z. Zhu, H.T. Zhao, B. Kalyanaraman, B. Frei, Metal-independent production of hydroxyl radicals by halogenated quinones and hydrogen peroxide: An ESR spin trapping study, Free Radical Bio. Med. 32 (2002) 465-473.

[65] B.K.Sinha, F.Leinisch, S.Bhattacharjee, R.P.Mason, DNA cleavage and detection of DNA radicals formed from hydralazine and copper (II) by ESR and immuno-spin trapping. Chem. Res. Toxicol. 27 (2014)674-682.

[66] A. Viswanathan, A.N. Shetty, Facile in-situ single step chemical synthesis of reduced graphene oxide-copper oxide-polyaniline nanocomposite and its electrochemical performance for supercapacitor application, Electrochim. Acta 257 (2017) 483-493.

[67] J. Cai, H. Gong, The influence of Cu/Al ratio on properties of chemical-vapor-deposition-grown p-type Cu-Al-O transparent semiconducting films, J. Appl. Phys. 98 (2005) 033707.

[68] G. Ertl, R .Hierl, H. Knözinger, N. Thiele, H.P. Urbach, XPS study of copper aluminate catalysts, Appl. Surf. Sci. 5 (1980) 49-64.

[69] J.J. Teo, Y. Chang, H.C. Zeng, Fabrications of hollow nanocubes of Cu$_2$O and Cu via reductive

self-assembly of CuO nanocrystals, Langmuir 22 (2006) 7369-7377.

[70] T.Ghodselahi, M.A. Vesaghi, A. Shafiekhani, A.Baghizadeh, M. Lameii, XPS study of the $Cu@Cu_2O$ core-shell nanoparticles. Appl. Surf. Sci. 255 (2008) 2730-2734.

[71] Y.Sun, X.Li, J.Gandhi, S.Luo, T.Jiang, Adhesion improvement for polymer dielectric to electrolytic-plated copper. In Electronic Components and Technology Conference (ECTC). Proceedings 60th, IEEE. (2010) 1106-1111.

[72] C.Zhu, A.Osherov, M.J.Panzer, Surface chemistry of electrodeposited Cu_2O films studied by XPS. Electrochim. Acta 111 (2013) 771-778.

[73] N.A. Merino, B.P. Barbero, P. Eloy, L.E. Cadus, $La_{1-x}Ca_xCoO_3$ perovskite-type oxides: identification of the surface oxygen species by XPS, Appl. Surf. Sci. 253 (2006) 1489-1493.

[74] W. Li, G.V. Gibbs, S.T. Oyama, Mechanism of ozone decomposition on a manganese oxide catalyst. 1. In situ Raman spectroscopy and ab initio molecular orbital calculations, J. Am. Chem. Soc. 120 (1998) 9041-9046.

[75] U. Von Gunten, Ozonation of drinking water: Part I. Oxidation kinetics and product formation, Water Res. 37 (2003) 1443-1467.

[76] W.F.L.M. Hoeben, Pulsed corona-iduced degradation of organic materials in water. Technische Universiteit Eindhoven: Eindhoven, 2000 The Netherlands.

[77] T.V. Popova, N.V. Aksenova, Complexes of copper in unstable oxidation states. Russ, J. Coord. Chem. 29 (2003) 743-765.

[78] T.Zhang, H.Zhu, J.P.Croué, Production of sulfate radical from peroxymonosulfate induced by a magnetically separable $CuFe_2O_4$ spinel in water: efficiency, stability, and mechanism. Environ. Sci. Technol.47 (2013) 2784-2791.

[79] T.Zhang, W.Li, J.P. Croué, A non-acid-assisted and non-hydroxyl-radical- related catalytic ozonation with ceria supported copper oxide in efficient oxalate degradation in water. Appl. Catal. B 121 (2012) 88-94.

[80] L.Q. Hatcher, K.D. Karlin, Oxidant types in copper-dioxygen chemistry: the ligand coordination defines the Cu_n-O_2 structure and subsequent reactivity, J. Biol. Inorg. Chem. 9 (2004) 669-683.

[81] A.N. Pham, G. Xing, C.J. Miller, T.D. Waite, Fenton-like copper redox chemistry revisited: Hydrogen peroxide and superoxide mediation of copper-catalyzed oxidant production, J. Catal. 301 (2013) 54-64.

[82] A.C. Silva, J.S. Pic, G.L. Sant'Anna, M. Dezotti, Ozonation of azo dyes (Orange II and Acid Red 27) in saline media. J. Hazard. Mater. 169 (2009) 965-971.

[83] Y.C. Hsu, J.T. Chen, H.C. Yang, J.H. Chen, Decolorization of dyes using ozone in gas- induced a reactor. AIChE J. 47 (2001) 169-176.

Chapter 4 High-efficiency oxidation process involving peroxymonosulfate activated by CuFe$_2$O$_4$ magnetic nanoparticles

Example of Bisphenol A degradation over spinel in water

4.1 Introduction

Bisphenol A (2,2-bis(4-hydroxyphenyl) propane) is an endocrine disruptor (ED) which is widely used for the production of epoxy resins, polyacrylate and polycarbonate plastics [1]. Due to its widespread use, BPA has been ubiquitously found in food, drinking water, aquatic animals and human beings [2]. Owing to the ability to disrupt endocrine function, BPA has potentially posed a threat to ecology and public health. For example, the wildlife exposed to low concentrations of BPA may show symptoms of puberty, especially as a result of early postnatal exposure [3]. Moreover, even after municipal wastewater treatment, low doses (μg/L to mg/L levels) of BPA released into effluent water are also considered to be a risk to the general public [4].

Conventional treatment processes, such as adsorption [5] and biodegradation technology [6], have been utilized to remove BPA from wastewater. However, these processes have some disadvantages in terms of time and efficiency [7]. Hence, it is necessary to develop more effective techniques to remove BPA from wastewater. During the past few years, advanced oxidation processes (AOPs) based on the formation of highly reactive species such as hydroxyl radicals (HO$^{\bullet}$) and sulfate radicals (SO$_4{}^{\bullet-}$) have gained popularity due to their high oxidative capacity [8]. SO$_4{}^{\bullet-}$-based AOPs using peroxydisulfate (PDS, S$_2$O$_8{}^{2-}$) or peroxymonosulfate (PMS, HSO$_5{}^-$) as oxidant have been recognized as effective methods for the degradation of hazardous and non-biodegradable contaminants [9-14]. SO$_4{}^{\bullet-}$ can be produced from peroxymonosulfate (PMS) following activation by UV, heat, electron transfer, alkaline conditions or transition metal ions (Fe^{2+}, Co^{2+}, Cu$^+$, etc.). As the most effective catalyst, Co^{2+} has been found to efficiently initiate PMS decomposition to generate sulfate radicals according to Eq. (4-1) and Eq. (4-2) [9].

$$Co^{2+} + HSO_5{}^- \rightarrow Co^{3+} + SO_4{}^{\bullet-} + OH^- \tag{4-1}$$

$$Co^{3+} + HSO_5^- \rightarrow Co^{2+} + SO_5^{\bullet-} + H^+ \tag{4-2}$$

The homogeneous Co^{2+}/PMS system has been used for the degradation of azo dyes [15], phenolic pollutants [16,17], naphthalene and atrazine [9] and other pollutants [18] but the cobalt catalytic degradation process is not effective for practical application in water treatment owing to the toxicity of Co^{2+}. Thus, heterogeneous cobalt catalysts, such as Co oxides (Co_3O_4) [19] and other supported Co catalysts have been investigated for sulfate radical production [20-24]. Various Co-bearing composites including TiO_2 [25], SiO_2 [26], SBA-15 [27], graphene oxide [28], and other materials [29] were also studied. The use of heterogeneous Co-bearing catalysts has indeed reduced the amount of leaching of Co^{2+}, but has not been eliminated entirely from published processes. Consequently, search for alternative heterogeneous catalysts (e.g. metal oxides) to efficiently activate PMS is of necessity and importance. CuO particles and Fe_3O_4 nanoparticles have been used as a heterogeneousactivator of PMS for the fast degradation of phenol in aqueous solution via a sulfate radical approach [30,31].

The spinel ferrites having a general chemical composition of MFe_2O_4 (M = Mn, Cu, Zn, Co etc.) are widely used as magnetic materials. Copper iron spinel type oxide $CuFe_2O_4$, as one of spinel ferrites, has played an important role in various catalytic applications and has been developed as a catalyst in the removal of gaseous pollutants in the water gas shift reaction [32] and the steam reforming of dimethyl ether [33]. Recently, $CuFe_2O_4$ magnetic materials as a heterogeneous catalyst have attracted great interest in heterogeneous AOP systems. Ding et al. [34] and Zhang et al. [35] have reported a fast degradation of iopromide and TBBPA, respectively, by using $CuFe_2O_4$ particles to activate PMS. They both proposed that sulfate radical as the main reactive radical would be produced from the decomposition of PMS, though different sulfate radical generated mechanisms were discussed. The biggest controversy about the

mechanism lay in the role of two metal elements (Fe and Cu) in the activation process and consequently this is the focus of our research.

In the present work, the performance of the $CuFe_2O_4$/PMS system in the mineralization of BPA was investigated through examination of some important factors such as initial pH, BPA concentration, PMS concentration, catalyst dosage, batch dosing and the presence of anions such as Cl^-, F^-, ClO_4^- and $H_2PO_4^-$. Furthermore, the stability and reusability of the catalyst were estimated and electron paramagnetic resonance (EPR) technology combined with various radical scavengers and methylene blue probe experiments have been employed to investigate the activation mechanism.

4.2 Experimental section

4.2.1 Chemicals

BPA was obtained from Aladdin Chemistry Co. Ltd. (Shanghai, China) and used without further purification. 5,5-Dimethyl-1-pyrrolidine N-oxide (DMPO, 97%) was purchased from Sigma-Aldrich, $Cu(NO_3)_2 \cdot 3H_2O$, $Fe(NO_3)_3 \cdot 9H_2O$, citric acid, t-BuOH, MeOH and Oxone ($2KHSO_5 \cdot KHSO_4 \cdot K_2SO_4$) was purchased from Sinopharm Chemical Reagent Co., Ltd. (Shanghai, China) and were of analytical grade. NaOH, H_2SO_4, NaCl, NaF, NaH_2PO_4 and methylene blue were analytical grade reagents and purchased from Sinopharm Chemical Reagent Co., Ltd. (Shanghai, China). All aqueous solutions were prepared with deionized water.

4.2.2 Synthesis of catalysts and characterization

$CuFe_2O_4$ MNPs were prepared by a citrate combustion method as reported in the literature [35]. Copper nitrate (2.86 mmol), ferric nitrate (5.71 mmol), and citric acid (9.4 mmol) were dosed into a certain volume deionized water. The resultant homogeneous solution was stirred for 4 h and then evaporated to remove water. The sticky gel was calcined at 400 °C for 2h to decompose the citricacid until fine oxide

powders were obtained. After calcination, the particles were finely ground, washed several times until the pH reached neutral and further dried at 105 °C. By contrast, CuO and Fe_2O_3 nanoparticles were also prepared by the same method but using $Cu(NO_3)_2$ and $Fe(NO_3)_3$ as a precursor, respectively.

XPS was recorded on a KRATOS XSAM800 spectrometer equipped with Mg Kα X-ray source. The N_2 Brunauer-Emmett-Teller (BET) method was performed on an ASAP2020 analyzer (USA). pH_{pzc} (pH at which the surface is zero-charged) was determined with acid-base titration. The morphology of samples was observed on a field-emission scanning electron microscope (Zeiss SIGMA FESEM, German). The atomic composition of samples was elucidated by EDS microanalysis (EDAX Genesis, USA). XRD patterns of samples were analyzed using Cu Kα radiation ($\lambda = 1.5406$ Å) operating at 36 kV and 30 mA, respectively (XPert Pro, Netherlands). The FTIR analyzer was employed to determine the functional groups present for understanding the chemistry of the samples (Nicolet FTIR 5700, USA).
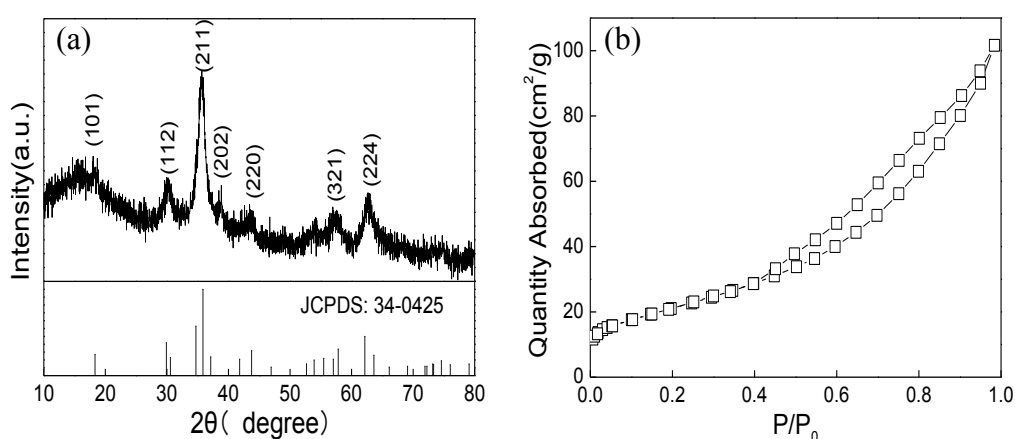
4.2.3 Experimental procedures and analysis

Batch degradation experiments of BPA were carried out in a conical flask (250 mL) Unless otherwise specified, the initial pH (pH_0) of the BPA solution was measured with a Mettler-Toledo FE20 pH-meter (Mettler-Toledo Instruments Co., Ltd., Shanghai) and adjusted appropriately with sulfuric acid or sodium hydroxide. The catalyst was added into 200 mL of the BPA solution with constant stirring around 360 r/min by using an mechanical stirrer (RW 20, IKA, Germany). At predetermined time intervals, samples were taken and filtered through 0.22 μm membranes (Millipore Co.) before immediate TOC analysis. The residual BPA concentration was measured after 1 mL methanol was added in each sample (1 mL) to terminate the reaction. In addition, the residual BPA concentration was monitored by a high performance liquid chromatography (HPLC)

system consisting of a LC-20AB pump, a SPDM20A chromatograph equipped with a C-18 column (Shim-PackVP-ODS-C8) and a SPD-10A UV-visible detector set at the maximum absorption wavelength of BPA (280 nm). The absorbance of methylene blue was measured at λ_{max}= 664 nm using a Rayleigh UV-9100 spectrophotometer (Rayleigh Co., China). The concentration of residual PMS was determined by an iodometric titration method [13]. The TOC of the sample was determined by an Analytik Jena Multi N/C 3100 analyzer with non-dispersive infrared absorption detector (NDIR). Fluorescence spectra of the supernatant liquid were measured with a fluorescence spectrophotometer (Shimadzu F-4500 FL Spectrophotometer). The concentration of the dissolved iron and copper ions in the solution was systematically evaluated using Atomic Absorption Spectroscopy (AAS, Perkin Elmer A Analyst 800). EPR signals of radicals trapped by DMPO were recorded at ambient temperatures on a JES-FA200 spectrometer. The settings for the EPR spectrometer were: center field, 3260 G; sweep width, 100 G; microwave frequency, 9.14 GHz; modulation frequency, 100 kHz.

4.3 Results and discussion

4.3.1 Characterization of CuFe$_2$O$_4$

Element	Wt %	At %
O K	24.01	53.59
FeK	47.88	30.61
CuK	28.11	15.80

c:\edax32\genspc.spc 25-Aug-2014 16:30:35
Chlorite (Nrm.%= 38.86, 20.96, 34.83, 1.14, 3.84, 0.28)   LSecs : 48
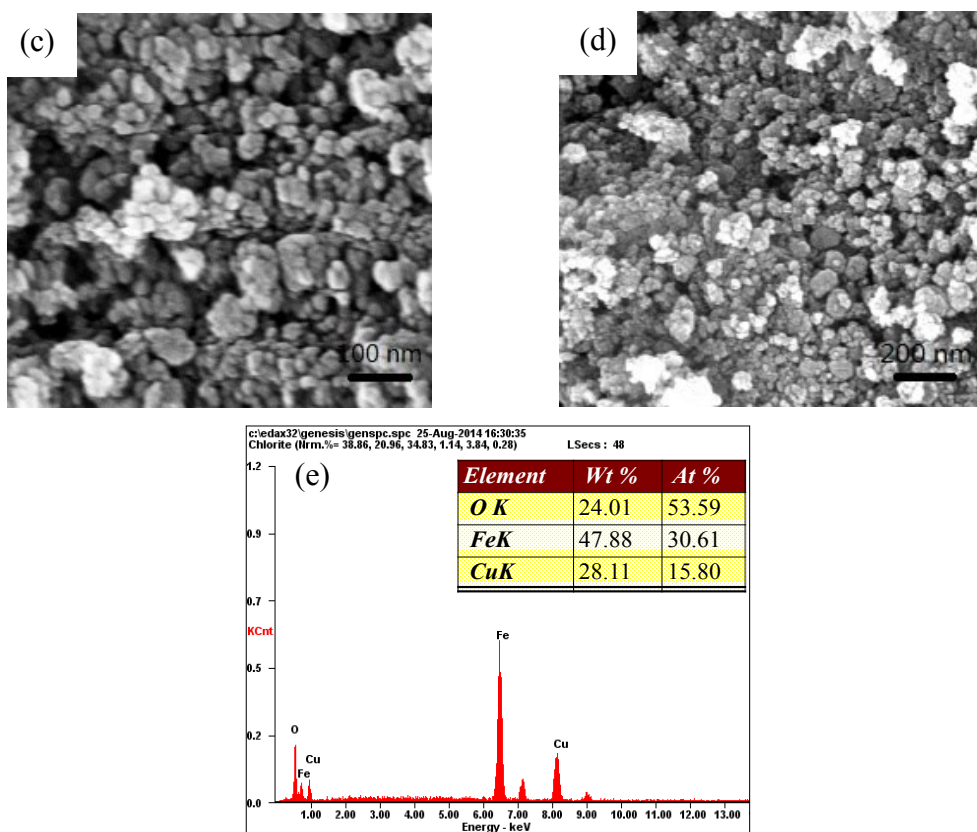
Figure 4-1 Characterization of CuFe$_2$O$_4$ MNPs. (a) XRD patterns; (b) BET; (c) SEM images;

(d) EDS

Figure 4-2 XRD patterns of (a) Fe$_2$O$_3$ and (b) CuO samples

The synthetic CuFe$_2$O$_4$ MNPs were characterized as indicated in Fig. 4-1. The

XRD pattern of fresh CuFe$_2$O$_4$ MNPs (Fig. 1a) show three intense diffraction peaks at

2θ=30.7°, 35.9° and 62.2°. The diffraction patterns matched well with the published

XRD pattern of the tetragonal CuFe$_2$O$_4$ spinel (JCPDS File No.34-0425), suggesting

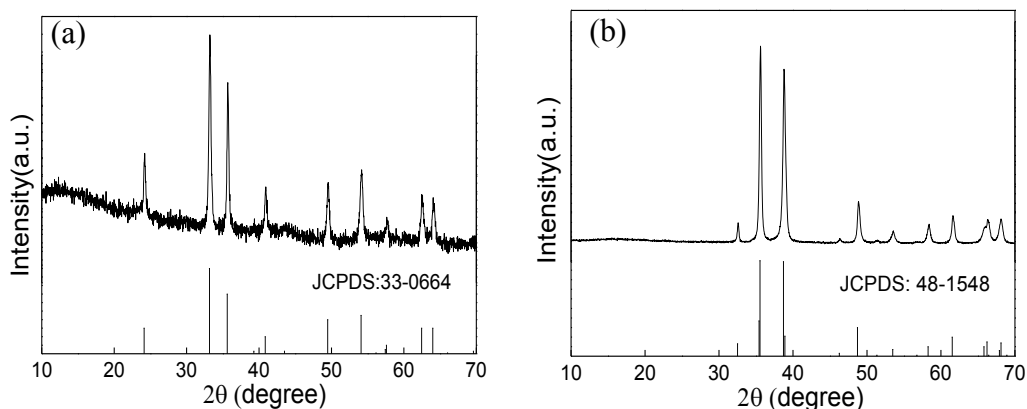the formation of $CuFe_2O_4$ with a considerable degree of crystallization [36]. Similarly, the XRD pattern (Fig. 4-2) of CuO and Fe_2O_3 catalysts corresponded well with the standard JCPDS File No. 48-1548, and JCPDS File No. 33-0664, respectively.The surface area and the pore structures of the catalysts were studied by N_2 adsorption-desorption isotherms (Fig. 4-1b). The BET surface area and average pore size of the crystals were 77.51 m^2/g and 8.11 nm for $CuFe_2O_4$; 4.88 m^2/g and 8.62 nm for CuO; and 29.84 m^2/g and 15.14 nm for Fe_2O_3, indicating a large increase in the specific surface area of the $CuFe_2O_4$ compared with CuO and Fe_2O_3. The SEM images showed that $CuFe_2O_4$ MNPs were mostly quasi-spherical with particle sizes of about 20 nm (Fig.4-1c). EDS analysis of these zones were used to investigate the bulk chemical composition of the catalyst and proved that the $CuFe_2O_4$ MNPs are composed of copper (Cu), iron (Fe) and oxygen (O) and the atomic ratio of Cu to Fe was nearly equal to 1:2 in the sample (Fig. 4-1d), which was consistent with the molecular formula of the catalyst.

4.3.2 Removal of BPA using different systems
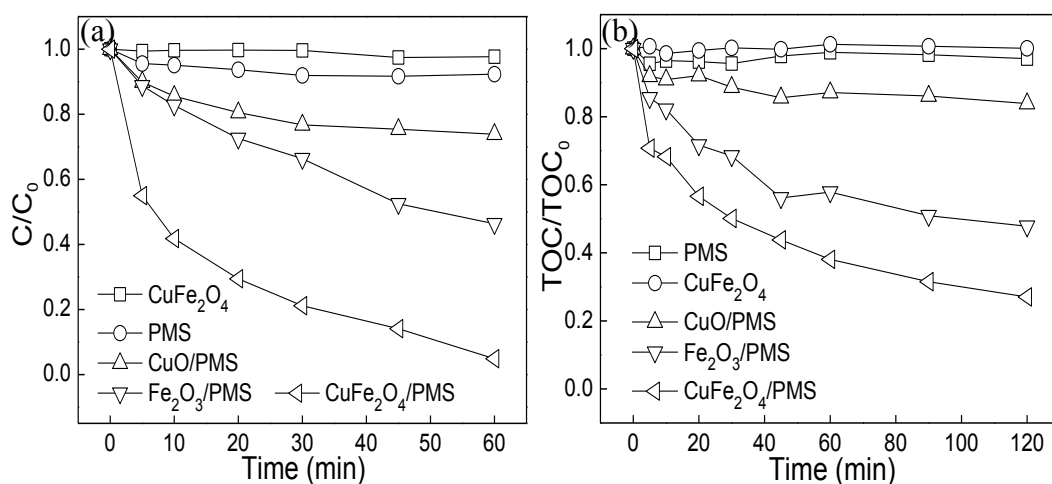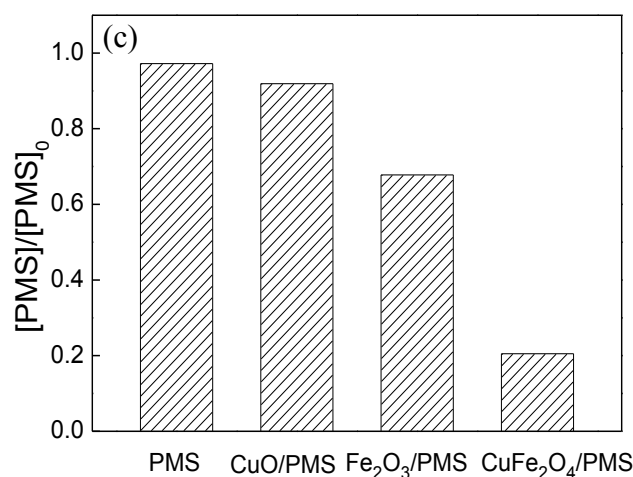
Figure 4-3 Degradation of BPA (a, b) and remaining percentage of PMS (c) using different systems ([BPA]= 50 mg L^{-1}, [$CuFe_2O_4$] = 0.4 g L^{-1}, [CuO] = 0.4 g L^{-1}, [Fe_2O_3] = 0.4 g L^{-1}, [PMS] = 0.5 g L^{-1}, pH_0 6.72)
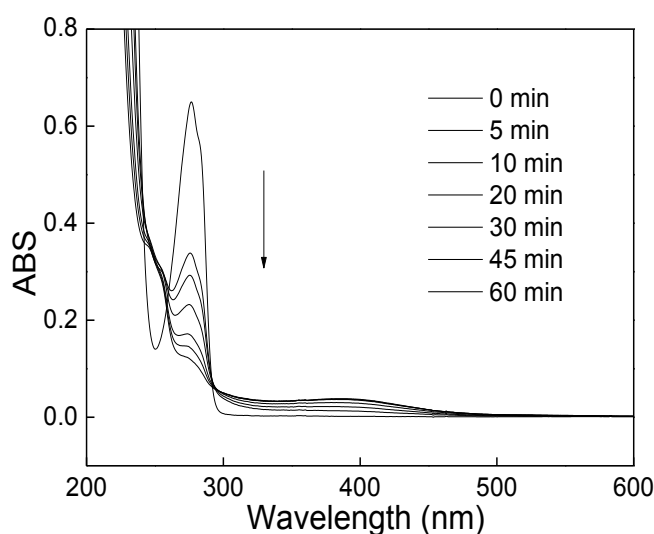
Figure 4-4 The changes in the UV-visible spectrum with reaction time ([BPA] = 50 mg L^{-1}, [$CuFe_2O_4$] = 0.6 g L^{-1}, [PMS] = 0.3 g L^{-1}, pH_0 6.72)

It can be seen from Fig. 4-3 that the simultaneous use of $CuFe_2O_4$/PMS enhanced the BPA degradation significantly, producing a BPA removal of 95.2% in 60 min and TOC removal of 72.9% in 120 min, which was higher than the BPA removal of 53.7% and TOC removal of 52.2% achieved using Fe_2O_3 as catalyst. When CuO/PMS was used the results for BPA removal were 26.1% and TOC removal of 16.1%. Fig. 4-4

shows the UV-visible spectral changes of BPA during the CuFe$_2$O$_4$/PMS process. As the oxidation proceeded, the height of the peak around 270 nm in the UV region gradually decreased, which confirmedthe BPA degradation continuously during the reaction time. As indicated in Fig. 4-3c, the decomposition of 79.5% PMS was achieved in the CuFe$_2$O$_4$/PMS process, while the CuO/PMS and Fe$_2$O$_3$/PMS process only induced 9.1% and 29.2% PMS decomposition, respectively. These results indicate that the three catalysts could activate PMS to decompose BPA presumably via a radical oxidation process. Moreover, the synergistic effect of the Cu and Fe active sites on the catalyst surface may result in the superior activity of CuFe$_2$O$_4$ MNPs.

4.3.3 Analysis of reaction parameters and toxicity test
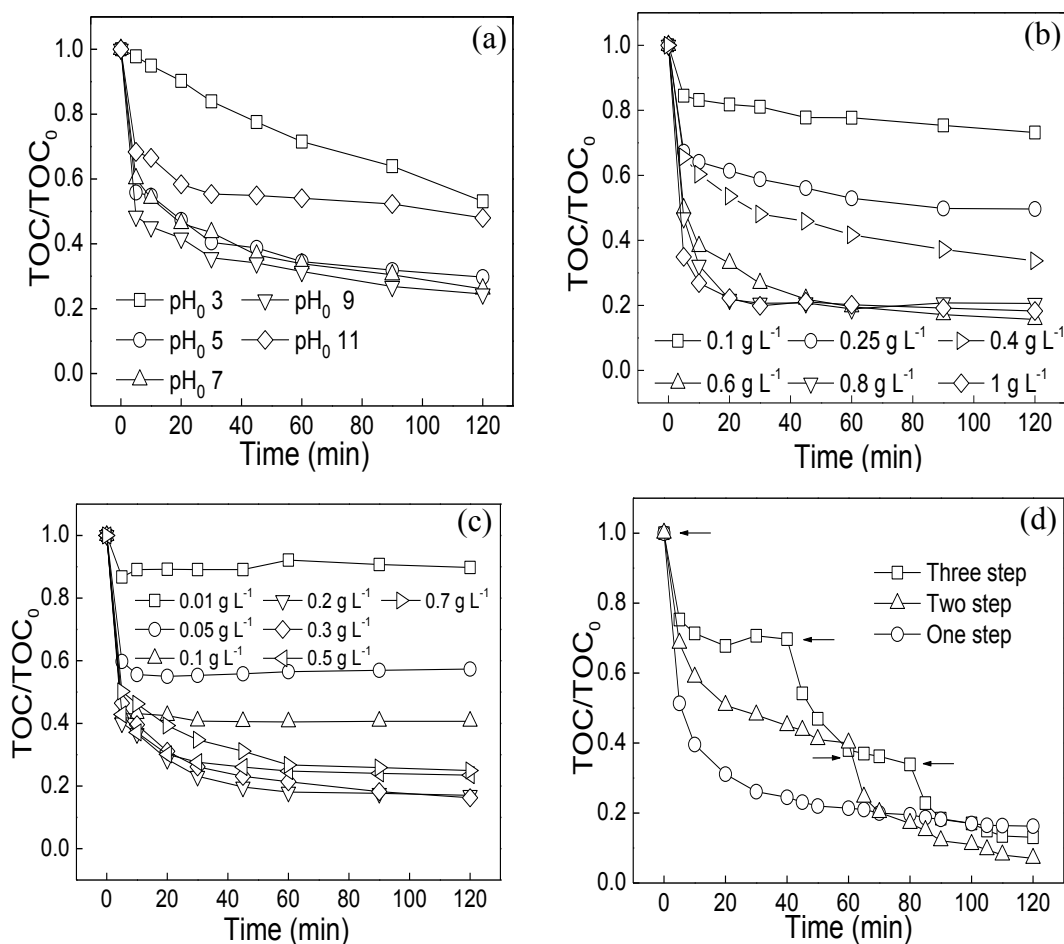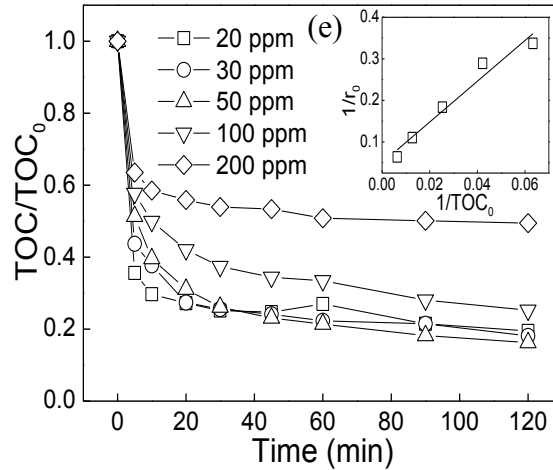
Figure 4-5 Effect of reaction parameters: (a) initial pH ($[CuFe_2O_4]$ = 0.4 g L^{-1}, [PMS] = 0.5 g L^{-1}); (b) catalyst dosage ([PMS] = 0.5 g L^{-1}, pH_0 6.72); (c) PMS concentration ($[CuFe_2O_4]$ = 0.6 g L^{-1}, pH_0 6.72); (d) catalyst dosing mode (catalyst was added in a single step, in two steps or in three steps, respectively) ([BPA] = 50 mg L^{-1}, $[CuFe_2O_4]$ = 0.6 g L^{-1}, [PMS] = 0.3 g L^{-1}, pH_0 6.72) and (e) initial BPA concentration ($[CuFe_2O_4]$ = 0.6 g L^{-1}, [PMS] = 0.3 g L^{-1}, pH_0 6.72)

To obtain the suitable conditions for BPA mineralization by $CuFe_2O_4$/PMS process, the effect of initial pH, PMS concentration, the dosage and dosing regime of catalyst were investigated.

4.3.3.1 Effect of initial pH (pH_0)

The effect of initial pH on BPA mineralization is presented in Fig. 4-5a. In the pH_0 range of 3 to 11, the PMS/$CuFe_2O_4$ system achieved the highest BPA mineralization between pH_0 5 and 9. The mineralization efficiencies of BPA were 70.3% to 73.9% and the corresponding initial mineralization rate of BPA varied from 0.171 to 0.220 mg/(L min) for pH_0 ranging from 5 to 9. However, the TOC removal efficiency decreased greatly when the solution became acidic or strongly alkaline and showed an initial mineralization rate of BPA of 0.0059 mg/(L min) and 0.1015 mg/(L min) at initial pH_0 3.0 and 11.0, respectively. This can be explained by several aspects. On the one hand, the relative amounts of different PMS species were affected by the pH value. For

example, the pK_{a1} of H_2SO_5 is nearly 0 and pK_{a2} is 9.0. Thus HSO_5^- will be the dominant PMS species in solution at an acid-neutral pH, but much more SO_5^{2-} will exist at pH > 9.0. On the other hand, pH will also influence the zeta potentials of the catalysts. The pH_{pzc} of $CuFe_2O_4$ was determined to be around 7.8 so the catalyst surface charge will be negative when the solution pH is above pH_{pzc}. When the pH is increased to above pH_{pzc}, more divalent SO_5^{2-} anions would be formed in alkaline conditions (Eq. (4-5)). The increased negative catalyst surface would repel the negative HSO_5^- anion and inhibit the static interaction between the oxide surface and the PMS species, thus leading to less PMS catalyzed to produce active radicals on the catalyst surface. As a result, the BPA mineralization efficiency will decrease at alkaline pH.

$$HSO_5^- + OH^- \rightarrow SO_5^{2-} + H_2O \qquad (4-5)$$

It has been reported that H^+ has a stabilization effect on the HSO_5^- so at acidic conditions, H-bond formation between H^+ and the O-O group of HSO_5^- becomes more significant and hinders the interaction between HSO_5^- and the positive catalyst surface. Therefore, a decreased mineralization efficiency was observed at a lower pH (pH_0 3). This is consistent with the previous reported work where the high mineralization efficiency of the $PMS/CuFe_2O_4$ system at neutral pH (pH_0 5-9).

4.3.3.2 Effect of catalyst dosage

As seen in Fig. 4-5b, with catalyst dosage increasing from 0.1 to 0.6 g/L within the 120 min reaction time, the mineralization efficiencies of BPA increased from 26.8% to 84.3% and the initial mineralization rate increased from 0.048 to 0.206 mg/(L min). This significantly increased mineralization efficiency can be attributed to the formation of greater yields of radicals produced by the activation of PMS with the introduction of the catalyst. More active sites, such as the metal species Cu and Fe would be available at higher catalyst dosage and would activate PMS leading to an increase in

mineralization. However, when the catalyst dosage was further increased to 0.8 or 1.0 g/L, a slight decrease in mineralization was observed. The mineralization efficiencies were 79.4% and 81.7% when the corresponding catalyst dosages were 0.8 and 1.0 g/L, respectively, though the initial mineralization rate did rise. This was due to a diffusion limitation phenomenon in heterogeneous reactions [35]. PMS, with the molecular weight of 113 Da, a negative charge and smaller size can diffuse much faster toward the active sites of the catalyst particles than BPA with a molecular weight of 228 Da. When extra catalyst is added, reactive radicals are generated in excess on the catalyst surface before BPA is adsorbed, thus inducing considerable disappearance of radicals via dimerization of sulfate radicals (Eq. (4-6)) or invalid decomposition of persulfate (Eqs. (4-7)-(4-9)). In the meantime, the interaction reaction between Fe and Cu on the surface of the CuFe$_2$O$_4$ and sulfate radicals may directly quench sulfate radicals via Eq. (4-10) and Eq. (4-11) [3].

$$SO_4^{\bullet-} + SO_4^{\bullet-} \rightarrow 2SO_4^{2-} \tag{4-6}$$

$$HSO_5^- + SO_4^{\bullet-} \rightarrow SO_5^{\bullet-} + H^+ + SO_4^{2-} \tag{4-7}$$

$$HSO_5^- + HO^\bullet \rightarrow SO_5^{\bullet-} + H_2O \tag{4-8}$$

$$SO_5^{2-} + HO^\bullet \rightarrow SO_5^{\bullet-} + OH^- \tag{4-9}$$

$$\equiv Fe(II) + SO_4^{\bullet-} \rightarrow \equiv Fe(III) + SO_4^{2-} \tag{4-10}$$

$$\equiv Cu(I) + SO_4^{\bullet-} \rightarrow \equiv Cu(II) + SO_4^{2-} \tag{4-11}$$
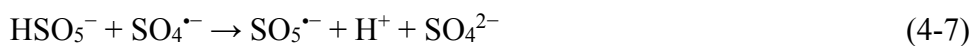
4.3.3.3 Effect of PMS concentration

As the source of sulfate radicals (SO$_4^{\bullet-}$), PMS plays a significant role in the PMS/CuFe$_2$O$_4$ process. Fig. 4-5c shows the BPA mineralization by CuFe$_2$O$_4$ activated PMS at various PMS dosages. The removal of BPA increased from 10.2% to 83.8% and the initial mineralization rate increased from 0.043 to 0.260 mg/(L min) with the increase of initial PMS concentration from 0.01 to 0.3 g/L. However, with higher PMS

concentrations, the mineralization efficiency and initial mineralization rate decreased slightly to 76.5% and 0.236 mg/(L min) at 0.5 g/L PMS and 75.1% and 0.197 mg/(L min) at 0.7 g/L PMS, respectively.

The improvement of mineralization efficiency at 0.01-0.3 g/L PMS is due to the availability of PMS, which at low concentration restricts the yield of reactive radicals though more radicals would be generated at higher PMS concentration. However, mineralization efficiency slowly increases with the PMS concentration at 0.2-0.3 g/L. This is due to the fact that the given catalyst dosage determined the number of active sites on the catalyst surface, which gradually became the limiting factor with the increasing PMS concentration. So the radical yield was almost independent of PMS when the PMS dosage exceeded the optimal value. The mineralization efficiency was found to begin to drop when the PMS dosage was greater than 0.5 g/L because the scavenging reaction between extra HSO_5^- and the produced reactive radicals ($HO^{\bullet}$, $SO_4^{\bullet-}$) became more significant.

4.3.3.4 Effect of the dosing regime

Apparently, the mineralization of BPA does not proceed further when the reaction time is longer than 20 min in most cases (Fig. 4-5a,b,c), indicating that the decomposition of HSO_5^- by the $CuFe_2O_4$ catalyst is a faster reaction and a sufficient amount of radicals is generated rapidly when the HSO_5^- is adsorbed. It may be considered that all the added PMS is completely decomposed within 20 min after the addition of the catalyst. However, it was found that around 30% of the PMS still remained unreacted after 20 min, which suggests that the complete consumption of the oxidant PMS is not the reason for the slow mineralization of BPA beyond 20 min.

It is considered that the surface of the catalyst might be passivated during the reaction process and the quenching of sulfate radicals becomes marked when both the

concentration of the PMS and BPA are reduced and the amount of mineralization intermediates increase after 20 min. In order to control both the inactivation of the catalyst and the quenching of sulfate radicals, the $CuFe_2O_4$ catalyst (0.6 g/L) was added in a single step (at 0 min), in two steps (at 0 and 60 min) and in three steps (at 0, 40, and 80 min), respectively. It was found that when the catalyst was added in two steps the mineralization of BPA increased to 92.9%, which was considerably higher than that of adding all the catalyst in one step (83.8%) (Fig. 4-5d). Therefore, the addition of the $CuFe_2O_4$ catalyst stepwise favored the mineralization of BPA though, interestingly, mineralization was found to decrease slightly (86.9%) when catalyst was added in three steps. This might be attributed to the excessive consumption of PMS and the surface deactivation of catalyst in the first two steps.

4.3.3.5 Effect of initial BPA concentration and kinetic modeling

Fig.4-5e shows that the mineralization efficiency decreased with the increase of initial BPA concentration from 50 to 200 mg/L. This can be attributed to two factors operating during the $PMS/CuFe_2O_4$ process. Firstly, although the initial BPA concentration is altered, the amount of radicals produced is assumed to be constant. So the probability of an oxidation reaction between the BPA and the reactive species would decrease with the increase of BPA concentration. On the other hand, PMS would be decomposed at the active sites of the catalyst to generate oxidative radicals. The increased BPA molecules would compete with PMS for adsorbance onto the catalyst surface, thus decreasing the surface sites available for the activation of PMS. Moreover, the intermediates may also compete with the parent pollutant for reactive radicals.

Langmiur–Hinshelwood expression has been employed to model the kinetics of heterogeneous catalysis process. To further investigate the kinetic of BPA removal in the heterogeneous reaction, the data in Fig. 4-5e were applied to the Langmuir–

Hinshelwood model which is commonly expressed as follows:

$$r_0 = -\frac{dTOC}{dt} = -\frac{k\,K_A\,TOC_0}{1 + K_A\,TOC_0} \tag{4-12}$$

$$\frac{1}{r_0} = \frac{1}{k\,K_A}\,\frac{1}{TOC_0} + \frac{1}{k} \tag{4-13}$$

where r_0 is the initial mineralization rate (mg/(Lmin)), TOC_0 is the initial total organic cabon of BPA (mg/L), k is the apparent reaction rate constant (mg/(Lmin)), and K_A is the adsorption equilibrium constant (L mg^{-1}).

Based on the TOC removal curves under different initial concentrations of BPA (Fig. 4-5e), the initial reaction rates r_0 were calculated. $1/r_0$ were plotted versus $1/TOC_0$ and a straight line was obtained with an intercept of $1/k$ and a slope of $1/(kK_A)$. According to the Langmiur-Hinshelwood (L-H) kinetics formula, k and K_A were estimated at 20.4 mg/(L min) and 0.011 L/mg. The regression line had a correlation coefficient of 0.98, $1/r_0$ correlated to $1/TOC_0$ well (inset of Fig. 4-5e), confirming the applicability of the Eq. (4-13) so the mineralization of BPA fitted with the Langmiur-Hinshelwood (L-H) kinetics model. This suggested that the catalytic degradation of BPA relied mainly on the surface oxidation destruction reaction attacked by the oxidants or radicals adsorbed on the surface of the catalysts.

4.3.3.6 Changes in toxicity druing degradation
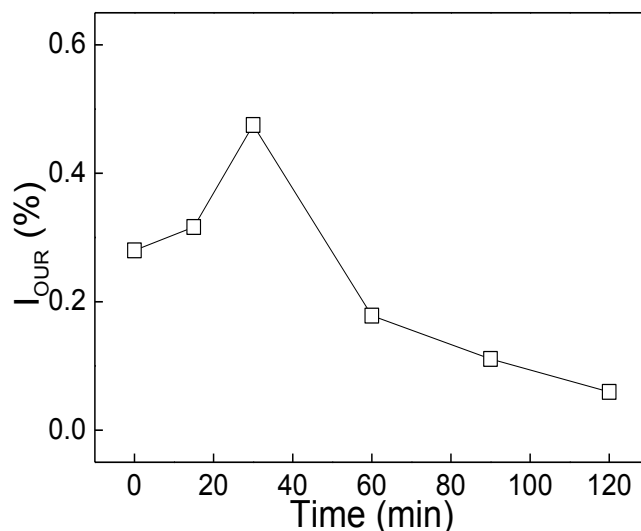
Figure 4-6 Changes in toxicity with reaction time ($[CuFe_2O_4]$ = 0.6 g L^{-1}, [PMS] = 0.3 g L^{-1}, pH$_0$ 6.72)

Based on the section 4.3.3, the high mineralization efficiency of BPA in the PMS/CuFe$_2$O$_4$ system was obtained at neutral pH (pH$_0$ 6.72) by the use of 0.6 g/L CuFe$_2$O$_4$ catalyst and 0.3 g/L PMS. Although the CuFe$_2$O$_4$/PMS heterogeneous oxidation process could achieve a higher TOC removal efficiency (about 80%), there are still some degradation byproducts at the end of the reaction. Thus an activated sludge inhibition test was used to assess the acute toxicity of reaction intermediates according to the procedure described in the ISO 8192 Method [37,38]. As can be seen from Fig. 4-6, the relative inhibition originally being 28% for the BPA solution increased considerably to 48% after 30 min treatment time, possibly indicating the generation of more toxic products. Similar result was also observed by Olmez-Hanci et al. [7] who reported the formation of toxic intermediates during hot persulfate process. The percentage inhibition decreased gradually and fell to around 6% after 120 min which may due to the destruction of more toxic products.

4.3.4 Stability and reusability of the CuFe₂O₄ catalyst
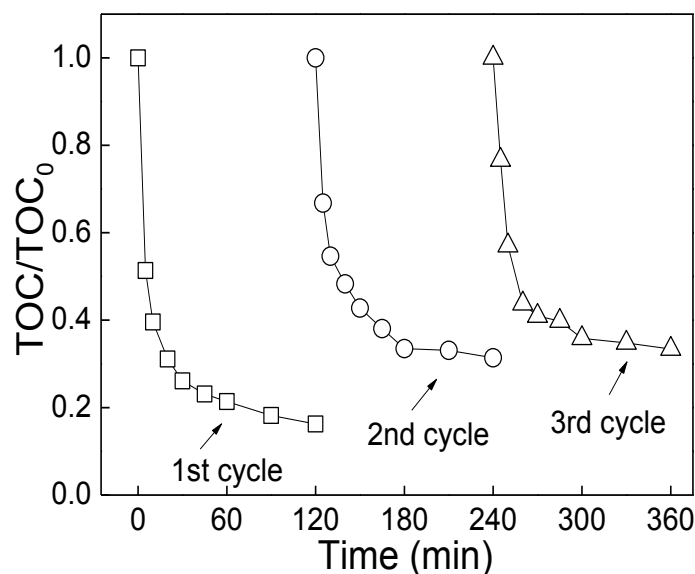
Figure 4-7 Recycling study of the mineralization of BPA ([BPA] = 50 mg L^{-1}, [CuFe$_2$O$_4$] = 0.6 g L^{-1}, [PMS] = 0.3 g L^{-1}, pH$_0$ 6.72)

To clarify the contribution of homogeneous phase reactions, less than 10.0% of BPA removal was detected in the leaching solution with the addition of 0.3 g/L PMS, which is much lower than that of the CuFe$_2$O$_4$/PMS system, indicating that the mineralization BPA was mainly a heterogeneous process. As seen in Fig. 4-7, the mineralization efficiency was above 80.0% after 120 min of reaction and the leaching percentages of Fe and Cu were 0.124% and 0.795%, respectively, in the first cycle. The leached Cu concentration was 1.27 mg/L in the first cycle, which dropped to 0.70 mg/L in the second one. Both are lower than the legal limit (2.7 mg/L) imposed by the directives of the United States Environmental Protection Agency [39]. The corresponding Fe concentration was 0.35 and 0.19 mg/L, which are lower than the10.0 mg/L of discharge limit (GB 8978-2002) regulated by Chinese Environmental Protection Agency [40]. The mineralization efficiency was still very high (>70.0%) in the second and third cycle, though the BPA mineralization efficiency had decreased slightly after the first use. The slight decrease in efficiency may be attributed to the

adsorption of reaction intermediates on the catalyst surface [41], the leaching of metal ions and the conglomeration of the catalyst [30]. To investigate the possible adsorption of reaction intermediates on the catalyst surface, FT-IR spectra of the fresh catalyst and the used catalyst were recorded as illustrated in Fig. 4-8. The distinctive peak around 584 cm^{-1} was attributed to the characteristic Fe-O bond [42]. The broad band located at 3400 cm^{-1}, which is indicative of the presence of surface hydroxyl functional groups, became stronger after reaction due to the hydroxylation of CuFe$_2$O$_4$ surface in the catalytic oxidation. Comparing with the FTIR spectrum of the fresh CuFe$_2$O$_4$, some new absorption bands could be observed. One is at 1720 cm^{-1}, which is corresponding to carboxylic C=O absorption, and the other one is assigned to aromatic ring C-C stretching vibration at 1500 cm^{-1}. In addition, two weak absorption peaks were appeared at 2895 and 2950 cm^{-1}, which are referred to C-H vibration. Meanwhile, several relatively weak bands at 1210 and 830 cm^{-1} are observed, which are due to C-O stretching vibration and C-H out-plane bending vibration, respectively [43]. Hence the intermediates cannot be completely removed by simple washing with water and the decrease of catalytic ability can be explained by the adsorption of intermediates on the surface of the catalyst.
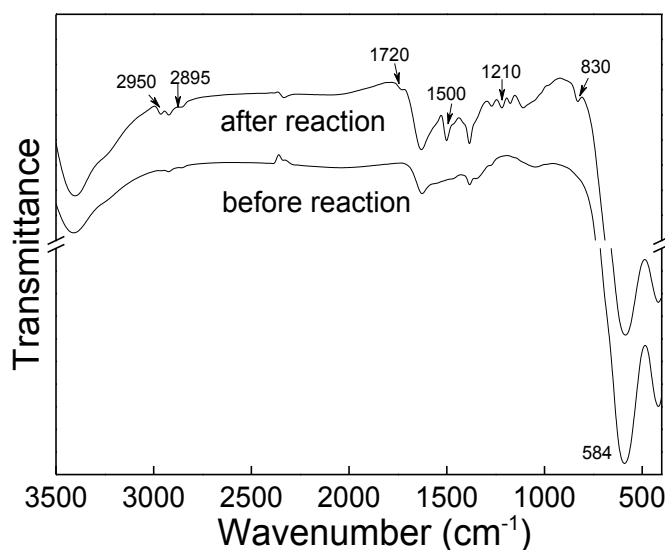

Figure 4-8 FTIR spectra of CuFe$_2$O$_4$ before and after reaction

4.3.5 Influence of anions
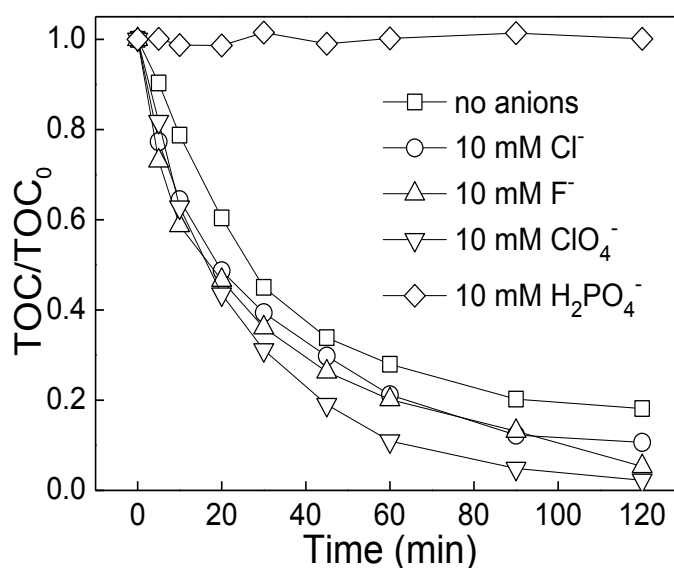
Figure 4-9 Effect of anions on BPA mineralization ([BPA] = 50 mg L^{-1}, [CuFe$_2$O$_4$] = 0.6 g L^{-1}, [PMS] = 0.3 g L^{-1}, pH$_0$ 3.22)

An increase in ionic strength is known to reduce the zeta potential of colloid particles and this could influence outer-sphere interactions such as electrostatic bonding between the solute and the solid surface. NaClO$_4$ was used to evaluate the influence of ionic strength on the BPA mineralization in the CuFe$_2$O$_4$/PMS system. Fig. 4-9 shows that BPA mineralization efficiency was hardly influenced and even enhanced when the concentration of NaClO$_4$ was 10 mM, revealing that there existed a strong inner-sphere interaction between the HSO$_5^-$ and the active sites on the catalyst surface. The enhanced oxidation efficiency may due to the high oxidation potential of perchlorate (1.389V). The strong inner-sphere interaction between the surface metal sites and the HSO$_5^-$, might be responsible for the remarkable increase in theformation of powerful radicals which lead to the rapid mineralization of BPA and this is not affected by increased ion addition. It has been reported that fluoride shows strong catalyst adsorption and the concentration of surface hydroxyl groups on the catalyst could be controlled by fluoride-exchange [44]. It is considered that the radical group generated on the catalyst surface might be suppressed accordingly but results reported here indicate that fluoride

had little enhancement on the mineralization of BPA. This is consistent with the explanation above that there exists a strong inner-sphere interaction between the HSO_5^- and the active sites on the catalyst surface. It is significant to note that the presence of anions as hydrogen acceptor F^- was found to largely decrease the activation energy of the oxygen atom transfer by interacting with the proton of the PMS, in agreement with the enhanced oxidation rate [45]. $Cl^•$ has been reported to be produced from $SO_4^{•-}$ oxidation of chloride ions (rate constant = 3.0×10^8 $M^{-1}s^{-1}$) [46]. $SO_4^{•-}$ would react with Cl^- to produce $Cl^•$ with a high redox potential of 2.4 V, the $Cl^•$ might mineralize BPA in a similar manner to $SO_4^{•-}$. Thus it was observed that the chloride ion concentration of 10 mM enhanced the BPA mineralization efficiency slightly (Fig.4-9). It is interesting that the removal of BPA is almost completely inhibited by the presence of 10 mM $H_2PO_4^-$. It has been found that phosphate has a strong affinity for the surface of goethite [47] and it forms an inner-sphere complex with the surface Fe(III), inducing its maximum substitution for surface hydroxyl groups on the catalyst in water (Eqs. (4-14)-(4-16)).

$$Fe\text{-}OH + H_2PO_4^- \rightleftharpoons FeH_2PO_4 + OH^- \tag{4-14}$$

$$Fe\text{-}OH + H_2PO_4^- \rightleftharpoons FeHPO_4^- + H_2O \tag{4-15}$$

$$Fe\text{-}OH + H_2PO_4^- \rightleftharpoons FePO_4^{2-} + H_2O + H^+ \tag{4-16}$$
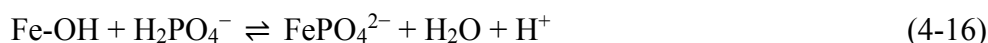
It may be assumed that the observed inhibition phenomenon in the $CuFe_2O_4$/PMS system by phosphate is similar to the inhibition process of goethite/O_3 by phosphate, which is related to the substitution of the active sites such as surface hydroxyl groups [48]. It is speculated that replacement of the surface hydroxyl groups influenced the catalyzing capacity of the $CuFe_2O_4$ catalyst implying that the surface hydroxyl groups of $CuFe_2O_4$ may play an important role in the catalytic degradation of BPA.

4.3.6 Degradation mechanism - EPR experiments
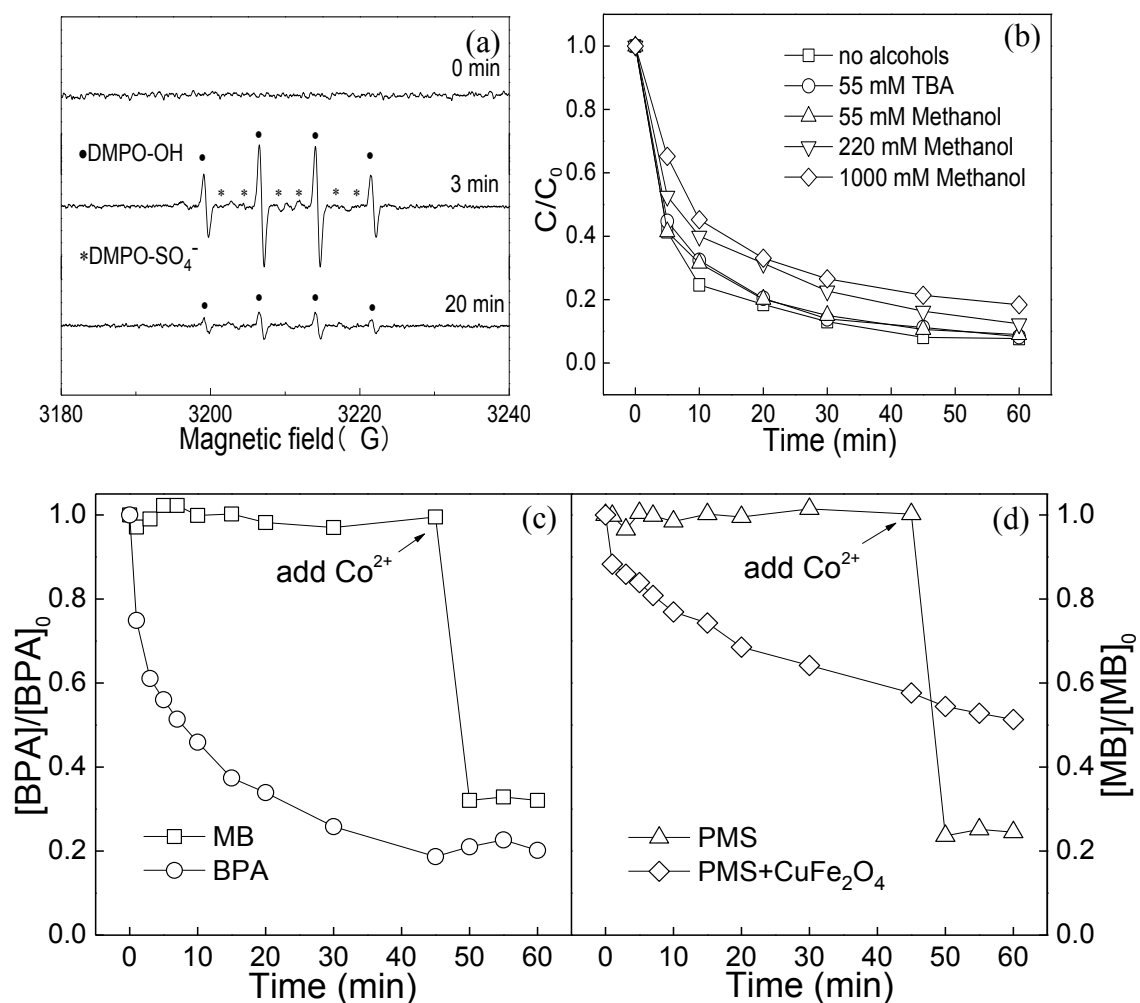
Figure 4-10 (a) ESR spectrum at reaction times of 0, 3, 20 min, (b) Effect of quenching agents TBA and MeOH on BPA degradation. Condition (a, b): [BPA] = 50 mg L^{-1}, [CuFe$_2$O$_4$] = 0.6 g L^{-1}, [PMS] = 0.3 g L^{-1}, [DMPO] $\approx$ 0.08 N, pH$_0$ 6.72. (c) Decoloration of methylene blue and degradation of BPA in the CuFe$_2$O$_4$/PMS solution, ([BPA] = 50 mg L^{-1}, [MB] = 50 mg L^{-1}, [CuFe$_2$O$_4$] = 0.6 g L^{-1}, [PMS] = 0.3 g L^{-1}, pH$_0$ 3.22, [Co^{2+}/PMS]$_{mol}$ = 0.025) (d) Decoloration of methylene blue in PMS and CuFe$_2$O$_4$/PMS solutions. ([MB] = 50 mg L^{-1}, [CuFe$_2$O$_4$] = 0.6 g L^{-1}, [PMS] = 0.3 g L^{-1}, pH$_0$ 3.22, [Co^{2+}/PMS]$_{mol}$ = 0.025)
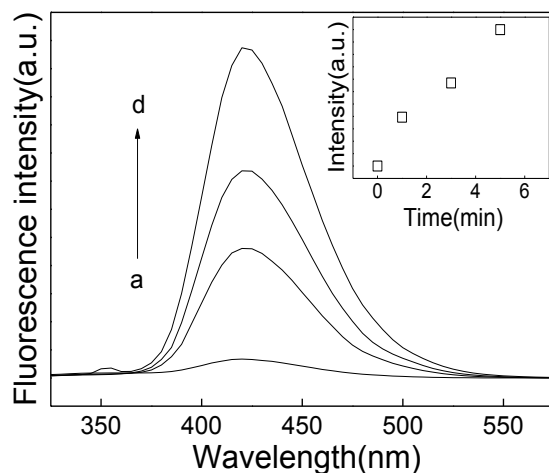
Figure 4-11 Fluorescence spectra of TAOH at (a) 0; (b) 1; (c) 3; and (d) 5 min using the CuFe$_2$O$_4$/PMS system (λ_{ex} = 315 nm). ([BPA] = 50 mg L^{-1}, [CuFe$_2$O$_4$] = 0.6 g L^{-1}, [PMS] = 0.3 g L^{-1})

DMPO-SO$_4^-$ DMPO-OH
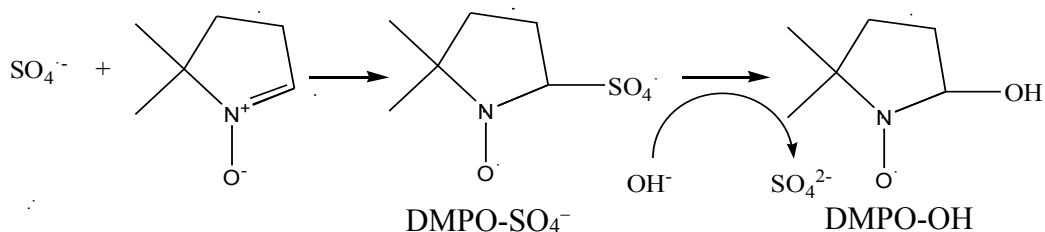
Figure 4-12 Transformation of DMPO adducts with SO$_4^{\bullet-}$ and HO$^\bullet$

EPR experiments with DMPO were performed in order to detect any radicals produced and directly confirm that the CuFe$_2$O$_4$/PMS process involved radical reactions. Hydroxyl and sulfate radicals could be discerned by determination of the typical DMPO-SO$_4$ and DMPO-OH signals based on their hyperfine splitting constants (DMPO-OH: aH=aN= 14.8 G; DMPO-SO$_4$: aN= 13.2 G, aH= 9.6 G, aH= 1.48 G, and aH= 0.78 G) [49,50]. At 3 min, the special hyperfine coupling constants (aN= 14.8 G, aH= 14.8 G) were consistent with that of DMPO-OH adducts and the HO$^\bullet$ spectrum is indicated by the intensity ratio of each characteristic peak being "1: 2: 2: 1" in Fig. 4-10a [51], indicating that hydroxyl radicals are produced during the initial phase. It was found that the concentrations of reactive oxidants at the beginning in the CuFe$_2$O$_4$/PMS process were much higher due to the fact that the intensity of the signals from the

DMPO radical adducts is proportional to the concentrations of reactive oxidants.

It is very interesting to note that only DMPO-OH was detected while little of the characteristic peak of DMPO-SO$_4$ was observed during the initial phase (3 min). This is similar with the PMS system described in previous studies [52,53]. Moreover, the use of the terephthalate dosimeter confirmed the production of hydroxyl radicals during the early stages of the reaction. It is known that HO$^\bullet$ will react with terephthalic acid (TA) and generate 2-hydroxyterephthalic acid (TAOH) which emits fluorescence at around 426 nm on the excitation of the 315 nm absorption band [54]. Fig. 4-11 shows the fluorescence spectra of the supernatant solution from the CuFe$_2$O$_4$ suspension containing 1 mM TA and 0.3 g/L PMS. It can be seen that there is fluorescence at 426 nm indicative of the presence of 2-hydroxyterephthalic acid (TAOH). Therefore, it may be concluded that TAOH was generated during the reaction process of TA with HO$^\bullet$, as a result of HO$^\bullet$ being formed in the CuFe$_2$O$_4$/PMS system which plays a vital role in the degradation of BPA. Fig. 4-11 (inset) also shows that the formation rate of HO$^\bullet$ increases linearly for 5min. The DMPO-OH spectrum was still obvious and observed at 20 min which might indicate that HO$^\bullet$ is the main oxidant. The fact that only DMPO-OH was detected while no characteristic peak of DMPO-SO$_4$ was observed within 20 min, could be interpreted in a number of ways. Firstly, the sulfate radical seems to be unstable in the CuFe$_2$O$_4$/PMS process and is rapidly transformed into HO$^\bullet$ by the reaction of the sulfate radical with H$_2$O (Eq. (4-17)) [9]. Secondly, the hydrolysis equilibrium of HSO$_5^-$ is also reported to generate peroxide so any hydroxyl radical observed might be produced from H$_2$O$_2$ so any hydroxyl radical observed might be produced from H$_2$O$_2$ (Eq. (4-18)) [55]. Thirdly, sulfate radicals are generated in the catalytic oxidation during the initial phase but during the EPR experiment, the fast transformation from DMPO-SO$_4$ adducts to DMPO-OH adducts by nucleophilic

substitution results in no detection of the DMPO-SO4 adducts (Fig.4-12). At the end, little or no signals from DMPO-SO4 adducts could be detected, which also possibly suggests the depletion of sulfate radicals by the rapid reaction [53].

$$SO_4^{\bullet-} + H_2O \rightarrow SO_4^{2-} + HO^{\bullet} + H^+ \tag{4-17}$$

$$HSO_5^- + H_2O \rightarrow HSO_4^{2-} + H_2O_2 \tag{4-18}$$

4.3.7 Radical scavenging experiment

In order to evaluate the contribution of different radical species to BPA mineralization, two radical scavengers, methanol (MeOH) and *tert*-butyl alcohol (TBA) were employed. Methanol (containing an α-hydrogen) can rapidly react with both hydroxyl and sulfate radicals with rate constants of 9.7×10^8 $M^{-1}s^{-1}$ and 3.2×10^6 $M^{-1}s^{-1}$ respectively. In contrast, *tert*-butyl alcohol, which does not have an α-hydrogen, has very different reaction rate constants and rapidly reacts with hydroxyl radicals (rate constant = $3.8\sim7.6 \times 10^8$ $M^{-1}s^{-1}$) but has a much lower reactivity (rate constant = $4\sim9.1 \times 10^5$ $M^{-1}s^{-1}$) with the sulfate radical [52].

As shown in Fig. 4-10b, 55 mM TBA or MeOH had negligible influence on the removal of BPA. In order to eliminate the limiting effect of scavenger concentration, the methanol concentration used was increased from 220 mM to 1000 mM which takes into account the high reaction rate constants between methanol and both hydroxyl/sulfate radical. The inhibiting effect of 220 mM methanol did not significantly affect the overall results but the presence of 1000 mM methanol suppressed the oxidation process somewhat with the degradation efficiency declining from 92.3% to 81.6%. These data indicate that $SO_4^{\bullet-}$ and $HO^{\bullet}$ are generated during the $CuFe_2O_4$/PMS process, though some of the hydroxyl and sulfate radicals are quenched. According to previous research, it was found that the scavengers did not retard the interactions between HSO_5^- and the $CuFe_2O_4$ catalyst surface [35]. Therefore, methanol (or *tert*-

butyl alcohol) could not compete with HSO_5^- for the catalyst adsorption sites due to its low affinity for the catalyst surface. Moreover, scavengers are easily oxidized by radicals and the rate constant of reaction between radicals and scavengers is nearly 10^8 $M^{-1}s^{-1}$ – a rate close to the diffusion limit. Furthermore, methanol and *tert*-butyl alcohol are hydrophilic compounds so it is difficult to believe that they will accumulate on the catalyst surface to a significant extent [56]. Therefore, the scavengers (methanol or *tert*-butyl alcohol) are more likely to compete for free radicals in liquid phase [10,56]. In other words, the quenching effect of scavengers would be not obvious if the surface-bound $HO^{\bullet}$ and $SO_4^{\bullet-}$ played a dominant role in the catalytic oxidation reaction. Along with the effect of anions discussed above, it is proposed that the BPA mineralization reaction may occur on the catalyst surface and surface-bound radicals, instead of free radicals, act as the main oxidant. Furthermore, bisphenol A being a phenolic compound might readily approach the catalyst surface where it could react with the radicals which exist in close proximity to catalyst surface.

4.3.8 Methylene blue (MB) indicator experiment

In order to confirm that free radicals have not been mainly generated in solution, a methylene blue (MB) dye experiment (a commonly used indicator showing the formation of reactive radicals such as hydroxyl and sulfate) [45], was conducted to distinguish between surface-bound radical reactions and free radical reactions in the solution. No decoloration of MB was seen but considerable degradation of BPA in the $CuFe_2O_4$/PMS system occurred. A further addition of Co^{2+} led to strong dye decoloration (Fig. 4-10c) because reactive radicals produced in solution by the fast reactions between Co^{2+} and PMS degraded the methylene blue dye.

This additional evidence supported the surface-bound radical reaction pathway in $CuFe_2O_4$/PMS reaction. Without BPA, the $CuFe_2O_4$/PMS system partly degrades MB

though the decoloration efficiency is lower than the Co^{2+}/PMS system (Fig. 4-10d), indicating that only a minimal amount of free hydroxyl radical and sulfate radical ($HO^\bullet_{free}$ and $SO_4^{\bullet-}_{free}$) exists in the $CuFe_2O_4$/PMS system. Decreased dye decoloration was observed in the $CuFe_2O_4$/PMS system after the addition of Co^{2+}, owing to less HSO_5^- being available in solution after substantial consumption of HSO_5^- by the degradation of BPA within the first 45 min. Thus, it is concluded that $HO^\bullet_{ads}$ and $SO_4^{\bullet-}_{ads}$ play a dominant role in the BPA mineralization process using the PMS/$CuFe_2O_4$ system.

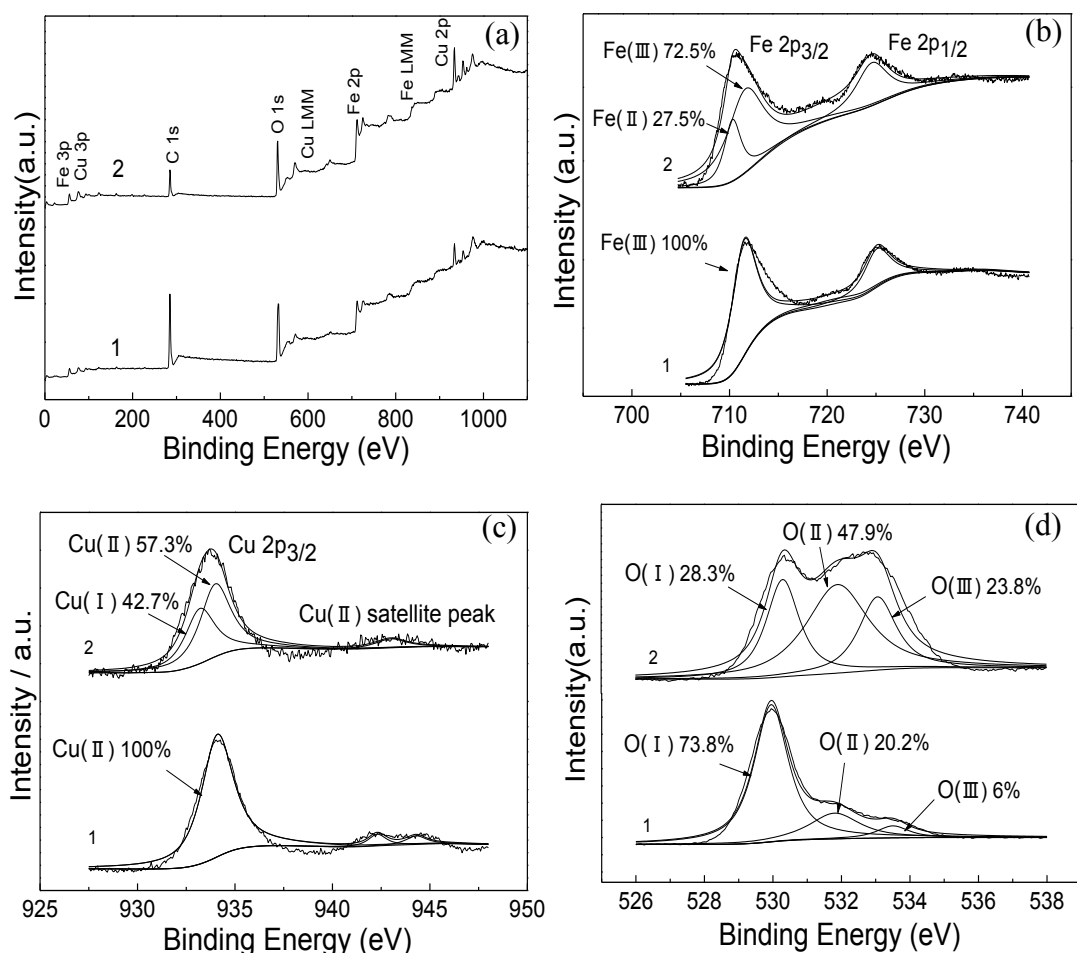**4.3.9 XPS spectra of CuFe₂O₄ before and after treatment**

Figure 4-13 (a) Wide survey XPS spectra and (b) Fe 2p and (c) Cu 2p and (d) O 1s XPS envelop of (1) the fresh and (2) used $CuFe_2O_4$ catalyst

As discussed above, the generation of reactive radicals and BPA mineralization occurs mainly on the catalyst surface. To better understand the surface composition and

chemical states of the catalyst before and after the degradation process, and the roles of the Cu and Fe species and hydroxyl groups during the activation of PMS, XPS spectra of $CuFe_2O_4$ before and after treatment were compared. Fig. 4-13a shows only C, O, Fe and Cu on the surface of the fresh and used samples. The binding energy occurring at 934.1 and 712.0 eV in the fresh $CuFe_2O_4$ was assigned to the Cu $2p_{3/2}$ of Cu(II) and Fe $2p_{3/2}$ of Fe(III), respectively [34]. The peak of Cu $2p_{3/2}$ and Fe $2p_{3/2}$ slightly shifted to lower binding energy value at 933.2 eV and 710.5 eV in the used catalyst (Fig. 4-13b and Fig. 4-13c) suggesting that the valence of the Cu and Fe species had changed, and consisted of a mixture of species after the catalytic degradation of BPA. Especially, double satellite peaks (940 eV ~ 945 eV) were observed in the Cu(II) of the fresh sample. After catalytic ozonation, just one weak satellite peak was found in the used sample, confirming the formation of surface Cu(I). A similar negative shift of binding energy value of $2p_{3/2}$ orbit was also reported by Ji et al. [30] who used CuO as a heterogeneous catalyst for the degradation of phenol in the presence of oxone and found that the peak of Cu $2p_{3/2}$ slightly declined from 933.3 eV in the fresh CuO to 932.5 eV after the catalytic reaction. Based on the deconvolution of Cu (2p) and Fe (2p) envelope, Cu(I) and Fe(II) accounted for 42.7% and 27.5% in the used catalyst, respectively, indicating that electron capture occurred for some of the Cu(II) and Fe(III) on the surface of the used catalyst during treatment, i.e., Cu(II) and Fe(III) were transformed partially to Cu(I) and Fe(II).

As shown in Fig.4-13d, the O 1s peak with the observed position around 531.0 eV had undergone a major change. The main peak around 530.0 eV is attributed to the lattice oxygen O which accounts for 73.8% of all surface oxygen in $CuFe_2O_4$ before use. For the used $CuFe_2O_4$ catalyst, the percentage of O 1s OH component at 531.8 eV and the O in adsorbed H_2O at 533.0 eV increased greatly with the decrease of the lattice

oxygen O with the component at 530.0 eV, indicating that the $CuFe_2O_4$ surface is strongly hydroxylated after the degradation experiment. According to Sui et al., the surface hydroxyl groups are the active sites for catalytic decomposition and reactive radical generation [47]. A large number of the surface hydroxyl groups may be beneficial for enhancement of the oxidation degradation process.
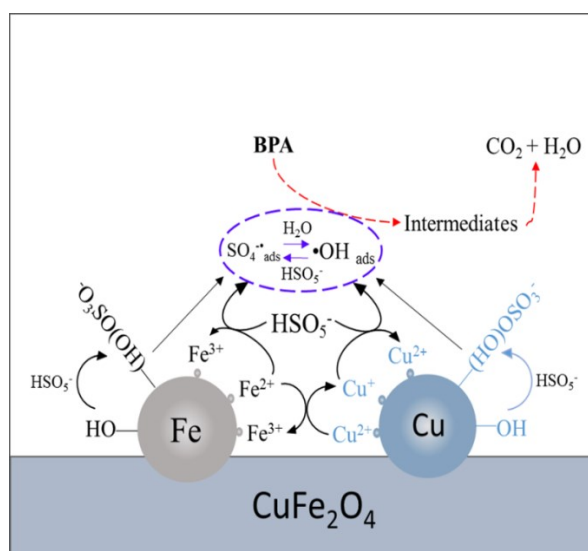
Figure 4-14 Schematic diagram of the mechanism of the PMS activation by $CuFe_2O_4$

Based on these experimental results, a possible mechanism of activation of PMS by $CuFe_2O_4$ is proposed (Fig. 4-14), which may involve two parts: on the one hand, after addition of PMS, Fe(III) and Cu(II) on the catalysts would first react with HSO_5^- to generate Fe(II) and Cu(I) and, subsequently, Fe(II) and Cu(I) react with HSO_5^- to produce $HO^•$ and then some initially generated $HO^•$ species will react with PMS to generate $SO_4^{•-}$ (Eqs. (4-19)-(4-24)) [34]. On the other hand, H_2O molecules are physically adsorbed on some of the Fe or Cu sites of the catalyst to generate Fe(II/III)-$^-$OH, Cu(I/II)-$^-$OH (where Fe(II/III)-$^-$OH and Cu(I/II)-$^-$OH represent active sites on the hydroxyl-covered $CuFe_2O_4$ catalyst surface. Then, Fe(II/III)-(HO)OSO$_3$ and Cu(I/II)-(HO)OSO$_3$ are generated by the formation of a complex by ligand displacement between the hydrated surface of Fe(II/III)-$^-$OH, Cu(I/II)-$^-$OH and HSO_5^-, which subsequently decomposed to produce $SO_4^{•-}$ (Eqs. (4-25)-(4-28)). Furthermore, owing

to the standard reduction potential of Cu^{2+}/Cu^+ (0.17 V) being lower than that of Fe^{3+}/Fe^{2+} (0.77 V) [57] the reduction of Fe^{3+} by Cu^+ is thermodynamically favorable. Thus, the generated Cu^+ not only forms reactive radicals by Eq. (4-29), but also produces more Fe^{2+} species on the surface of the catalyst. The efficient regeneration of the surface Fe(II) in this manner may contribute to the enhancement of BPA degradation. Also, dissolved metal ions (Fe^{3+} and Cu^{2+}) resulting from dissolution of iron oxides might disperse into the bulk solution and then react with PMS to generate free radicals. In addition, a minimal amount of surface-bound radicals might diffuse from the surface of the catalyst into the bulk solution. In conclusion, BPA is degraded and mineralized mainly by radicals bound to the surface of the catalyst with little contribution from free radicals in the bulk solution (Eq. (4-22)).

$$\equiv Fe(III) + HSO_5^- \rightarrow \equiv Fe(II) + SO_5^{\bullet-} + H^+ \tag{4-19}$$

$$\equiv Fe(II) + HSO_5^- \rightarrow \equiv Fe(III) + HO^{\bullet} + SO_4^{2-} \tag{4-20}$$

$$\equiv Cu(II) + HSO_5^- \rightarrow \equiv Cu(I) + SO_5^{\bullet-} + H^+ \tag{4-21}$$

$$\equiv Cu(I) + HSO_5^- \rightarrow \equiv Cu(II) + HO^{\bullet} + SO_4^{2-} \tag{4-22}$$

$$HO^{\bullet} + HSO_5^- \rightarrow SO_5^{\bullet-} + H_2O \tag{4-23}$$

$$SO_5^{\bullet-} + SO_5^{\bullet-} \rightarrow 2SO_4^{\bullet-} + O_2 \tag{4-24}$$

$$\equiv Fe(II)\text{-}^-OH + HSO_5^- \rightarrow \equiv Fe(II)\text{-}(HO)OSO_3 + OH^- \tag{4-25}$$

$$\equiv Fe(II)\text{-}(HO)OSO_3 \rightarrow \equiv Fe(III)\text{-}^-OH + SO_4^{\bullet-} \tag{4-26}$$

$$\equiv Cu(I)\text{-}^-OH + HSO_5^- \rightarrow \equiv Cu(I)\text{-}(HO)OSO_3 + OH^- \tag{4-27}$$

$$\equiv Cu(I)\text{-}(HO)OSO_3 \rightarrow \equiv Cu(II)\text{-}^-OH + SO_4^{\bullet-} \tag{4-28}$$

$$\equiv Cu(I) + \equiv Fe(III) \rightarrow \equiv Cu(II) + \equiv Fe(II) \tag{4-29}$$

$$BPA + radicals \rightarrow intermediate \rightarrow CO_2 + H_2O \tag{4-30}$$
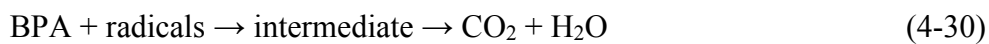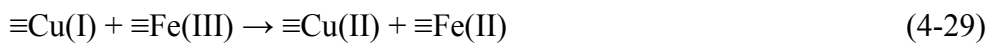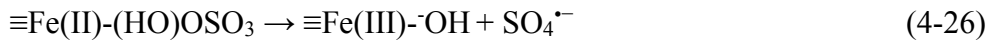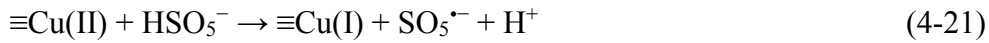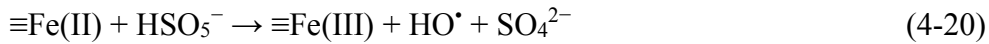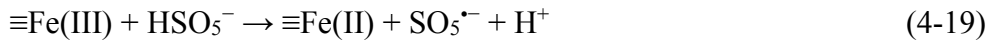
4.4 Conclusions

In summary, $CuFe_2O_4$ MNPs were prepared and used as a heterogeneous catalyst

to activate PMS for the mineralization of BPA. It was found that $CuFe_2O_4$ MNPs, in comparison with Fe_2O_3 and CuO, exhibited a higher catalytic activity towards the degradation of BPA in the presence of PMS. The use of 0.6 g/L $CuFe_2O_4$ catalyst and 0.3 g/L PMS yielded 92.3% removal of the BPA (50 mg/L) in 60 min and 84.0% removal of TOC in 120 min at neutral pH. The XPS analysis, EPR tests and other experimental results indicate that the high catalytic activity is attributed to the synergistic effect of Cu(I)/Cu(II) and Fe(II)/Fe(III) redox pairs. In particular, $HO^{\bullet}_{ads}$ and $SO_4^{\bullet-}{}_{ads}$, especially the hydroxyl radical, generated in the reaction may play a dominant role in the catalytic oxidation reaction.

References

[1] T. Colborn, F.S. vom Saal, A.M. Soto, Developmental effects of endocrine-disrupting chemicals in wildlife and humans, Environ. Health Perspect.101 (1993) 378.

[2] T. Geens, L. Goeyens, A. Covaci, Are potential sources for human exposure to bisphenol A overlooked? Int. J. Hyg. Environ. Health 214 (2011) 339-347.

[3] K.L. Howdeshell, A.K. Hotchkiss, K.A. Thayer, J.G. Vandenbergh, F.S. Vomsaal, Environmental toxins: exposure to bisphenol A advances puberty, Nature 401 (1999) 763-764.

[4] C.A. Staples, P.B. Dorn, G.M. Klecka, S.T. O'Block, D.R. Branson, L.R. Harris, Bisphenol A concentrations in receiving waters near US manufacturing and processing facilities, Chemosphere 40 (2000) 521-525.

[5] G. Liu, J.Ma, X. Li, Q. Qin, Adsorption of bisphenol A from aqueous solution onto activated carbons with different modification treatments,J. Hazard. Mater. 164 (2009) 1275-1280.

[6] C. Zhang, G. Zeng, L. Yuan, J. Yu, J. Li, G. Huang, B. Xi, H. Liu, Aerobic degradation of bisphenol A by achromobacterxylosoxidans strain B-16 isolated from compost leachate of municipal solid waste, Chemosphere 68 (2007) 181-190.

[7] T. Olmez-Hanci, I. Arslan-Alaton, B. Genc, Bisphenol A treatment by the hot persulfate process: oxidation products and acute toxicity,J. Hazard. Mater. (2013) 283-290.

[8] Y. Xu, Z.Y. Lin, H. Zhang, Mineralization of sucralose by UV-based advanced oxidation processes: UV/PDS versus UV/H_2O_2, Chem. Eng. J. 285 (2016) 392-401.

[9] G.P. Anipsitakis, D.D. Dionysiou, Degradation of organic contaminants in water with sulfate radicals generated by the conjunction of peroxymonosulfate with cobalt, Environ. Sci. Technol. 37 (2003) 4790-4797.

[10] S.Y. Yang, X. Yang, X.T. Shao, R. Niu, L.L. Wang, Activated carbon catalyzed persulfate oxidation of Azo dye acid orange 7 at ambient temperature, J. Hazard. Mater. 186 (2011) 659-666.

[11] J. Wu, H. Zhang, J.J. Qiu, Degradation of Acid Orange 7 in aqueous solution by a novel electro/Fe^{2+}/peroxydisulfate process,J. Hazard. Mater. 215-216 (2012) 138-145.

[12] C. Cai, L.G. Wang, H. Gao, L.W. Hou, H. Zhang, Ultrasound enhanced heterogeneous activation of peroxydisulfate by bimetallic Fe-Co/GAC catalyst for the degradation of Acid Orange 7 in water, J. Environ. Sci. China 26 (2014) 1267-1273.

[13] H. Lin, J. Wu, H. Zhang, Degradation of clofibric acid inaqueous solution by an EC/Fe^{3+}/PMS process, Chem. Eng. J. 244 (2014) 514-521.

[14] H. Lin, H. Zhang, L.W. Hou, Degradation of C. I. Acid Orange 7 in aqueous solution by a novel electro/Fe_3O_4/PDS process, J. Hazard. Mater. 276 (2014) 182-191.

[15] X. Chen, X. Qiao, D. Wang, J. Lin, J. Chen, Kinetics of oxidative decolorization and mineralization of Acid Orange 7 by dark and photoassisted Co^{2+}-catalyzed peroxymonosulfate system, Chemosphere 67 (2007) 802-808.

[16] G.P. Anipsitakis, D.D. Dionysiou, M.A. Gonzalez, Cobalt-mediated activation of peroxymonosulfate and sulfate radical attack on phenolic compounds. Implications of chloride ions,Environ. Sci. Technol. 40 (2005) 1000-1007.

[17] G.P. Anipsitakis, T.P. Tufano, D.D. Dionysiou, Chemical and microbial decontamination of pool water using activated potassium peroxymonosulfate, Water Res. 42 (2008) 2899-2910.

[18] M. Pagano, A. Volpe, G. Mascolo, A. Lopez, V. Locaputo, R. Ciannarella, Peroxymonosulfate-Co(II) oxidation system for the removal of the non-ionic surfactant Brij 35 from aqueous solution, Chemosphere 86 (2012) 329-334.

[19] G.P. Anipsitakis, E. Stathatos, D.D. Dionysiou, Heterogeneous activation of oxone using Co_3O_4, J. Phys. Chem. B. 109 (2005) 13052-13055.

[20] L. Hu, X. Yang, S. Dang, An easily recyclable Co/SBA-15 catalyst: heterogeneous activation of peroxymonosulfate for the degradation of phenol in water, Appl. Catal. B: Environ. 102 (2011) 19-26.

[21] P.R. Shukla, S.B. Wang, H.Q. Sun, H.M. Ang, M.O. Tadé, Activated carbon supported cobalt catalysts for advanced oxidation of organic contaminants in aqueous solution, Appl. Catal. B: Environ. 100 (2010) 529-534.

[22] P.R. Shukla, S.B. Wang, K. Singh, H.M. Ang, M.O. Tadé, Cobalt exchanged zeolites for heterogeneous catalytic oxidation of phenol in the presence of peroxymonosulphate, Appl. Catal. B: Environ. 99 (2010) 163-169.

[23] Y. Hardjono, H.Q. Sun, H. Tian, C.E. Buckley, S.B. Wang, Synthesis of Co oxide doped carbon aerogel catalyst and catalytic performance in heterogeneous oxidation of phenol in water, Chem. Eng. J. 174 (2011) 376-382.

[24] S. Muhammad, E. Saputra, H.Q. Sun, J.D. Izidoro, D.A. Fungaro, H.M. Ang, M.O. Tade,; S.B. Wang, Coal fly ash supported Co_3O_4 catalysts for phenol degradation using peroxymonosulfate, RSC Adv. 2 (2012) 5645-5650.

[25] Q. Yang, H. Choi, D.D. Dionysiou, Nanocrystalline cobalt oxide immobilized on titanium dioxide nanoparticles for the heterogeneous activation of peroxymonosulfate, Appl. Catal. B: Environ. 74 (2007) 170-178.

[26] P.R, Shukla, H.Q. Sun, S.B. Wang, H.M. Ang, M.O. Tadé, Nanosized Co_3O_4/SiO_2 for heterogeneous oxidation of phenolic contaminants in waste water, Sep. Purif. Technol. 77 (2011) 230-236.

[27] C. Cai, H. Zhang, X. Zhong, L.W. Hou, Ultrasound enhanced heterogeneous activation of peroxymonosulfate by a bimetallic Fe-Co/SBA-15 catalyst for the degradation of orange II in water, J. Hazard. Mater. 283 (2015) 70-79.

[28] P. Shi, R. Su, F. Wan, M. Zhu, D. Li, S. Xu, Co_3O_4 nanocrystals on graphene oxide as a synergistic catalyst for degradation of Orange II in water by advanced oxidation technology based on sulfate radicals, Appl. Catal. B: Environ. 123 (2012) 265-272.

[29] D. Chen, X. Ma, J. Zhou, X. Chen, G. Qian, Sulfate radical-induced degradation of Acid Orange 7 by a new magnetic composite catalyzed peroxymonosulfate oxidation process, J. Hazard. Mater. 279 (2014) 476-484.

[30] F. Ji, C. Li, L. Deng, Performance of CuO/Oxone system: heterogeneous catalytic oxidation of phenol at ambient conditions, Chem. Eng. J. 178 (2011) 239-243.

[31] C.Q. Tan, N.Y. Gao, Y. Deng, J. Deng, S.Q. Zhou, J. Li, X.Y. Xin, Radical induced degradation of acetaminophen with Fe_3O_4 magnetic nanoparticles as heterogeneous activator of peroxymonosulfate. J. Hazard. Mater. 276 (2014) 452-460.

[32] W.F. Shangguan, Y. Teraoka, S. Kagawa, Promotion effect of potassium on the catalytic property of $CuFe_2O_4$ for the simultaneous removal of NOx and diesel soot particulate, Appl. Catal. B: Environ. 16 (1998) 149-154.

[33] K. Faungnawakij, N. Shimoda, T. Fukunaga, R. Kikuchi, K Eguchi, Crystal structure and surface species of $CuFe_2O_4$ spinel catalysts in steam reforming of dimethyl ether, Appl. Catal. B: Environ. 92 (2009) 341-350.

[34] Y.B. Ding, L.H. Zhu, N. Wang, H.Q. Tang, Sulfate radicals induced degradation of tetrabromobisphenol A with nanoscaled magnetic $CuFe_2O_4$ as a heterogeneous catalyst of peroxymonosulfate, Appl. Catal. B: Environ. 129 (2013) 153-162.

[35] T. Zhang, H. Zhu, J.P. Croué, Production of sulfate radical from peroxymonosulfate induced by a magnetically separable $CuFe_2O_4$ spinel in water: efficiency, stability, and mechanism, Environ. Sci. Technol. 47 (2013) 2784-2791.

[36] P. Laokul, V. Amornkitbamrung, S. Seraphin, S. Maensiri, Characterization and magnetic properties of nanocrystalline $CuFe_2O_4$, $NiFe_2O_4$, $ZnFe_2O_4$ powders prepared by the aloe vera extract solution, Curr. Appl. Phys. 11 (2011) 101-108.

[37] ISO 8192. Water quality; test for inhibition of oxygen consumption by activated sludge, 1986.

[38] I. Arslan Alaton, T. Olmez-Hanci, N. Ayten, Photo-fenton-like treatment of the commercially important h-acid: process optimization by factorial design and effects of photocatalytic treatment on activated sludge inhibition, Appl. Catal. B Environ. 96 (2010) 208-217.

[39] Guidance Manual for Electroplating and Metal Finishing Pretreatment Standards, United States Environmental Protection Agency, (EPA68-01-6514), http://citeseerx. ist.psu. edu/viewdoc/download?doi=10.1.1.405.4460&rep=rep1&type=Pdf.

[40] Integrated Wastewater Discharge Standard, National Standard of People's Republic of China (in Chinese) GB 8978-2002.

[41] W.D. Oh, Z.L. Dong, Z.T. Hu, T.T. Lim, A novel quasi-cubic $CuFe_2O_4$–Fe_2O_3 prepared at low temperature for enhanced oxidation of bisphenol A via peroxymonosulfate activation, J. Mater. Chem. A 3 (2015) 22208-22217.

[42] W.D. Oh, S.K. Lua, Z.L. Dong, T.T. Lim, High surface area DPA-hematite for efficient detoxification of bisphenol A via peroxymonosulfate activation, J. Mater. Chem. A 2 (2014) 15836-15845.

[43] W. Li, P.X. Wu, Y.J. Zhu, Z.J. Huang, Y.H. Lu, Y.W. Li, Z. Dang, Catalytic degradation of

bisphenol A by CoMnAl mixed metal oxides catalyzed peroxymonosulfate: Performance and mechanism, Chem. Eng. J. 279 (2015) 93-102.

[44] Y. Chen, S. Yang, K. Wang, L. Lou, Role of primary active species and TiO_2 surface characteristic in UV-illuminated photodegradation of Acid Orange 7,J. Photoch. Photobio. A Chem.172 (2005) 47-54.

[45] Z.H. Wang, R.T. Bush, L.A. Sullivan, C.C. Chen, J.S. Liu, Selective oxidation of arsenite by peroxymonosulfate with high utilization efficiency of oxidant, Environ. Sci. Technol. 48 (2014) 3978-3985.

[46] Y. Yang, J.J. Pignatello, J. Ma, W.A. Mitch, Comparison of halide impacts on the efficiency of contaminant degradation by sulfate and hydroxyl radical-based advanced oxidation processes (AOPs), Environ. Sci. Technol. 48 (2014) 2344-2351.

[47] M. Sui, L. Sheng, K. Lu, F. Tian, FeOOH catalytic ozonation of oxalic acid and the effect of phosphate binding on its catalytic activity, Appl. Catal. B: Environ. 96 (2010) 94-100.

[48] Y.H. Guan, J. Ma, Y.M. Ren, Y.L. Liu, J.Y. Xiao, L.Q. Lin, C. Zhang, Efficient degradation of atrazine by magnetic porous copper ferrite catalyzed peroxymonosulfate oxidation via the formation of hydroxyl and sulfate radicals, Water Res. 47 (2013) 5431-5438.

[49] G.S. Timmins, K.J. Liu, E.J.H. Bechara, Y. Kotake, H.M. Swartz, Trapping of free radicals with direct in vivo EPR detection: a comparison of 5,5-dimethyl-1-pyrroline-N-oxide and 5-diethoxyphosphoryl-5-methyl-1-pyrroline-N-oxide as spin traps for $HO\bullet$ and $SO_4^{\bullet-}$, Free Radical Bio. Med. 27(1999) 329-333.

[50] G.D. Fang, J. Gao, D.D. Dionysiou, C. Liu, D.M. Zhou, Activation of persulfate by quinones: Free radical reactions and implication for the degradation of PCBs, Environ. Sci. Technol. 47 (2013) 4605-4611.

[51] Y.F. Huang, Y.H. Huang, Behavioral evidence of the dominant radicals and intermediates involved in Bisphenol A degradation using an efficient Co^{2+}/PMS oxidation process, J. Hazard. Mater. 167(2009) 418-426.

[52] Z. Huang, H. Bao, Y. Yao, W. Lu, W. Chen, Novel green activation processes and mechanism of peroxymonosulfate based on supported cobalt phthalocyanine catalyst, Appl. Catal. B: Environ.154-155 (2014) 36-43.

[53] Y. Wang, H.Q. Sun, H.M. Ang, M.O. Tadé, S.B. Wang, Facile synthesis of hierarchically structured magnetic MnO_2/$ZnFe_2O_4$ hybrid materials and their performance in heterogeneous activation of peroxymonosulfate, ACS Appl. Mater. Interfaces6 (2014) 19914-19923.

[54] T. Hirakawa, Y. Nosaka, Properties of $O_2^{\bullet-}$and $\bullet OH$ formed in TiO_2 aqueous suspensions by photocatalytic reaction and the influence of H_2O_2 and some ions, Langmuir 18 (2002) 3247-3254.

[55] S. Dubey, S. Hemkar, C.L. Khandelwal, P.D. Sharma, Kinetics and mechanism of oxidation of hypophosphorous acid by peroxomonosulphate in acid aqueous medium, Inorg. Chem. Commun.5 (2002) 903-908.

[56] X.B. Wang, Y.L. Qin, LH. Zhu, H.Q. Tang, Nitrogen-Doped Reduced Graphene Oxide as a Bifunctional Material for Removing Bisphenols: Synergistic Effect between Adsorption and Catalysis, Environ. Sci. Technol. 49 2015 6855-6864.

[57] X.Y. Zhang, Y.B. Ding, H.Q. Tang, X.Y. Han, L.H. Zhu, N. Wang, Degradation of bisphenol A by hydrogen peroxide activated with $CuFeO_2$ microparticles as a heterogeneous Fenton-like catalyst: efficiency, stability and mechanism,Chem. Eng. J. 236 (2014) 251-262.

Chapter 5 Perovskite conversion into hierarchical porous ε-MnO₂ via acid treatment: application to the formaldehyde total oxidation

5.1 Introduction

Formaldehyde (HCHO) is one of the major indoor air pollutants, mainly emitting from various building materials and household products such as paints, textiles, adhesives, pressed-wood products (plywood, fiber board and particle board) and other decorating materials [1]. The exposure to HCHO could threaten human health and cause symptoms such as edema, eye and skin irritation, headaches, and nasal tumors [1-3]. Various approaches have been proposed to remove formaldehyde in the air, such as plasma technology [4], adsorption [5,6], heterogeneous catalysis oxidation including photocatalysis [7-9] and thermal oxidation [10,11]. Low temperature - ideally room temperature - catalytic oxidation has been deemed as a promising strategy for the elimination of indoor HCHO owing to its mild control conditions and low energy demand.

Among various classes of catalysts, noble metal-based catalysts (e.g., Pt, Au, Rh, and Pd) are extensively used for air pollutants remediation [12,13], especially as they were reported to oxidize VOCs (e.g., HCHO) totally at relatively low temperatures. For instance, HCHO is efficiently converted into CO_2 at low temperature (below 50 °C, and even at room temperature) over supported noble metals [13,14]. Nevertheless, their current application will be restricted owing to their high cost and the needs to reduce the amount of critical materials of strategic importance such as PGM. However, converting HCHO at low temperature remains challenging with noble metal free catalysts. Most efficient catalysts reported are pure and doped manganese (IV) oxides [13]. Then, HCHO conversion (when calculated from CO_2 production) generally occurs at temperature above 120-150 °C for pure manganese oxide [10,15]. However, even if conversion occurs only above 100 °C, abatement of formaldehyde can be achieved at ambient temperature, due to the adsorption/saturation of the material surface. Therefore,

the search for low-cost and efficient catalysts based on readily available elements has brought supported or unsupported transition metal oxides to the forefront for environmental clean air applications (NO_x decomposition and reduction, oxidization of toxic hydrocarbons, CO and VOCs) [9,13]. Among the available metal oxides, rich chemistry of manganese oxide promote various polymorphs (β-MnO_2, γ-MnO_2, α-Mn_2O_3, γ-Mn_2O_3, α-Mn_3O_4, and Mn_5O_8...) wherein manganese elements can be found with various oxidation states (+II, +III, +IV). Moreover, low volatility and low toxicity of manganese oxide make it promising as a viable noble-free catalytic system. In order to reduce the performance gap between noble metals and transition metal oxides, the improvement of textural properties (surface area, pore shape/size/orientation) requests the use of sophisticated procedures involving time and energy consuming template removal processes [16]. To our knowledge, ε-MnO_2 phase with hierarchical porosity was only obtained by electrodeposition of nanostructured manganese oxides on bubble-covered Ni foam used as host support [17]. In consequence, ε-MnO_2 solids were rarely reported for catalysis [18,19]. In our work, we took advantage of the acid etching process developed earlier [20-22] by using perovskite as ε-MnO_2 precursor. Acid etching is a soft chemical method commonly used to modify the structure of materials [23-27], improving their catalytic activity [20-22, 28-31] or some functions like their conductivity [32]. Herein, we propose the first application of a template-free hierarchical ε-MnO_2 catalyst for HCHO oxidation at low temperature. A facile one-step approach was developed to form *in situ* a series of high surface area perovskites with A-site (La) deficiency, MnO_2/perovskite and pure ε-MnO_2 materials with hierarchical porosity by adjusting acid treatment conditions. Successful perovskite conversion mechanism was unveiled for the first time.

5.2 Experimental section

5.2.1 Synthesis of catalysts

LaMnO$_{3.15}$ was prepared following a conventional citric acid complexation method starting from the metal nitrate precursors Mn(NO$_3$)$_2$·xH$_2$O (98.0%, Aldrich) and La(NO$_3$)$_3$·6H$_2$O ($\geq$ 99.0%, Sigma-Aldrich), and citric acid (+99.5% , Alfa Aesar). For the synthesis, a molar ratio (n$_{Mn}$ + n$_{La}$)/n$_{citric\ acid}$ of 1 was applied. 3.7 g of manganese nitrate and 7.0 g lanthanum nitrate were dissolved in 40 mL of distilled water. In a second beaker 6.9 g of citric acid were dissolved in 40 mL of distilled water, and the resulting clear solution was added drop-wise to the solution containing the metal precursors under magnetic stirring. The resulting homogeneous solution was stirred for 1 h at 40 °C, and overnight at room temperature. A rotary evaporation step was used to remove the excess of water, resulting in a gel. The obtained gel was thermally treated in a muffle oven under air over two steps: 180 °C for 1h (3 °C/min), and 700 °C for 8h (2 °C/min). During the acid treatment step, 1.0 g of LaMnO$_{3.15}$ (LMO) was added to 250mL of a 3M nitric acid (65~70%, Alfa Aesar) solution and stirred at 200 rpm. At selected time intervals of 10 min, 60 min, 180 min, 240 min, 360 min, 14 hours, and 22 hours, the solid was filtered on a 0.2 μm PTFE membrane filter (Whatman^{TM}), washed with deionized water and dried in the oven at 60 °C for 24h. The as-obtained samples were labeled LM-10, LM-60, LM-180, LM-240, LM-360, LM-14h and LM-22h, respectively.

5.2.2 Catalytic oxidation of formaldehyde (HCHO)

The catalytic oxidation of formaldehyde (HCHO) was carried out in a fixed bed reactor (internal diameter = 8 mm), loaded with 0.20 g of the catalyst (Fig. 5-1). Catalyst activation was performed *in situ* at 300 °C for 1h under 20 vol% O$_2$/He, with a flow rate of 100 mL·min^{-1}. Gaseous formaldehyde was produced from paraformaldehyde in

a permeation tube placed in a permeation chamber (Dynacalibrator, VICI Metronics, Inc.), which was kept at a constant temperature of 100 °C. The reacting gas containing 100 ppm of HCHO mixed with the carrier gas 20 vol% O_2/He was stabilized at 300 °C for another 1h. Afterwards, the reacting gas was sent toward the fixed bed reactor and its temperature was controlled following a decreasing rate of 0.5 °C/min from 300 °C to 100 °C, an a rate of 0.2 °C/min in the range of 100~25 °C. The total flow rate was 100 mL min^{-1}, corresponding to a gas hourly space velocity (GHSV) of 30 000 mL g_{cat}^{-1} h^{-1}. The effluent gas was monitored online by a gas chromatograph (GC, Varian) equipped with a thermal conductivity detector. Separations were performed using two columns: one CP-Sil 5 CB column channel (8 m) for HCHO analysis, and one COX column channel (1 m) for CO_2 analysis.
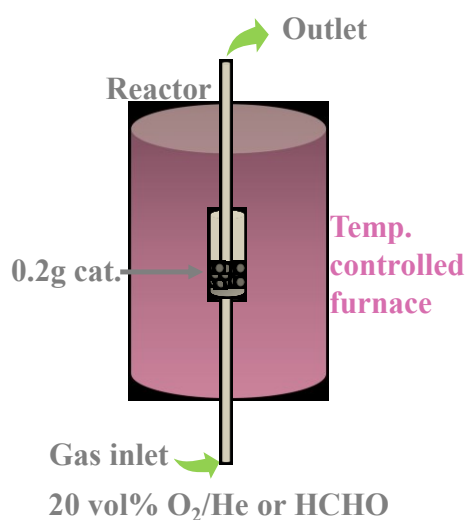
Figure 5-1 Schematic diagram of the experimental set-up

The formaldehyde (HCHO) oxidation into CO_2 was expressed as HCHO conversion, while HCHO elimination refers to the removal efficiency of HCHO. They were calculated using the following equations, respectively:

$$\text{HCHO conversion (into } CO_2\text{) (\%)} = \frac{[CO_2]_t}{[HCHO]_0} \times 100 \qquad (5\text{-}1)$$

$$\text{HCHO elimination (\%)} = \frac{[HCHO]_0 - [HCHO]_t}{[HCHO]_0} \times 100 \qquad (5\text{-}2)$$

Where [HCHO]$_t$ and [CO$_2$]$_t$ are assigned to the concentration at time t as monitored by GC, and [HCHO]$_0$ is the initial HCHO concentration (100 ppm).

During the stability test, a fresh catalyst was first activated as indicated before (300 °C, 1h under 20 vol% O$_2$/He, 100 mL min^{-1}). Then the reacting gas (100 ppm HCHO in 20 vol% O$_2$/He, 100 mL min^{-1}) was passed through the catalyst bed at 99 °C (based on LM-22h T50 results) for at least 55h.

5.2.3 Characterization

X-ray diffraction patterns (XRD) were collected on a Bruker D8 Advanced AXS diffractometer equipped with Cu K$_{\alpha 1}$ monochromatic radiation source (λ = 1.5418 Å) and operated at 40 kV and 30 mA. X-ray diagrams were recorded within the 10°-80° region with a 0.02° step size (step time = 1s). Nitrogen sorption measurements were performed at 77K on a Micromeritics Flow Sorb III serial 416 apparatus. Samples were degassed at 423K during 6h prior analysis. Specific surface area (S_{BET}) was calculated according to the Brunauer-Emmett-Teller (BET) method. Additional N$_2$-physisorption isotherms were recorded at -196 °C on a gas sorption system Tristar II Plus from Micromeritics. Before analysis, the samples were outgassed under dynamic vacuum at 423K for 6h. The textural properties were determined from the adsorption/desorption isotherms by using the MicroActiveTristar II Plus software version 2.03. The BET surface area was determined using the multipoint BET algorithm in the P/P$_0$ range of 0.10-0.25. Average pore diameter (D_{pore}) was determined by the Barrett-Joyner-Halenda (BJH) equation on the desorption branch.

The Fourier transformed infrared spectra (FTIR) were recorded over the 4000-400 cm^{-1} range on a Thermo Scientific Nicolet iS50 FTIR spectrophotometer. Morphological properties and related punctual atomic composition of the samples were observed by transmission electron microscopy (TEM Jeol 2100 plus) operated at 200

kV and equipped with a LaB$_6$ crystal, and a field-emission scanning electron microscope (SEM-FEG Hitachi SU-70) with an EDS microanalysis (EDAX Genesis). X-ray Photoelectron Spectroscopy (XPS) was performed on a AXIS Ultra^{DLD} spectrometer (Kratos Analytical) with a monochromatic Al Kα X-ray source (1486.6 eV). High resolution spectra were collected with a constant pass energy (PE = 20 eV) and the binding energy was calibrated with the adventitious C1s (284.8 eV). Quantification and spectral decomposition were processed using CasaXPS software.

Temperature programmed reductions (TPR) were carried out on 60 mg of sample under 5 vol% H$_2$/Ar gas flow (50 mL/min) with a heating rate of 10 °C/min up to 1000 °C using a Micromeritics Autochem II 2920 apparatus. Stoichiometry of La and Mn in the solids and in the filtrates (following the acid washing process) were monitored by inductively coupled plasma-optical emission spectroscopy (ICP-OES) (Agilent Technologies 700 Series spectrometer). Before elemental analysis, the solids were dissolved in a concentrated HCl/HNO$_3$ mixture.

5.3 Results and Discussion
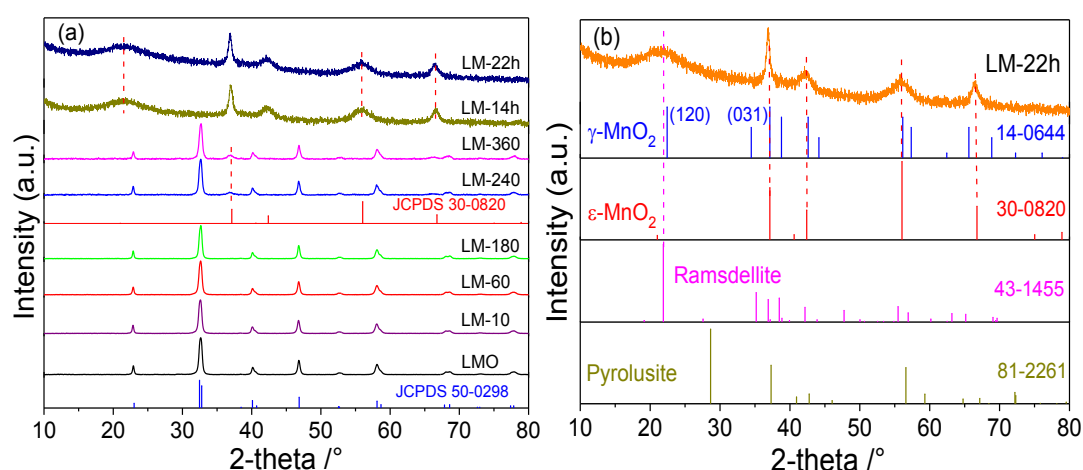
5.3.1 Crystal phase structure

Figure 5-2 Wide-angle XRD patterns of (a) acid treated samples, (b) XRD pattern of LM-22h in comparison with the standard XRD patterns

In order to link the perovskite structure dissolution with time under acid treatment,

XRD patterns of LaMnO$_{3.15}$ (LMO) solids treated with different durations (from 10 min to 22h) have been recorded. As depicted in Fig. 5-2a, below 180 min of acid treatment all diffraction peaks can be indexed by a rhombohedral lattice of pure LMO perovskite (JCPDS No. 50-0298) [33]. This indicates that, up to 180 min, the native perovskite is structurally unchanged. The average crystallite size of raw LMO and LMO treated for 10 min, 60 min, and 180 min present similar values of 25.4 nm, 25.1 nm, 24.6 nm and 27.4 nm respectively, according to the Scherrer equation applied to the (024) plane (2θ = 46.9°). The Scherrer equation is not applied to main (110) and (104) planes (2θ = 32.5° and 32.8°) because their resulting diffraction peaks were confounded into one large peak. Now, the application of the acid treatment for more than 240 minutes gave rise to a new diffraction peak at 2θ = 37.1°. This peak becomes more noticeable after 360 min. Interestingly, the average crystallite sizes of the LMO phase decreases to 17.8 nm and 17.1 nm after 240 min and 360 min, respectively. After 14h, the perovskite phase completely disappears to the profit of a new crystalline phase. In the previous work of Si *et al*. [20], they reported that the acid etching of a 3D ordered macroporous (3DOM) LMO perovskite led to the formation of a ε-MnO$_2$ phase (JCPDS No. 14-0644). In our case, different features are clearly obtained when etching is performed under our conditions (Fig. 5-2b). Albeit some diffraction peaks (2θ = 21.9°, 37.1°, 40.5°, and 56.0°) can be indexed by a ε-MnO$_2$ phase already found by Si *et al*., the other peaks are missing from the XRD patterns of LM-14h and LM-22h. In literature, De Wolff *et al*. suggested that the γ-MnO$_2$ structure was built from microscopic intergrowths of ramsdellite and pyrolusite (β-MnO$_2$) phases, forming an alternation of (1×2) and (1×1) tunnels [34,35]. One model was further proposed by Chabre and Pannetier [36], which allowed a successful correlation between structural features and surface properties. In this model, the degree of intergrowth (called the De Wolff disorder) could be quantified

by the shift of the (120) line [36]. In addition, a second type of growth defect in the ramsdellite lattice, named microtwinning (Tw), was assumed and used to amend the (120) line shift [37]. According to the above model, the X-ray diffraction patterns of LM-14h and LM-22h exhibit only two broad and symmetrical reflexions in the range $54° < 2\theta < 71°$ (see Fig. 5-1a the two red dotted lines at high 2θ domain), which are comparable to the XRD patterns of manganese dioxide prepared electrochemically (EMDs) [17-19,38]. Additionally, the absence of the diffraction peak indexed (031) further indicates that LM-14h and LM-22h sample structures belong unambiguously to ε-MnO_2 phase (JCPDS No. 30-0820) [36]. As highlighted in Fig. 5-2b, all diffraction peaks in the sample LM-22h can be indexed by the ε-MnO_2 phase reference. The large shoulder above $2\theta = 21.9°$ could be attributed to the presence of highly charged Mn^{4+} cations located in antiphase domain boundaries, causing a local lattice expansion by electrostatic repulsion [38]. Hence, we report here for the first time a ε-MnO_2 phase obtained from a pure LMO perovskite using a simple acid treatment method.

5.3.2 Textural properties

The N_2 adsorption/desorption isotherms and subsequent pore size distribution profiles of the solid series are presented in Fig. 5-3. The related textural properties are summarized in Table 5-1.

Table 5-1 Textural and structural properties of the raw and acid treated LMO samples

Sample	S_{BET} (m²/g)	Crystalline phase[a]	V_{pore} (cm³/g)	D_{pore} (nm)
LMO	18	LMO	0.10	21.8
LM-10	23	LMO	0.07	23.2
LM-60	37	LMO	0.12	11.1
LM-180	49	LMO	0.16	13.3
LM-240	147	LMO/ε-MnO_2	0.31	6.7
LM-360	178	LMO/ε-MnO_2	0.36	6.9
LM-14h	193	ε-MnO_2	0.71	13.8
LM-22h	181	ε-MnO_2	0.73	19.0

[a]Crystalline phases identified by X-ray diffraction

As depicted in Fig. 5-3, pure LMO exhibits a type II isotherm as highlighted by

the mono-multilayer adsorption profile and the weak slope obtained in the BET linear domain, corroborating with the formation of a non porous-macroporous perovskite material. Derived LM-10, LM-60 and LM-180 acid treated samples display a similar isotherm profile with additional H4 or H3 hysteresis loop, revealing a type II-type IV composite isotherm with a weak adsorption step due to capillary condensation at relative pressures (P/P_0) $\sim$ 0.5-0.9 and $\sim$ 0.9-1.0, suggesting the formation of some mesoporosity within the sample (Fig. 5-3a). Progressive formation of a steep adsorption step accompanied with a large hysteresis loop is occuring in the materials LM-240 and LM-360, with well-distributed pore diameters around 7 nm. In parallel, the lower average pore diameter determined on the desorption branch and the twofold increase of the total pore volume (Table 5-1) all point toward the generation of small mesopores on LM-240 and LM-360. These latter features coincide with the presence of the first traces of ε-MnO$_2$ obtained by XRD, thus reasonably suggesting that the self-ordering of ε-MnO$_2$ nanocrystals leads to the formation of a tailored intercrystalline mesoporosity. From 14h of acid treatment, it can be noticed that the obtained ε-MnO$_2$ materials (LM-14h and LM-22h) display a predominant type IV isotherm with H3 hysteresis loop and a strong perturbation at high relative pressure with the absence of plateau, revealing the formation of a hierarchical meso/macro-porous ε-MnO$_2$ material (Fig. 5-3a). As shown in Fig. 5-3b, the pore diameter distribution becomes wider and moves toward larger pore sizes. To conclude, acid treatment led to the formation of intercrystalline mesoporosity which evolves due to the further growth of the ε-MnO$_2$ crystals.
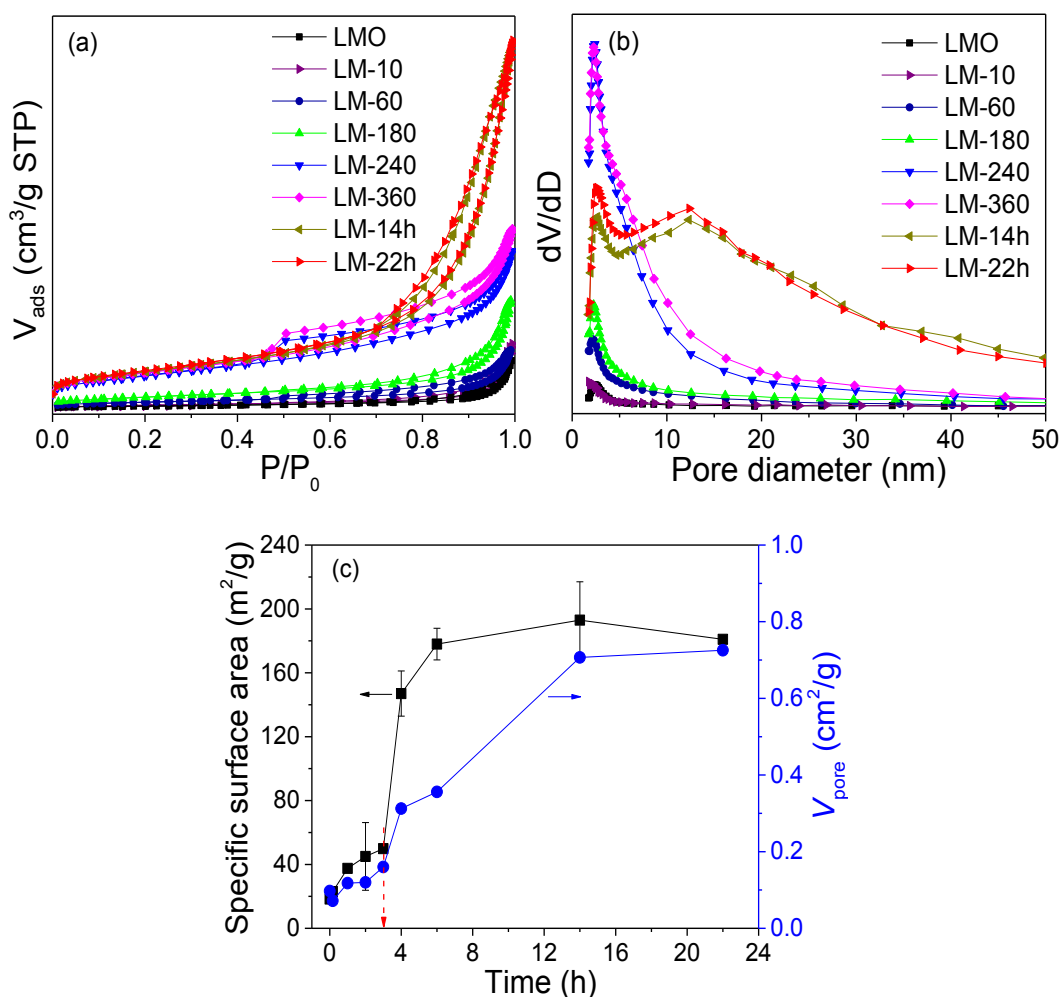
Figure 5-3 (a) N_2 physisorption isotherms and (b) pore-size distributions of the raw and acid treated samples, (c) The change of specific surface area and the total pore volume with reaction time of acid treatment (error bar calculated from two independent experiments)

To demonstrate the impact of the acid treatment on the resulting textural properties, the BET surface area and the total pore volume were correlated to the acid treatment duration in Fig. 5-3c. As expected, the surface area of pure LMO perovskite obtained by the conventional "citrate" complexation route is only 18 m^2/g, typical of native LMO perovskites [33]. BET surface area of samples increased significantly upon acid treatment time. Before 180 min, the BET surface area of the samples progressively increased and reached a value of 49 m^2/g with a total pore volume of 0.16 cm^3/g (Table 5-1). After 240 min, a sharp increase of the BET surface area is observed, from 49 m^2/g to 147 m^2/g, which is corroborated with the formation of ε-MnO_2 nanosheets as earlier

indicated by the XRD patterns. Finally, extending the acid treatment time to 14h and 22h boosts the BET surface areas of the resulting ε-MnO_2 materials up to 180 m^2/g (Fig. 5-3c) with total pore volumes exceeding 0.70 cm^3/g (Table 5-1). Hence, we demonstrate a clear correlation between acid treatment time and textural properties of the materials. LMO physical properties can be modified, and controlled to some extent, by applying a judicious time of acid treatment.

5.3.3 Morphology (TEM and SEM)

Surface morphologies (including elemental analysis) of LMO perovskite particles and their acid-treated counterparts were directly visualized by TEM/EDS (Fig. 5-4) and SEM (Fig. 5-5) analyses. As shown in Fig. 5-4a, the raw LMO perovskite is composed of agglomerated small particles with size ranging from 20 to 50 nm, that could form intercrystalline mesopores (Fig. 5-6a,b) in a macroporous network (Fig. 5-7a,b). The energy dispersive spectrometry (EDS01) (inset of Fig. 4a) indicated that these raw particles are La-enriched (Table 5-2) which is typically observed on native perovskites [39]. From the high-resolution TEM (HRTEM) in Fig. 5-4b, d-spacing values of 0.28 nm and 0.39 nm can be indexed by the (110) and (012) planes ($d_{(110)}$ = 0.276 nm and $d_{(012)}$ = 0.386 nm) of raw LMO.

Table 5-2 EDS results as indicated in Figure 5-4

elements / atomic ratio	La (%)	Mn (%)	O (%)	La/Mn
EDS01	20.7	15.1	64.2	1.37
EDS02	18.0	17.9	64.1	1.01
EDS03	1.0	27.6	71.4	0.04
EDS04	-	32.3	67.7	-
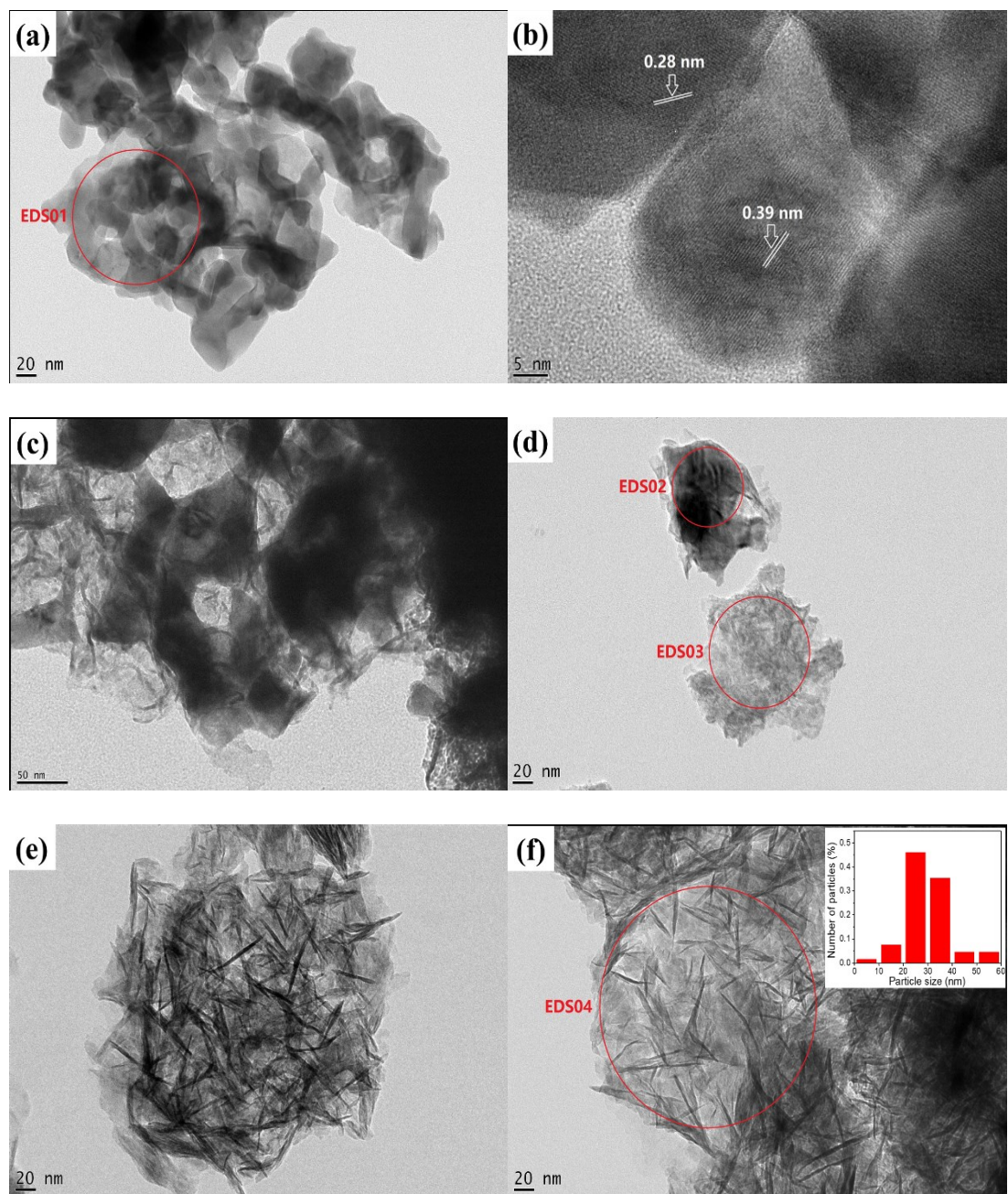
Figure 5-4 TEM images and EDS elemental mapping (insets) of (a and b) LMO, (c) LM-180, (d) LM-240, (e and f) LM-22h
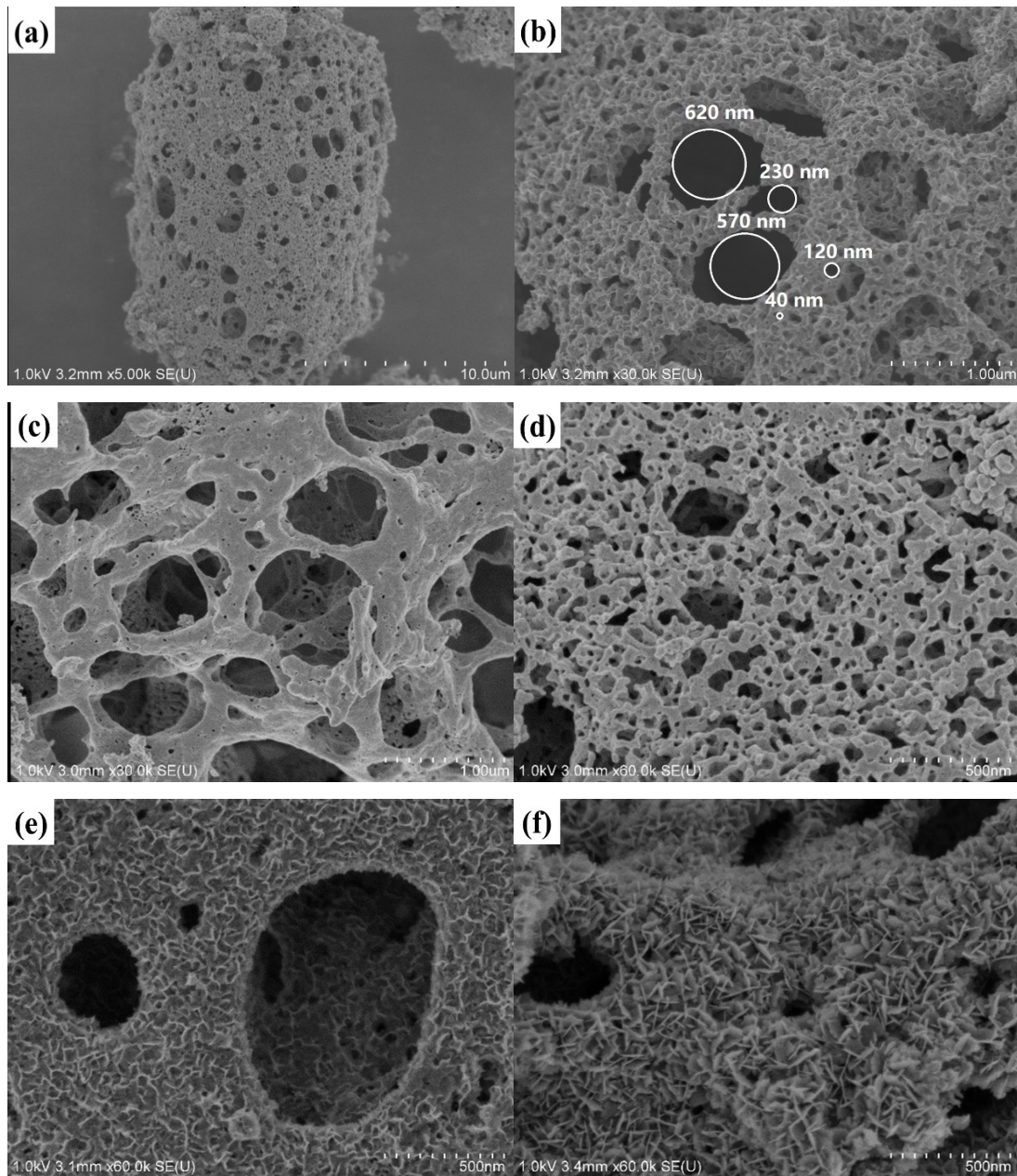
Figure 5-5 SEM images of (a and b) LM-180, (c-e) LM-240, (f) LM-22h
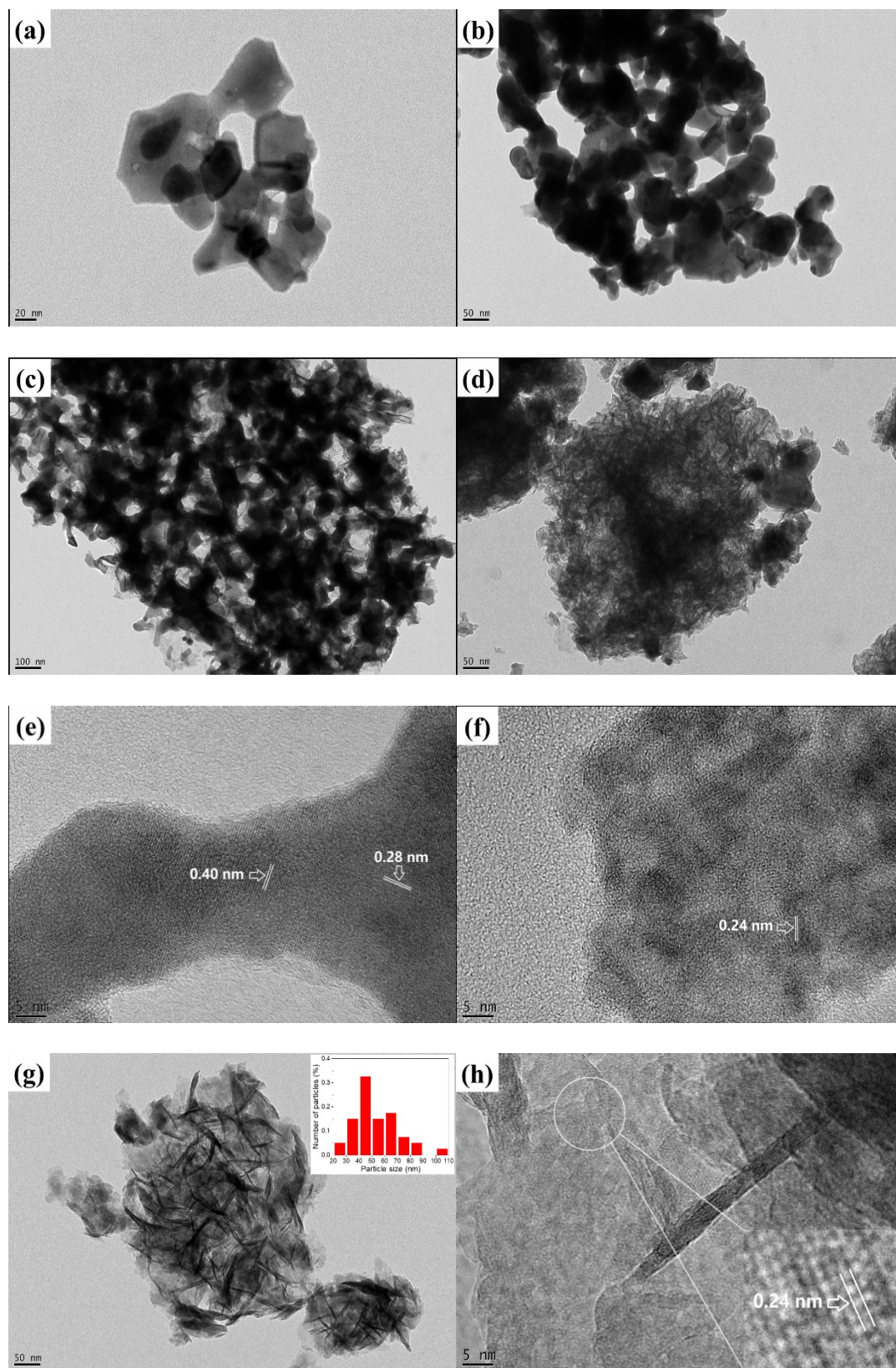
Figure 5-6 TEM images of the acid treated samples: (a and b) LMO, (c) LM-180, (d-f) LM-240, (g and h) LM-22h
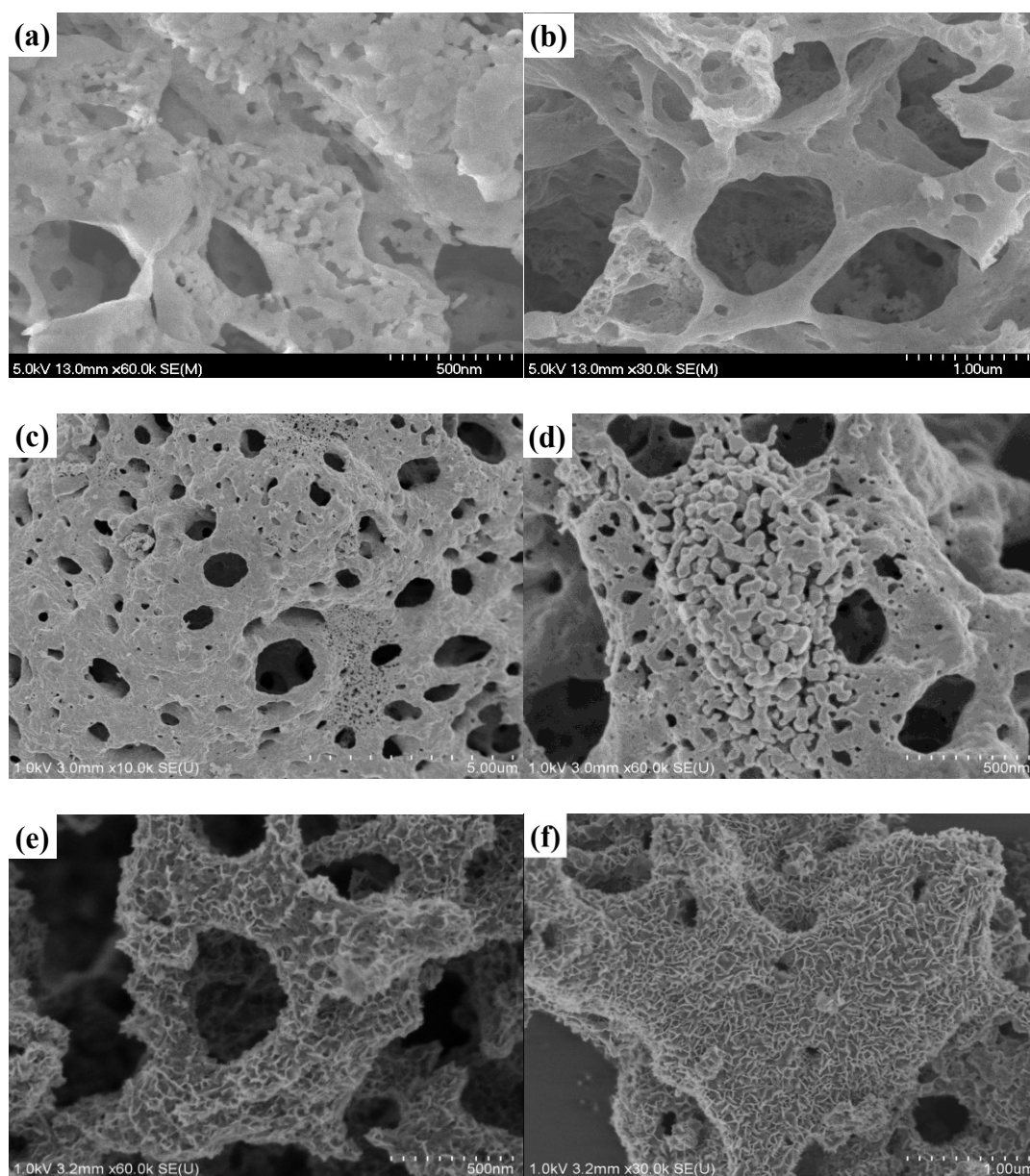
Figure 5-7 SEM images of as-made LMO (a and b), and the acid treated samples: LM-240 (c-e) and LM-22h (f)

After 180 min of acid treatment, a mixture of two particle morphologies is observed: smooth and visible particles comparable to the initial perovskite particles, and filiform solids at their surface (Fig. 5-4c and 5-6c). This observation is coherent with the textural characterization, showing an overall increase of both BET surface area

and total pore volume. Between LM-180 and LM-240, few differences can be seen at low magnitude (Fig. 5-5(a-d)). Both samples are composed of macrostructures exhibiting a disordered yet interconnected meso/macro-porous network (Fig. 5-5a and 5c) and generally made of aggregated particles of LMO perovskite (Fig. 5-5b and 5d, Fig. 5-S2c and S2d). However, their rough surface (Fig. 5-5a,b) was smoothened (Fig. 5-5c,d) under acid etching. Moreover, additional features can be further observed on several regions in LM-240, with their surface presenting a filiform morphology (Fig. 5-5e, S1d and S2e). Correlated to ε-MnO_2 detection by XRD, EDS (Fig. 5-4d) clearly demonstrates that the filiform morphology can be attributed to almost pure manganese oxide particles (EDS03, La/Mn=0.04) (Table 5-2), while the smooth particles present the elemental composition of raw LMO perovskite (EDS02, La/Mn=1.01) (Table 5-2). Finally, different lattice fringes can be measured by HRTEM on LM-240. In Fig. 5-S1e, the presence of residual LMO perovskite phase ($d_{(110)}$=0.276 nm and $d_{(012)}$=0.386 nm) was confirmed. A d-spacing value of 0.40 nm is observed which can be indexed to (012) plane of raw LMO (d_{LMO} (012) = 0.386 nm), or to plane of ε-MnO_2 (d = 0.42 nm, JCPDS PDF# 30-0820), or (101) plane of ramsdellite (d(101) = 0.405 nm, JCPDS PDF# 43-1455). Additionally, d-spacing value of 0.24 nm (Fig. 5-S2f) can be indexed by the (100) plane of ε-MnO_2 ($d_{(100)}$=0.242 nm) [38]. These results support the formation of mixed macro/meso-porous LMO/ε-MnO_2 material (LM-240) as deduced from XRD analysis (Fig. 5-2).

After 22h, LMO perovskite particles are completely converted into nanosheets of ε-MnO_2 (Fig. 5-4e, 5f, 7f) presenting a desert rose morphology. Those intergrown nanosheets present a length size comprised between 20 and 90 nm (average: 41.5 nm) as indicated by the particle size distribution (inserts in Fig. 5-4f and 6g), and average thickness of 3.8 nm. The macrostructure still retains pores ranging from the mesopore

to the macropore domains, which is coherent with N_2 physisorption isotherms. Sole ε-MnO_2 presence is comforted by HRTEM (Fig. 5-6h) where only one lattice fringe is observed with a *d*-spacing value of 0.24 nm, indexed by its (100) plane. Moreover, the EDS analysis (EDS04, insert in Fig. 5-4f) confirms that the nanosheets are exempt from lanthanum (Table 5-2). Those datas are consistent with XRD. From these above considerations, the combination of TEM and SEM allowed us to visualize a morphological transformation happening during the acid treatment, from smooth and aggregated particles of LMO perovskite to intergrown nanosheets of ε-MnO_2. Absence of lanthanum was confirmed by EDS in LM-22h. However, the large macrostructure seems barely affected by this conversion, advocating for a pseudomorphic transformation process which will be discussed after.

5.3.4 ICP and XPS analysis

Surface composition and surface chemical states were evaluated by X-ray photoemission spectroscopy (XPS). The quantitative elemental compositions including atomic concentration of La $3d_{5/2}$ and Mn $2p_{3/2}$, and atomic ratio of La/Mn and Mn^{4+}/Mn^{3+} are summarized on Table 5-3. The N 1s XPS peaks were also recorded and show similar, low trace of nitrogen species at the XPS limit detection in all samples (not shown here).
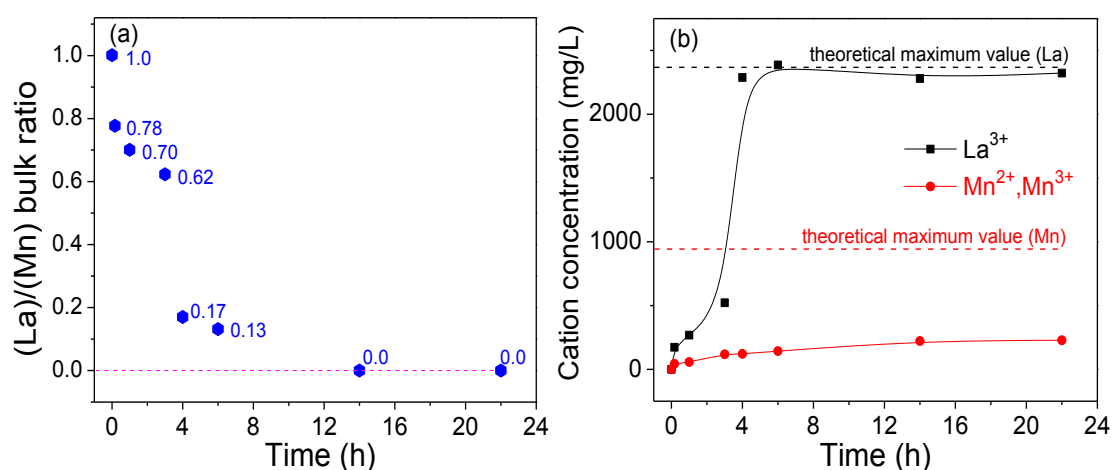
Figure 5-8 Evolutions of (a) La/Mn cation ratio in bulk samples and (b) the cations (La and Mn) dissolution in filtrate with reaction time according to the ICP analysis

First, the surface La/Mn atomic ratio as given by XPS for raw LMO perovskite (La/Mn=1.27) is higher than the bulk value (La/Mn=1.00) obtained by ICP (Fig. 5-8a), which is comparable to the theoretical value of LMO perovskite (La/Mn=1). This higher atomic ratio is in agreement with the reported A-site enrichment at the surface of raw LMO perovskite. According to ICP and XPS (Table 5-3), both bulk and surface La/Mn atomic ratios decrease with increasing the acid treatment duration. Notably, the decreasing rate of La/Mn atomic ratio in the bulk (ICP) was slower than at the surface (XPS), which might indicate that the acid etching is an outside-inward process. This observation further supports a pseudomorphic transformation process.

Now, in order to investigate the dissolution process, we studied the cation concentrations within the acidic filtered liquor at various treatment times by ICP (Fig. 5-8b). As illustrated, La^{3+} species gradually increased and almost reached the maximal theoretical value after 360 min. This trend is consistent with XPS (Fig. 5-9), showing a gradual decrease of the La 3d peaks intensity. In contrast, the Mn^{2+} concentration increased slowly and was nearly stable after 14h, corresponding to a loss of about 25% of the Mn from the raw LMO perovskite (Fig. 5-8b). These results directly confirm that the composition of the materials changes from La-rich to Mn-rich surface, with almost pure ε-MnO_2 materials obtained after 14h.

XPS spectra in the Mn 2p region can be observed in Fig. 5-10. The asymetrical main Mn $2p_{3/2}$ peak shows the presence of both Mn^{3+} and Mn^{4+}, which present a multiplet splitting [40]. That is why the decomposition of Mn $2p_{3/2}$ was obtained based on reference spectra of Mn_2O_3 and MnO_2 powder samples with binding energies at 641.6 and 642.2 eV, respectively [41]. For the raw LMO, the surface Mn^{4+}/Mn^{3+} atomic

ratio is about 0.28. After acid treatment, as indicated in Table 5-3, the Mn^{4+}/Mn^{3+} atomic ratio increased gradually with the decreasing La/Mn atomic ratio. This result can be attributed to the dismutation reaction of dissolved Mn^{3+}, which will be discussed in the following part. This reaction seems to proceed slowly and the Mn^{4+}/Mn^{3+} atomic ratio reached 1.71 after 22h of acid treatment (Table 5-3), confirming the increased presence of Mn^{4+} species which may also promote the stabilisation of surface oxygen vacancies [27].

Table 5-3 Relative surface abundances of the elements constituting the rawand acid treated LMO samples

Sample	La/Mn atomic ratio		La 3d$_{5/2}$	Mn 2p$_{3/2}$	Mn^{4+}/Mn^{3+}
	ICP	XPS	at.%	at.%	
LMO	1.00	1.27	21.7	17.1	0.28
LM-10	0.78	0.79	12.6	16.0	0.32
LM-60	0.70	0.65	13.9	21.5	0.72
LM-180	0.62	0.35	8.9	24.7	0.87
LM-240	0.17	0.12	3.5	29.3	1.09
LM-360	0.13	0.07	2.0	28.9	1.28
LM-14h	0	0.003	0.1	33.7	2.00
LM-22h	0	0.005	0.2	33.0	1.71
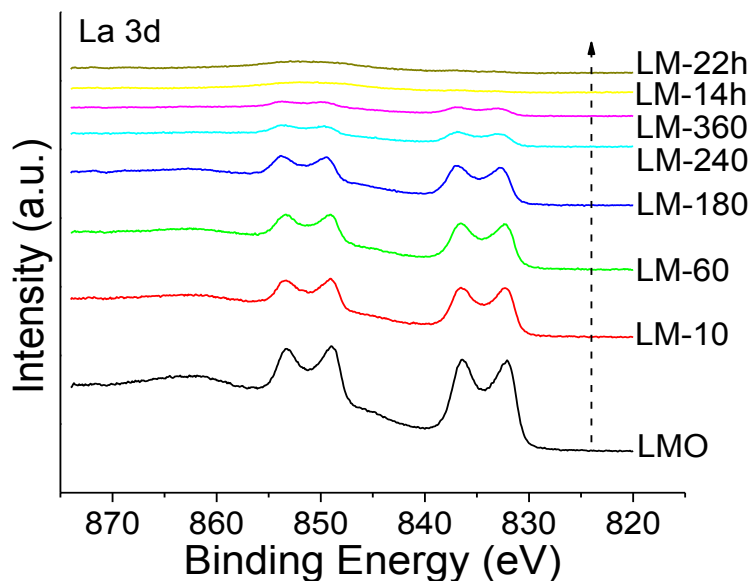
Figure 5-9 Typical XPS spectra La 3d of the raw and acid treated samples
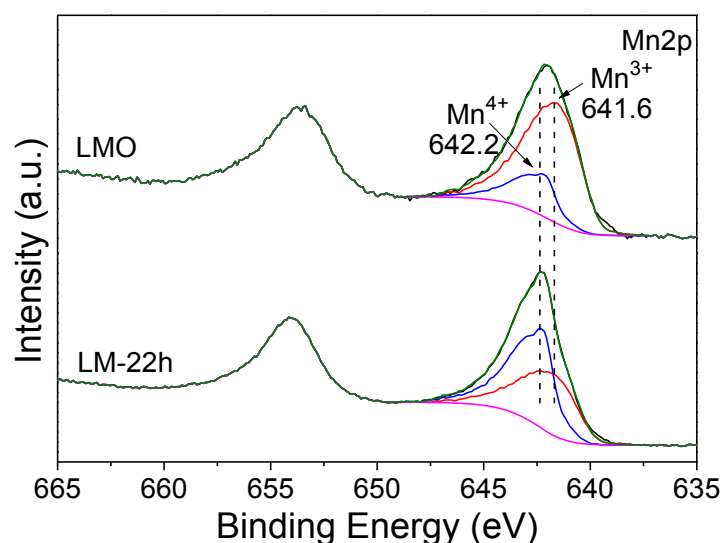
Figure 5-10 Typical XPS spectra of Mn 2p of the acid treated samples: cases of LMO and LM-22h

5.3.5 Tentative mechanismof perovskite conversion toward ε-MnO$_2$

Owing to the different characterization techniques used, we unveiled the conversion process of the LMO perovskite toward the ε-MnO$_2$ phase in the presence of 3M nitric acid. The La^{3+} species are completely dissolved from the perovskite structure, as proven by EDS (Fig. 5-4f), ICP (Fig. 5-8) and XPS (Table 5-3). We also observe by ICP (Fig. 5-8b) a partial dissolution of the manganese species, up to 25% of the theoretical maximum value. Meanwhile, the Mn^{4+}/Mn^{3+} molar ratio gradually increases overtime within the solids (XPS, Table 5-3). Regarding the literature, the acid digestion of Mn$_2$O$_3$ ores to produceε-MnO$_2$ was extensively studied for batteries application. While Mn^{4+} presents a low solubility, and thus is likely to remain as MnO$_6$ building blocks, Mn^{3+} has a consequent solubility at room temperature and high acid concentration [35]. Moreover, under acidic conditions Mn^{3+} is highly sensitive to dismutation-precipitation reactions. Thus Mn^{3+} ions in solution will dismute into Mn^{2+}

and Mn^{4+} following the overall reaction (5-3):

$$Mn_2O_3 + 2H^+ \leftrightarrow MnO_2 + Mn^{2+} + H_2O \qquad (5\text{-}3)$$
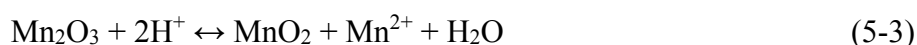
This reaction is highly products-favoured [35], and explains both the presence of manganese in solution as Mn^{2+}, which is highly soluble [35], and the increase of the Mn^{4+}/Mn^{3+} molar ratio. Furthermore, as (1) is highly products-favoured, we can assume that the mobility of the dissolved Mn^{3+} species during the process is low. This implies that Mn^{4+} ions are formed at the vicinity of the solid particles and precipitate back to assemble with the MnO_6 building blocks. The MnO_6 aggregations may grow in size by the continuous supply of MnO_6 units and in an oriented fashion, generating ε-MnO_2 nanosheets, while the presence of Mn^{3+} species generate microstructural defaults *via* the condensation of hydroxylated $[Mn(OH_2)_5(OH)]^{2+}$ species [35]. We assume that those microstructural defaults are responsible for the ε-MnO_2 structure [36]. This implies that, if a LMO perovskite sample was soaked for a sufficient time under strong acidic conditions, pure ε-MnO_2 should be obtained. Finally, as the macrostructure seems preserved and enlarged during the total conversion of LMO perovskite particles into ε-MnO_2 nanosheets (SEM, Fig. 5-5f), a pseudomorphic transformation mechanism has been tentatively proposed as illustrated in Fig. 5-11. This mechanism, reported in the case of metal-organic frameworks [42], zeolites [43], and alumina [44], is based on a subtile equilibrium between dissolution and recrystallization kinetics which we clearly observed under our experimental conditions.
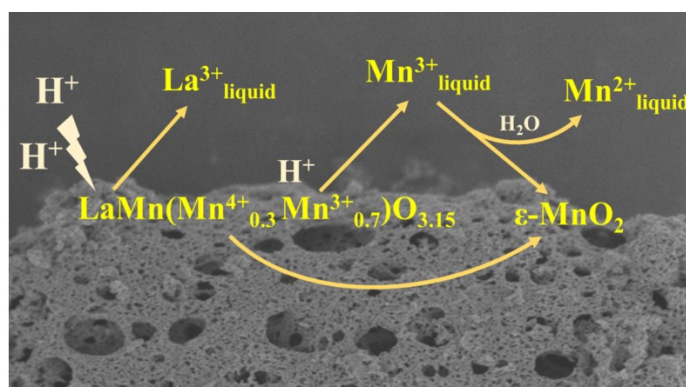
Figure 5-11 A mechanism of pseudomorphic transformation from LMO into ε-MnO$_2$

5.3.6 Reducibility studies

Temperature programmed reduction (TPR) of H$_2$ was conducted to examine the reducibility of the material series characterized above, which should be closely related to their catalytic performance. The H$_2$-TPR profiles of the prepared samples are presented in Fig. 5-12, and their quantitative analysis data are listed in Table 5-4. For the pure LMO, the main peak is centered at 371°C, with a shoulder at 430°C which can be assigned to the reduction of Mn^{4+} to Mn^{3+} and the reduction of some Mn^{3+} located in a coordination-unsaturated microenvironment into Mn^{2+}, respectively [45,46]. Moreover, the weak peak at 270°C is most likely due to the removal of over-stoichiometric oxygen accommodated within the lattice and oxygen adsorbed species (adspecies), which are weakly bounded [27,46,47]. The intense peak in the range of 600-900°C corresponds to the reduction of the remaining Mn^{3+} to Mn^{2+}. Theoretically, if all of the manganese ions in LMO perovskite (Mn^{3+} and Mn^{4+}) were reduced to Mn^{2+}, the H$_2$ consumption of LaMnO$_{3.15}$ should be 2.70 mmol/g. As shown in Table 5-4, the calculated total H$_2$ consumption of the raw LMO is 2.66 mmol/g, which is close to the theoretical value. During the initial step of acid treatment (10 to 180 min), the main peak at 371°C shifts toward lower temperatures, which can be attributed to a facilitated reduction of Mn^{4+} owing to the formation of a meso/macro-porous network [46]. Meanwhile, the intensity of the peak at 270°C increased gradually, which means that the acid treatment increases the total amount of oxygen species accommodated within the lattice. The peak at 430°C fades away, which may be due to the loss by dissolution and/or dismutation of Mn^{3+}. In addition, the H$_2$ consumption in the range of 200-500°C increased gradually with a H$_2$-uptake of 1.56, 1.73, 1.90 and 1.93 mmol/g for samples LMO, LM-10, LM-60 and LM-180, respectively (Table 5-4). This is correlated to the

increase of the Mn^{4+}/Mn^{3+} atomic ratio, as observed by XPS. Furthermore, the samples LM-240 and LM-360 exhibited similar TPR curves with only two reduction temperatures at 302/309°C and 410°C, which can be reasonably attributed to the two reduction steps of manganese oxide: $Mn^{4+} \rightarrow Mn^{3+}$ and $Mn^{3+} \rightarrow Mn^{2+}$ [20]. As shown by XRD, these two samples were mixtures of LMO perovskite and manganese oxide, which is supported here by observing a small peak at 783°C with a H_2-uptake of 0.40 (LM-240) and 0.29 (LM-360) mmol/g. This peak is ascribed to the reduction of Mn^{3+} in acid-treated LMO phase, which appears earlier than that of raw LMO (818°C).

Finally, no reduction peak over 600°C was observed in samples LM-14h and LM-22h, demonstrating the formation of pure MnO_2. The position of the main peak at 297°C (LM-14h) and 294°C (LM-22h) were the lowest among all samples, further suggesting that they present low-temperature reducibility and high oxygen mobility [20], which should have a positive effect over their catalytic performance for organic combustion. As calculated from the H_2-TPR profiles, by means of the acid treatment, the H_2 consumption at low temperature (200-500°C), as well as the total H_2 consumption of materials increased gradually, and a drastic boost was found after 240 min of acid treatment (Table 5-4). This indicates that the average valence of Mn cations increased significantly, as proven by XPS data (Table 5-3).

Table 5-4 H_2 consumption deduced from the H_2-TPR for the raw and acid treated LMO samples

Materials	T reduction peaks (°C)		H_2 consumption (mmol/g)		
	Low T (200-500°C)	High T (500-900°C)	Low T (200-500°C)	High T (500-900°C)	Total
LMO	371	818	1.56	1.10	2.66
LM-10	354	816	1.73	1.07	2.80
LM-60	348	805	1.90	0.98	2.88
LM-180	354	843	1.93	1.19	3.12
LM-240	302	783	6.46	0.40	6.86

LM-360	309	783	6.76	0.29	7.05
LM-14h	297	-	8.98	-	8.98
LM-22h	294	-	7.99	-	7.99
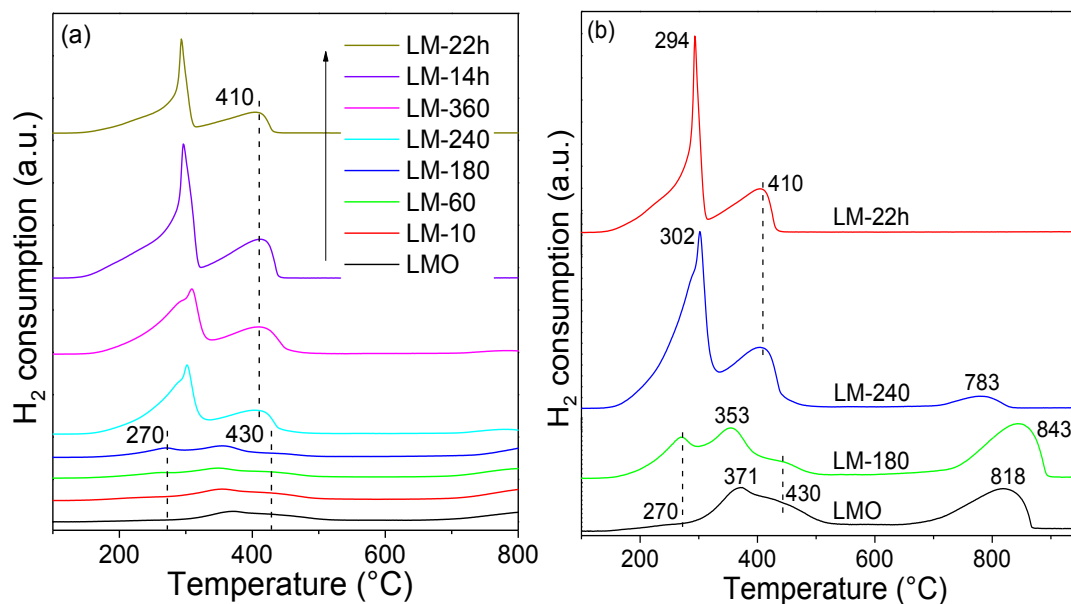
Figure 5-12 The H_2-TPR profiles of the raw and acid treated samples

5.3.7 Catalytic activity
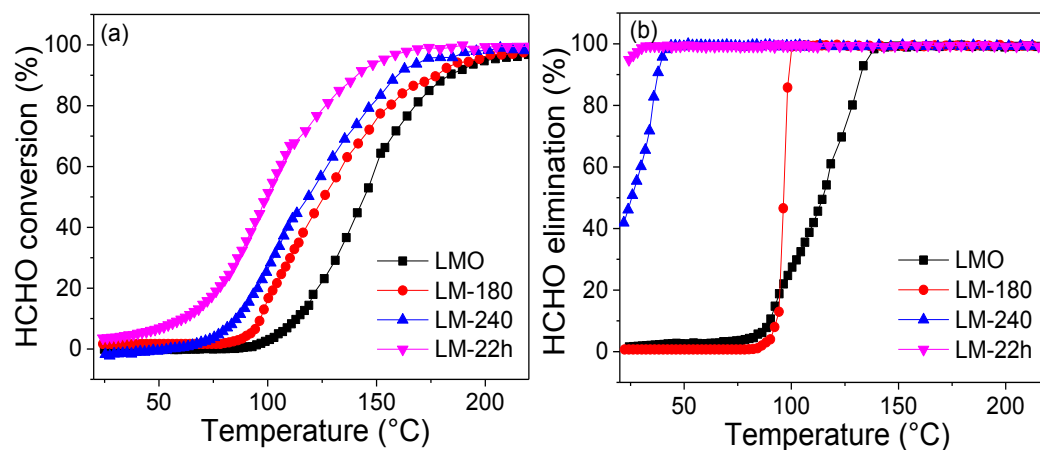
Figure 5-13 Catalytic performance of HCHO over the typical four samples: (a) HCHO conversion (into CO_2), (b) HCHO elimination

Formaldehyde (HCHO) oxidation was investigated for the LMO, LM-180, LM-240 and LM-22h (ε-MnO_2) materials. Fig. 5-13a shows the conversion efficiency of HCHO to CO_2 over the four catalysts with increasing temperature. The reaction

temperatures of T10, T50, and T90 (corresponding to HCHO conversions of 10, 50, and 90% respectively) are summarized in Table 5-5. As expected, the catalytic performance for HCHO oxidation using the acid treated samples (LM-180, LM-240 and LM-22h) were better than that of the raw LMO.

As given in Table 5-5, the sample LM-22h corresponding to the hierarchical ε-MnO_2 catalyst achieved a remarkably low T50 temperature of 99°C, which is substantially lower than that of LM-240 (118°C), LM-180 (126°C) and LMO (145°C). In comparison with other MnO_2 materials reported in literature with the same conditions (100 ppm HCHO, GHSV is 30 000 mLg_{cat}^{-1} h^{-1}), the ε-MnO_2 phase produced here is showing the highest catalytic activity among existing MnO_2 phases, and possess comparable performance with respect to doped Ce-$MnO_2$ catalyst [10]. Additionally, as shown in Fig. 5-13b, the hierarchical ε-MnO_2 catalyst could totally eliminate, by adsorption, the HCHO at room temperature. As discussed above, ε-MnO_2 catalyst owned the largest BET surface area, as well as the highest surface Mn^{4+}/Mn^{3+} atomic ratio and O_{latt}/O_{ads} atomic ratio among all tested catalysts. Hence these advantages may be the reason why the hierarchical ε-MnO_2 catalyst possessed the highest catalytic activity in HCHO oxidation, while retaining adsorption capacity at room temperature.

Table 5-5 Catalytic activity of four selected materials for HCHO oxidation

Samples	HCHO conversion temperature (°C)		
	T10	T50	T90
LMO	114	145	185
LM-180	97	126	177
LM-240	85	118	159
LM-22h	60	99	141

5.3.8 Mechanism of HCHO oxidation
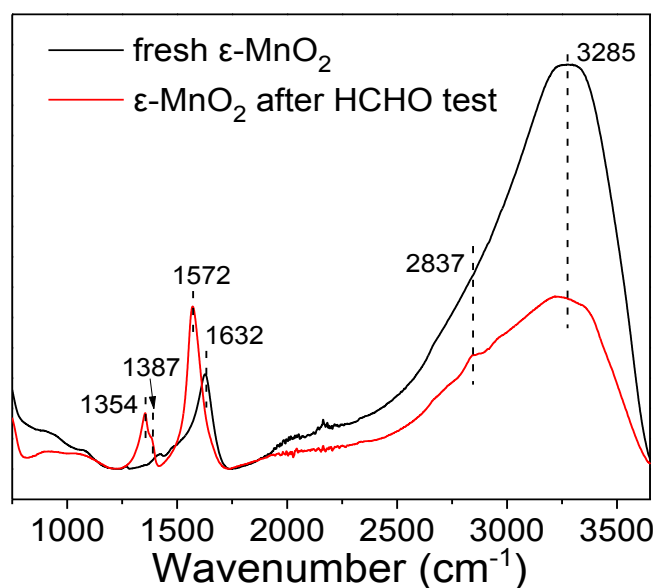

Figure 5-14 ATR-FTIR spectra of sample LM-22h (ε-MnO$_2$) before and after HCHO test

To further investigate the mechanism of HCHO decomposition, infrared spectroscopic measurements (ATR-FTIR) were performed to observe if any changes occured on pure ε-MnO$_2$ extreme surface after HCOH exposure. Spectra were recorded before and after HCHO catalytic oxidation testand are presented in Fig. 5-14. Over the fresh catalyst, two bands at 1632 cm^{-1} and 3285 cm^{-1} ascribable to adsorbed -OH groups (ν(OH) and δ(H$_2$O)) are observed. After HCHO oxidation, four new bands appeared: two at 1354 and 1572 cm^{-1}, belonging to the formate species ν_s(COO) and ν_{as}(COO) respectively; and two at 1387 and 2837 cm^{-1}, ascribed to hydrocarbonates δ(CH) and ν(CH) respectively [10,48]. As previously reported in literature [49,50], these results indicate that the oxidation of HCHO generate formate species, which may further react with surface oxygen species to form hydrocarbonates.

Moreover, the decrease of ν(OH) and δ(H$_2$O) intensities might suggest that the formation of carbonate and formate consumed the superficial -OH groups. It has been reported that superficial -OH groups play an important role during HCHO oxidation since they enhance the adsorption of HCHO *via* hydrogen bonding, especially at low

temperature [48]. The XPS C1s peaks of the sample before and after HCHO conversion were used to explore the formation of surface intermediates (Fig. 5-14d). Three peaks at 284.8 eV, 286.3 eV and 288.6 eV can be ascribable to sp^3-hybridized C (adventitious carbon), C-OH groups and carbonate (CO_3^{2-}) respectively. After the catalytic test, a new component at 288.3 eV belonging to the carboxylic C species (O=C-O) was observed, further confirming the formate formation during HCHO oxidation [48,49].

Our experimental results underline that HCHO oxidation on pure ε-MnO_2 is likely to follow the pathway: $HCHO \rightarrow HCOO^-_{ads} + OH^- \rightarrow CO_2 + H_2O$. That is, the formate species ($HCOO^-_{ads}$) will first be generated due to the reaction of the adsorbed HCHO with surface active oxygen (O_{latt}, O_2^-, O^-, or superficial -OH groups). At high temperature, the formate species will be further oxidized into CO_2 owing the successive participation of these oxygen species. This is in line with the literature [10, 48-51]. Moreover, the mole of water formed per mole of formaldehyde oxydized could regenerate the surface active oxygen, allowing to explain the long-term activity observed even in dry conditions.

Herein, the outstanding catalytic activity of the hierarchical ε-MnO_2 catalyst may be due to the cumulative effect of several factors. On one hand, ε-MnO_2 presents a meso/macro-porous skeleton and a large BET surface area, maximising the diffusion of HCHO within the catalyst and supplying more external active sites. Furthermore, more superficial -OH groups increase the adsorption capacity of HCHO. The chemisorption of HCHO at the surface of a catalyst is always the crucial step to trigger its oxidation [48]. On the other hand, the high oxidizing ability and the abundance of active oxygen species at the surface of ε-MnO_2 could further enhance its catalytic performance. The migration of oxygen species and oxygen activation are dependent on the redox cycle of Mn^{4+}/Mn^{3+}. The enrichment in Mn^{4+} maybe enhances the redox cycles of ε-MnO_2,

which is favorable for the oxidation of HCHO.

5.3.9 Stability test and Moisture effect
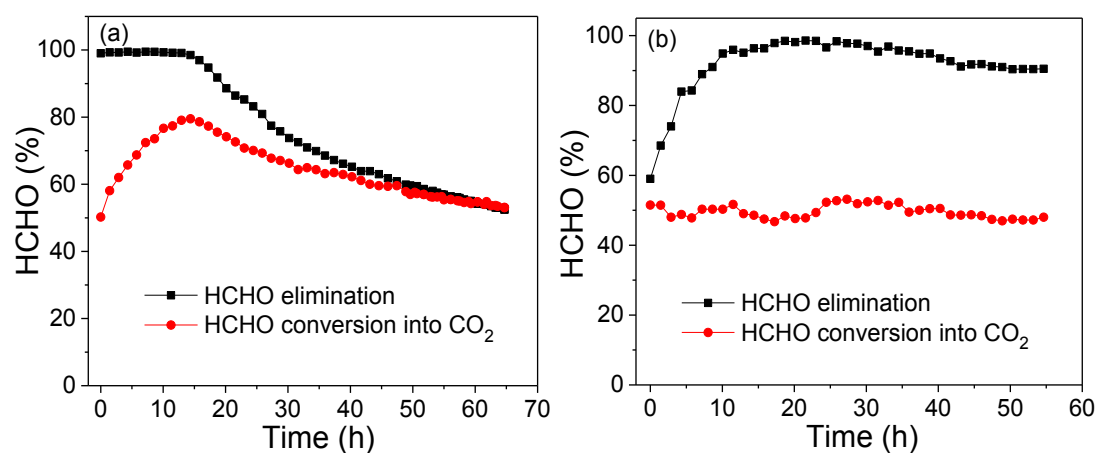
Figure 5-15 (a) HCHO conversion with time on stream over LM-22h (ε-MnO$_2$), (b) Effect of moisture on HCHO conversion with time on stream over LM-22h

From a practical point of view, stability issues of the catalysts should be taken into account. Fig. 5-15a illustrates the HCHO conversion over time on stream at 99°C (corresponding to HCHO conversion of 50%) over ε-MnO$_2$, which achieved an exemplary long-term stability after 65h. Interestingly, during the initial stage (0~12h) an enhancement of HCHO conversion is observed. After 12h, a continuous decrease of both the HCHO elimination and HCHO conversion into CO$_2$ was measured, indicating that during the initial stage HCHO was partly adsorbed until saturation. We speculate that the HCHO adsorbed on the catalyst from the beginning might interact with more HCHO molecules *via* hydrogen bonding in a similar manner than the superficial -OH groups or water and further enhance the conversion of HCHO. In addition, some highly active and non-renewable adsorbed oxygen species on the catalyst surface might be also involved in HCHO oxidation in the beginning. While the HCHO conversion decreased gradually after 12h at T50, stabilization occured from 65h, with comparable values obtained for HCHO elimination and HCHO conversion into CO$_2$.
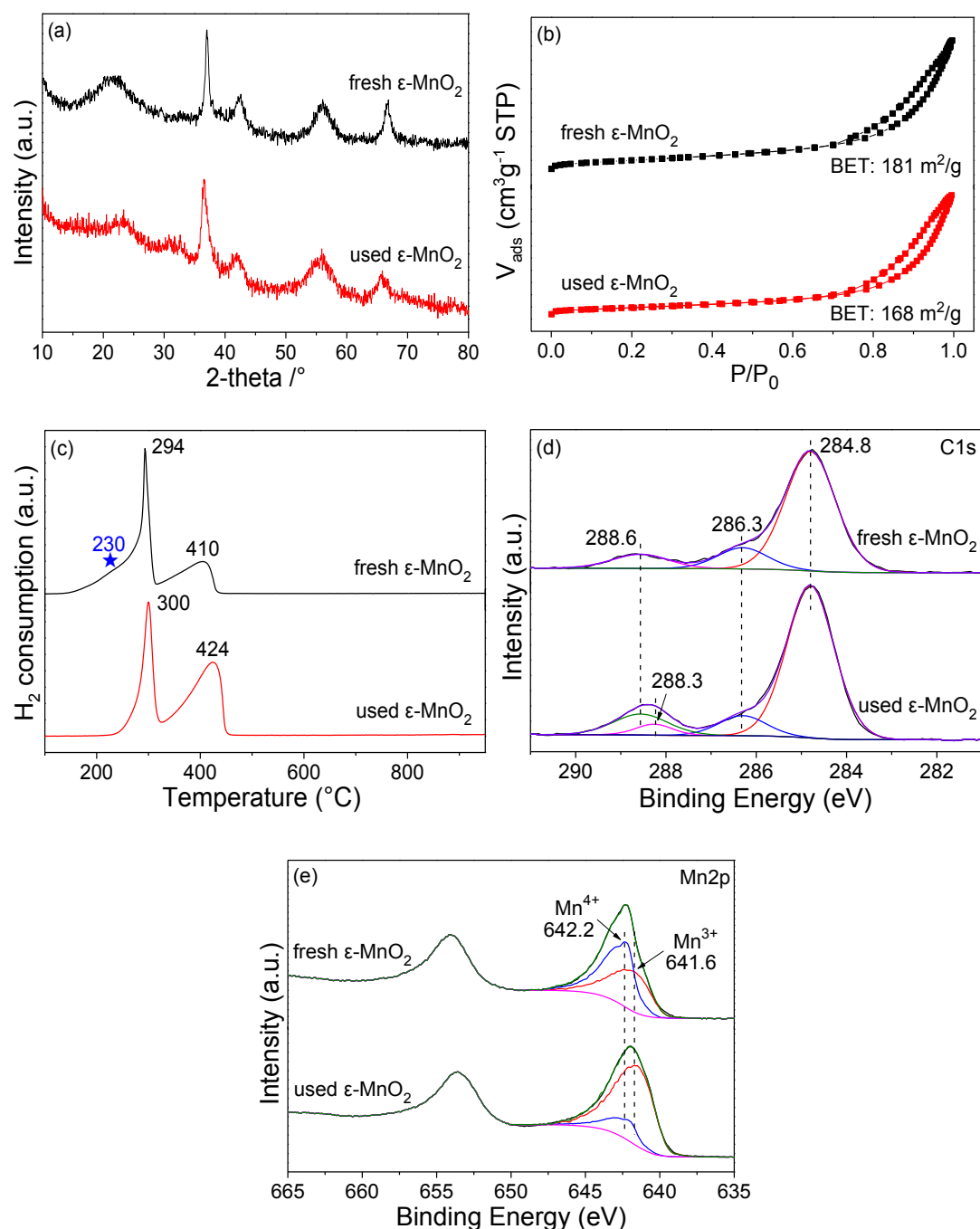
Figure 5-16 Characterization of (a) XRD, (b) BET, (c) TPR, (d) XPS spectra of C1s, (e) XPS spectra of Mn2p for sample LM-22h (ε-MnO$_2$) before and after HCHO stability test

The used ε-MnO$_2$ catalyst was further characterized by XRD, BET, XPS and TPR. As indicated in Fig. 5-16a and Fig. 5-16b, no appreciable changes of its textural or structural properties were observed compared to the as-made ε-MnO$_2$. Additionally, the H$_2$-TPR profile (Fig. 5-16c) of the used ε-MnO$_2$ exhibited small shifts to higher

temperatures, indicating that its reducibility was slightly lower [52]. Also, the amount of consumed H_2 was lower for the used sample (5.98 mmol/g) compared to the fresh one (7.99 mmol/g), implying that more Mn species with lower valence state are present in the used catalyst after HCHO oxidation. Moreover, the relative area ratio of the low (around 300°C) to the high-temperature (around 424°C) reductions was lower for the used sample in comparison with that of the fresh one (Fig. 5-16c), indicating a decreased Mn^{4+}/Mn^{3+} ratio after the stability test. Of note, a peak around 230°C (see the blue star) disappeared in H_2-TPR profile of the used ε-MnO_2, demonstrating the consumption of surface oxygen species during the HCHO oxidation. The evolution of Mn^{4+}/Mn^{3+} molar ratio over the sample before and after HCHO oxidation were further compared (Fig. 5-16e). After HCHO oxidation, the surface Mn^{4+}/Mn^{3+} atomic ratio decreased from 1.71 to 0.26, indicating that the valence of the used MnO_2 leans toward a +3 oxidation state, which is in good agreement with the H_2-TPR result. These results relate greatly with the oxidation of HCHO into formate species with the probable consumption of surface active oxygen, including lattice oxygen (O_{latt}), resulting in global manganese oxide reduction.

Moisture is a key factor in the catalytic oxidation of HCHO, which seems to have a dual role as either a promoting or an inhibiting effect on the conversion of HCHO [53]. It has been reported that moisture is one of the major reasons causing a negative effect on catalytic activity through its competitive adsorption on active sites [52]. Conversely, some previous works found that moisture could act as a promoter that enhance the catalytic oxidation of HCHO, as it not only facilitates the regeneration of superficial -OH groups but it is also beneficial to the desorption of carbonate *via* competitive adsorption [48,54]. The effect of moisture on the conversion of HCHO was investigated by adding water to the inlet gas (corresponding to a relative moisture

capacity of 46% at room temperature), as shown in Fig. 5-18b. Herein, the presence of water has no negative effect on the material activity, with only a slight decrease of the HCHO conversion (-2%) measured. Moreover, the catalytic stability seems improved over time. This could be due to the regeneration of surface active oxygen species, as previously reported [48,54].

5.4 Conclusions

In this work, we report a simple and straightforward method adapted from a soft chemical process to prepare for the first time hierarchical porous ε-MnO$_2$ catalysts derived from a pure LaMnO$_{3.15}$ perovskite. Complementary experiments used in this study demonstrate that the complete dissolution of La^{3+} cations could occur in the presence of 3M HNO$_3$ while preserving the macroporous skeleton of the native perovskite. Moreover, direct link is given between material's properties (i.e. BET surface areas, total pore volumes) and the acid treatment time applied. More specifically, XPS and H$_2$-TPR analyses revealed more Mn^{4+} active species present in the acid-treated material compared to the raw LMO perovskite. At the light of the results, A pseudomorphic transformation is proposed to occur *via* a dissolution/recrystallization process involving dismuted Mn^{4+}, leading to the formation of a meso/macro-porous macrostructure composed of intergrown nanosheets of ε-MnO$_2$. The hierarchical porous ε-MnO$_2$ was found to be stable and highly-efficient for low-temperature catalytic oxidation of HCHO, owing to an increase of its BET surface area and an improvement of its redox properties. In addition, excellent stability toward water presence is measured, confirming the potential of these materials for indoor depollution processes.

References

[1] T. Salthammer, S. Mentese, R. Marutzky, Formaldehyde in the indoor environment, Chem. Rev. 110 (2010) 2536-2572.

[2] J.J. Collins, R. Ness, R.W. Tyl, N. Krivanek, N.A. Esmen, T.A. Hall, A review of adverse pregnancy outcomes and formaldehyde exposure in human and animal studies, Regul. Toxicol. Pharm. 34 (2001) 17-34.

[3] ARC.IARC, press release no.153, International Agency for Research on Cancer: Lyon, (2004).

[4] W.J. Liang, J. Li, J.X. Li, T. Zhu, Y.Q. Jin, Formaldehyde removal from gas streams by means of $NaNO_2$ dielectric barrier discharge plasma, J. Hazard. Mater. 175 (2010) 1090-1095.

[5] K.J. Lee, N. Shiratori, G.H. Lee, J. Miyawaki, I. Mochida, S.-H. Yoon, J. Jang, Activated carbon nanofiber produced from electrospun polyacrylonitrile nanofiber as a highly efficient formaldehyde adsorbent, Carbon 48 (2010) 4248-4255.

[6] J.P. Bellat, I. Bezverkhyy, G. Weber, S. Royer, R. Averlant, J.M. Giraudon, J.F. Lamonier, Capture of formaldehyde by adsorption on nanoporous materials, J. Hazard. Mater. 300 (2015) 711-717.

[7] T. Noguchi, A. Fujishima, P. Sawunyama, K. Hashimoto, Photocatalytic degradation of gaseous formaldehyde using TiO_2 Film, Environ. Sci. Technol. 32 (1998) 3831-3833.

[8] X. Zhu, C. Jin, X.-S. Li, J.-L. Liu, Z.-G. Sun, C. Shi, X. Li, A.-M. Zhu, Photocatalytic formaldehyde oxidation over plasmonic Au/TiO_2 under visible light: Moisture indispensability and light enhancement, ACS Catal. 7 (2017) 6514-6524.

[9] S. Royer, D. Duprez, F. Can, X. Courtois, C. Batiot-Dupeyrat, S. Laassiri, H. Alamdari, Perovskites as substitutes of noble metals for heterogeneous catalysis: Dream or reality, Chem. Rev. 114 (2014) 10292-10368.

[10] J. Quiroz, J.M. Giraudon, A. Gervasini, C. Dujardin, C. Lancelot, M. Trentesaux, J.F. Lamonier, Total oxidation of formaldehyde over $MnOx$-CeO_2catalysts: The effect of acid treatment, ACS Catal. 5 (2015) 2260-2269.

[11] C. Ciotonea, R. Averlant, G. Rochard, A.-S. Mamede, J.-M. Giraudon, H. Alamdari, J.-F. Lamonier, S. Royer, A simple and green procedure to prepare efficient manganese oxide nanopowder for the low temperature removal of formaldehyde, ChemCatChem 9 (2017) 2366-2376.

[12] L.F. Liotta, Catalytic oxidation of volatile organic compounds on supported noble metals, Appl. Catal. B100 (2010) 403-412.

[13] J. QuirozTorres, S. Royer, J.P. Bellat, J.M. Giraudon, J.F. Lamonier, Formaldehyde: Catalytic oxidation as a promising soft way of elimination, ChemSusChem6 (2013) 578-592.

[14] L. Nie, J. Yu, M. Jaroniec, F.F. Tao, Room-temperature catalytic oxidation of formaldehyde on catalysts, Catal. Sci. Technol. 6 (2016) 3649-3669.

[15] J. Chen, D. Yan, Z. Xu, X. Chen, X. Chen, W. Xu, H. Jia, J. Chen, A novel redox precipitation to synthesize Au-doped α-MnO_2 with high dispersion toward low-temperature oxidation of formaldehyde, Environ. Sci. Technol. 52 (2018) 4728-4737.

[16] Y.Wang, H. Arandiyan, J.Scott, A.Bagheri, H.Dai, R.Amal, Recent advances in ordered meso/macroporous metal oxides for heterogeneous catalysis: a review. Journal of Materials Chemistry A, 5(2017) 8825-8846.

[17] X.Hu,F.Cheng,X.Han, T.Zhang, J. Chen, Oxygen Bubble-Templated Hierarchical Porous ε-MnO_2 as a Superior Catalyst for Rechargeable Li-O_2 Batteries. Small, 11(2015) 809-813.

[18]H.Chen, Y.Wang, Y.K. Lv, Catalytic oxidation of NO over MnO_2 with different crystal structures. RSC Advances, 6(2016) 54032-54040.

[19] S.H.Kim, B.C.Park, Y.S.Jeon, Y.K.Kim, MnO_2 Nanowire-CeO_2 Nanoparticle Composite Catalysts for the Selective Catalytic Reduction of NO_x with NH_3. ACS applied materials & interfaces, 10 (2018) 32112-32119.

[20] W. Si, Y. Wang, Y. Peng, J. Li, Selective Dissolution of A-Site Cations in ABO_3 Perovskites: A New Path to High-Performance Catalysts. Angewandte Chemie International Edition, 54(2015), 7954-7957.

[21] W. Si, Y. Wang, Y. Peng, X. Li, K. Li, J. Li, A high-efficiency γ-MnO_2-like catalyst in toluene combustion, Chem. Commun. 51 (2015) 14977-14980.

[22] W. Si, Y. Wang, S. Zhao, F. Hu, J. Li, A Facile Method for in Situ Preparation of the $MnO_2/LaMnO_3$ Catalyst for the Removal of Toluene, Environ. Sci. Technol. 50 (2016) 4572-4578.

[23] J. Erlebacher, M.J. Aziz, A. Karma, N. Dimitrov, K. Sieradzki, Evolution of nanoporosity in dealloying, Nature 410 (2001) 450.

[24] M. Kudo, H. Ohkawa, W. Sugimoto, N. Kumada, Z. Liu, O. Terasaki, Y. Sugahara, A layered tungstic acid $H_2W_2O_7 \cdot nH_2O$ with a double-octahedral sheet structure: Conversion process from an aurivillius phase $Bi_2W_2O_9$ and structural characterization, Inorg. Chem. 42 (2003) 4479-4484.

[25] J. Gopalakrishnan, Chimie douce approaches to the synthesis of metastable oxide materials, Chem. Mater. 7 (1995) 1265-1275.

[26] W. Sugimoto, M. Shirata, Y. Sugahara, K. Kuroda, New conversion reaction of an aurivillius phase into the protonated form of the layered perovskite by the selective leaching of the bismuth oxide sheet, J. Am. Chem. Soc. 121 (1999) 11601-11602.

[27] A.H. Janssen, A.J. Koster, K.P. de Jong, Three-dimensional transmission electron Microscopic observations of mesopores in dealuminated Zeolite Y, Angew. Chem. Int. Edit. 40 (2001) 1102-1104.

[28] K. Huang, X. Chu, L. Yuan, W. Feng, X. Wu, X. Wang, S. Feng, Engineering the surface of perovskite $La_{0.5}Sr_{0.5}MnO_3$ for catalytic activity of CO oxidation, Chemical Communications, 50 (2014) 9200-9203.

[29] Y. Wei, L. Ni, M. Li, J. Zhao, A template-free method for preparation of MnO_2 catalysts with high surface areas, Catal. Today 297 (2017) 188-192.

[30] Y. Ding, S. Wang, L. Zhang, Z. Chen, M. Wang, S. Wang, A facile method to promote $LaMnO_3$ perovskite catalyst for combustion of methane, Catal. Commun. 97 (2017) 88-92.

[31] D. Wang, Y. Peng, Q. Yang, S. Xiong, J. Li, J. Crittenden, Performance of Modified $La_xSr_{1-x}MnO_3$ Perovskite Catalysts for NH_3 Oxidation: TPD, DFT, and kinetic Studies, Environ. Sci. Technol. 52 (2018) 7443-7449.

[32] H.-Z. Geng, K.K. Kim, K.P. So, Y.S. Lee, Y. Chang, Y.H. Lee, Effect of acid treatment on carbon nanotube-based flexible transparent conducting films, J. Am. Chem. Soc. 129 (2007) 7758-7759.

[33] G. Kéranguéven, S. Royer, E. Savinova, Synthesis of efficient Vulcan-$LaMnO_3$ perovskite nanocomposite for the oxygen reduction reaction, Electrochem. Commun. 50 (2015) 28-31.

[34] P.M. De Wolff, Interpretation of some γ-MnO_2 diffraction patterns, Acta Crystallographica, 12 (1959) 341-345.

[35] D.K. Walanda, G.A. Lawrance, S.W. Donne, Kinetics of Mn_2O_3 digestion in H_2SO_4 solutions, J. Solid State Chem. 182 (2009) 1336-1342.

[36] Y. Chabre, J. Pannetier, Structural and electrochemical properties of the proton/γ-MnO_2 system, Prog. Solid State Ch. 23 (1995) 1-130.

[37] C. de A. Dias, H. de Santana, M.A.L. Nobre, M.C. Lopes, The relation between structural features and electrochemical activity of MnO_2 nanoparticles synthesized from a polyol-made Mn_3O_4 precursor, J. Solid State Electr. 17 (2013) 1967-1976.

[38] C.-H. Kim, Z. Akase, L. Zhang, A.H. Heuer, A.E. Newman, P.J. Hughes, The structure and ordering of ε-MnO_2, J. Solid State Chem. 179 (2006) 753-774.

[39] D. Neagu, G. Tsekouras, D.N. Miller, H. Ménard, J.T.S. Irvine, In situ growth of nanoparticles through control of non-stoichiometry, Nature Chem. 5 (2013) 916-923.

[40] M.C. Biesinger, B.P. Payne, A.P. Grosvenor, L.W.M. Lau, A.R. Gerson, R.S.C. Smart, Resolving surface chemical states in XPS analysis of first row transition metals, oxides and hydroxides: Cr, Mn, Fe, Co and Ni, Appl. Surf. Sci. 257 (2011) 2717-2730.

[41] E. Symianakis, D. Malko, E. Ahmad, A.-S. Mamede, J.-F. Paul, N. Harrison, A. Kucernak, Electrochemical characterization and quantified surface termination obtained by low energy ion scattering and X-ray photoelectron spectroscopy of orthorhombic and rhombohedral $LaMnO_3$ powders, J. Phy. Chem. C 119 (2015) 12209-12217.

[42] J. Reboul, S. Furukawa, N. Horike, M. Tsotsalas, K. Hirai, H. Uehara, M. Kondo, N. Louvain, O. Sakata, S. Kitagawa, Mesoscopic architectures of porous coordination polymers fabricated by pseudomorphic replication, Nature Mater. 11 (2012) 717.

[43] M. Choi, K. Na, R. Ryoo, The synthesis of a hierarchically porous BEA zeolitevia pseudomorphic crystallization, Chem. Commun (2009) 2845-2847.

[44] H. de Souza Santons, P.K. Kiyohara, P. de Souza Santos, Pseudomorphic transformations of

euhedral crystals of γ-AlOOH into aluminas, Ceram. Int. 20 (1994) 175-181.

[45] S. Royer, H. Alamdari, D. Duprez, S. Kaliaguine, Oxygen storage capacity of $La_{1-x}A'_xBO_3$ perovskites (with A'=Sr, Ce; B=Co, Mn)-relation with catalytic activity in the CH_4 oxidation reaction, Appl. Catal. B58 (2005) 273-288.

[46] Y. Liu, H. Dai, Y. Du, J. Deng, L. Zhang, Z. Zhao, Lysine-aided PMMA-templating preparation and high performance of three-dimensionally ordered macroporous $LaMnO_3$ with mesoporous walls for the catalytic combustion of toluene, Appl. Catal. B 119-120 (2012) 20-31.

[47] Y. Zhu, Y. Sun, X. Niu, F. Yuan, H. Fu, Preparation of La-Mn-O perovskite catalyst by microwave irradiation method and its application to methane combustion, Catal. Lett. 135 (2010) 152-158.

[48] J. Wang, P. Zhang, J. Li, C. Jiang, R. Yunus, J. Kim, Roomtemperature oxidation of formaldehyde by layered manganese oxide: Effect of water, Environ. Sci. Technol. 49 (2015) 12372-12379.

[49] S. Selvakumar, N. Nuns, M. Trentesaux, V.S. Batra, J.M. Giraudon, J.F. Lamonier, Reaction of formaldehyde over birnessite catalyst: A combined XPS and ToF-SIMS study, Appl. Catal. B 223 (2018) 192-200.

[50] J. Wang, J. Li, C. Jiang, P. Zhou, P. Zhang, J. Yu, The effect of manganese vacancy in birnessite-type MnO_2 on room-temperature oxidation of formaldehyde in air, Appl. Catal. B 204 (2017) 147-155.

[51] C. Zhang, F. Liu, Y. Zhai, H. Ariga, N. Yi, Y. Liu, K. Asakura, M. Flytzani-Stephanopoulos, H. He, Alkali-Metal-Promoted Pt/TiO_2 opens a more efficient pathway to formaldehyde oxidation at ambient temperatures, Angew. Chem. Int. Edit. 51 (2012) 9628-9632.

[52] X. Tang, Y. Li, X. Huang, Y. Xu, H. Zhu, J. Wang, W. Shen, MnO_x-CeO_2 mixed oxide catalysts for complete oxidation of formaldehyde: Effect of preparation method and calcination temperature, Appl. Catal. B62 (2006) 265-273.

[53] M. Daté, M. Haruta, Moisture Effect on CO oxidation over Au/TiO_2 catalyst, J. Catal. 201 (2001) 221-224.

[54] D.W. Kwon, P.W. Seo, G.J. Kim, S.C. Hong, Characteristics of the HCHO oxidation reaction over Pt/TiO_2 catalysts at room temperature: The effect of relative humidity on catalytic activity, Appl. Catal. B 163 (2015) 436-443.

Chapter 6 Alkali and alkaline earth-promoted perovskites for formaldehyde total oxidation

6.1 Introduction

Alkali ions modification have gained a lot of attention in the past few decades due to their promotion effects on many important heterogeneous catalytic reactions. Furthermore, catalysts doped with alkali metal ions have shown higher performances for the oxidation of VOCs [1-6]. While alkali ions effectively promote HCHO oxidation when using noble metal-based catalysts, very few studies reported the effect of alkali and alkaline earth ions on the catalytic activity of noble metals-free oxides for the oxidation of HCHO [7-9]. Furtheromore, to our best knowledge, no alkali-modified perovskite-based materials have been evaluated for formaldehyde oxidation, though perovskite materials have been used for VOCs combustion [10]. In addition, the research is few about the subsitution of A cations with alkali ions such as K^+ and Na^+ used in environment catalysis area [11-14].

In this work, a series of alkali- and alkaline earth-modified $LaMnO_3$ perovskites were prepared using partial substitution of the La^{3+} cation, post-synthesis alkali treatment, and sodium nitrate impregnation, in order to insight into two aspects of contents. Firstly, as La^{3+} at A-site is partly replaced by lower valency cation especially K^+ or Na^+, whether the surface physicochemical properties of perovskites will be altered, and then affect the catalytic activity especial in HCHO oxidation. Secondly, whether the addition of alkali ion in perovskite also has a promotion for HCHO oxidation, similar to the previous reports using noble metal based catalyst. The study will provide the clearing understanding of catalytic oxidaiton of HCHO at alkali-modified perovskites. Such materials were thoroughly characterized by XRD, N_2 physisorption, ICP, XPS, FTIR and TPR, and comparatively investigated for the catalytic oxidation of HCHO at mild temperature. We believe thatthis workwill guide the synthesis and optimization of cost-effective perovskite-based catalysts for mild-temperature catalytic

oxidation of HCHO.

6.2 Experimental section

6.2.1 Synthesis of catalysts

Pure $LaMnO_3$ and alkali- and alkaline earth-substituted perovskites: $La_{0.8}A_{0.2}MnO_3$ (A= K, Na, Sr, Ca) were prepared following a conventional citric acid complexation method, starting from the metal nitrate precursors $Mn(NO_3)_2 \cdot xH_2O$ (98.0 %, Aldrich) and $La(NO_3)_3 \cdot 6H_2O$ ($\geq$99.0 %, Sigma-Aldrich), and citric acid (+99.5 % , Alfa Aesar), KNO_3 ($\geq$ 99.0 %, Fluka), $NaNO_3$ (+99 %, Acros), $Sr(NO_3)_2$ ($\geq$ 99.0 %, Fluka), $Ca(NO_3)_2$ $4H_2O$ (99.0 % ~ 103.0 %, Sigma- Aldrich).

For the synthesis of pure $LaMnO_3$, a molar ratio (n_{Mn} + n_{La})/$n_{citric\ acid}$ of 1 was applied. 3.7 g of La nitrate and 7.0 g of Mn nitrate were dissolved in 40 mL of distilled water. In a second beaker 6.9 g of citric acid were dissolved in 40 mL of distilled water, and the resulting clear solution was added drop-wise to the solution containing the metal precursors under magnetic stirring. The resulting homogeneous solution was stirred for 1 h at 40 °C, and overnight at room temperature. A rotary evaporation step was used to remove the excess of water, resulting in a gel. The obtained gel was thermally treated in a muffle oven under air over two steps: 180 °C for 1 h (3 °C min^{-1}), and 650 °C for 8 h (2 °C min^{-1}). The reference perovskite was labeled LMO.

A similar procedure was applied for the synthesis of alkali- and alkaline earth-substituted perovskites, keeping the (n_A + n_{Mn} + n_{La})/$n_{citric\ acid}$ molar ratio constant of 1, as well as a molar ratio (n_A + n_{La})/n_{Mn} of 1 and a molar ratio n_A/n_{La} of 0.25. In a typical synthesis, stoichiometric amounts of alkali and alkaline earth (K, Na, Sr, Ca) nitrate, manganese nitrate and lanthanum nitrate required for preparing 5g of perovskite oxide were dissolved. The substituted perovskites containing K, Na, Sr and Ca were labeled LKMO, LNMO, LSMO and LCMO, respectively.

For comparison, two other post-synthesis methods were applied for preparing Na^+-modified LMO. LMO-Na was prepared by a classical impregnation method: 0.0396 g of $NaNO_3$ was dissolved in distilled water (10 mL ethanol + 2 mL water) and then 0.50 g of LMO was slowly added into the solution. After overnight stirring, the obtained solid was dried in oven (60 °C for 24 h) and after calcined at 650 °C for 8 h (2 °C/min). The weight ratio of Na in LMO-Na is about 2.1 wt%, which is comparable to the LNMO sample. LMO-OH was prepared by treating LMO with caustic soda. 1.0 g of LMO was added to 250 mL of a 6 M NaOH (> 98 %, Sigma-Aldrich) and stirred at 200 rpm. After 1 hour, the solid was filtered on a 0.2 μm membrane filter (Fibre de verre, Prat Dumas France), dried in the oven at 60 °C for 24 h.

6.2.2 Catalytic oxidation of formaldehyde (HCHO)

The procedure of catalytic oxidation of formaldehyde (HCHO) has been described in Section 5.2.2. The formaldehyde (HCHO) oxidation into CO_2 was expressed as HCHO conversion, while HCHO elimination refers to the removal efficiency of HCHO. Especially, the HCHO adsorption was expressed as carbon balance. They were calculated using the following equations, respectively:

$$HCHO \text{ conversion (into } CO_2) (\%) = \frac{[CO_2]_t}{[HCHO]_0} \times 100 \tag{6-1}$$

$$HCHO \text{ elimination } (\%) = \frac{[HCHO]_0 - [HCHO]_t}{[HCHO]_0} \times 100 \tag{6-2}$$

$$Carbon \text{ balance } (\%) = 100 - (HCHO \text{ elimination} - HCHO \text{ conversion}) \tag{6-3}$$

Where $[HCHO]_t$ and $[CO_2]_t$ are their concentration at time t as monitored by GC, and $[HCHO]_0$ is the initial HCHO concentration (100 ppm).

During the stability test, a fresh catalyst was first activated as indicated before (300°C, 1h under 20 vol% O_2/He, 100 mL min^{-1}). Then the reacting gas (100 ppm HCHO in 20 vol% O_2/He, 100 mL min^{-1}) was passed through the catalyst bed at a temperature corresponding to HCHO conversion of 50% (T50) for at least 64h.

6.2.3 Characterization

The detailed information about the characterizaiton techniques including X-ray diffraction patterns (XRD), Nitrogen sorption measurements, Fourier transformed infrared spectra (FTIR), X-ray Photoelectron Spectroscopy (XPS), and Temperature programmed reduction (TPR) spectra is shown before (5.2.3). Stoichiometry of alkaliand alkaline earth ions, La and Mn in the solids were monitored by inductively coupled plasma-optical emission spectroscopy (ICP-OES) (Agilent Technologies 700 Series spectrometer). Before analysis, the solids were dissolved in a concentrated HCl/HNO$_3$ mixture.

6.3 Results and Discussion

6.3.1 Physicochemical properties

The XRD patterns of the samples, displayed in Fig. 6-1, all present the typical diffraction pattern of rhombohedral LaMnO$_{3.15}$ (JCPDS 50-0298) with characteristic peaks at 2θ= 23.0°, 32.5°, 40.1°, 46.9°, 58.1°, 68.6° and 77.8°. No obvious diffraction peaks for impurities like La$_2$O$_3$ and MnO$_x$ were observed. As seen in Table 6-1, comparable crystallite size (d_{LMO}) of about 19 to 26 nm were obtained for all samples when applying the Sherrer equation to the (024) plane (2θ = 46.9°). The Scherrer equation was not applied to main (110) and (104) planes (2θ = 32.5° and 32.8°) because their resulting diffraction peaks were confounded into one large peak.
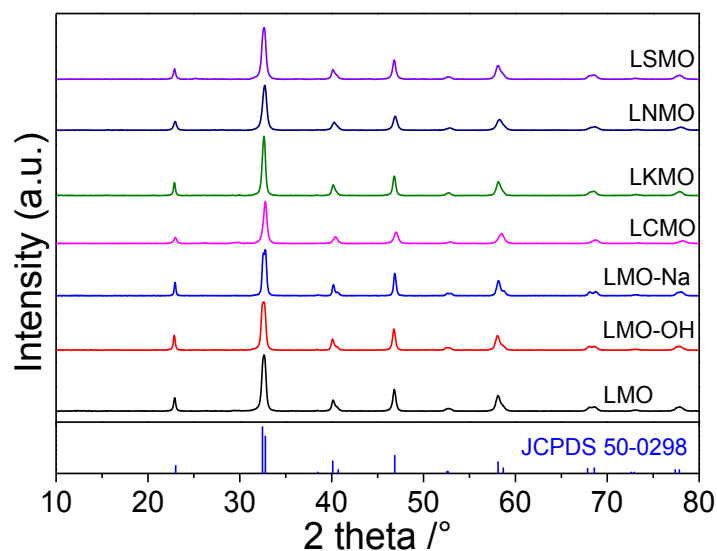
Figure 6-1 Wide-angle XRD patterns of LMO and the alkali- and alkaline earth-promoted perovskites

Table 6-1 Textural and structural properties of the reference and alkali- and alkaline earth-modified LMO samples

Sample	S_{BET} (m^2/g)	V_{pore} (cm^3/g)	d_{LMO} (nm)
LMO	18	0.10	25
LMO-OH	14	0.06	26
LMO-Na	6	0.01	26
LCMO	23	0.14	19
LKMO	18	0.06	25
LNMO	22	0.06	19
LSMO	20	0.07	25

The N$_2$ adsorption/desorption isotherms of all samples, and their relating textural properties are presented in Table 6-1, respectively. As expected for perovskite materials, all catalysts had relatively low specific surface areas (from 18 to 23 m^{2}g^{-1}) due to high temperature calcination and lack of internal porosity. One may note that the S_{BET} of LMO-Na and LMO-OH is even lower, 6 m^{2}g^{-1} and 14 m^{2}g^{-1} respectively.

6.3.2 Elemental analysis

Surface element compositions and chemical states were evaluated by X-ray photoemission spectroscopy (XPS), while the bulk composition was determined by inductively coupled plasma analysis (ICP). The quantitative elemental compositions including surface atomic ratios of A(Sr, Na, K, Ca)/Mn, La/Mn, A/La and Mn/(La+A+Mn), as well as the molar ratio of adsorbed oxygen species are summarized on Table 6-1.

Table 6-1 Relative surface abundance of the elements constituting LMO and the alkali- and alkaline earth-promoted perovskites

Samples	A/Mn		La/Mn	A/La	Mn/(La+A+Mn)	AOS (Mn)	O_{ads}/O_{tot}
	ICP	XPS	XPS	XPS	XPS	XPS	XPS
LMO	-[a]	-	1.12 (1.0)	-	0.47 (0.50)	3.40	0.34
LMO-OH	-	-	1.18 (1.0)	-	0.46 (0.50)	3.31	0.38
LMO-Na	0.22 (0.22)[b]	0.96 (0.22)	1.31 (1.0)	0.73 (0.22)	0.31 (0.45)	3.29	0.36
LCMO	0.20 (0.20)	0.26 (0.20)	1.16 (0.8)	0.22 (0.25)	0.41 (0.50)	3.40	0.36
LKMO	0.20 (0.20)	0.37 (0.20)	1.08 (0.8)	0.34 (0.25)	0.41 (0.50)	3.63	0.46
LNMO	0.30 (0.20)	0.56 (0.20)	1.23 (0.8)	0.46 (0.25)	0.36 (0.50)	3.55	0.45
LSMO	0.19 (0.20)	0.22 (0.20)	0.92 (0.8)	0.24 (0.25)	0.47 (0.50)	3.51	0.43

[a]"-"means no detected
[b]The data inbrackets are the nominal compositions of the reference and modified LMO samples

Within experimental and apparatus errors, the determined atomic ratios of A/Mn by ICP were in close agreement with the nominal values except in the case of LNMO, characterizing either extra-lattice Na^+ or a preferential substitution of La^{3+} by Na^+. On the other hand, LMO perovskite particles are known to present A-site enrichment at their surface, leading to higher A/Mn atomic ratios as obtained by XPS. By comparing ICP and XPS results, it seems clear that little extra-lattice Na^+ is remaining in the case of LNMO, and most of the sodium ions are actually located at the surface of perovskite particles in the case of LMO-Na. This latter observation was expected as impregnation

was made in non-destructive conditions.

The Mn 2p XPS spectra for all samples is shown in Fig. 6-2a. It exhibited two peaks at ~642 eV and ~653 eV, which are respectively assigned to Mn $2p_{3/2}$ and Mn $2p_{1/2}$. High-resolution XPS spectra in the Mn 3s region can be observed in Fig. 6-2b. The average oxidation state (AOS) of the surface Mn was estimated from the binding energies of the doublet separation of Mn 3s (ΔE_s) following the correlation: AOS (Mn) = $8.956 - 1.126 \times \Delta E_s$ [15]. For the raw LMO, the surface AOS (Mn) is about 3.40 (Table 6-1) which is little higher than the theoretical value (3.3) in $LaMnO_{3.15}$, agreeing with a mixture of $Mn^{4+/3+}$ with Mn^{3+} as the predominant cation [16]. The Sr, Na and K substituted samples (LSMO, LNMO and LKMO) showed higher AOS (Mn), with values of 3.51, 3.55 and 3.63 respectively. This suggests that the valence of these three samples tends to +4 oxidation state after the A-site substitution of perovskite. However, the Ca^{2+}-substituted sample (LCMO) presents comparable AOS (Mn) value (3.40) with the LMO sample, implying that the substitution did not induce a Mn^{3+} to Mn^{4+} transformation. This is in accordance with a previous report [17]. In addition, The two post-synthesis modified samples (LMO-OH and LMO-Na) presentend a slightly lower average oxidation state.
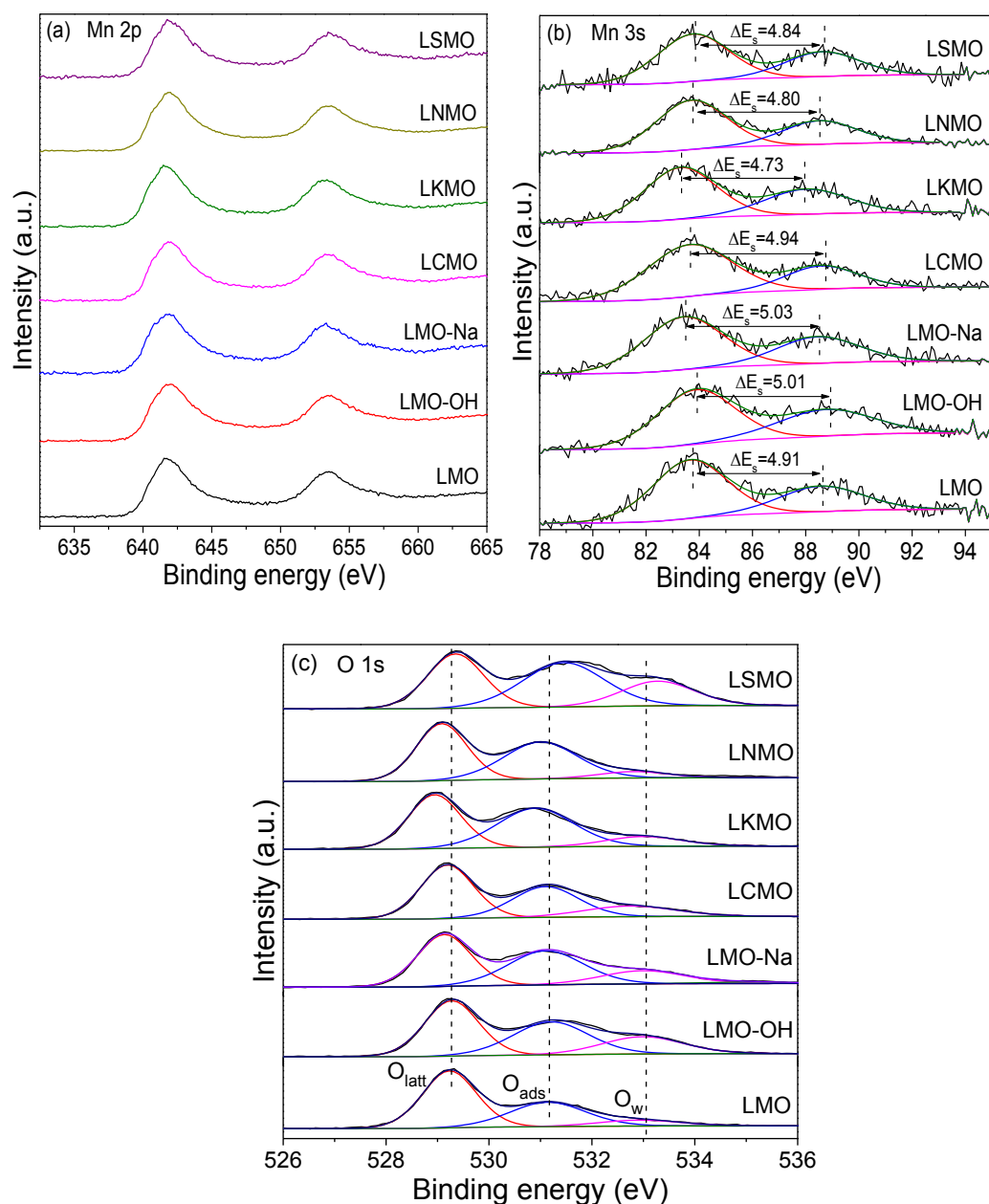
Figure 6-2 Typical XPS spectra of (a) Mn 2p, (b) Mn 3s and (c) O 1s of LMO and the alkali- and alkaline earth-promoted perovskites

By substituting the A-site cation of LMO perovskite (La^{3+}) by lower valency cations (e.g., Sr^{2+}, Na^+, K^+, Ca^{2+}), and according to the principle of electron neutrality, the total charge of the lattice has to be balanced either by increasing the average oxidation state of the B-site cation ($La_{1-x}^{3+}A_x^{z+}Mn_{0.7-x(3-z)}^{3+}Mn_{0.3+x(3-z)}^{4+}O_{3.15}$) or by the formation of oxygen vacancy (V_0) ($La_{1-x}^{3+}A_x^{z+}(V_0)_yMn_{0.7}^{3+}Mn_{0.3}^{4+}O_{3.15-y}$) [18]. Both factors will improve the bulk oxygen mobility and redox properties of a catalyst, further

impacting its catalytic activity.

In Fig. 6-2c are displayed high-resolution XPS spectra in the O1s region for all samples. Three peaks can be observed aroud 529.3, 531.1, and 532.9 eV, representing the surface lattice oxygen (O^{2-}, denoted as O_{latt}), the surface adsorbed oxygen species and some surface oxygen containing groups such as hydroxyl and/or carbonated species (O_2^{2-}/O^-, denoted O_{ads}), and the water adsorbed on the surface (denoted O_w), respectively [19,20]. Surface adsorbed oxygen species are usually linked to surface oxygen vacancies [21], the latter providing sites for adsorption, activation and migration of oxygen species. While LMO-Na and LCMO presents a similar O_{ads}/O_{tot} (total amount of O species, denoted O_{tot}) ratio than the reference LMO (0.36 and 0.35, respectively), the O_{ads}/O_{tot} molar ratio in LSMO, LNMO and LKMO increased significantly from 0.34 to 0.43, 0.45 and 0.46, respectively (Table 6-1). Supposing constant surface oxygen containing groups owing to the use of the same synthesis protocol,this increase can be ascribed to a higher concentration of surface adsorbed oxygen species, and thus to a higher concentration of surface oxygen vacancies [22].

Both surface adsorbed oxygen species and oxygen vacancies play a role in the enhancement of the catalytic performance for formaldehyde oxidation [5,6]. The alkali-treated perovskite, LMO-OH, also present a slight increase of the O_{ads}/O_{tot} molar ratio, which might due to additional surface hydroxyl groups [4,5,23,24]. It should be note that the binding energy of O_{latt} shifted to the lower value in LNMO and LKMO samples, which might due to the weakening of the Mn-O bonds [8], and then enhancing the lattice oxygen mobility.
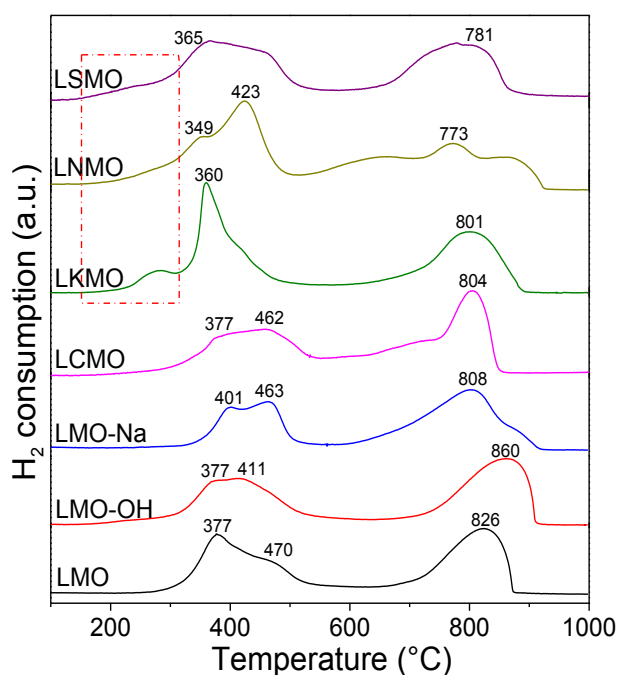
6.3.3 Reducibility studies

Figure 6-3 The H$_2$-TPR profiles of LMO and the alkali- and alkaline earth-promoted perovskites

Table 6-2 H$_2$ consumption deduced from the H$_2$-TPR for LMO and the alkali- and alkaline earth-promoted perovskites

Samples	H$_2$ consumption (mmol/g)				
	Low T		Low temperature range	High T	Total
	(<315°C)	(315-600°C)		(600-1000°C)	
LMO	0.04	1.33	1.37	1.29	2.66
LMO-OH	0.09	1.05	1.14	1.34	2.48
LMO-Na	-	0.97	0.97	1.59	2.56
LCMO	0.06	1.23	1.29	1.55	2.84
LKMO	0.31	1.36	1.67	1.33	3.00
LNMO	0.19	1.44[a]	1.63	1.33[b]	2.96
LSMO	0.19	1.39	1.58	1.27	2.85

[a,b] The data in low T and high T are calculated on 315-500 °C and 500-1000 °C, respectively.

Temperature programmed reduction (TPR) by H$_2$ was conducted to investigate the reducibility of all samples. The H$_2$-TPR profiles are shown in Fig. 6-3, and the data are

summarized in Table 6-2. For LMO, the main peak is centered at 377°C, with a shoulder at 470°C which can be assigned to the reduction of Mn^{4+} into Mn^{3+} and the reduction of some Mn^{3+} located in a coordination-unsaturated microenvironment into Mn^{2+}, respectively [16]. In the high temperature region of 600-1000 °C, the intense peak refers to the reduction of the remaining Mn^{3+} to Mn^{2+}. Theoretically, if all of the Mn ions in LMO perovskite (Mn^{3+} and Mn^{4+}) were reduced to Mn^{2+}, the H_2 consumption of $LaMnO_{3.15}$ should be 2.70 mmol/g. As indicated in Table 6-2, the calculated total H_2 consumption of the raw LMO is 2.66 mmol/g, which is close to the theoretical value.

The main peak in Sr- and K-substituted samples LSMO and LKMO shifted to lower temperatures (365 °C and 360 °C respectively), while a low temperature shoulder (349 °C) appears with LNMO. These features can be attributed to a facilitated reduction of Mn^{4+}. Additionally, a small shoulder appears between 150 °C and 315 °C with those samples (see the dotted box in Fig. 6-3), which is most likely due to the removal of surface oxygen adsorbed species (adspecies). In addition, the onset temperature (T_{onset}) of reduction is about 150 °C which is also lower than that in other four samples. These results indicated that the partial substitution of the A-site La^{3+} cations by Sr^{2+}, Na^+ and K^+ promotes low temperature reducibility of the LMO-based catalysts, in addition to increasing the concentration of surface oxygen species, as well as oxygen vacancies, which should have a beneficial effect for the oxidation of HCHO. In contrast, the opposite behaviour was observed on the other samples, with the main peak shifting toward higher temperatures, such as 462 °C for LCMO, 463 °C for LMO-Na and 411 °C for LMO-OH. The total H_2 consumption at low temperature was 1.58, 1.63 and 1.67 mmol/g for samples LSMO, LNMO and LKMO, respectively, while 1.37 mmol/g of H_2 was consumed in the same temperature range by the reference LMO. Lower H_2 consumption was measured for LCMO, LMO-Na and LMO-OH. Those results

correlate well with the average oxidation state (AOS) of Mn determined by XPS (Table 6-1).
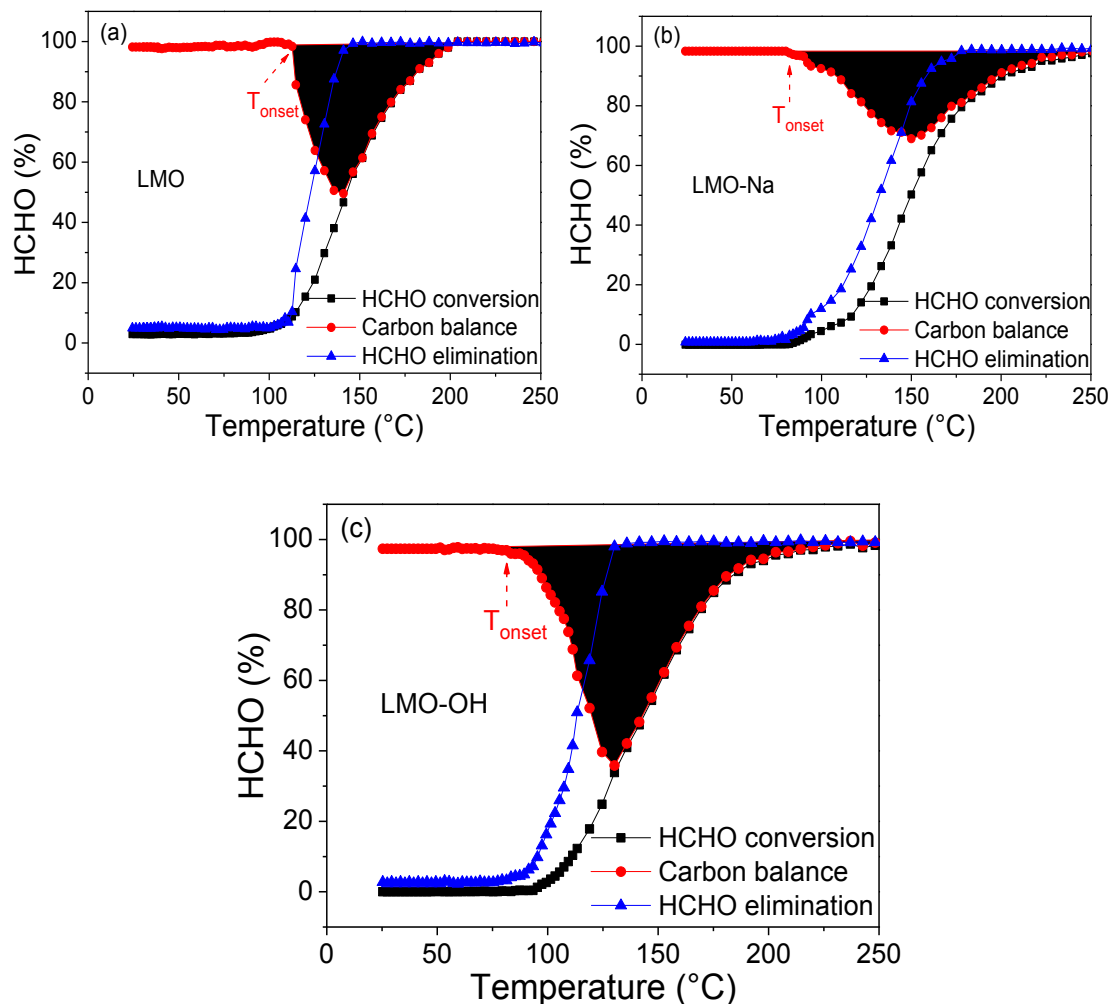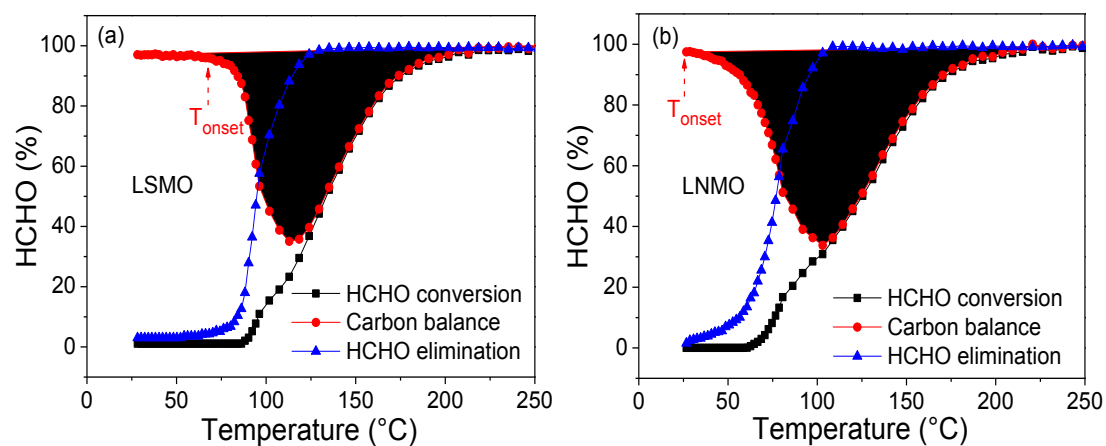
6.3.4 Catalytic activity

Figure 6-4 Catalytic oxidation of HCHO over (a) LMO and two alkali-promoted LMO samples: (b) LMO-Na and (c) LMO-OH
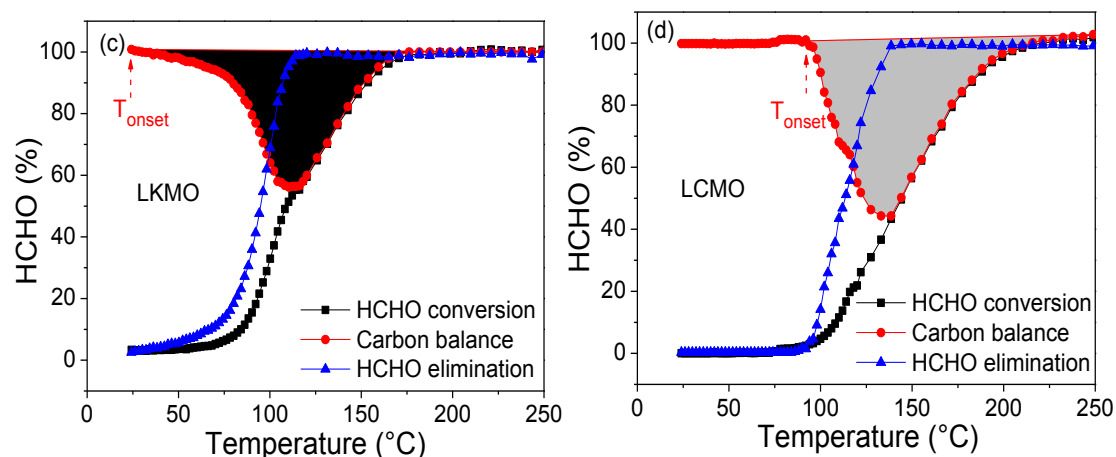
Figure 6-5 Catalytic oxidation of HCHO over four alkali- and alkaline earth-modified LMO samples: (a) LSMO, (b) LNMO, (c) LKMO, (d) LCMO

Formaldehyde (HCHO) oxidation was conducted on all the samples (Fig. 6-4 and Fig. 6-5). According to the literature review [4,5,23,24], some modication approaches, such as addition of sodium cation through impregnation orthe treatment with NaOH solution washing, are proposed to enhance the catalytic activity of a catalyst for the HCHO oxidation. In order to investigate whether these methods will be also working in our perovskites, the sodium supported on LMO (LMO-Na) and NaOH solution treated LMO (LMO-OH) were first evaluated for the catalytic oxidation of HCHO.

Fig. 6-4 exhibits the conversion efficiency of HCHO (into CO_2), the elimination of HCHO as well as the carbon balance over LMO, LMO-OH and LMO-Na with increasing reaction temperature. The T10, T50, and T90 reaction temperatures (corresponding to HCHO conversions of 10, 50, and 90% respectively) are summarized in Table 6-3. Within our experimental conditions, no clear promotion effect of the sodium was observed on the T50 (145 °C over LMO against 150 °C and 144 °C for LMO-Na and LMO-OH, respectively). However, the onset temperature (T_{onset}) related to the carbon balance for LMO-Na and LMO-OH is 82 °C, which is lower than that of LMO (112 °C). This result suggests that after alkali modification, the LMO-Na and LMO-OH have better low-temperature adsorption capacities toward HCHO, which is

line with previous reports [23,24]. Particularly, the sample treated with an alkali solution (LMO-OH) seems to have a larger adsorption capacity of HCHO in comparison with Na supported LMO (LMO-Na). This is likely to be an effect of the increased surface hydroxyl groups.

Table 6-3 Catalytic activity ofseven perovskites for HCHO oxidation

Samples	HCHO conversion temperature			
	T10	T50	T90	T_{onset}
LMO	114	145	185	112
LMO-OH	111	144	185	82
LMO-Na	117	150	200	82
LCMO	108	145	184	93
LKMO	84	108	153	25
LNMO	87	123	167	25
LSMO	96	133	175	68

The catalytic activity of the four substituted LMO samples with alkali and alkaline earth cations (Ca, Sr, Na, K) were compared in Fig. 6-5. Except for LCMO, lower reaction temperatures were obtained with those promoted catalysts compared to the reference LMO. Especially, LKMO achieved a remarkably low T50 temperature of 108 °C, substantially lower than LNMO (123 °C), LSMO (133 °C) and LMO (145 °C) (Table 6-3). Additionally, the substituted samples LSMO, LNMO and LKMO promote the elimination, by adsorption and oxidation, of HCHO at lower temperature. The onset temperature (T_{onset}) of carbon balance for LNMO and LKMO is the room temperature 25 °C, while it is 68 °C for LSMO and 93 °C for LCMO. These values are much lower than for LMO (112 °C), further confirming the good low-temperature HCHO adsorption capability of those alkali-promoted perovskites. Of note, by integration of the carbon balance (grey area), their adsorption capability can be ranked as follows:

LNMO > LSMO > LCMO > LKMO ≈ LMO. The adsorption capability of LCMO seems also to be enhanced slightly compated with the LMO but this enhancement did not result in the improvement of HCHO conversion. The lower adsorption capability of LKMO might due to the fast dissociation of HCHO and its oxidation intermediates such as formate on catalyst surface during HCHO oxidation process.

The improved catalytic activity from the substituted LMO (LSMO, LNMO and LKMO) perovskites might stem from the cumulative effect of two main factors. On one hand, the alkali modified perovskites present the enhanced adsorption capacity of HCHO at low temperature (Fig. 6-5) due to the higher concentration of surface adsorbed oxygen species (O_{ads}). It is known that the chemisorption of HCHO on the surface of a catalyst is always the crucial step to trigger its oxidation. In addition, the surface oxygen species such as structural hydroxyl groups can directly react with HCHO to form formate or carbonate species [25]. Especially, the abundant surface oxygen vacancies in these alkali modified samples are beneficial to activate, adsorb molecule oxygen, and provide the lattice sites of oxygen migration.

On the other hand, their high oxidizing ability also plays a crucial role in the enhancement of catalytic performance. The migration of oxygen species and the oxygen activation on the oxygen vacancies are dependent on the redox cycle of Mn^{4+}/Mn^{3+}. The enrichment in Mn^{4+} not onlyis more favorable for the formation of oxygen vacancies, similar to the behavior with regard to the increase of Co^{3+} in Co_3O_4 [6], but also would enhance the catalytic action of the redox cycle in which Mn^{4+} was reduced in the course of supplying the necessary oxygen species for the oxidation reaction, and then was re-oxidized via the uptaking of molecular oxygen through the oxygen transfer mechanism [21,26]. Briefly, the catalytic oxidation of HCHO may be considered as a function of the adsorbed oxygen species, oxygen vacancies and the redox cycle of

Mn^{4+}/Mn^{3+} at the surface of a catalyst.

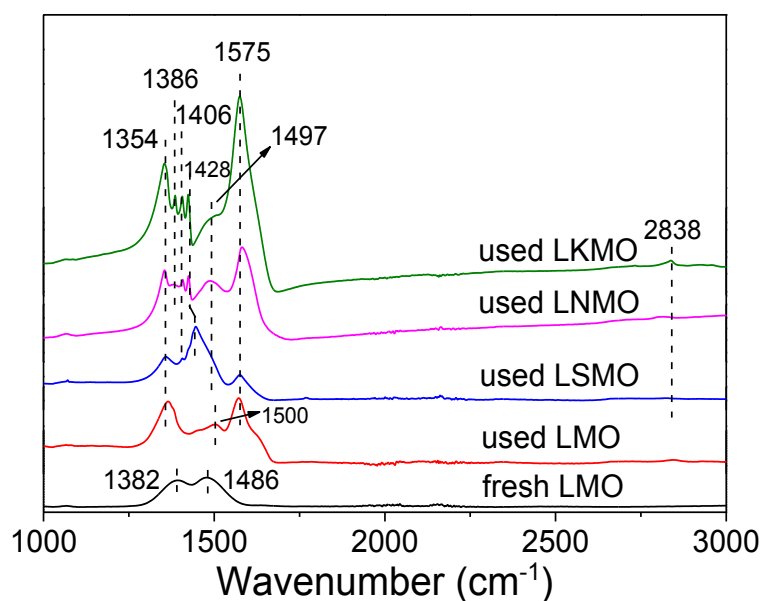## 6.3.5 Possible mechanism of HCHO oxidation

Figure 6-6 ATR-FTIR spectra of LSMO, LNMO, LKMO and LMO before and after HCHO oxidation

To illustrate the formation of intermediate species on the catalysts surface, ATR-FTIR spectra of the reference and the most performing catalysts (LMO, LSMO, LNMO and LKMO) were recorded before and after HCHO exposure (Fig. 6-6). Over LMO, two main bands at 1382 cm^{-1} and 1476 cm^{-1} are observed, belonging to the C-O stretching of carbonate species resulting from the combustion of citrate ions during the preparation of perovskite [27]. The three substituted peroskites also exhibited the same bands (not shown here).

After HCHO oxidation, two new strong bands appeared in all samples at 1354 and 1575 cm^{-1}, ascribing to formate species $v_s(COO)$ and $v_{as}(COO)$ respectively. Two other bands, around 1386 and 2838 cm^{-1}, are also assigned to formate species (eg., $\delta(CH)$ and $v(CH)$) [25,28]. Additionally, three bands of lower intensity can be observed on the spectra of the promoted perovskites. One is around 1428 cm^{-1} ($\delta(CH_2)$) and can be attributed to dioxymethylene (DOM) [29], which is well-known intermediate that easily

oxidize to formate [8]. Two other bands at 1406 and 1497 cm^{-1}, are belong to the surface carbonate species [4,25]. In contrast, a very weak shoulder around 1500cm^{-1} (carbonate species) is observed in the used LMO. Those observations underline the improved adsorption of dioxymethylene, formate and carbonate species on the surface of the substituted perovskites. This is in line with the study of S. Selvakumar [30], who reported that formate species can interact both with Mn ions or alkali ions (potassium), while carbonate species interact only with alkali ions (potassium).

Prior investigations reported that oxidation of HCHO first generates formate species, which are further oxidized to CO_2 in the presence of surface oxygen species [4,6,25,28,30]. Two mechanisms are usually discussed [4,6]. While not uncompatible, they are likely to present different reaction kinetics mainly depending on the degree of participation of superficial -OH groupsinto the HCHO oxidation. Namely, when abundant surface OH groupis present, the direct formate oxidation with surface hydroxyls is preferred (route A). In contrast, when a catalyst lacks surface -OH groups, the formate species may tend to decompose into surface CO being the intermediate product and water, and then are oxidized to CO_2 by the active oxygen (O^*) species (route B).

Route A: $HCHO \rightarrow HCOO^-_{ads} + OH^- \rightarrow CO_2 + H_2O$

Route B: $HCHO \rightarrow HCOO^-_{ads} \rightarrow CO + O^* \rightarrow CO_2$

Following route A, the adsorbed formate species ($HCOO^-_{ads}$) are further decomposed into CO_2 by consuming surface adsorbed oxygen species (mainly superficial -OH groups), which could be regenerated owing to the release of water [28]. As previously reported, surface -OH species play a critical role in HCHO oxidation at low temperature since they enhance the adsorption of HCHO *via* hydrogen bonding while facilitating its activation [25]. On the basis of XPS and TPR results, the

substituted LMO samplespossess higher concentrations of surface adosrbed oxygen species, which may explain their higher catalytic activity at low temperature.

It should be note that the surface -OH species are considered to be consumed quicklyat relativately high temperature [6], and then their supplement relies on the migration of O^{2-} (O_{latt}) species from the oxides.The O^{2-} species are considered to play animportant role in oxidation reaction [31]. Surface activeoxygen (O_2^-, O^-, etc.) could be formed via the complex migration between surface O^{2-} and oxygen vacancy with the sustaining dissociation of dioxygen. That is, oxygen vacancy can be formed by losing one O^{2-}, or vice versa. Molecular oxygen could be adsorbed on oxygen vacancy and activated to generate surface active oxygen species [22,32]. The surface -OH group is then regenerated though the reaction with water (O_2^-, $O^- + H_2O \rightarrow 2OH^-$).

Given that oxygen vacancies participate in the adsorption and dissociation of dioxygen into active oxygen species, and in their further migration [32], thus, owing to their high content of oxygen vacancies, a significant contribution of this mechanism to the global catalytic activity of the substituted perovskites LSMO, LNMO and LKMO is also expected.

6.3.6 Stability test and moisture effect

Stability issues of the catalysts should be taken into account from a practical point of view. Fig. 6-7 illustrates the HCHO conversion and HCHO elimination over time on stream at T50 (corresponding to HCHO conversion of 50%) over LSMO, LNMO, LKMO and LMO. In the beginning, there is a certain rise of the conversion efficiency over the three promoted peroskites which might be due to highly active and non-renewable adsorbed oxygen species [31]. However, a substantial overtime decrease of both HCHO conversion into CO_2 (Fig. 6-7a) and HCHO elimination (Fig. 6-7b) was observed over the promoted perovskites, while LMO activity was relatively stable.
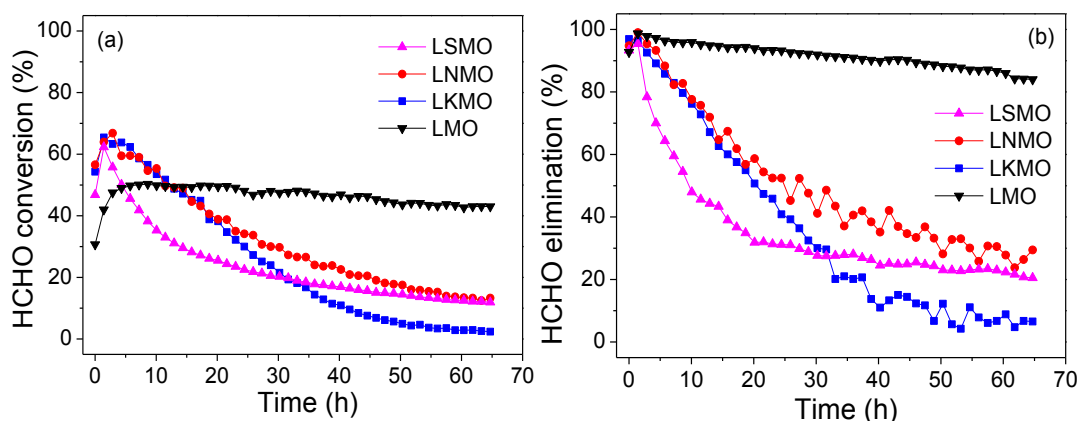
Figure 6-7 HCHO conversion with time on stream over LSMO, LNMO, LKMO and LMO: (a) HCHO conversion (into CO_2), (b) HCHO elimination
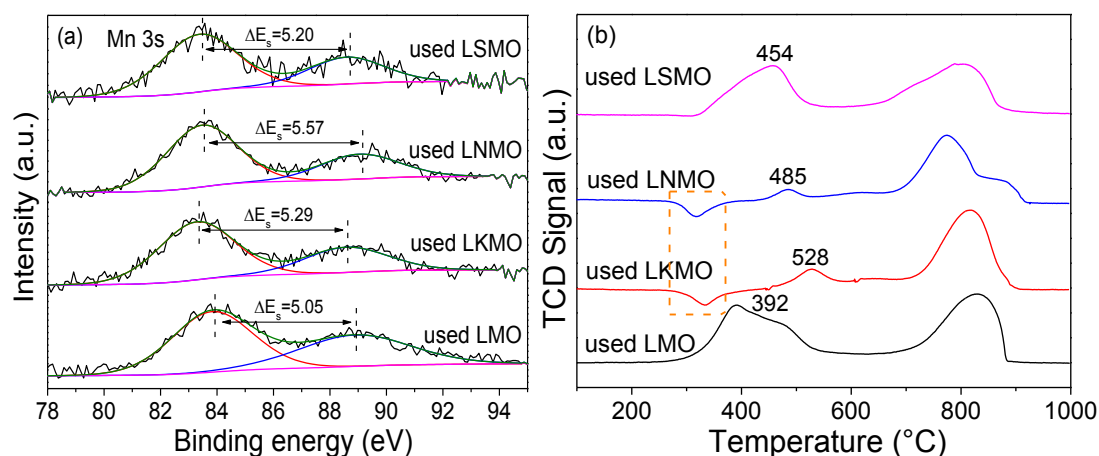

Figure 6-8 Characterization of (a) XPS spectra of Mn 3s, (b) TPR for sample LSMO, LNMO, LKMO and LMO after HCHO stability test

To better understand the undergoing phenomena, the catalysts were again characterized by XPS and TPR after the test. As displayed in Fig. 6-8a, an appreciable change of XPS spectra in the Mn 3s region was observed compared to the fresh catalysts. After HCHO oxidation, the surface average oxidation state of Mn decreased from 3.51 to 3.10, 3.55 to 2.68, 3.63 to 2.99 and 3.40 to 3.26 over LSMO, LNMO, LKMO and LMO, respectively. The substitution of La^{3+} by elements of lower valence thus favours the reduction of lattice Mn^{4+} into Mn^{3+}, maybe even into Mn^{2+}. Obviously, more serious

consumption of Mn^{4+} were found in the alkali modified catalysts (LSMO, LNMO and LKMO).

Similarly, at low temperature region in 200-650 °C of TPR profile (Fig. 6-8b), the amount of consumed H_2 is lower for the used samples (0.83 mmol/g for LSMO and 1.12 mmol/g for LMO) compared to the fresh LSMO (1.58 mmol/g) and LMO (1.37 mmol/g), implying that more Mn species with lower valence state are present in the used catalysts after HCHO oxidation. Moreover, the reducibility ratio (Mn^{4+}/Mn^{3+}) in LSMO is lower than in LMO. This is in good agreement with XPS. Additionally, the H_2-TPR profile of all used catalysts shifts to higher temperatures, indicating that their reducibility becomes lower. Remarkably, in the used alkali-modified samples (LNMO and LKMO) two negative peaks around 320 °C are underlined by the dotted area in Fig.6-8b. It is assumed that this peak belongs to HCHO intermediates, such as formate and carbonate species, which were firmly adsorbed on the catalysts surface.
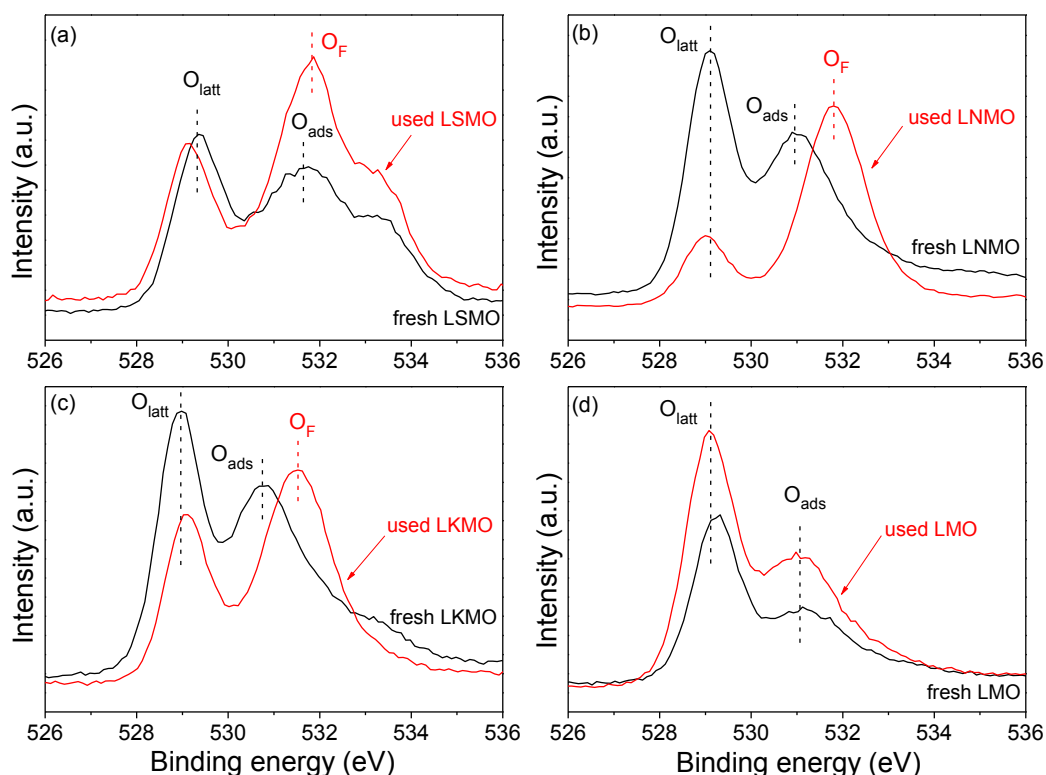

Figure 6-9 Characterization of XPS spectra of O 1s for sample (a) LSMO, (b) LNMO, (c)

LKMO and (d) LMO before and after HCHO stability test

XPS spectra in the O1s region of the catalysts before and after reaction are superposed in Fig. 6-9. After reaction, the intensity of lattice oxygen species (O_{latt}) decreased considerably in LNMO (Fig. 6-9b) and LKMO (Fig. 6-9c), while it decreased only slightly in LSMO (Fig. 6-9a). This correlates with the observed global manganese reduction as O_{latt} were consumed during HCHO oxidation. During the stability test, the transfer from gas-phase oxygen to O_{latt} through the oxygen transfer mechanism seems hindered by the presence of promoters, especially the alkali elements. In contrast, no decrease even enhancement of O_{latt} was found in the used LMO (Fig. 6-9d), which may be used to explain why just the LMO sample has a good stability during long term test.Also, a new intense band noted O_F appeared at high binding energy (531.5 eV) for LSMO, LNMO and LKMO (Fig. 6-9). This new band is associated to O=C and O-C groups from adsorbed formaldehyde and formate species [30].
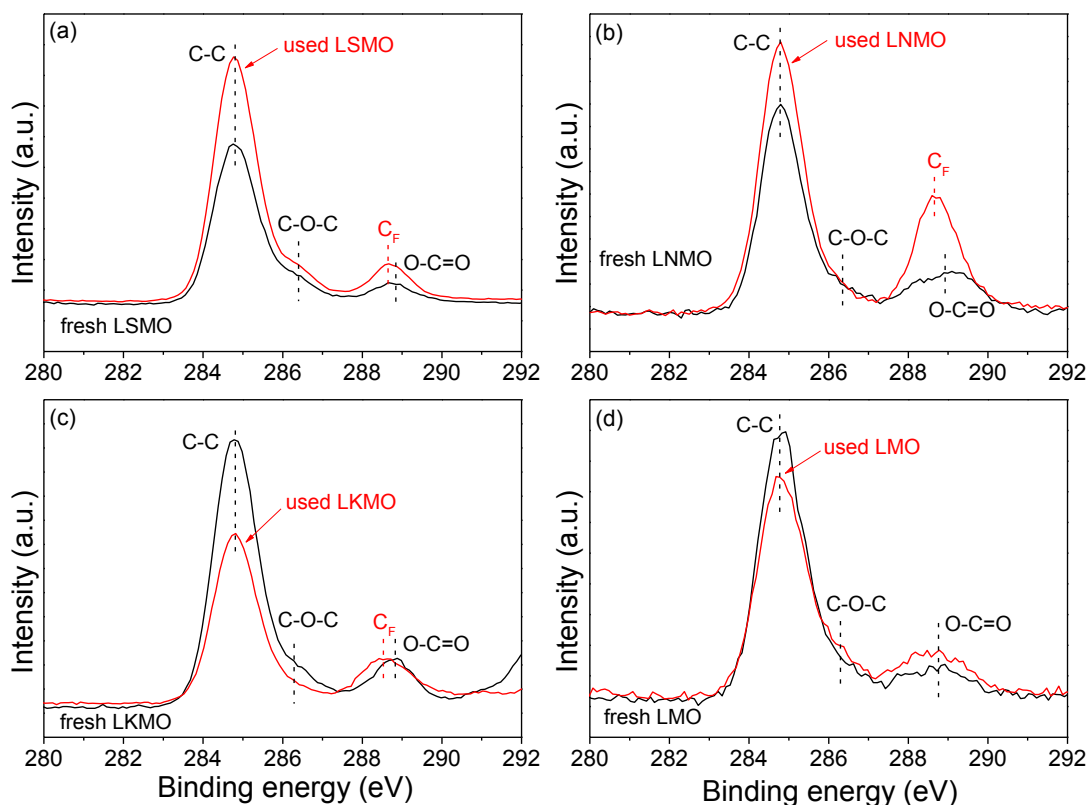

Figure 6-10 Characterization of XPS spectra of C 1s for sample (a) LSMO, (b) LNMO, (c)

LKMO and (d) LMO before and after HCHO stability test

Similar phenomena were also found in XPS spectra of C1s region (Fig. 6-10). Three XPS peaks around 284.8 eV, 286. 3 eV and 288.8 eV are commonly seen, which can be attributed to C-C, C-O-C and O-C=O groups from carboxylate species, repectively. After HCHO oxidation, a new low intensity band named C_F emerged around 288.6 eV for the three substituted perovskites. This binding energy is comparable to the binding energy of adsorbed HCHO on TiO_2 surface [33]. Moreover, C1s binding energy should be similar for both formate and HCHO species, assuming that the molecules are bonded end-on through the oxygen atom [30]. Therefore C_F contribution could be attributed to the presence of both HCHO and formate species on the surface of the substituted perovskites, which is line with the XPS O1s and ATR-FTIR observations. No or less accumulation of formaldehyde, formate or carbonate species over LMO might imply that these species transform or desorb faster over LMO surface.

In a typical HCHO oxidation process, HCHO is first adsorbed on the catalyst surface, and then oxidized by surface active oxygen species into DOM, formate, carbonate and finally to CO_2. Then the consumed surface oxygen species are replenished via the adsorption and dissociation of dioxygen and/or water. Thus, the catalytic cycle is looped [34]. In the short term, the adsorption and accumulation of HCHO and intermediates on catalyst surface allows to obtain higher conversions. However, during the long time stability test, a large accumulation of these species on the surface will not only result in a drastic consumption of surface active oxygen species and high valence state of Mn (Mn^{4+}), as shown by XPS and H_2-TPR, but it also prevents the adsorption and activation of dioxygen and/or water on the catalyst surface because of steric hindrance [9,35-37]. Consequently, the HCHO oxidation activity of the

substituted perovskites was rapidly inhibited.

According to the literature [4,5], the doping of noble metal-supported catalysts by alkali ions such as Na or K has a drastic promotion effect on HCHO oxidation, and their tests were usually conducted under controlled humidity. In fact, moisture is considered as a key factor for the catalytic oxidation of HCHO, having a dual role as either an inhibitor or a promoter [38]. High relative moisture capacity in the reactive stream has been reported to provoke a notable loss of HCHO oxidation activity due to competitive adsorption on active sites [26]. Meanwhile, another study reported that controlled amounts of moisture is not only beneficial to the desorption of carbonate *via* competitive adsorption on the active sites, but it also facilitates the regeneration of surface -OH groups [25]. Thus it is essential to investigate whether a controlled moisture capacity can improve the performances of the alkali-substituted perovskites (LNMO and LKMO).

The effect of moisture on the conversion of HCHO was investigated by adding water to the carrier gas (corresponding to a relative moisture capacity of 46% at room temperature), as shown in Figure 11. Compared to the stability results in dry conditions (Fig. 6-7), the presence of H_2O greatly improved the catalytic activity of LNMO and LKMO, with only a slight overtime decrease of HCHO conversion and HCHO elimination. In addition, the K-promoted perovskite presents a more durable activity than the Na-promoted perovskite.
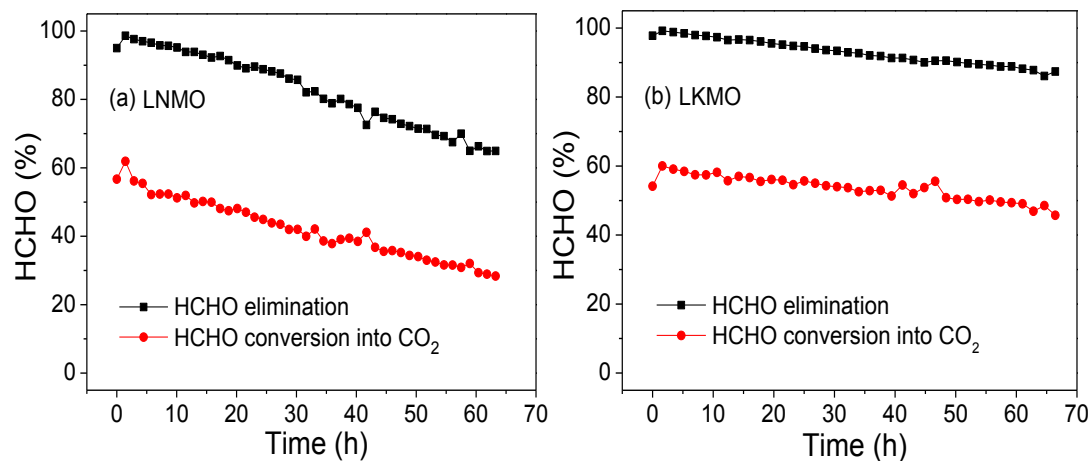
Figure 6-11 Effect of moisture on HCHO conversion with time on stream over (a) LNMO and (b) LKMO

Thus in our conditions and as reported in the case of birnessite [25], moisture helps avoiding an accumulation of formate and carbonate species on the surface of the catalysts, and surface -OH groups can be regenerated by the reaction between surface active oxygen species and water. Moreover, the authors proposed that HCHO could be adsorbed *via* hydrogen bonding with the water bonded on the surface of the catalyst. In addition, the doping of LMO perovskite with alkali or alkaline earth ions would facilitate the activation of H_2O and chemisorbed oxygen, therefore leading to higher performance of the catalyst for the HCHO oxidation [4]. These elements allow to explain the long-term activity observed in moisture condition.

6.4 Conclusions

In summary, this study is devoted to the development of novel modified perovskites for the oxidation of HCHO. A series of alkali- and alkaline earth-modified perovskites were synthesized from a reference $LaMnO_3$ (LMO). Following the first tests, three catalysts based on the partial substitution of La^{3+} by Sr^{2+}, Na^+ and K^+ (LSMO, LNMO and LKMO) presented higher HCHO oxidation activity than the reference LMO. Especially, a T50 of 108 °C was obtained with LKMO, which is one

of the lowest temperatures reported so far with perovskites. Those improved catalytic performances stem from a larger amount of active oxygen species, oxygen vacancies and higher Mn^{4+}/Mn^{3+} ratio at the surface of the catalysts.

Stability tests in dry and humid conditions were conducted over 55h on LMO and the three substituted LMO perovskites. While the substituted perovskites initially presented higher catalytic activity, a fast deactivation was observed under dry conditions. This deactivation was minimized when humidity was added to the carrier gas, allowing the catalysts to present long-term activity. In brief, these results shed light on the catalytic promoting effect of alkali- and alkaline earth-modified perovskites, which shall guide future research toward the further improvement of perovskite-based catalysts. This would be beneficial to the development of common, low-cost and high-efficiency materials for indoor pollution control.

References

[1] G.Avgouropoulos, E. Oikonomopoulos, D. Kanistras, T. Loannides, Complete oxidation of ethanol over alkali-promoted Pt/Al_2O_3 catalysts, Appl. Catal. B 65 (2006) 62-69.

[2] J.T. Hou, L.L.Liu, Y.Z. Li, M.Y. Mao, H.Q. Lv, X.J. Zhao, Tuning the K^+ concentration in the tunnel of OMS-2 nanorods leads to a significant enhancement of the catalytic activity for benzene oxidation, Environ. Sci. Technol. 47 (2013) 13730-13736.

[3] D.Q. Han, C.Q. Zhou, H.M. Yin, D.J.Zhang, X.H. Xu, Reactivity of the alkaline pretreated nanoporous gold for the CO oxidation, Catal. Lett. 141 (2011) 1026-1031.

[4] C.B.Zhang, F.D.Liu, Y.P. Zhai, H.Ariga, N. Yi, Y.C.Liu, K. Asakura, Alkali- metal- promoted Pt/TiO_2 opens a more efficient pathway to formaldehyde oxidation at ambient temperatures, Angew. Chem. Int. Ed. 51 (2012) 9628-9632.

[5] C.B. Zhang, Y.B. Li, Y.F. Wang, H. He, Sodium-promoted Pd/TiO_2 for catalytic oxidation of formaldehyde at ambient temperature, Environ. Sci. Technol. 48 (2014) 5816-5822.

[6] B.Bai, J. Li, Positive effects of K^+ ions on three-dimensional mesoporous Ag/Co_3O_4 catalyst for HCHO oxidation, ACS Catal. 4 (2014) 2753-2762.

[7] F.Xu, Z.Huang, P. Hu, Y. Chen, L. Zheng, J. Gao,X.Tang, The promotion effect of isolated potassium atoms with hybridized orbitals in catalytic oxidation,Chem. Commun. 51 (2015) 9888-9891.

[8] S.P.Rong, K.Z.Li, P.Y.Zhang, F.Liu, J.Y.Zhang. Potassium associated manganese vacancy in birnessite-type manganese dioxide for airborne formaldehyde oxidation, Catal. Sci. Technol. 8 (2018) 1799-1812.

[9] J.Wang, J.Li, P. Zhang, G. Zhang, Understanding the "seesaw effect" of interlayered K^+ with different structure in manganese oxides for the enhanced formaldehyde oxidation,Appl. Catal. B224 (2018) 863-870.

[10] S.Royer, D. Duprez, F. Can, X.Courtois, C.B.Dupeyrat, S.Laassiri, H. Alamdari, Perovskites as substitutes of noble metals for heterogeneous catalysis: dream or reality, Chem. Rev. 114 (2014) 10292-10368.

[11] Y.N.Lee, R.M.Lago, J.L.G. Fierro, V.Cortes, F.Sapina, E.Martinez, Surface properties and catalytic performance for ethane combustion of $La_{1-x}K_xMnO_{3+\delta}$ perovskites, Appl. Catal. A207 (2001) 17-24.

[12] W.Hong, Z.Zhen, C.M. Xu, L. Jian, Nanometric $La_{1-x}K_xMnO_3$, perovskite-type oxides – highly active catalysts for the combustion of diesel soot particle under loose contact conditions, Catal. Letters, 102 (2005)251-256.

[13] A.Giroir-Fendler, S.Gil, A. Baylet, $(La_{0.8}A_{0.2})MnO_3$ (A= Sr, K) perovskite catalysts for NO and $C_{10}H_{22}$ oxidation and selective reduction of NO by $C_{10}H_{22}$,Chinese J. Catal. 35 (2014) 1299-1304.

[14] F.C. Buciuman, F.Patcas, J. Menezo, J. Barbier, T.Hahn, H.Lintz, Catalytic properties of $La_{0.8}A_{0.2}MnO_3$(A = Sr, Ba, K,Cs) and $LaMn_{0.8}B_{0.2}O_3$(B = Ni, Zn, Cu) perovskites: 1. Oxidation of hydrogen and propene,Appl. Catal. B 35 (2002) 175-183.

[15] Y.Yang, J. Huang, S.Wang, S.Deng, B.Wang, G. Yu, Catalytic removal of gaseous unintentional POPs on manganese oxide octahedral molecular sieves,Appl. Catal. B 142-143 (2013) 567-568.

[16] S. Royer, H.Alamdari, D.Duprez, S.Kaliaguine, Oxygen storage capacity of $La_{1-x}A'_xBO_3$ perovskites (with A′= Sr, Ce; B= Co, Mn)-relation with catalytic activity in the CH_4 oxidation reaction, Appl. Catal. B 58 (2005) 273-288.

[17] W. P.Stege, L.E. Cadús, B.P. Barbero, $La_{1-x}Ca_xMnO_3$ perovskites as catalysts for total oxidation of volatile organic compounds, Catal. Today172 (2011) 53-57.

[18] B.P.Barbero, J.A.Gamboa, L.E. Cadús, Synthesis and characterisation of $La_{1-x}Ca_xFeO_3$ perovskite-type oxide catalysts for total oxidation of volatile organic compounds, Appl.Catal. B 65 (2006) 21-30.

[19] V.P. Santos, M.F.R.Pereira, J.J.M. Órfão, J.L. Figueiredo, The role of lattice oxygen on the activity of manganese oxides towards the oxidation of volatile organic compounds, Appl. Catal. B99 (2010) 353-363.

[20] N.A. Merino, B.P. Barbero, P. Eloy, L.E. Cadús, $La_{1-x}Ca_xCoO_3$ perovskite-type oxides: identification of the surface oxygen species by XPS, Appl. Surf. Sci. 253 (2006) 1489-1493.

[21] J.G.Deng, L. Zhang, H.X. Dai, H. He, C.T. Au,Strontium-doped lanthanum cobaltite and manganite: highly active catalysts for toluene complete oxidation, Ind. Eng. Chem. Res. 47 (2008) 8175-8183.

[22] J.J. Zhu, H.L. Li, L.Y. Zhong, P. Xiao, X.L. Xu,X.G. Yang, Z. Zhao, J.L. Li, Perovskite oxides: Preparation, characterizations, and applications in heterogeneous catalysis, ACS Catal. 4 (2014) 2917-2940.

[23] J. Yu, X. Li, Z. Xu, W. Xiao, NaOH-modified ceramic honeycomb with enhanced formaldehyde adsorption and removal performance, Environ. Sci. Technol. 47 (2013) 9928-9933.

[24] Y.C. Huang, W.J.Fan, B. Long, H.B. Li, W.T. Qiu, F.Y.Zhao, Y.X. Tong, H.B. Ji, Alkali-modified non-precious metal 3D-NiCo$_2$O$_4$ nanosheets for efficient formaldehyde oxidation at low temperature, J. Mater. Chem. A 4 (2016) 3648-3654.

[25] J.L.Wang, P.Y.Zhang, J.G. Li, C.J. Jiang, R. Yunus, J. Kim, Room-temperature oxidation of formaldehyde by layered manganese oxide: effect of water, Environ, Sci. Technol. 49 (2015) 12372-12379.

[26] X.F. Tang, Y.G. Li, X.M.Huang, Y. Xu, H.Q. Zhu, J.G. Wang, W.J. Shen, MnO$_x$-CeO$_2$ mixed oxide catalysts for complete oxidation of formaldehyde: effect of preparation method and calcination temperature, Appl. Catal. B 62 (2006) 265-273.

[27] Y.Y. Li, L.H. Xue, L.F. Fan, Y.W. Yan, The effect of citric acid to metal nitrates molar ratio on sol-gel combustion synthesis of nanocrystalline LaMnO$_3$ powders, J. Alloy. Compd. 478 (2009) 493-497.

[28] J. Quiroz, J.M. Giraudon, A. Gervasini, C. Dujardin, C. Lancelot, M. Trentesaux, J.F. Lamonier, Total oxidation of formaldehyde over MnO$_x$-CeO$_2$ catalysts: The effect of acid treatment, ACS Catal. 5 (2015) 2260-2269.

[29] J.Arana, J.M. Dona-Rodrıguez, C.G. Cabo, O. González-Dıaz, J.A. Herrera-Melián, J. Pérez-Peña, FTIR study of gas-phase alcohols photocatalytic degradation with TiO$_2$ and AC-TiO$_2$, Appl. Catal. B 53 (2004) 221-232.

[30] S. Selvakumar, N. Nuns, M. Trentesaux, V.S. Batra, J.M. Giraudon, J.F. Lamonier, Reaction of formaldehyde over birnessite catalyst: A combined XPS and ToF-SIMS study, Appl. Catal. B 223 (2018) 192-200.

[31] J.H.Zhang, Y.B. Li, L.Wang, C.B.Zhang, H.He, Catalytic oxidation of formaldehyde over manganese oxides with different crystal structures, Catal. Sci. Technol. 5 (2015) 2305-2313.

[32] X.W.Liu, K.B.Zhou, L.Wang, B.Y.Wang, Y.D. Li, Oxygen vacancy clusters promoting reducibility and activity of ceria nanorods, J. Am. Chem. Soc. 131 (2009) 3140-3141.

[33] Q. Yuan, Z.F.Wu, Y.K. Jin, L.S.Xu, F.Xiong, Y.S. Ma, W.X. Huang, Photocatalytic cross-coupling of methanol and formaldehyde on a rutile TiO$_2$ (110) surface, J. Am. Chem. Soc. 135 (2013) 5212-5219.

[34] J.L.Wang, J.G.Li, C.J. Jiang, P. Zhou, P.Y. Zhang, J.G. Yu, The effect of manganese vacancy in birnessite-type MnO$_2$ on room-temperature oxidation of formaldehyde in air, Appl. Catal. B 204 (2017) 147-155.

[35] J.Zhao, X.D. Yang, Photocatalytic oxidation for indoor air purification: a literature review, Build. Environ. 38 (2003) 645-654.

[36] A.P.V. Soares, M.F.Portela, A.Kiennemann, L.Hilaire, Mechanism of deactivation of iron-molybdate catalysts prepared by coprecipitation and sol-gel techniques in methanol to formaldehyde oxidation, Chem. Eng. Sci. 58 (2003)1315-1322.

[37] X.F.Zhu, B. Cheng, J.G. Yu, W.K. Ho, Halogen poisoning effect of Pt-TiO$_2$ for formaldehyde catalytic oxidation performance at room temperature, Appl. Surf. Sci. 364 (2016) 808-814.

[38] M.Date, M. Haruta, Moisture effect on CO oxidation over Au/TiO$_2$ catalyst, J. Catal. 201 (2001) 221-224.

Chapter 7 La-deficient lanthanum manganite perovskitesfor catalytic oxidation of formaldehyde: Impact of cationic vacancy?

7.1 Introduction

While most of the research effort focused on stoechiometric lanthanum manganite perovskites with varying oxygen excess, commonly noted $LaMnO_{3+\delta}$, it should be noted that those structures are actually defective in both La and Mn positions [1,2]. Thus, a more rigourous formula would be $La_{1-x}Mn_{1-x}O_3$. For instance, a δ value of 0.158 corresponds to 5% of La and Mn vacancies ($La_{0.95}Mn_{0.95}O_3$), though the La/Mn vacancy ratio can also be controversial [3,4]. In particular, a deficiency of A-site ions in the perovskite lattice ($A_{1-x}B_{1-y}O_3$, with x>y) leads to self- (or vacancy-) doped perovskites [5]. However, the latter materials showed some different results in heterogeneous catalysis and especially in oxidation reactions [6-10]. Thus it is necessary to further clarify the role of cationic vacancy in catalytic process.In this work, a series of lanthanum-deficient LaMn perovskite-based materials was prepared. The molar concentration of lanthanum was modulated during the synthesis, resulting in materials having $La_{1-x}Mn$ as a general formula (with x = 0.1, 0.2, 0.3 and 0.4). This series was extensively characterized and tested for the mild oxidation of HCHO. By combining characterization and catalytic results, a deeper understanding of the influence of cationic vacancies on the catalytic performances of perovskite-based materials will be obtained.

7.2 Experimental section

7.2.1 Synthesis of catalysts

A series of manganese-based $La_{1-x}Mn$ perovskite-based materials (with x = 0, 0.1, 0.2, 0.3 and 0.4) was prepared following a conventional citric acid complexation method, starting from the metal nitrate precursors $Mn(NO_3)_2 \cdot 4H_2O$ (97.0 %, Aldrich) and $La(NO_3)_3 \cdot 6H_2O$ ($\geq$ 99.0 %, Sigma-Aldrich), and citric acid (+99.5 %, Alfa Aesar).

For the synthesis of the reference perovskite as the same to the description in

Section 5.2.1, a molar ratio $(n_{Mn} + n_{La})/n_{citric\ acid}$ of 1 was applied. A certain amount of La nitrate, Mn nitrate and citric acid were dissolved and mixed in distilled water under magnetic stirring. The resulting homogeneous solution was stirred overnight at room temperature. A rotary evaporation step was used to remove the excess of water, resulting in a gel. The obtained gel was thermally treated in a muffle oven under air over two steps: 180 °C for 1 h (3 °C min^{-1}), and 700 °C for 8 h (2 °C min^{-1}). This perovskite was labeled LaMn. The same procedure was applied for the synthesis of La-deficient perovskites, keeping the $(n_{Mn} + n_{La})/n_{citric\ acid}$ molar ratio constant of 1, as well as a molar ratio n_{La}/n_{Mn} of 0.9, 0.8, 0.7, and 0.6. The corresponding perovskites were labeled La$_{0.9}$Mn, La$_{0.8}$Mn, La$_{0.7}$Mn, La$_{0.6}$Mn, respectively. In the case of La$_{0.7}$Mn and La$_{0.6}$Mn, the second temperature step was adjusted at 750°C to obtain fully crystalline perovskite phases. The reason will be discussed in section 3.1.

7.2.2 Catalytic oxidation of formaldhyde (HCHO)

The catalytic oxidation of formaldehyde (HCHO) was carried out as described in section 5.2.2. The formaldehyde (HCHO) oxidation into CO$_2$ was expressed as HCHO conversion, while HCHO elimination refers to the removal efficiency of HCHO. They were calculated using the following equations, respectively:

$$\text{HCHO conversion (into CO}_2\text{) (\%)} = \frac{[CO_2]_t}{[HCHO]_0} \times 100 \tag{7-1}$$

$$\text{HCHO elimination (\%)} = \frac{[HCHO]_0 - [HCHO]_t}{[HCHO]_0} \times 100 \tag{7-2}$$

Where $[HCHO]_t$ and $[CO_2]_t$ are their concentration at time t as monitored by GC, and $[HCHO]_0$ is the initial HCHO concentration (100 ppm).

During the stability test, a fresh catalyst was first activated as indicated before (300 °C, 1h under 20 vol% O$_2$/He, 100 mL·min^{-1}). Then the reacting gas (100 ppm HCHO in 20 vol% O$_2$/He, 100 mL·min^{-1}) was passed through the catalyst bed at T50 reaction temperature (corresponding to 50 % HCHO conversion) for at least 63h.

7.2.3 Characterization

In situ XRD experiments were performed on a Brücker D8 Advance diffractometer with monochromatized Cu K$_{\alpha 1}$ radiation. The samples were deposited on a kanthal sample holder and XRD patterns were collected every 50 °C from room temperature to 1123 °C, under a gas mixture composed of 3% H$_2$ diluted in He (50 mL min^{-1}). All diffractograms were collected after 30 min after stabilizing the sample at the desired temperature. *Insitu* experiments allowed us to follow the evolution of the sample structure with the reduction degree. Nitrogen sorption measurements were performed at -196 °C on a Micromeritics Flow Sorb III serial 416 apparatus. Samples were degassed at 150 °C during 6h prior analysis. Specific surface area (S_{BET}) was calculated according to the Brunauer-Emmett-Teller (BET) method.The detailed information about other characterization techniques such as X-ray diffraction patterns (XRD), X-ray Photoelectron Spectroscopy (XPS), and Temperature programmed reductions (TPR) is shown in Section 5.2.3. Stoichiometry of La and Mn in the solids and in the filtrates were monitored by Inductively coupled plasma-optical emission spectroscopy (ICP-OES) (Agilent Technologies 700 Series spectrometer). Before analysis, the solids were dissolved in a concentrated HCl/HNO$_3$ mixture.

7.3 Results and Discussion
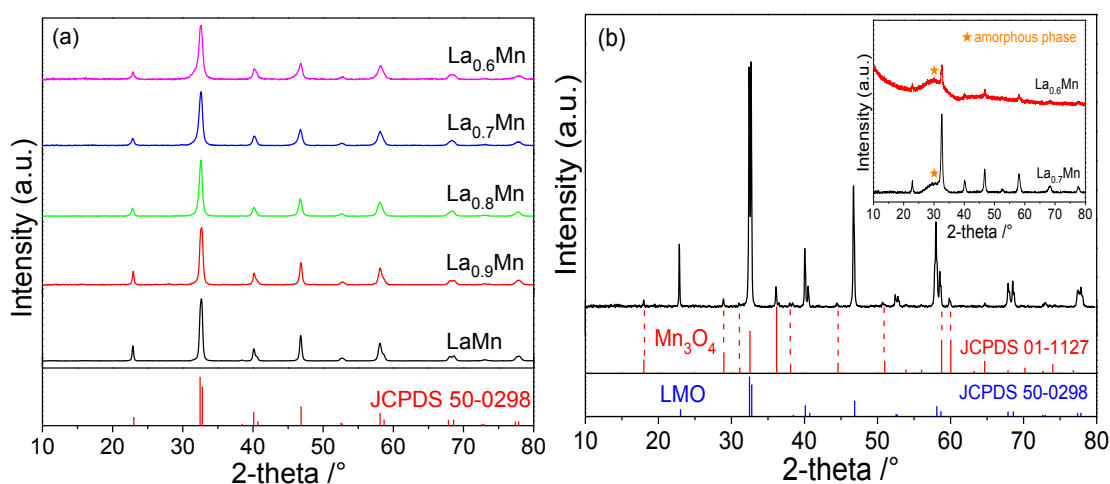
7.3.1 Crystal phase structure

Figure 7-1 Wide-angle XRD patterns of (a) LaMn and la-deficient perovskites, (b) XRD pattern of $La_{0.6}Mn$ calcined at 1000 °C in comparison with the standard XRD patterns

XRD patterns of as-synthesized samples are shown in Fig. 7-1. The first three samples (LaMn, $La_{0.9}Mn$, $La_{0.8}Mn$) calcined at 700 °C present the typical diffraction pattern of LaMn (JCPDS 50-0298) with characteristic peaks at $2\theta = 23.0°$, $32.5°$, $40.1°$, $46.9°$, $58.1°$, $68.6°$ and $77.8°$. No obvious diffraction peaks for impurities like La_2O_3 and MnO_x were observed. However, for the samples $La_{0.7}Mn$ and $La_{0.6}Mn$ annealed at 700 °C, a broad hump around 29° was observed obviously which can be indexed to the retained amorphous phase (i.e. manganese oxides) (inset of Fig. 7-1b) [11,12]. This bump disappeared after higher temperature (750 °C) calcination (Fig. 7-1a). As reported in previous literature [4,11], manganese oxide phases such as Mn_3O_4 usually form in lanthanum-deficient perovskites. Herein, no impurities can be observed which can be due 1) to their low crystallinity or 2) to their low concentration in the sample. In order to verify this point, the selected sample $La_{0.6}Mn$ was further calcined at 1000 °C during 4h and the XRD pattern was exhibited in Fig. 7-1b. A secondary crystalline phase, Mn_3O_4, can unambigously be observed. Thus it can be concluded that the most La-

deficient samples ($La_{0.6}Mn$ and $La_{0.7}Mn$) are actually composed of a mixture of LaMn perovskite and Mn_3O_4.

As seen in Table 7-1, crystallite size (d_{LaMn}) of the samples decreased from 26 to 19 nm with decreasing the ratio of La/Mn, when applying the Sherrer equation to the (024) plane ($2\theta = 46.9°$). The Scherrer equation was not applied to main (110) and (104) planes ($2\theta = 32.5°$ and $32.8°$) because their resulting diffraction peaks were confounded into one large peak. The textural properties are also presented in Table 7-1. As expected for perovskite materials, all catalysts had relatively low specific surface areas (from 18 to 24 m^2 g^{-1}) due to high temperature calcination and lack of internal porosity.

Table 7-1 Textural and structural properties of the $La_{1-x}Mn$ samples

Samples	Crystalline phases[a]	S_{BET} (m^2/g)	d_{LaMn} (nm)
LaMn	LMO[b]	18	26
$La_{0.9}Mn$	LMO	22	24
$La_{0.8}Mn$	LMO	20	23
$La_{0.7}Mn$	LMO/Mn_3O_4	24	21
$La_{0.6}Mn$	LMO/Mn_3O_4	22	19

[a]As identified by X-ray diffraction.
[b]LMO means peroviskite phase.
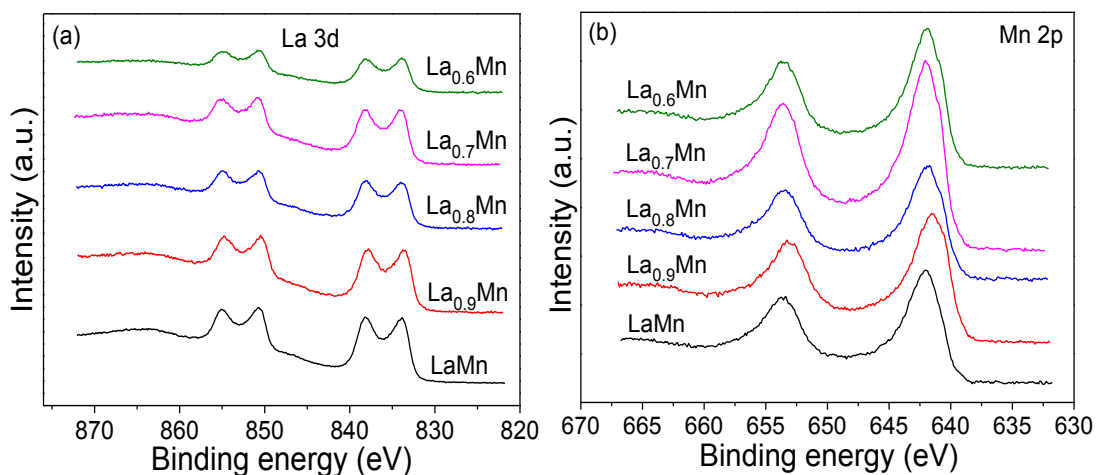
7.3.2 ICP and XPS analysis

Figure 7-2 Typical XPS spectra of (a) La3d and (b) Mn2p of LaMn and la-deficient perovskites
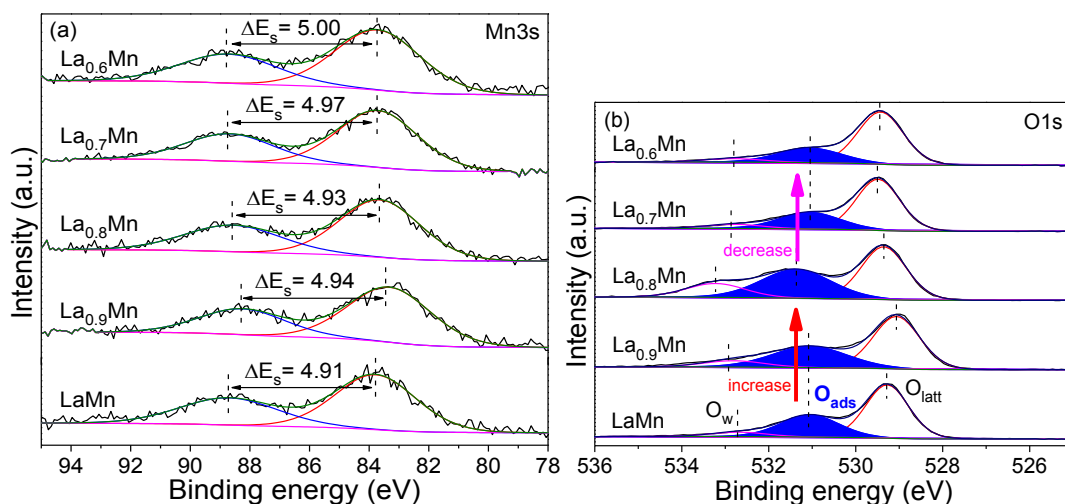

Figure 7-3 Typical XPS spectra of (a) Mn 3s and (b) O 1s of LaMn and la-deficient perovskites

Surface properties (elemental composition and chemical states) were investigated by X-ray photoemission spectroscopy (XPS), while the bulk composition was evaluated by ICP analysis. XPS spectra for La3d and Mn2p, Mn3s and O1s core levels are illustrated in Fig. 7-2 and Fig. 7-3, respectively. The quantitative elemental compositions including surface atomic ratios of La/Mn, Mn/O and La/O, as well as the molar ratio of lattice oxygen and adsorbed oxygen species are summarized in Table 7-2. Within experimental and apparatus errors, the determined atomic ratios of La/Mn by ICP follow closely the La/Mn ratios in the initial reactive solutions. For XPS analysis, the LaMn perovskite particles are known to present A-site enrichment at their surface.

However, in La-deficient perovskites ($La_{1-x}Mn$, x= 0.1, 0.2, 0.3, 0.4), the La/Mn atomic ratios in XPS tended to be slightly lower than that in ICP, which might indicate that the la-deficient perovskites have a promotion for the dispersion of La and the exposure of Mn on the surface. Additionally, the study provides a method to overcome one disadvantage of raw perovskite (typical A-site enrichment on the surface), that is, decrease the lanthanum excess at the surface thanks to the la-deficient synthesis. The La 3d XPS spectra of all samples (Fig. 7-2a) showed the decrease of peak intensity, indicating the deficiency of La. The corresponding Mn 2p XPS spectra are shown in Fig. 7-2b. It exhibited two peaks at ~642 eV and ~653 eV, assigning to Mn $2p_{3/2}$ and Mn $2p_{1/2}$ respectively. High-resolution Mn 3s XPS spectra can be observed in Fig. 7-3a. The average oxidation state (AOS) of the surface Mn was determined by the binding energies of the doublet separation of Mn 3s (ΔE_s) following the correlation: AOS (Mn) = $8.956 - 1.126 \times \Delta E_s$ [13]. For the reference LaMn, the surface AOS (Mn) is about 3.42 (Table 7-2) which is little higher than the theoretical value (3.3) in LaMn, in agreement with a mixture of $Mn^{4+/3+}$ with Mn^{3+} as the predominant cation. The La-deficient samples ($La_{0.9}Mn$ and $La_{0.8}Mn$) showed little change of AOS (Mn) with values of 3.40 and 3.41 respectively. This suggests that the average valence of these two samples tend to be stable when a similar thermal post-treatment is applied [5]. The presence of Mn_3O_4 in the two other samples ($La_{0.7}Mn$ and $La_{0.6}Mn$) lowered the AOS (Mn) to 3.36 and 3.33. Assuming a constant AOS of the La-deficient perovskite particles, this implies that part of Mn_3O_4 are present in the samples, respectively.

Table 7-2 Relative surface abundances of the elements constituting the $La_{1-x}Mn$ samples

Samples	La/Mn		Mn/O	La/O	AOS (Mn)	O_{latt}/O_{tot}	O_{ads}/O_{tot}
	ICP	XPS					
LaMn	1.00	1.27	0.95:3	1.06:3	3.42	0.59	0.34
$La_{0.9}Mn$	0.88	0.87	0.83:3	0.73:3	3.40	0.56	0.35
$La_{0.8}Mn$	0.84	0.73	0.71:3	0.52:3	3.41	0.46	0.39
$La_{0.7}Mn$	0.69	0.49	1.14:3	0.56:3	3.36	0.64	0.29
$La_{0.6}Mn$	0.60	0.42	1.21:3	0.51:3	3.33	0.68	0.26

Usually, by substituting the A-site cation (La^{3+}) of perovskite by an external lower valency cation (e.g., Sr^{2+}) without destroying the lattice, the oxidation state of B-site cation as well as the oxygen vacancy in the structure will be adjusted to be balanced either by increasing the average oxidation state of the B-site cation ($La_{1-x}^{3+}A_x^{z+}Mn_{0.7-x(3-z)}^{3+}Mn_{0.3+x(3-z)}^{4+}O_{3.15}$) or by the formation of oxygen vacancy (V_0) ($La_{1-x}^{3+}A_x^{z+}(V_0)_yMn_{0.7}^{3+}Mn_{0.3}^{4+}O_{3.15-y}$) [14]. In contrast, the La-deficient LaMn perovskite herein seems to possess a relatively large amount of V_0 as the average oxidation state of Mn do not increase. As shown in Table 7-2, the slight deficency of La ($La_{0.9}Mn$ and $La_{0.8}Mn$) in the structure induce the decrease of surface atomic ratios of La/O (the value decrease from 1.06:3 to 0.52:3) as well as Mn/O (the value decrease from 0.95:3 to 0.71:3), suggesting that the La deficiency resulted in not only the formation of lanthanum vacancy (V_{La}), but also the formation of Mn vacancy (V_{Mn}) on the surface.

However, when the La/Mn atomic ratio further decreased from 0.69 to 0.60, the atomic ratios of La/O seemed to be stable but the atomic ratios of Mn/O increased dramatically. According to the analysis above, the lowest La/Mn molar ratio in LaMn perovskite might be around 0.80. Below this ratio, the excess of manganese will form the most stable oxide phase, which is Mn_3O_4 under our conditions. While $La_{0.6}Mn$ and $La_{0.7}Mn$ is below the theoretical limit, thus explaining the presence of Mn_3O_4.

Fig. 7-3b displays the XPS spectra in the O1s region for all samples. Three peaks

can be observed aroud 529.3, 531.1, and 532.8 eV, representing the surface lattice oxygen (O^{2-}, denoted as O_{latt}), the surface adsorbed oxygen species (such as O_2^{2-} or O^- belonging to defect-oxide and OH group, denoted O_{ads}), and likely to be associated with the molecular water adsorbed on the surface (denoted O_w), respectively [15,16]. Surface adsorbed oxygen species are usually linked to surface oxygen vacancies [17]. The former was considered to have a high mobility, while the latter tend to provide sites for adsorption, activation and migration of oxygen species.

As exhibited in Fig. 7-3b and Table 7-2, the ratio of O_{ads}/O_{tot} (total amount of O species, denoted O_{tot}) initially increases with the deficiency in lanthanum. This increase is probably due to a higher concentration of surface adsorbed oxygen species as described above, and thus to a higher concentration of surface oxygen vacancies [18]. However, the samples $La_{0.7}Mn$ and $La_{0.6}Mn$ without a high ratio of O_{ads}/O_{tot} but possess a high ratio of O_{latt}/O_{tot} (0.64 and 0.68) due to the formation of Mn_3O_4. Some literatures reported that the O_{ads} plays an important role in the oxidaiton of HCHO [19,20], while other researchers though that the active lattice oxygen species could also dominate the catalytic activity during the VOCs oxidation, such as in HCHO oxidation [21, 22] and toluene/ethanol/ethyl acetate oxidation [23]. Thus, it is considered that both of them plays a key role on the catalytic activity of VOCs decomposition. The mechanism involving lattice or surface adsorbed oxygen species might be related to the specific reaction environment during the oxidation process, such as the type of target pollutant, the different catalyst material, reaction temperature and so on.

Briefly, according to the value of La/Mn atomic ratio, the La-deficient perovskite could be divided into two different stages. Initially, samples in the composition range $0.8 \leq (La/Mn)_{ratio} < 1.0$ did not induce the obvious change of average manganese valence. Importantly, this la-deficient process resulted in the formation of cation vacancies such

as V_{La}, as well as especially V_{Mn} on the surface. These cation vacancies (V_{La} and V_{Mn}) facilitated the generation of surface adsorbed oxygen species [24], which were confirmed by the increased ratio of O_{ads}/O_{tot}. Afterwards, further decreasing the La/Mn ratio from 0.8 to 0.6, the structure of la-deficient perovskite was broken with the formation of parasitic manganese oxide (Mn_3O_4) phase. The average manganese valence of the samples decreased accordingly while the relative content of lattice oxygen species increased. It has been reported that the formed Mn_3O_4 phase could improve the catlytic performance of VOCs oxidation owing to the increase of the reactivity and mobility of lattice oxygen [23]. In addition, oxygen vacancies would be formed to maintain electrostatic balance when the low valence of Mn ($Mn^{3+/2+}$) appeared in the oxide as following [18], Mn^{4+}-(O^{2-})-Mn^{4+} = Mn^{3+}-($\square$)-Mn^{3+} + $0.5O_2$ or Mn^{3+}-(O^{2-})-Mn^{3+} = Mn^{2+}-($\square$)-Mn^{2+} + $0.5O_2$ ("$\square$" represents oxygen vacancy). Thus, the higher ratio of $Mn^{2+/3+}/Mn^{4+}$ probably means the higher content of oxygen vacancies in perovksite structure during the formation of surface Mn_3O_4, which play an important role as active site for oxygen migration between surface lattice oxygen and molecular oxygen, further impacting the catalytic activity of solid and the performance of VOCs oxidation.
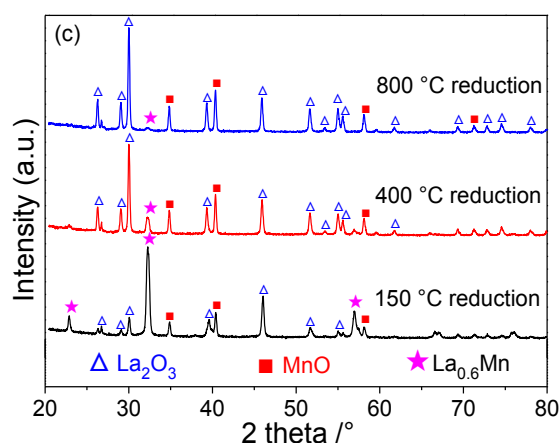
7.3.3 Reducibility studies
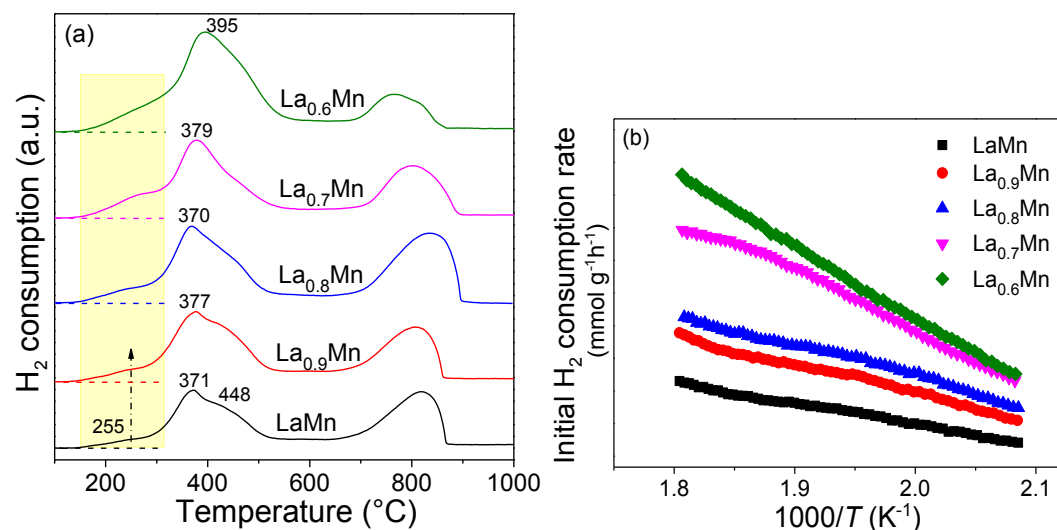
Figure 7-4 (a) H_2-TPR profiles of the five samples, (b) initial H_2 consumption rates of the five samples and (c) *in situ* XRD of $La_{0.6}Mn$ during temperature programmed reduction

Temperature programmed reduction (TPR) by H_2 was performed to investigate the reducibility of solid materials. The H_2-TPR profiles and the data are shown in Fig. 7-4a and Table 7-3, respectively. For LaMn, the main peak is centered at 371 °C, with a shoulder at 448 °C which can be assigned to the reduction of Mn^{4+} into Mn^{3+} and the reduction of a part of Mn^{3+} ions into Mn^{2+}, respectively. In the high temperature region of 600-1000 °C, the intense peak corresponds to the reduction of the remaining Mn^{3+} to Mn^{2+}. The calculated total H_2 consumption is 2.66 mmol/g (Table 7-3), which is close to the theoretical value (2.70 mmol/g) when all Mn ions (Mn^{3+} and Mn^{4+}) in LaMn perovskite were reduced to Mn^{2+}.

The main peak in the initial two La-deficient perovskite ($La_{0.9}Mn$ and $La_{0.8}Mn$) seemed to be stable (between 370 °C and 377 °C). In contrast, decreasing the atomic ratio of La/Mn, the main peak in the samples $La_{0.7}Mn$ and $La_{0.6}Mn$ shifted to higher temperatures (from 379 °C to 395 °C), which can be attributed to the generation of new phase Mn_3O_4 [10,25]. One should note that a small shoulder is observed in the low temperature around 255 °C with all samples (see the yellow area in Fig. 7-4a), which is most likely due to the removal of surface reactive oxygen species. In addition, its intensity increased gradually with the decrease of La/Mn atomic ratio.

To better understand the low temperature reducibility of these solids, the initial H_2 consumption rates of the first reduction shoulder before the occurrence of phase transformation have been calculated [26], and the results are indicated in Fig. 7-4b. Obviously, the initial H_2 consumption rate increased in the sequence of $La_{0.6}Mn >$ $La_{0.7}Mn > La_{0.8}Mn > La_{0.9}Mn > LaMn$. It means that the low temperature reducibility of these oxides followed the above order. These results indicated that the partial deficiency of the A-site (La^{3+}) cations promotes low temperature reducibility of the LaMn-based catalysts, as well as increasing the concentration of surface reactive species (such as O_2^{2-}, O^-, OH group and O_{latt}), which should have a beneficial influence on the oxidation of HCHO.

Table 7-3 H_2 consumption deduced from the H_2-TPR for the $La_{1-x}Mn$ samples

Samples	T_{max} reduction peaks (°C)		H_2 consumption (mmol/g）		
	t1	t2	peak 1	peak 2	Total
LaMn	371	818	1.56	1.10	2.66
$La_{0.9}Mn$	377	806	1.83	1.06	2.89
$La_{0.8}Mn$	370	830	1.71	1.34	3.05
$La_{0.7}Mn$	379	803	2.11	1.10	3.21
$La_{0.6}Mn$	395	766	2.81	0.58	3.39

As shown in Table 7-3, the total H_2 consumption at low temperature (t1) was 1.83, 1.71, 2.11 and 2.81 mmol/g for samples $La_{0.9}Mn$, $La_{0.8}Mn$, $La_{0.7}Mn$ and $La_{0.6}Mn$, respectively, while 1.52 mmol/g of H_2 was consumed in the same temperature range by the reference LaMn. Of note, the higher H_2 consumption (e.g. both calculated from the first peak and the total) herein does not correlate with the average oxidation state (AOS) of Mn, because the deficience of La in the sample could result in the higher content of Mn in the solid per unit mass, thus increasing a higher H_2 comsuption, which in line with the previous literature [8].

To get more insights from the reduction mechanism, an *in-situ* XRD experiment with the La$_{0.6}$Mn sample was conducted to evidence the progressive Mn^{4+} reduction process. The XRD of the sample reduced at 150 °C, 400 °C and 800 °C were collected in Fig. 7-4c. Unexpectedly, small peaks referred to the La$_2$O$_3$ and MnO were observed in the XRD pattern of La$_{0.6}$Mn at 150 °C under reducing conditions. Mn$_3$O$_4$ could be directly reduced into MnO and a small reduction peak of Mn$_3$O$_4$ at low temperature was also reported though the peak was found at somewhat higher temperature in the literature [25]. The reduction process started at low temperature (150 °C) further revealed the presence of labile species with different Mn-O (or La-O) strengths, which may be attributed to the generation of active Mn$_3$O$_4$ phase on the surface. Those species seemed not strongly stabilized within the oxide lattice, and can be regarded as the surface reactive species. Furthermore, the features of the La$_{0.6}$Mn sample were greatly weaken at 400 °C reduction which also confirmed a facilitated reduction of Mn$^{4+/3+}$ on the surface. The intensities of La$_2$O$_3$ and MnO reflections gradually increased with increasing the temperature of reduction. After 800 °C reduction, little characteristic peak of La$_{0.6}$Mn in the XRD pattern was seen, indicating the complete reducation of the sample.

7.3.4 Catalytic activity

Performance of all the samples for formaldehyde (HCHO) oxidation was exhibited on Fig. 7-5a. As seen, the La-deficient perovskites promoted the conversion efficiency of HCHO (into CO$_2$)in the sequence of La$_{0.6}$Mn > La$_{0.7}$Mn > La$_{0.8}$Mn > La$_{0.9}$Mn > LaMn. The T10, T50, and T90 reaction temperatures (corresponding to 10, 50, and 90% HCHO conversions, respectively) are summarized in Table 7-4. The T50 for the best catalyst La$_{0.6}$Mn is 128 °C, which is significantly lower than that of LaMn (145 °C).
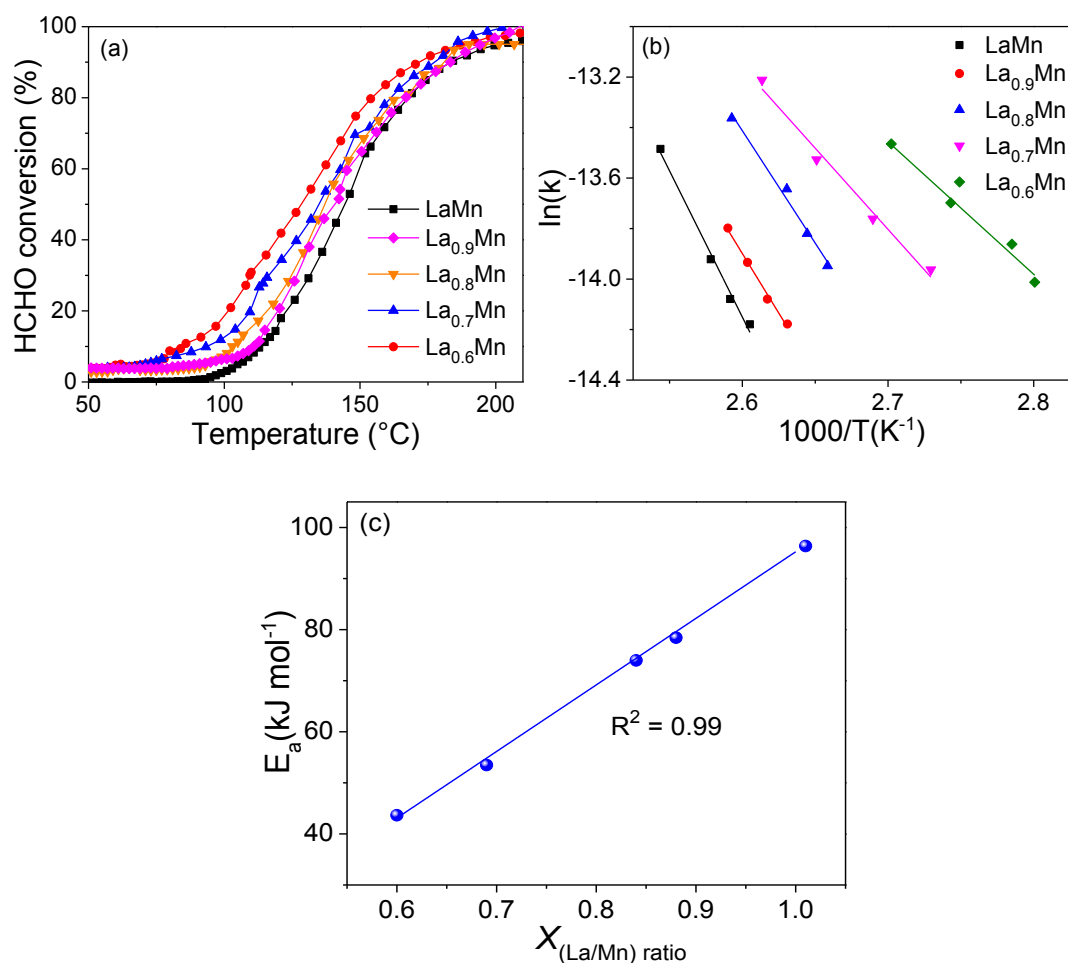
Figure 7-5 Catalytic performance of HCHO over the five samples: (a) HCHO conversion (into CO_2), (b) Arrhenius plots for the reaction, (c) Correlation of the apparent activation energy (E_a) with the atomic ratio of La/Mn (ICP)

The apparent activation energy (E_a) was also calculated at the HCHO conversion rate less than 20 % according to Arrhenius plots for each sample (Fig. 7-5b) [24,27]. The value of E_a for $La_{0.6}Mn$, $La_{0.7}Mn$, $La_{0.8}Mn$, $La_{0.9}Mn$ and LaMn samples were 43.7, 53.5, 74.0, 78.4 and 96.4 kJ/mol, respectively. E_a value of $La_{0.6}Mn$ (43.7 kJ/mol) is comparable to E_a of reported birnessites (34.3-56.6 kJ/mol) [24] and is lower than E_a of Ag/hollandite manganese oxide (51-57 kJ/mol) [28] and Au/MnO_2 (68.8-78.8 kJ/mol) [29]. This result is very promising since it implies that La-deficient LaMn perovskites can outperform noble metal-based catalysts in the case of HCHO oxidation. Interestingly, a clear correlation is observed between the E_a and the atomic ratio of

La/Mn (ICP) in the bulk and found the linear decrease of apparent activation energy with the increasing La/Mn ratio (Fig. 7-5c). In catalytic reaction, the surface active oxygen species such as O_{ads} and O_{latt} are generally proposed to be responsible for the oxidation of HCHO. These surface oxygen species most likely led to the difference in E_a.

Table 7-4 Catalytic activity of all samples for HCHO oxidation

Samples	HCHO conversion temperature (°C)		
	T10	T50	T90
LaMn	114	145	183
$La_{0.9}Mn$	111	141	183
$La_{0.8}Mn$	103	137	183
$La_{0.7}Mn$	93	135	177
$La_{0.6}Mn$	84	128	171

To resume, this catalytic improvement might stem from the cumulative effect of several factors at two different stage: (1) Initially, with the atomic ratio of La/Mn between 1.0 and 0.8, the samples ($La_{0.9}Mn$ and $La_{0.8}Mn$) without an observed new phase could provide more cation vacancies such as V_{La}, and especially V_{Mn} on the surface compared with the reference perovskite LaMn. Based on the characteristic and experimental results, we assumed that the presence of cation vacancies (V_{La} and V_{Mn}) could induce some unsaturated oxygen species and further facilitate the formation of surface active oxygen species as confirmed by the XPS and TPR analysis. This conclusion is well in line with the recent literature [24]. Of note, the cation vacancy (e.g. Mn) was also considered to enhance the lattice oxygen activity and lower the formation energy of oxygen vacancies [30]. All the metioned factors would improve the performance of HCHO oxidation.

And then (2), with the decreasing La/Mn ratio from 0.8 to 0.6, the samples $La_{0.7}Mn$

and $La_{0.6}Mn$ were obtained with parasitic phase on the surface (manganese oxide (Mn_3O_4)). The presence of Mn_3O_4 could enhance the relative content of surface lattice oxygen species as proved by XPS, and also promote the reactivity and mobility of lattice oxygen [23]. Besides, oxygen vacancies would be generated when more low valence of Mn formed in the structure of oxides. It is universally acknowledged that active lattice oxygen and abundant oxygen vacancies could improve the catlytic activity of solid for HCHO oxidation. Additionally, it should be noted that the la-deficient samples possessed the better low-temperature reducibility ranked as follows: $La_{0.6}Mn >$ $La_{0.7}Mn > La_{0.8}Mn > La_{0.9}Mn > LaMn$. This result suggested that the surface oxygen species in la-deficient samples becomes more reducible and reactive, which were also beneficial for catalytic oxidation of HCHO. In brief, the catalytic oxidation of HCHO herein may be considered as a function of the surface active oxygen species (O_{ads} and O_{latt}), oxygen vacancies and low-temperature reducibility of a catalyst.

7.3.5 Stability test and Moisture effect

Stability of the catalysts should be taken into account from a practical point of view. Fig. 7-6 illustrates the HCHO conversion into CO_2 and HCHO elimination in dry air stream over the sample$La_{0.6}Mn$ at T50. In the beginning, there is a certain rise of the conversion efficiency over the sample which might be due to highly active and non-renewable adsorbed oxygen species [22]. As seen, the sample $La_{0.6}Mn$ maintain a relatively stable activity performance, with a slightlydecrease of the HCHO conversion and elimination yields over time.
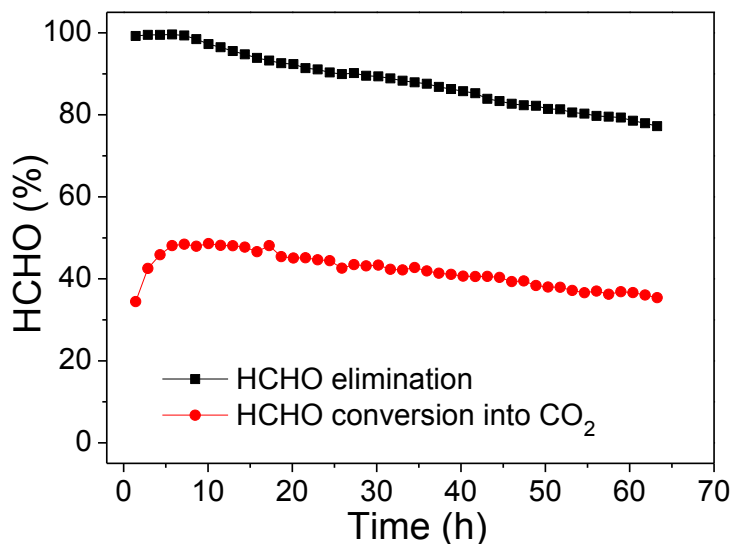
Figure 7-6 HCHO conversion with time on stream over $La_{0.6}Mn$

To investigate the possible changes of surface properties, the $La_{0.6}Mn$ catalyst was again characterized by XRD, XPS and TPR after test. The X-ray diffraction pattern (Fig. 7-7a) of the used catalyst do not change significantly over the course of the reaction though its intensity decreased a little. However, the TPR profile of the used $La_{0.6}Mn$ displayed in Fig. 7-7b reveals that the amount of consumed H_2 in the low temperature region (100-600 °C) is lower (2.22 mmol/g) to the fresh $La_{0.6}Mn$ (2.81 mmol/g), implying that more Mn species with lower valence state are present in the used catalysts after HCHO oxidation. Moreover, the onset temperature of reduction for the used catalyst is shifted to an higher temperature (225 °C instead of 147 °C). Additionally, a shoulder (marked as red star in Fig. 7-7b) can be clearly observed at 465 °C. All the H_2-TPR data suggest that theLa$_{0.6}$Mn catalyst reducibility is decreased after the catalytic test, which is in line with the decrease of its catalytic activity on stream.
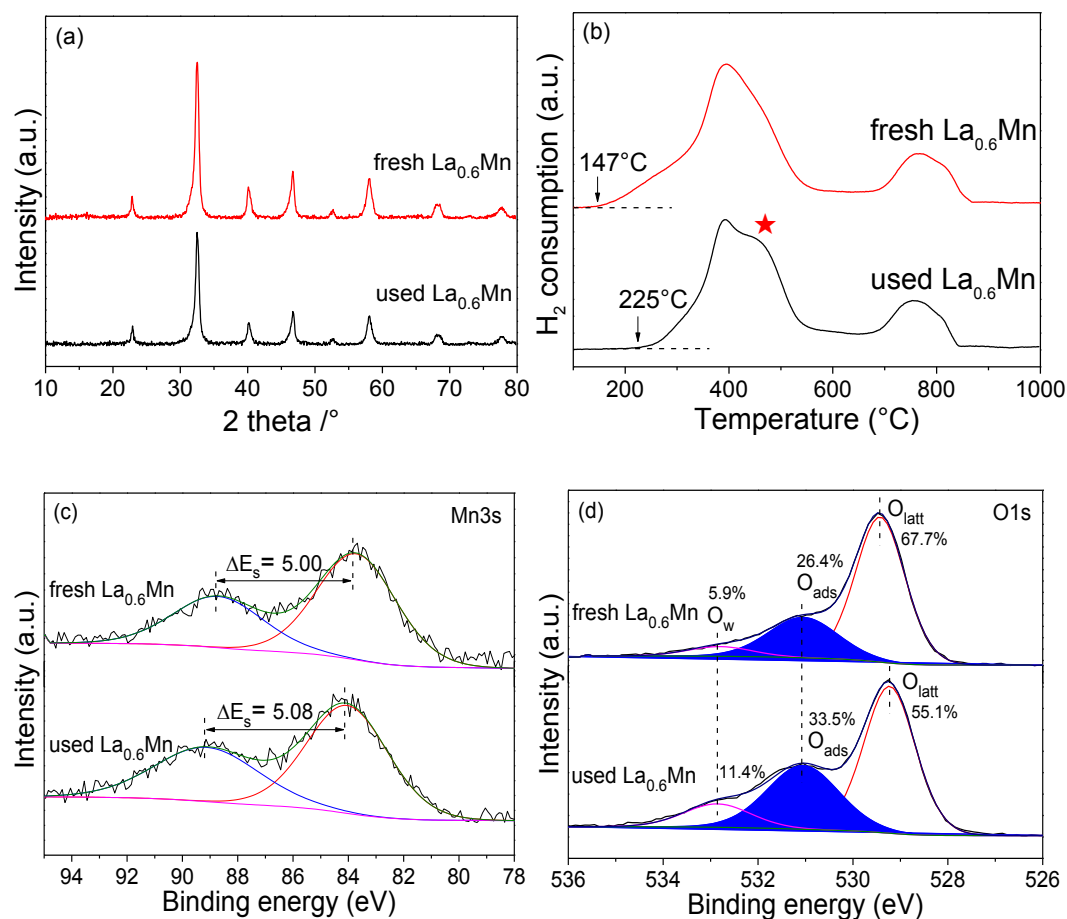
Figure 7-7 Characterization of (a) XRD, (b) TPR, XPS spectra of (c) Mn 3s, and (d) O1safter HCHO stability test

Similarly, a slight change on XPS spectra in the Mn 3s region was observed compared to the fresh catalyst (Fig. 7-7c). The surface average oxidation state of Mn decreased slightly from 3.33 to 3.24 after HCHO oxidation, which is in good agreement with TPR. Notably, no serious consumption of higher valence of Mn was found here, which may imply that the reactive Mn ions in $La_{0.6}Mn$ would improve the catalytic action of the redox cycle in which $Mn^{4+/3+}$ was reduced in the course of supplying the sufficient oxygen species for the oxidation reaction, and then was re-oxidized via the uptaking of molecular oxygen through the oxygen transfer mechanism [21,17].

XPS spectra in the O1s region of the catalyst before and after reaction is shown in Fig. 7-7d. After test, the relative content of lattice oxygen species (O_{latt}) decreased

considerably from 67.7% to 55.1%. This correlates with the observed global manganese reduction as O_{latt} were consumed during HCHO oxidation.Also, an increased relative content of surface adsorbed oxygen species (O_{ads}) and surface water (O_w) were seen in the used catalyst. The enhancement might be due to the formation of surface oxygen species (mainly superficial -OH groups) and adsorbed water respectively, as a result of the decomposition of adsorbed formate species ($HCOO^-_{ads}$) [31], which is an intermediate product of oxidation of HCHO. Also, Lin et al.reported that part of O_{ads} increase could be also linked to adsorption of O_2 molecules at the surface of catalyst. Namely, O_2 molecules adsorbed on oxygen vacancy would dissociate to replenish the active oxygen species [32]. This slight enhancement of O_{ads} would counterbalance the decrease of O_{ads} (or further O_{latt}) during HCHO oxidaiton process, and thus maintain the activity over long periods.

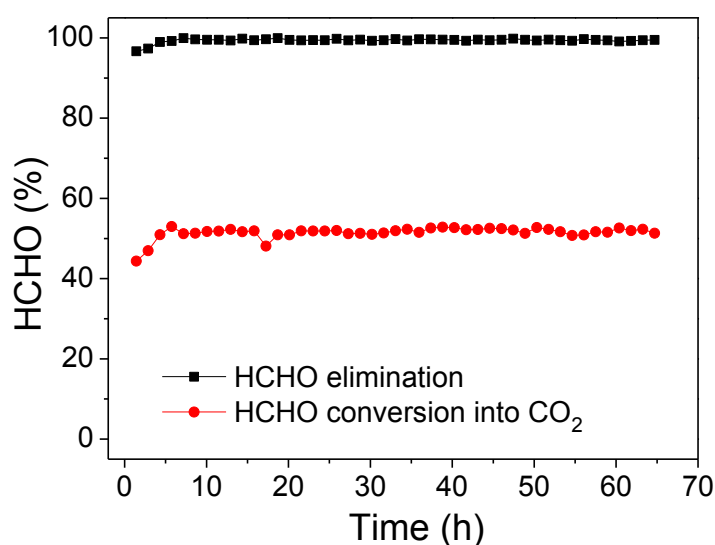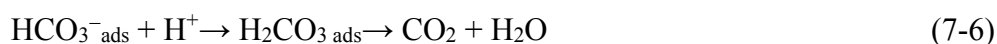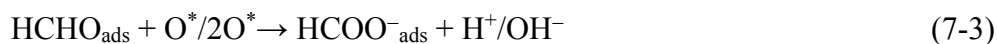**Figure 7-8** Effect of moisture on HCHO conversion with time on stream over $La_{0.6}Mn$

Mild temperature catalytic oxidation is known to be greatly affected by moisture, the presence of which is unavoidable in most practical applications. Previous research reported that the moisture was considered to result in a loss of HCHO oxidation activity due to competitive adsorption on active sites [21]. However, a recent study reported

that a controlled moisture is not only beneficial to the desorption of carbonate adsorbed on the active sites, but it also facilitates the regeneration of surface -OH groups, greatly enhancing the activity of a catalyst [19]. Here we evaluated the catalytic activity of La-deficient $La_{0.6}Mn$ in humid (corresponding to a relative moisture capacity of 46% at room temperature) air stream over time. Results are shown in Fig. 7-8. Compared to the catalytic results in dry conditions (Fig. 7-6), the presence of H_2O greatly improved the catalytic activity of $La_{0.6}Mn$, with constant HCHO elimination and conversion yields up to 63 hours.

In a typical HCHO oxidation process, HCHO is first adsorbed on the catalyst surface, and then oxidized by surface active oxygen species (O^*: O_2^-, O^-, OH group, O^{2-}, etc) into formate species (Eq. (7-3)) [19,24,30]. The further oxidation of formate by O^* generates carbonate species (Eq. (7-4)) and finally CO_2 (Eq. (7-5) and Eq. (7-6)) [19,33]. The consumed surface active oxygen species such as O_2^-, O^- can be regenerated by the complex migration between surface O_{latt} and oxygen vacancy with the continuous dissociation of molecular oxygen, while the transfer from gas-phase oxygen to O_{latt} can be completed via the oxygen transfer mechanism [18,19]. Additionally, the surface OH groups can be also replenished via the reaction between active oxygen (O_2^-, O^-, etc.) and water (Eq. (7-7)). Thus, the catalytic cycle is looped.

$$HCHO_{ads} + O^*/2O^* \rightarrow HCOO^-_{ads} + H^+/OH^- \qquad (7\text{-}3)$$

$$HCOO^-_{ads} + O^* \rightarrow HCO_3^-_{ads} \qquad (7\text{-}4)$$

$$HCO_3^-_{ads} + OH^- \rightarrow CO_3^{2-}_{ads} + H_2O \qquad (7\text{-}5)$$

$$HCO_3^-_{ads} + H^+ \rightarrow H_2CO_{3\,ads} \rightarrow CO_2 + H_2O \qquad (7\text{-}6)$$

$$H_2O + O^* \rightarrow 2OH^- \qquad (7\text{-}7)$$

In our condition of the la-deficiency sample $La_{0.6}Mn$ with Mn_3O_4 formed on the surface and as reported in the case of manganese oxide [19], moisture may compensate

the surface hydroxyl groups and help avoiding an accumulation of formate or carbonate species on the surface of a catalyst [20]. This process facilitated the activation of H_2O and chemisorbed oxygen, therefore resulting in higher performance of the catalyst for the HCHO oxidation.

7.4 Conclusions

This work makes it possible to develop the nonstoichiometric/la-deficient perovskites for the complete oxidation of HCHO. Following the tests, the perovskite structure becomes more active for the catalytic oxidation of HCHO by the la-deficient synthesis. The sample $La_{0.6}Mn$ presented the highest activity with a T50 of 128°C and it apparent activation energy (E_a) is only 43.7 kJ/mol in HCHO oxidation. The La deficiency of perovskite has a benefical for the generation of cation vacancies such as V_{La} and V_{Mn}. These cation vacancies presents higher ratio of surface adsorbed xygen species which is more reducible and active. Moreover, the Mn_3O_4 phase would be formed besides the main phase of perovskite during the material synthesis of $La_{0.6}Mn$ and $La_{0.7}Mn$. The presence of Mn_3O_4 will further improve the performance of HCHO oxidation owing to the enhanced reactivity and mobility of lattice oxygen, as well as the low-temperature reducibility of metal species. In brief, these results shed light on the catalytic promoting effect of nonstoichiometric perovskite on HCHO oxidation. This would be beneficial to the development of low-cost and high-efficiency materials for indoor pollution control. Also, efforts should be still made to improve its room temperature catalytic activity for practical use.

References

[1] B.C. Tofield, W.R. Scott, Oxidative nonstoichiometry in perovskites, an experimental survey; the defect structure of an oxidized lanthanum manganite by powder neutron diffraction, J. Solid State Chem. 10 (1974) 183-194.

[2] J.A.M. Van Roosmalen, E.H.P. Cordfunke, R.B. Helmholdt, H.W. Zandbergen. The defect chemistry of $LaMnO_{3\pm\delta}$: 2. Structural aspects of $LaMnO_{3+\delta}$. J. Solid State Chem. 110 (1994) 100-105.

[3] J.A. Alonso, M.J. Martinez-Lope, M.T. Casais, J.L. MacManus-Driscoll, P.S. De Silva, L.F. Cohen, M.T. Fernandez-Diaz, Non-stoichiometry, structural defects and properties of $LaMnO_{3+\delta}$ with high δ values ($0.11 \leq \delta \leq 0.29$), J. Mater. Chem. 7 (1997) 2139-2144.

[4] G. Dezanneau, A. Sin, H. Roussel, M. Audier, H. Vincent, Magnetic properties related to structure and complete composition analyses of nanocrystalline $La_{1-x}Mn_{1-y}O_3$ powders, J. Solid State Chem. 173 (2003) 216-226.

[5] A.N. Ulyanov, H.J. Shin, D.S. Yang, S.V. Savilov, N.E. Pismenova, E.A. Goodilin, Hybridization of electronic states and magnetic properties of self-doped $La_{1-x}MnO_{3+\delta}$ ($0 \leq x \leq 0.15$) perovskites: XANES study, J. Magn. Magn. Mater. 458 (2018) 134-136.

[6] R. Spinicci, A. Tofanari, A. Delmastro, D. Mazza, S. Ronchetti, Catalytic properties of stoichiometric and non-stoichiometric $LaFeO_3$ perovskite for total oxidation of methane, Mater. Chem. Phys. 76 (2002) 20-25.

[7] A. Delmastro, D. Mazza, S. Ronchetti, M. Vallino, R. Spinicci, P. Brovetto, M. Salis, Synthesis and characterization of non-stoichiometric $LaFeO_3$ perovskite. Mater. Sci. Eng. B 79 (2001) 140-145.

[8] J. Faye, A. Baylet, M. Trentesaux, S. Royer, F. Dumeignil, D. Duprez, S. Valange, J.M. Tatibouët, Influence of lanthanum stoichiometry in $La_{1-x}FeO_{3-\delta}$ perovskites on their structure and catalytic performance in CH_4 total oxidation. Appl. Catal. B 126 (2012) 134-143.

[9] J. Chen, M. Shen, X. Wang, G. Qi, J. Wang, W. Li, The influence of nonstoichiometry on $LaMnO_3$ perovskite for catalytic NO oxidation, Appl. Catal. B 134 (2013) 251-257.

[10] Z. Gao, H. Wang, H. Ma, Z. Li, Preparation and characterization of the non-stoichiometric La-Mn perovskites, J. Alloy. Compd. 646 (2015) 73-79.

[11] V. Markovich, I. Fita, D. Mogilyansky, A. Wisniewski, R. Puzniak, L. Titelman, L. Vradman, G. Gorodetsky, Magnetic properties of nanocrystalline $La_{1-x}MnO_{3+\delta}$ manganites: size effects, J. Phys. Condens. Mat. 19 (2007) 346210.

[12] A.R. Shelke, N.G. Deshpande, Influence of the Calcination Temperature on the Combustion Synthesized Perovskite $LaMnO_3$ Compound, J. Nano-Electron. Phys. 7 (2015) 03009-1.

[13] Y. Yang, J. Huang, S. Wang, S. Deng, B. Wang, G. Yu, Catalytic removal of gaseous unintentional POPs on manganese oxide octahedral molecular sieves, Appl. Catal. B 142-143 (2013) 567-568.

[14] B.P. Barbero, J.A. Gamboa, L.E. Cadús, Synthesis and characterisation of $La_{1-x}Ca_xFeO_3$ perovskite-type oxide catalysts for total oxidation of volatile organic compounds, Appl.Catal. B 65 (2006) 21-30.

[15] V.P. Santos, M.F.R. Pereira, J.J.M. Órfão, J.L. Figueiredo, The role of lattice oxygen on the activity of manganese oxides towards the oxidation of volatile organic compounds, Appl. Catal. B 99 (2010) 353-363.

[16] N.A. Merino, B.P. Barbero, P. Eloy, L.E. Cadús, $La_{1-x}Ca_xCoO_3$ perovskite-type oxides: identification of the surface oxygen species by XPS, Appl. Surf. Sci. 253 (2006) 1489-1493.

[17] J.G. Deng, L. Zhang, H.X. Dai, H. He, C.T. Au, Strontium-doped lanthanum cobaltite and manganite: highly active catalysts for toluene complete oxidation, Ind. Eng. Chem. Res. 47 (2008) 8175-8183.

[18] J.J. Zhu, H.L. Li, L.Y. Zhong, P. Xiao, X.L. Xu, X.G. Yang, Z. Zhao, J.L. Li, Perovskite oxides: Preparation, characterizations, and applications in heterogeneous catalysis, ACS Catal. 4 (2014) 2917-2940.

[19] J.L. Wang, P.Y. Zhang, J.G. Li, C.J. Jiang, R. Yunus, J. Kim, Room-temperature oxidation of formaldehyde by layered manganese oxide: effect of water, Environ. Sci. Technol. 49 (2015) 12372-12379.

[20] C.B. Zhang, F.D. Liu, Y.P. Zhai, H. Ariga, N. Yi, Y.C. Liu, K. Asakura, Alkali- metal-promoted Pt/TiO_2 opens a more efficient pathway to formaldehyde oxidation at ambient

temperatures, Angew. Chem. Int. Ed. 51 (2012) 9628-9632.

[21] X.F. Tang, Y.G. Li, X.M. Huang, Y. Xu, H.Q. Zhu, J.G. Wang, W.J. Shen, MnO_x-CeO_2 mixed oxide catalysts for complete oxidation of formaldehyde: effect of preparation method and calcination temperature, Appl. Catal. B 62 (2006) 265-273.

[22] J.H. Zhang, Y.B. Li, L. Wang, C.B. Zhang, H. He, Catalytic oxidation of formaldehyde over manganese oxides with different crystal structures, Catal. Sci. Technol. 5 (2015) 2305-2313.

[23] V.P. Santos, M.F.R. Pereira, J.J.M. Órfão, J.L. Figueiredo, The role of lattice oxygen on the activity of manganese oxides towards the oxidation of volatile organic compounds, Appl. Catal. B 99 (2010) 353-363.

[24] J.L. Wang, J.G. Li, C.J. Jiang, P. Zhou, P.Y. Zhang, J.G. Yu, The effect of manganese vacancy in birnessite-type MnO_2 on room-temperature oxidation of formaldehyde in air, Appl. Catal. B 204 (2017) 147-155.

[25] E.D. Stobbe, B.A. De Boer, J.W. Geus, The reduction and oxidation behaviour of manganese oxides, Catal. Today 47 (1999) 161-167.

[26] F. Wang, H. Dai, J. Deng, G. Bai, K. Ji, Y. Liu, Manganese oxides with rod-, wire-, tube-, and flower-like morphologies: highly effective catalysts for the removal of toluene, Environ. Sci. Technol. 46 (2012) 4034-4041.

[27] Y. Wang, X. Zhu, M. Crocker, B. Chen, C. Shi, A comparative study of the catalytic oxidation of HCHO and CO over $Mn_{0.75}Co_{2.25}O_4$ catalyst: The effect of moisture, Appl. Catal. B 160 (2014) 542-551.

[28] Y. Chen, Z. Huang, M. Zhou, P. Hu, C. Du, L. Kong, J.M. Chen, X.F. Tang, The active sites of supported silver particle catalysts in formaldehyde oxidation, Chem. Commun. 52 (2016) 9996-9999.

[29] J. Chen, D. Yan, Z. Xu, X. Chen, X. Chen, W.J. Xu, H.P. Jia, J. Chen, A novel redox precipitation to synthesize Au-doped α-MnO_2 with High Dispersion toward low-temperature oxidation of formaldehyde, Environ. Sci. Technol. 52 (2018) 4728-4737.

[30] S. Rong, K. Li, P. Zhang, F. Liu, J. Zhang, Potassium associated manganese vacancy in birnessite-type manganese dioxide for airborne formaldehyde oxidation, Catal. Sci. Technol. 8 (2018) 1799-1812.

[31] J. Quiroz, J.M. Giraudon, A. Gervasini, C. Dujardin, C. Lancelot, M. Trentesaux, J.F. Lamonier, Total oxidation of formaldehyde over MnO_x-CeO_2 catalysts: The effect of acid treatment, ACS Catal. 5 (2015) 2260-2269.

[32] X.T. Lin, S.J. Li, H. He, Z. Wu, J. Wu, L.M. Chen, D.Q. Ye, M.L. Fu, Evolution of oxygen vacancies in MnO_x-CeO_2 mixed oxides for soot oxidation, Appl. Catal. B 223 (2018) 91-102.

[33] C. Ma, D. Wang, W. Xue, B. Dou, H. Wang, Z. Hao, Investigation of formaldehyde oxidation over Co_3O_4-CeO_2 and Au/Co_3O_4-CeO_2 catalysts at room temperature: effective removal and determination of reaction mechanism, Environ. Sci. Technol. 45 (2011) 3628-3634.

Chapter 8 General conclusion and perspectives

8.1 General conclusion

Based on the results obtained in Chapter 3 to Chapter 7, it was clearly demonstrated that multiples factors can affect the heterogeneous advanced oxidation processes in water, as well as the thermal catalytic oxidation of formaldehyde in gas. In addition to the key reaction parameters, several important points concerning the surface properties of the catalysts affect the catalytic activity and especially their surface area, electron transfer capacity, active site, and structure defects.

Below are drawn achievements of the PhD work:

(1) We demonstrated the better performance of spinel precursors for catalytic compared to highly crystalline spinels, which is rarely reported. It infers that more attention should be paid to improving some key parameters on the material prepared in this study, such as surface area, active site and electron transfer capacity rather than just considering the crystal phase to enhance the catalytic activity.

(2) FTIR spectra of adsorbed pyridine experiments showed that the amount of Lewis acid sites on the surface of spinel $CuAl_2O_4$ decreased with increasing calcination temperature of the samples. Cyclic voltammetry (CV) behaviors of $CuAl_2O_4$ with ozone were carried out to clarify the probable role of electron transfer/redox couple of copper at water-catalyst interface.

(3) Experiments indicated that $CuAl_2O_4$ is a promising catalyst for ozonation of contaminants in aqueous solution. Also the catalytic improvement of $CuAl_2O_4$ arise from a synergic effect between CuO and Al_2O_3 promoting a higher decomposition rate of aqueous ozone. $\equiv Al^{3+}$ could act as a reservoir for surface active sites such as hydroxyl groups and Lewis acid sites, while $\equiv Cu^{2+}$ could provide the possibility of electron transfer with ozone.

(4) Employing spinel $CuFe_2O_4$ in combination with peroxymonosulfate can degrade

bisphenol A effectively. The degradation reaction mainly takes place on the solid surface and the leaching of ions during the reaction remains very limited.

(5) The surface-bound $SO_4^{\bullet-}{}_{ads}$ and $HO^{\bullet}{}_{ads}$ generated by a surface catalyzed-redox cycle involving both Fe(III) and Cu(II), are postulated to be responsible for the degreadation of bisphenol A. The superior catalytic activity of $CuFe_2O_4$ was ascribed to the synergy effect of Cu and Fe active site on the surface.

(6) The Mn-based perovskites were used in catalytic oxidation of formaldehyde in the gas phase for the first time.

(7) The transformation of $LaMnO_3$ perovskite into pure ε-MnO_2 based on acid etching was investigated comprehensively for the first time.

(8) The obtained MnO_2 materials exhibited a superior catalytic activity on HCHO oxidation and excellent catalytic stability in the presence of moisture.

(9) Experimental results indicated that the HCHO oxidation was possibly related to cumulated effects of meso/macro-porous morphology with a large surface area, high redox ability and an abundance of active surface oxygen species on the surface of catalyst.

(10) Alkali and alkaline earth metals-promoted $LaMnO_3$ perovskites were synthesized, following cations doping ($La_{0.8}A_{0.2}MnO_3$ with A = K, Na, Sr, Ca), post-synthesis impregnation (LMO-Na) and alkali treatment (LMO-OH).

(11) Based on the T50, the overall catalyst ranking in terms of the catalytic activity was $La_{0.8}K_{0.2}MnO_3$> $La_{0.8}Na_{0.2}MnO_3$> $La_{0.8}Sr_{0.2}MnO_3$> $LaMnO_3 \approx$ $La_{0.8}Ca_{0.2}MnO_3 \approx$ LMO-OH $\approx$ LMO-Na. Additionally, a tentative mechanism was proposed.

(12) Stability tests, under humid and dry conditions, were conducted on these alkali-modified catalysts. A gradual deactivation of the substituted perovskites (K, Na, Sr) was observed. This may due to the blocking effects caused by the adsorbed

oxidation intermediates, inducing the loss of surface active oxygen species and high-valence Mn.

(13) Study of La-deficient La$_x$MnO perovskite-based materials indicated that the cation vacancies inside would affect their physico-chemical properties.

(14) The cation La and Mn vacancies in perovskite could increase the concentration of active oxygen species, improve the low-temperature reducibility at their surface to some degree. In contrast, further La vacancy would result in the formation of Mn$_3$O$_4$ as a parasitic phase. The surface Mn$_3$O$_4$ could increase the concentration, the mobility and reactivity of the active (lattice) oxygen species which play an important role in the enhancement of HCHO oxidation.

8.2 Perspectives

➤ In heterogeneous reactions such as catalytic ozone and sulfate radical based AOPs, the exact impact of the solids surface properties (e.g. surface oxygen species, anion/cation vacancy) is not very clear though we are convinced that it plays an important role. Thus an in-depth study using *operando* characterizations would be required to better apprehend it.

➤ In AOPs, uauslly there are many kinds of reactive oxygen species (HO$^{\bullet}$, SO$_4^{\bullet-}$, O$_2^{\bullet-}$ and ^{1}O$_2$ et al.) generated in the reaction. Thus future investigations on the quantitative calculation of different reactive radicals indeed involved in the oxidation of pollutants would be highly interesting.

➤ Lanthanum manganite perovskites have a promising application for catalytic oxidation of HCHO. The mechanism, role of of A site (La) as well as B site (Mn) participating in oxidation process need to be further clarified by coupling the results of characterization techniques such as *in-situ* FTIR and TOF-SIMS.

➤ For the structural defects in the perovskite, we need also to use more direct

techniques to investigate the distribution and content of some defects such as oxygen vacancy (using UV Raman spectra) and cation vacancy (using extended X-ray Absorption Fine Structure (EXAFS)). And then evaluate the influence of each defect in the heterogeneous oxidation.

➢ Very recently, perovskite-type oxides have been widely reported for the treatment of organic pollutants in water by heterogeneous advanced oxidation processes, and the related research could be expanded and deepened.

Publications

[1] **<u>Yin Xu</u>**, Jia Ai, Hui Zhang, The mechanism of degradation of bisphenol A using the magnetically separable $CuFe_2O_4$/peroxymonosulfate heterogeneous oxidation process, ***Journal of Hazardous Materials*** 309 (2016) 87-96.

[2] **<u>Yin Xu</u>**, ZiyanLin, Yanyan Zheng, Jean-Philippe Dacquin, Sebastien Royer, Hui Zhang[*], Mechanism and kinetics of catalytic ozonation for elimination of organic compounds with spinel-type $CuAl_2O_4$ and its precursor, ***Science of The Total Environment*** 651 (2019) 2585-2596.

[3] **<u>Yin Xu</u>**, Ziyan Lin, Hui Zhang[*], Mineralization of sucralose by UV-based advanced oxidation processes: UV/PDS versus UV/H_2O_2, ***Chemical Engineering Journal*** 285 (2016) 392-401.

[4] **<u>Yin Xu</u>**, Ziyan Lin, Yan Wang, Hui Zhang[*], The UV/peroxymonosulfate process for the mineralization of artificial sweetener sucralose, ***Chemical Engineering Journal*** 317 (2017) 561-569.

[5] **<u>Yin Xu</u>**, Heng Lin, Yukun Li, Hui Zhang[*], The mechanism and efficiency of MnO_2 activated persulfate process coupled with electrolysis. ***Science of The Total Environment*** 609 (2017) 644-654.

[6] **<u>Yin Xu</u>**, Ying Wu, Wei Zhang, Xiaohui Fan, Yan Wang[*], Hui Zhang[*], Performance of artificial sweetener sucralose mineralization via UV/O_3 process: Kinetics, toxicity and intermediates, ***Chemical Engineering Journal*** 353 (2018) 626-634.

[7] **<u>Yin Xu</u>**, Xin Zhong, Hui Zhang, Absorption kinetics of ozone with ultrasonic radiation in gas-liquid-solid three phase loop-lift reactor, ***Water Science and Technology*** 73 (2016) 1796-1801.

[8] **<u>Yin Xu</u>**, Jérémy Dhainaut, Guillaume Rochard, Jean-Philippe Dacquin, Anne-Sophie Mamede, Jean-Marc Giraudon, Jean-François Lamonier, Hui Zhang[*], and Sébastien Royer[*], Hierarchical porous ε-MnO_2 from perovskite precursor: Application to the formaldehyde total oxidation, 2019, ***To be submitted***.

[9] **<u>Yin Xu</u>** et al., Investigation of formaldehyde total oxidation using alkali and alkaline-earth doped perovskites, 2019, ***To be submitted***.

[10] **<u>Yin Xu</u>** et al., Effect of nonstoichiometric manganese-based $La_{1-x}MnO_{3-\delta}$ perovskites for catalytic oxidation of formaldehyde, 2019, ***To be submitted***.